Dissertation
submitted to the
Combined Faculties for the Natural Sciences and for Mathematics
of the Ruperto-Carola University of Heidelberg, Germany
for the degree of
Doctor of Natural Sciences

Put forward by

Diplom-Physicist: Marcel Schuh

Born in: Bad Friedrichshall, Germany

Oral examination: 22.06.2011

Study of Higher Order Modes in Superconducting Accelerating Structures for Linac Applications

Referees: Prof. Dr.   André Schöning

                        Dr.   Carsten P. Welsch

Zusammenfassung

Moden höherer Ordnung (HOMs) können ein limitierender Faktor für den Betrieb supraleitender Hohlraumresonatoren in Linearbeschleunigern bei hohen Strahlströmen, hohem Tastverhältnis und komplexer Pulsstruktur sein. Aus diesem Grund muss das gesamte HOM-Spektrum bereits während der Designphase solcher Beschleuniger analysiert werden, um potentiell gefährliche Moden zu identifizieren und die Anforderungen an deren Dämpfung festzulegen.

Zu diesem Zweck wurde im Rahmen dieser Arbeit das Strahldynamikprogramm *Simulation of higher order Mode Dynamics* (SMD) entwickelt, das sich auf die Wechselwirkung zwischen HOMs und Strahl konzentriert. Das Programm ermöglicht eine detaillierte Analyse des Strahlverhaltens in Gegenwart von HOMs unter Berücksichtigung verschiedener wichtiger Effekte wie unterschiedliche Eingangsstrahlverteilungen, Pulsstrukturen, Fehler im Hochfrequenzsystem oder Positionierungsungenauigkeiten einzelner Elemente.

SMD wird verwendet, um den Einfluss von HOMs im *Superconducting Proton Linac* (SPL) am CERN im Detail zu untersuchen, insbesondere in Bezug auf deren Potential, Strahlinstabilitäten in der longitudinalen und transversalen Ebene zu verursachen. Basierend auf diesen Rechnungen werden die Anforderungen an HOM-Koppelantennen festgelegt. Zusätzlich werden die Linearbeschleuniger der *European Spallation Source* (ESS) und der *Spallation Neutron Source* (SNS) in Bezug auf den Einfluss von HOMs untersucht und die Ergebnisse mit den SPL-Simulationen verglichen.

Abstract

Higher Order Modes (HOMs) can severely limit the operation of superconducting cavities in a linear accelerator with high beam current, high duty factor and complex pulse structure. Therefore, the full HOM spectrum has to be analysed in detail to identify potentially dangerous modes already during the design phase and to define their damping requirements.

For this purpose a dedicated beam dynamics simulation code, *Simulation of higher order Mode Dynamics* (SMD), focusing on beam-HOM interaction, has been developed in the frame of this project. SMD allows to analyse the beam behaviour under the presence of HOMs, taking into account many important effects, such as for example the HOM frequency spread, beam input jitter, different chopping patterns, as well as klystron and alignment errors.

SMD is used to investigate in detail into the effects of HOMs in the *Superconducting Proton Linac* (SPL) at CERN and in particular their potential to drive beam instabilities in the longitudinal and transverse direction. Based on these results, HOM damping requirements for the HOM coupler design are then defined. In addition, the linear accelerators of the *European Spallation Source* (ESS) and the *Spallation Neutron Source* (SNS) are analysed with respect to HOM impact and the results are compared with the SPL simulations.

Acknowledgements

Contents

Symbols

$\Gamma(x)$	Gamma function
$\tilde{\alpha}(s)$, $\tilde{\beta}(s)$, $\tilde{\gamma}(s)$	Twist parameters
β	relativistic factor
$\bar{\beta}$	coupling
β_s	$\beta_s c$ - synchronous particle velocity
γ	relativistic γ
ϵ	phase space area
ϵ; ϵ_0, ϵ_r	permittivity free space, material
λ	RF wave length
μ; μ_0, μ_r	permeability; free space, material
π	mathematical constant: ratio of the circle's circumference to its diameter
ρ	electric charge density
σ	standard deviation
ϕ; ϕ_s	phase of particle with respect to RF field; synchronous phase
ω	angular frequency
$\vec{B}$	B-Field vector
$\vec{D}$	D-Field vector
E	total energy
$\vec{E}$	E-Field vector
E_z	accelerating field - z component of E-field
E_0	average accelerating field
$\vec{F}$	force vector
F	force
G	geometric constant
G_q	quadrupole gradient
$\vec{H}$	H-Field vector
$\Im$	imaginary part of an imaginary number
I; I_b	current; beam current
$\vec{J}$	current density

$J_m(x)$	Bessel function first kind and m^th order
$J'_m(x)$	first derivative of the Bessel function first kind and m^th order
L	defined length of an object
M	transfer matrix
N	amount of something
P	power
$\Re$	real part of an imaginary number
Q; Q_0, Q_L, Q_ex	quality factor; unloaded, loaded, external
(R/Q)	shunt impedance divided by quality factor
T_Index; T_d, T_d	time period; bunch repetition time, decay time
$T(\beta)$	transit time factor
T	temperature
U	energy
V	voltage
W	kinetic energy
c	speed of light
f	frequency
i	imaginary unit
$j_{n,m}$	n^th zero of the mth order Bessel function of first kind
$j'_{n,m}$	n^th zero of the first derivative of the mth order Bessel function of first kind
$\vec{k}$	wave vector
k_n	mode loss factor
l	length
m, n, p	mode index
m, m_{H^-}	mass of particle, mass of H^-
$\vec{n}$	normal vector
$\vec{p}$	momentum
q	charge of a particle
r	radius
r_a	shunt impedance
s	position
t	time
v, v_g, v_{ph}, v_s	velocity: particle, group, phase, synchronous particle
$\vec{x}$	position
$\vec{x}(x, y, z)$	Cartesian coordinates
$\vec{x}(r, \theta, z)$	Cylindrical coordinates

Acronyms and Abbreviations

ADS	Accelerator Driven System
AKS	Advanced Krylov Subspace Method
CAD	Computer Aided Design
CERN	European Organization for Nuclear Research
CLIC	Compact Linear Collider
CML	Chopping Machine Line
CPU	Central Processing Unit
CST	Computer Simulation Technology
CW	Continous Wave
EDA	Electronic Design Automation
EM	Electromagnetic
ERL	Energy Recovery Linac
ESS	European Spallation Source
EURISOL	European Isotope Separation On-Line radioactive ion beam facility
FDM	Finite Differential Method
FEL	Free Electron Laser
FEM	Finite Element Method
FIT	Finite Integration Technique
FPC	Fundamental Power Couper
FVM	Finite Volume Method
HFSS	High Frequency Structure Simulator
HOM	Higher Order Modes
ILC	International Linear Collider
ISOLDE	Isotope Separator OnLine DEvice
JDM	Jacobi-Davidson Method
LEP	Large Electron-Positron Collider
LHC	Large Hadron Collider
LHeC	Deep Inelastic Electron-Nucleon Scattering at the LHC
Linac	Linear Accelerator
ML	Machine Line

MS	Microsoft
MWS	Mircowave Studio
OS	Operating System
PDE	Partial Differential Equations
PEC	Perfect Electric Conducter
PSB	PS Booster
PUP	Power Upgrade Program for the SNS linac
R&D	Research and Development
RAM	Random Access Memory
RF	Radio Frequency
RIB	Radioactive Ion Beams
SC	Superconductivity
SF	SUPERFISH
SMD	Simulation of Higher Order Mode Dynamics
SNS	Spallation Neutron Source USA
SPL	Superconducting Proton Linac
SRF	Superconducting Radio Frequency
TE	Transverse Electric
TM	Transverse Magnetric
VBA	Visual Basic for Application
VBS	Visual Basic Script

List of Tables

Chapter 1

Introduction and Motivation

Since the 1920s particle accelerators have played an important role in research into the structure of matter. Over the last decades the need for accelerators for various applications has steadily increased. Today they are used in many fields, for example, in cancer therapy, as light or neutron sources, or to investigate the origin of our universe with huge particle colliders such as the *Large Hadron Collider* (LHC) [1, 2] at the *European Organization for Nuclear Research* (CERN[1]) [4].

A particle accelerator consists of two principal building blocks. One is responsible for guiding the particle beam and the other for the acceleration. The guidance of the beam is realised with multipole electric or magnetic fields, while the acceleration is normally realised with an electrostatic or a *radio frequency* (RF) electric field inside a cavity. With these two elements different accelerator architectures can be realised, these can be divided into two principal technical concepts: linear and circular machines. In a *linear accelerator* (linac) the beam passes the machine only once, while in a circular machine the beam is bent on a circular orbit and stays for many turns in the machine. One type of circular accelerator are synchrotrons, where the orbit of the beam is kept constant and the bending field is adjusted with the particle energy. If the bending field is kept constant, the particles are on a spiral orbit during acceleration which is the case in cyclotrons. There also exist machines where several concepts are combined, for example, recirculating electron linacs. There the beam passes several times through the same straight sections where the accelerating cavities are located but has different bending sections according to the beam energy. A more detailed overview over different accelerator types and the beam physics is given in [5, 6].

One of the key components in an accelerator are the cavities. There exist lots of different cavity types optimised for the dedicated application. In general, cavities can be divided into normal and superconducting structures, according to

---

[1] "Conseil Européen pour la Recherche Nucléaire", see [3]

their surface properties during operation. The main advantage of *superconducting radio frequency* (SRF) cavities are the low losses in the cavity surface, which are typically four to six orders of magnitude less than in normal conducting cavities. Hence, they are interesting for different applications. Some of the (SRF) linac applications are introduced in the following. They can be divided into two classes: lepton and hadron linacs, according to the particles which are accelerated.

The next generation electron-positron collider with a collision energy in the TeV range will be a linac to overcome the synchrotron radiation limitations of circular machines, which was the obstacle for the maximum energy in the *Large Electron-Positron Collider* (LEP) [7]. One concept is the *International Linear Collider* (ILC) [8–10], which uses two SC RF linacs of about 15 km to accelerate electrons and positrons up to 500 GeV. In total about 16.000 cavities with a very high accelerating gradient of more than 35 MeV/m are required to reach this energy. One of the key issues in such a long machine is to keep the beam size very small in order to maximise the collision rate. Hence, all kinds of instabilities, such as deflecting forces in the accelerating cavities, have to be minimised.

Other very important applications of electron linacs are 4th generation light sources, so called *Free Electron Lasers* (FELs) [11, 12]. After acceleration the electrons passes insertion devices with alternating transverse magnetic fields which force the electrons to undulate and to produce coherent synchrotron radiation. FELs can produce light with a higher brilliance than 3rd generation synchrotron based light sources, because the beam size can be much smaller due to the single passage of the beam. In order to provide such small beams, the impact of parasitic effects must be minimised. Another concept in this context are *Energy Recovery Linacs* (ERLs) [13, 14]. The accelerated electrons are sent through the application and afterwards travel through the linac again , where they are decelerated and the energy is transferred back to the cavities. With this method up to 98% of the energy can be recovered which can be used for acceleration again. In these machines the beam stability is even more important since the beam size increases during deceleration and the beam becomes more susceptible to deflecting effects such as dipole modes.

In contrast to electrons, protons and other hadrons have a significantly higher mass. Hence, the acceleration of these particles is different, because the relativistic β increases only slowly with the beam energy. In the past, normal conducting hadron linear accelerators were primarily used as injectors for synchrotrons. This picture changes with the request for several megawatt beam power with a kinetic energy of more than 500 MeV for various high power applications, especially in *continuous wave* (CW) operation. SC RF linacs are therefore the ideal choice.

The first high power superconducting proton linac started operation in 2006 at the *Spallation Neutron Source* (SNS) [15] and is used as "driver" linac. In this

facility protons are shot onto a liquid mercury target to produce neutrons which are used for scattering experiments. With this concept more intense neutron pulses can be produced than in reactor based sources and this enables new possibilities for the study of materials or processes such as the burning process in a petrol engine [16]. The *European Spallation Source* (ESS) [17] is an accelerator based neutron source, which is currently in the design stage. Both accelerators are discussed in detail in chapter 10 and 11.

Neutrons are also needed in fission reactors to drive the fission. In conventional fission reactors the required neutrons are produced during the fission itself. The neutron flux has to be controlled very carefully to control the chain reaction precisely. One idea is to add an accelerator based neutron source to the fission reactor, a so-called *accelerator driven system* (ADS) [18, 19]. Then the fission reactor would be sub-critical, which means that it does not produce enough neutrons to keep the chain reaction alive. Additional neutrons are needed, which are provided by the accelerator based neutron source. This concept is primarily discussed for nuclear waste transmutation, where the long-lived actinides with decay times more than 10^3 years are transmuted to "shorter" living products with decay times $\sim 5 \cdot 10^2$ years [20]. Currently the European ADS demonstrator MYRRHA [21–23] is in the design stage.

A high power proton beam is also needed in *radioactive ion beam facilities* (RIBs) such as the *European Isotope Separation On-Line radioactive ion beam facility* (EURISOL) [24] with the following working principle: A proton beam is shot on a target to produce rare radioactive isotopes which are studied afterwards. The amount of secondary particles depends on the beam energy and intensity of the primary beam.

In addition, most concepts for next generation neutrino facilities are based on high power proton linacs. In a beta-beam facility [25] radioactive ions, produced by a spallation process, decay via beta-decay in a storage ring and produce anti electron neutrinos. For the production of radioactive ions a high power proton beam with several GeV kinetic energy is needed. In a neutrino factory [26] the neutrinos are produced by muon beams. The muons are produced by pion decay and the pions by shooting a high energetic proton beam on a fixed target. Superconducting proton linacs for this applications are currently under development such as Project X at FermiLab [27] and the *Superconducting Proton Linac* (SPL) [28–31] at CERN.

All these applications of linear accelerators are either aiming for high beam power, in the case of the hadron linacs, or very small beam sizes, in the case of the lepton linacs. One effect, which limits the operation in both cases, is the influence of parasitic modes present in the cavities. The beam, travelling through the cavities, does not only interact with the accelerating mode of the cavity but

also excites modes with frequencies different from the accelerating mode, so-called *Higher Order Modes* (HOMs). The energy stored in these modes represents an additional load for the cryogenic cooling system and can thus drastically increase the cooling requirements or even lead to a thermal breakdown (*quench*[2]). HOMs also act back on the beam and can cause beam instabilities. Hence, their influence has to be studied carefully, taking into account the machine specific requirements. Based on the HOM analysis, machine specific HOM damping requirements can be defined and HOM damping devices can be designed according to the needs.

In this thesis the beam dynamics simulation tool ***S****imulation of Higher Order* ***M****ode* ***D****ynamics* (SMD) is developed to evaluate the influence of HOMs. A special focus in the code is set to model the longitudinal beam dynamics in hadron linacs correctly. In these machines the particles travel with a velocity lower than the speed of light. The change in velocity has several consequences on the beam stability in the context of HOMs and is discussed in detail. In SMD also other effects are taken into account such as beam noise, RF errors, or misalignment of elements. Their influence on the HOM excitation is analysed in detail.

SMD is used to analyse the risk potential of HOM caused instabilities in different linacs. A complete HOM analysis is performed in case of the SPL, starting with the analysis of the cavity RF design and performing beam dynamics simulations with SMD afterwards. With the simulation results, damping requirements as a function of the operation parameters are defined and based on this the development of HOM damping devices has been started. Furthermore a case study for ESS is performed, where two different operation frequencies are compared against each other in the context of HOMs. Finally an already build machine (SNS) is analysed to compare the simulation results with measurement data.

---

[2] *Quench*: Phase transition from the superconducting to the normal conducting state.

Chapter 2

The Superconducting Proton Linac Project

The SPL is an R&D project to develop a high power proton linear accelerator for the production of a proton beam in the MW range [28, 29, 31]. An international collaboration has been formed to share the work between different accelerator laboratories and institutes around the world under the leadership of CERN [32].

It is conceived as a 4 MW high power superconducting linac in pulsed operation, primarily as driver for a neutrino facility [25, 26], but it can also be used for other high power applications such as for example a radioactive ion beam facility [24]. A schematic drawing of the linac and a possible layout at the CERN site is shown in Figure 2.1 and Figure 2.2.
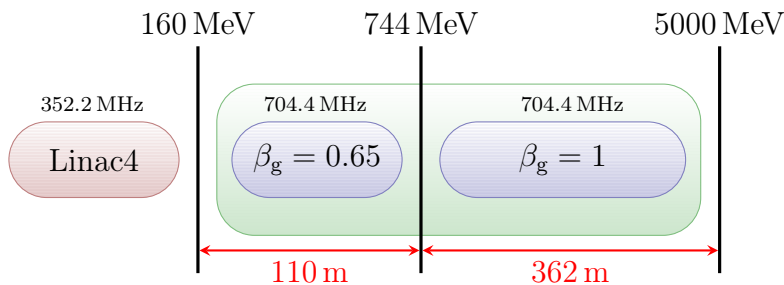
Figure 2.1: Schematic layout of the SPL.

Linac4 [34, 35], presently under construction, is conceived as the normal conducting front end of the SPL. In the first stage Linac4 will operate with 20 mA and a repetition rate of 1 Hz as injector for the PS Booster (PSB). It can be upgraded for the needs of the SPL at a later stage. Hence, all cavities are designed to be able to operate with 40 mA and a repetition rate of 50 Hz. The linac is placed in a way on the CERN site, that a direct injection into the SPL without a long transfer
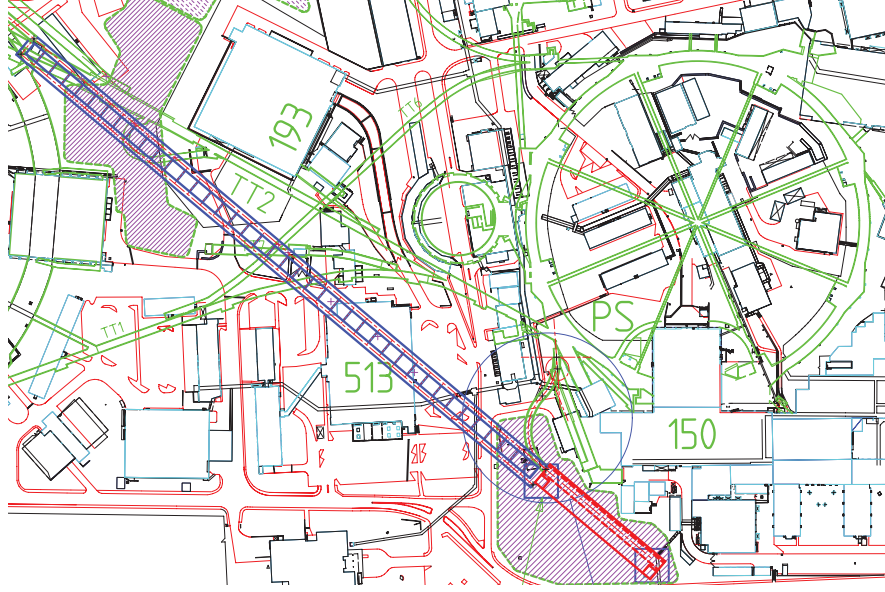
Figure 2.2: The planned SPL site layout on the CERN Meyrin site is marked in blue and Linac4 in red. In green existing accelerators and transfer lines are indicated [33].

line is possible. In this study the beam output parameters and simulation results from Linac4 will be used as injection parameters for the SPL.

In the SPL H^- is accelerated from 160 MeV up to an ultimate output energy of 5 GeV. Two families ($\beta_g = 0.65$ and $\beta_g = 1.0$) of 5 cell superconducting elliptical π-mode cavities, operating at 704.4 MHz, are used. A maximum pulse length of 1 ms is foreseen with an average pulse-current up to 40 mA and a repetition rate of 50 Hz. Different pulse substructures can be applied according to the requests by the users, which is realised with a high frequent chopper [36] at 3 MeV in the injector front end. All basic design parameters of the linac and the cavities used in this thesis are listed in Table 2.1 and 2.2. Throughout the thesis, the same numbers for current, pulse length and repetition rate are be used, which are not necessarily the same as in the latest design updates presented at the 5th SPL Collaboration Meeting [37]. The latest design parameters can be found on the project web page [38].

The SPL consists of two sections with SC RF elliptical cavities [28], differing in their geometrical β. In the medium beta section, 9 periods are planned, each containing 6 elliptical $\beta_g = 0.65$ five cell cavities and two quadrupole doublets. Afterwards 24 periods with 8 elliptical $\beta_g = 1.0$ five cell cavities and one quadrupole doublet compose the high beta section. A schematic layout of the periods in both sections is illustrated in Figure 2.3. There are also alternative layouts with other

Table 2.1: SPL parameters used throughout this thesis. The latest design parameters can be found in [38].

Parameter	Unit	Value
Output energy	[GeV]	4-5
Beam power	[MW]	4.0
Repetition rate	[Hz]	50
Maximum average pulse current	[mA]	40
Maximum peak pulse current	[mA]	64
Maximum beam pulse length	[ms]	1.0
Bunch frequency	[MHz]	352.2
Number of sections		2
Number of cavities		54/192
Cavities per cryostat		6/8
Period length	[m]	12.25 / 15.06
Maximum power per cavity	[MW]	1
Length	[m]	472

Table 2.2: Cavity design parameters.

Parameter	Unit	medium β	high β
Cells		5	5
Frequency	[MHz]	704.4	704.4
Geometrical beta β_g		0.65	1.0
$(R/Q)(\beta_g)$	[Ω]	320	560
Design gradient $E_0T(\beta_g)$	[MV/m]	19	25
Q_0		$5.8 \cdot 10^9$	$8.4 \cdot 10^9$

(a) Medium beta section

(b) High beta section
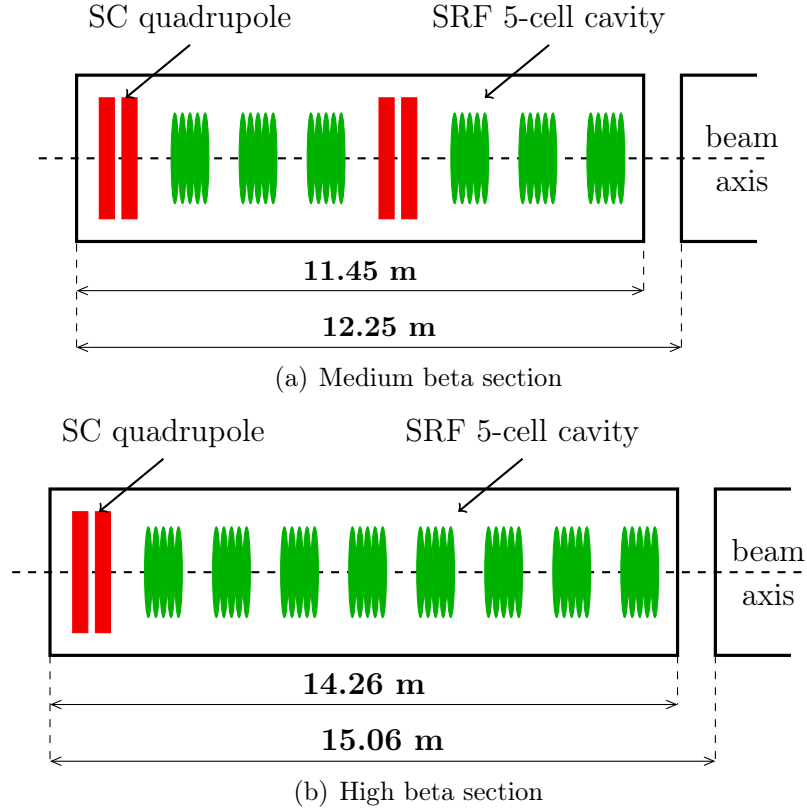
Figure 2.3: Period layout of the two linac sections.

sectorisations proposed [39, 40], which entail only minor differences with respect to beam dynamics and which are not discussed in this thesis. Possible extraction regions along the linac are also not considered in this study.

A key challenge of the SPL is to design a compact machine to meet the length constraints given on the CERN site. Hence, cavities with high accelerating gradients in the order of $25\,\mathrm{MeV/m}$ at $\beta = 1$ are needed, which will be discussed in detail in Chapter 5. Another point is the beam loss, which must be kept below $1\,\mathrm{W}$ per meter to allow hands on maintenance during shut-downs and technical stops. Beam losses can be caused by beam instabilities. One source for instabilities is the interaction of the beam with HOMs present in the cavities. The analysis of the risk potential of these modes in the SPL is a focus of this thesis and will be discussed in Chapter 8.

Chapter 3

Cavity Basics

According to the Oxford online dictionary [41] a cavity is "an empty space within a solid object". In an accelerator it is the building block, which is responsible for the acceleration of the particle beam[1]. There exists a complete "zoo" [42] of different cavity types specialised and optimised for various applications [43].

In this chapter the general properties of accelerating cavities are introduced with a focus on SRF elliptical cavities. The general structure follows [44, 45] and some SRF specific formulae are added from [46–48]. First of all the *electro magnetic* (EM) theory behind is briefly outlined following [49].

3.1 Maxwell's Equations

The basis for all electromagnetic calculations and simulations are *Maxwell's equations* [50]. They relate the electric fields $\vec{E}$, $\vec{D}$ and the magnetic fields $\vec{B}$, $\vec{H}$ with the charge and current sources. In differential form they are expressed as

$$\nabla \cdot \vec{D} = \rho \tag{3.1}$$

$$\nabla \cdot \vec{B} = 0 \tag{3.2}$$

$$\nabla \times \vec{E} = -\frac{\partial \vec{B}}{\partial t} \tag{3.3}$$

$$\nabla \times \vec{H} = \vec{J} + \frac{\partial \vec{D}}{\partial t}, \tag{3.4}$$

---

[1] Cavities used for other purposes such as beam deflection, (de-) bunching or as beam position monitor will be not addressed here.

where ρ is the electric charge density[2] and $\vec{J}$ the current density[3]. The *constitutive relations* are

$$\vec{D} = \epsilon\vec{E} \tag{3.5}$$

$$\vec{B} = \mu\vec{H}, \tag{3.6}$$

where ϵ is the permittivity and μ the permeability of the material in which the fields exist. In a linear, isotropic, non-dispersive, uniform material ϵ and μ are scalar constants:

$$\epsilon = \epsilon_r\epsilon_0 \tag{3.7}$$

$$\mu = \mu_r\mu_0, \tag{3.8}$$

where ϵ_r and μ_r are the material specific constants and ϵ_0 and μ_0 are universal constants, which have the following relation

$$c = \frac{1}{\sqrt{\epsilon_0\mu_0}} \tag{3.9}$$

where c is the speed of light in free space. In vacuum, such as inside a cavity, $\rho = 0$ and $\vec{J} = 0$, hence (3.1) - (3.4) simplifies to

$$\nabla \cdot \vec{E} = 0 \tag{3.10}$$

$$\nabla \cdot \vec{B} = 0 \tag{3.11}$$

$$\nabla \times \vec{E} = -\frac{\partial \vec{B}}{\partial t} \tag{3.12}$$

$$\nabla \times \vec{B} = \frac{1}{c^2}\frac{\partial \vec{E}}{\partial t}, \tag{3.13}$$

Maxwell's equations are linear, so the principal of superposition can be used to construct complicated electric and magnetic fields.

A non trivial solution of (3.10) can be found by separating the electric and magnetic field by using the curl of $\nabla \times \vec{E}$ and the vector relation [51]:

$$\nabla \times \nabla \times \vec{E} \equiv \nabla(\nabla \cdot \vec{E}) - \nabla^2\vec{E} = -\frac{\partial}{\partial t}\nabla \times \vec{B}. \tag{3.14}$$

With (3.10), and (3.13) one finds the wave equation

$$\nabla^2\vec{E} - \frac{1}{c^2}\frac{\partial^2\vec{E}}{\partial t^2} = 0. \tag{3.15}$$

---

[2] charge per volume

[3] current penetrating a certain cross-section

(3.15) can be solved by plane waves as function of the position $\vec{x}$ and time t

$$\vec{E}(\vec{x}, t) = \vec{E}_0 e^{i(\vec{k} \cdot \vec{x} - \omega t)}, \tag{3.16}$$

where $\vec{E}_0$ is a constant vector, which represents the amplitude, and $\vec{k}$ is the wave vector, which points in the direction of propagation and whose length is the phase shift per unit length. The phase velocity v_p of the wave is given by the *dispersion relation*

$$v_\mathrm{p} = \frac{\omega}{|k|} \tag{3.17}$$

and is equal to c in free space for a planar wave.

For the magnetic field a similar expression as (3.15) can be derived and has the following solution

$$\vec{B}(\vec{x}, t) = \vec{B}_0 e^{i(\vec{k} \cdot \vec{x} - \omega t)}, \tag{3.18}$$

where $\vec{B}_0$ is a constant vector and the phase velocity v_p of the wave is given by the same dispersion relation (3.17) as for the electric field. Combining (3.16) and (3.18) with Maxwell's equations, one gets the following constraints for the solutions

$$\vec{k} \times \vec{E}_0 = \omega \vec{B}_0 \tag{3.19}$$

$$\vec{k} \times \vec{B}_0 = -\frac{\omega}{c^2} \vec{E}_0 \tag{3.20}$$

$$\vec{k} \cdot \vec{E}_0 = 0 \tag{3.21}$$

$$\vec{k} \cdot \vec{B}_0 = 0. \tag{3.22}$$

Hence, the directions of $\vec{E}_0$, $\vec{B}_0$, and $\vec{k}$ are mutually perpendicular and the field amplitudes are related by $E_0/B_0 = c$. The wave vector $\vec{k}$ can be chosen freely and one can refer to a wave specified by a particular value of $\vec{k}$ as a *mode* of the electromagnetic field in free space. The frequency of each mode is determined by the dispersion relation. A single mode represents a plane wave of a single frequency with infinite extent in space and time. Other waves can be obtained by superimposing different modes. Also radial waves can be interpreted as a superposition of plane waves. The superposition of an outward and an inward radial wave can result in the field of a round hollow tube.

3.2 A Circular Waveguide

Before looking at the field distribution inside a cavity, the propagation of an EM-wave in an infinitely long hollow cylindrical tube with radius r_0 and perfect conducting walls is investigated, which correspond to a perfect circular waveguide[4].

---

[4] In a real waveguide the walls are not perfect conducting and the fields penetrate the surface, which lead to losses.

Inside the waveguide vacuum is assumed. A cylindrical coordinate system $\vec{x}(r, \theta, z)$ is chosen for all further calculations to better take into account the rotational symmetry of the problem. On the surface of a perfect conductor the following boundary conditions apply:

$$\vec{n} \times \vec{E} = 0, \quad \vec{n} \cdot \vec{B} = 0, \tag{3.23}$$

where $\vec{n}$ is the surface normal of the conductor (*Dirichlet boundary condition*).

There are two independent sets of solutions to this problem: *transverse magnetic* (TM) modes[5] and *transverse electric* (TE) modes[6]. In case of TM modes the longitudinal magnetic field vanishes everywhere, and the longitudinal electric field is the solution of the differential equation:

$$\left[\nabla^2 + \left(\left(\frac{\omega}{c} \right)^2 - k_z^2 \right) \right] E_z = 0, \quad B_z \equiv 0. \tag{3.24}$$

The boundary condition $E_z(r_0) = 0$ lead to the following solution in a circular waveguide

$$E_z \sim J_m \left(\frac{j_{n,m}}{r_0} r \right) e^{im\phi} \tag{3.25}$$

where $j_{n,m}$ is the nth zero of the mth order Bessel function[7] J_m and ϕ the phase.

The dispersion relation is then

$$\omega_{\text{TM},mn}^2 = \left(\frac{c j_{n,m}}{r_0} \right)^2 + k_z^2, \tag{3.26}$$

where k_z is the propagation constant in longitudinal direction. The dispersion diagram is shown in Figure 3.1. The phase velocity is always larger than the speed of light and only modes with frequencies above the cutoff frequency

$$f_{\text{TM},c}(m, n) = \frac{c}{r_0 2\pi} j_{n,m} \tag{3.27}$$

can propagate along the z-axis.

The same method can be applied for TE modes, which do not have a longitudinal electric field component. The solution for the longitudinal magnetic field is then

$$B_z \sim J_m \left(\frac{j'_{n,m}}{r_0} r \right) e^{im\phi}, \tag{3.28}$$

---

[5] also called E modes.

[6] also called H modes.

[7] The definition of the Bessel function and its properties are introduced in Appendix A.
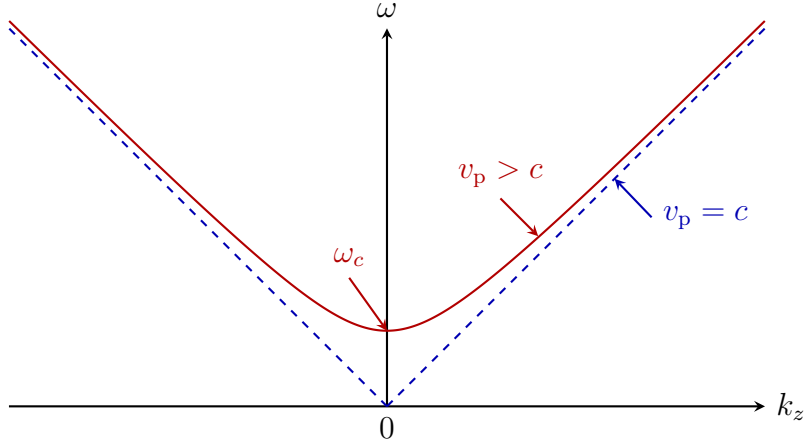
Figure 3.1: Dispersion diagram. The minimum propagation frequency is $f_{\mathrm{c}} = \omega_{\mathrm{c}}/2\pi$.

where $j'_{n,m}$ is the nth zero of the derivative of the mth order Bessel function. The dispersion relation is then

$$\omega^2_{\mathrm{TE},mn} = \left(\frac{cj'_{n,m}}{r_0}\right)^2 + k^2_{\mathrm{z}}, \tag{3.29}$$

with a cutoff frequency

$$f_{\mathrm{TE},c}(m,n) = \frac{c}{r_0 2\pi}j'_{n,m}. \tag{3.30}$$

The cutoff frequencies are also important for the modes' ability to propagate out of the cavity.

3.3 The Pillbox Cavity

Closing the hollow tube discussed before with perfect conducting end-plates at the axial coordinates $z = 0$ and l one gets a pillbox cavity with length l and radius R_{c}. This structure is the simplest cavity with rotational symmetry and the solution of the EM fields inside can be derived analytically.

The same two independent sets of solutions (TE,TM) exist in the pillbox cavity similar to the waveguide, which have a discrete mode spectrum since there are no degrees of freedom any more. A third index "p" is added to the nomenclature introduced before and the modes have the following dispersion relations

$$\omega_{\mathrm{TM},mnp} = c\sqrt{k^2_{\mathrm{TM},mn} + k^2_{\mathrm{z}}} \tag{3.31}$$

with $k_{\mathrm{TM},mn} = \frac{j_{mn}}{R_{\mathrm{c}}}$ and $k_{\mathrm{z}} = \frac{p\pi}{l}$ for TM modes and

$$\omega_{\mathrm{TE},mnp} = c\sqrt{k_{\mathrm{TE},mn}^2 + k_{\mathrm{z}}^2} \tag{3.32}$$

with $k_{\mathrm{TE},mn} = \frac{j'_{mn}}{R_{\mathrm{c}}}$ for TE modes.

The electric and magnetic field components of the TM_{mnp} modes in a pillbox cavity can be expressed analytically as follows:

$$E_{\mathrm{z}} = E_0 J_m\left(\frac{j_{mn}}{R_{\mathrm{c}}}r\right)\cos\left(m\theta\right)\cos\left(\frac{p\pi z}{l}\right)\mathrm{e}^{i\omega t} \tag{3.33}$$

$$E_{\mathrm{r}} = -\frac{p\pi}{l}\frac{R_{\mathrm{c}}}{j_{mn}}E_0 J'_m\left(\frac{j_{mn}}{R_{\mathrm{c}}}r\right)\cos(m\theta)\sin\left(\frac{p\pi z}{l}\right)\mathrm{e}^{i\omega t} \tag{3.34}$$

$$E_{\theta} = -\frac{p\pi}{l}\frac{mR_{\mathrm{c}}^2}{j_{mn}^2 r}E_0 J_m\left(\frac{j_{mn}}{R_{\mathrm{c}}}r\right)\sin(m\theta)\sin\left(\frac{p\pi z}{l}\right)\mathrm{e}^{i\omega t} \tag{3.35}$$

$$B_{\mathrm{z}} = 0 \tag{3.36}$$

$$B_{\mathrm{r}} = -i\frac{\omega}{c^2}\frac{mR_{\mathrm{c}}^2}{j_{mn}^2 r}B_0 J_m\left(\frac{j_{mn}}{R_{\mathrm{c}}}r\right)\sin\left(m\theta\right)\sin\left(\frac{p\pi z}{l}\right)\mathrm{e}^{i\omega t} \tag{3.37}$$

$$B_{\theta} = -i\frac{\omega}{c^2}\frac{R_{\mathrm{c}}}{j_{mn}}B_0 J'_m\left(\frac{j_{mn}}{R_{\mathrm{c}}}r\right)\cos(m\theta)\cos\left(\frac{p\pi z}{l}\right)\mathrm{e}^{i\omega t} \tag{3.38}$$

where $J_m(x)$ is the mth order the Bessel function and $J'_m(x)$ its derivative. The nth zero m^{th} order Bessel function is $j_{n,m}$ and $j'_{n,m}$ is the nth zero of the derivative of the mth order Bessel function. E_0 is the field amplitude. The physical meaning of the indices can be illustrated in more practical terms:

- m is the number of full period variations in θ of the field components

- n the number of zeros of the axial field component inside the structure without $r = 0$

- p is the number of half period variations along the z-axis of the field

Solutions of the wave equation in cylindrical coordinates expressed by Bessel functions of the second kind Y_m diverge at $r = 0$ and are hence excluded for cavities without central conductor while they are an essential part in coaxial lines or related geometries.

In the pillbox cavity the TM mode with the lowest frequency is the TM_{010} mode with $\omega_{010} = \frac{j_{0,1}c}{R_{\mathrm{c}}}$, which is defined by the cavity radius. It is independent of the cavity length. The electric and magnetic field profiles of the TM_{010} mode in the symmetry planes are shown in Figure 3.2. TE modes exist also in a pillbox cavity, which can be expressed in a similar way.

(a) Pillbox model   (b) E-Field   (c) B-Field
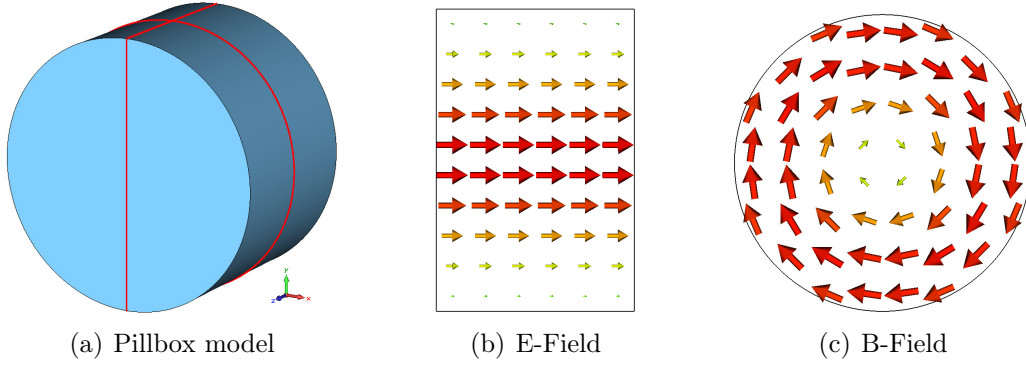
Figure 3.2: 3D model of a pillbox cavity with marked cut planes (a) and vector plots of the electric and magnetic field distribution of the TM_{010} mode. E-Field along the z-axis (b) and B-Field distribution perpendicular to the z-axis in the cavity mid-plane (c)

In order to accelerate the beam the longitudinal component of $\vec{E}$ may not vanish on the beam axis. This condition is only fulfilled by the Bessel function J_0, so all possible accelerating modes are of the type TM_{0np}. They are called monopole modes because of their rotational symmetrical field distribution. Dipole modes ($m = 1$) have a net deflecting field on axis. They disrupt the beam and are undesirable in accelerating cavities. Modes with $m = 2$ are called quadrupole modes, with $m = 3$ are sextupole modes and so on for higher m. Usually the mode TM_{010} is chosen as accelerating mode. It has the lowest eigenfrequency and the best accelerating properties. The general cavity properties of a pillbox cavity can be derived analytically.

In an accelerator, pillbox cavities cannot be directly used, because they don't have any openings for the beam passage. Adding these to this structure, the field properties and frequencies change. The eigenmodes cannot be solved analytically any more and one has to use numerical simulation tools, as introduced in chapter 4. Furthermore the boundary conditions change by introducing holes or beam pipes. Hence, there exist no pure TE modes inside these structures any more. The modes are a superposition of TE and TM modes and called hybrid modes. In general the same mode description (TE_{mnp},TM_{mnp}) as introduced for the pillbox cavity is used to characterise the modes in other cavities. But the field profile is not necessary exactly the same as the field profile of the corresponding mode in a pillbox cavity.

3.4   Superconducting Radio Frequency Cavities

SRF elliptical multi-cell cavities are the focus of this thesis. An example of a five cell cavity is shown in Figure 3.3. Their name stems from the cell shape, which is comprised of ellipses. A cavity half cell is shown in Figure 3.4. The connection area from one cell to the next is called iris and the connection area of the two half cells equator.
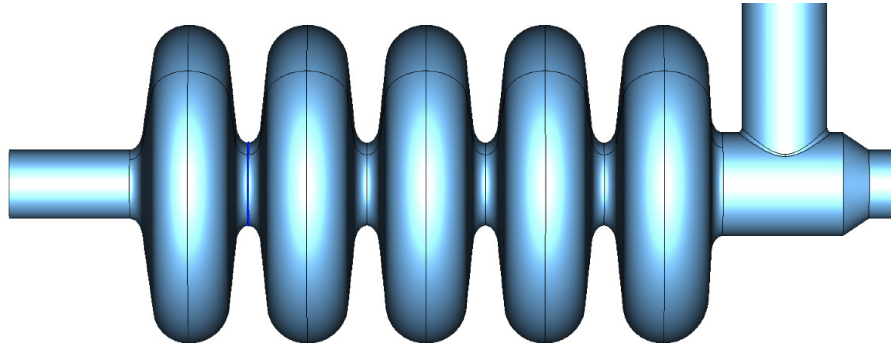
Figure 3.3: Cavity model of a five cell 704 MHz cavity with beam pipes at both ends and a coaxial power coupler on the right side.
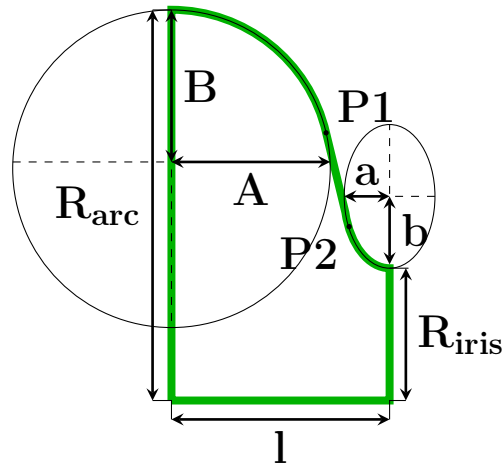
Figure 3.4: Geometry of an elliptical cavity half cell, with labelled geometry parameters used to describe the cavity shape. With this set of parameters, the cavity shape is uniquely defined.

The main differences to a pill box cavity are the round shape and the openings

(a) E-Field distribution

(b) H-Field distribution
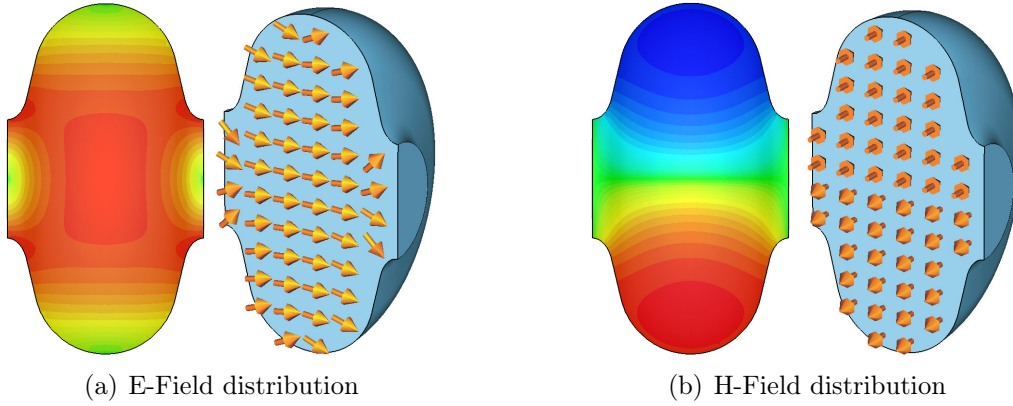
Figure 3.5: E-Field and H-Field distribution of the TM_{010} mode in an elliptical cavity cell. Red corresponds to high positive field, green to no field, and blue to high negative field. The arrows indicate the direction of the field. $\vec{E}$ and $\vec{H}$ are perpendicular to each other and 90° out of phase. The highest electric fields are at the cavity iris and the maximum magnetic fields are at the equator region of the cell.

for the beam. The shape is chosen to minimise the risk of multipactoring[8] and field emission[9], which both cause local surface heating and can lead to a quench.

The electric and magnetic field distribution of the TM_{010} mode in an elliptical cavity cell is illustrated in Figure 3.5. The peak magnetic surface field is in the equator region, while the peak electric surface field is in the iris region.

Superconductivity is lost above a material dependent critical temperature or when the surface magnetic field exceeds a critical field strength. Both values depend on each other. Currently Niobium is the most common material used to manufacture cavities. Niobium is a Type II superconductor with a critical temperature[10] $T_c = 9.2\,\text{K}$. Its critical RF magnetic surface field depends beside T also on the the surface properties and is measured to be consistent with the superheating field[11] [53–55]. This leads to a theoretical gradient limit of about $E_{\text{acc}} = 60\,\text{MV/m}$ with a typical elliptical cavity shape, which has not yet been reached on a regular basis. In 2010 the production yield for gradients of the ILC

---

[8] *Multipactoring*: Electrons hit the surface and trigger secondary electrons, which are accelerated and hit the surface at the same position. In case the secondary electron yield (SEY) is larger than 1, an avalanche process is started [46, 52].

[9] *Field Emission*: The electrons are emitted from imperfect surface structures with sharp edges and accelerated by high electric surface fields. They hit the cavity wall at another location [46, 52].

[10] No ambient magnetic field is present.

[11] $B_{\text{sh}}(T) \approx B_{\text{sh}}(0) \left[1 - \left(\frac{T}{T_c} \right)^2 \right]$; $B_{\text{sh}}(0) = 190\,\text{mT}$

test cavities[12] with $> 35 \, \mathrm{MV/m}$ was about 50% [57], which is up to now the best studied and performing multi-cell cavity.

The main advantage of superconducting cavities is the low surface power-loss, which is several orders of magnitude lower compared to normal conducting structures. The drawback of these low losses is that all other modes besides the accelerating mode also have naturally low losses, which means the decay time is very long.

Typically, elliptical cavities are characterised by a set of geometry and RF parameters, which will be introduced in the next section.

3.5 Cavity RF Parameters

The basic principle in all RF accelerators is to accelerate the beam with a time varying electric field, which must be synchronous with the passage of the beam bunches. The cavity can be seen as a kind of power transformer, which transfers the power from an RF source to the beam.

The field along the z-axis[13] of a standing electromagnetic wave inside a cavity is given by

$$E_{\mathrm{z}}\left(z,t\right) = E(z)e^{(i\omega t + i\phi)}, \tag{3.39}$$

where ϕ is the phase[14].

In the following subsections, first the properties of a single cavity cell are derived and then extended to multicell cavities, with a focus on the accelerating mode. Afterwards non-accelerating modes are characterised, before the concepts of power coupling and HOM damping are introduced.

3.5.1 Single Cell Cavity

In this subsection a set of RF parameters are introduced, which are generally used to characterise accelerating cavities. The index "0" is used to indicate the accelerating mode in general.

The time it takes for a particle travelling with a constant velocity $v = \beta c$ to pass through a cavity cell is equal to half an RF period for maximum acceleration kick. This defines the length of a cell (*geometrical cell length*) as

$$L_{\mathrm{c}} = \frac{\beta c \pi}{\omega_0} = \frac{\beta c}{2 f_0} = \frac{\beta \lambda}{2}, \tag{3.40}$$

---

[12]based on the TESLA cavity design [56]

[13]In this thesis the beam axis, along which the beam travels, is by convention always the z-axis.

[14]In a linac ϕ is defined as zero, if the particle is on crest of the RF-field, which is in contrast to a circular accelerator where $\phi = 0$ in the root of the RF.

where ω_0 is the angular frequency of the accelerating mode. In the following the reference or design β will be indicated with β_{g}, where "g" stands for geometrical. In literature it is common to specify the cavity properties at β_{g}, if no specific β value is stated.

Assuming a constant velocity $v = \beta c$, the energy gain of the particle in a single cell is defined as the integral over the z component of the electric field seen by the charged particle along the z-axis is

$$\Delta W = q \left(\cos(\phi_0) \int_{-\infty}^{\infty} E_{\mathrm{z}}(z) \cos(\omega \frac{z}{\beta c}) dz - \sin(\phi_0) \int_{-\infty}^{\infty} E_{\mathrm{z}}(z) \sin(\omega \frac{z}{\beta c}) dz \right),$$
(3.41)

where ϕ_0 is the phase at the origin of the chosen coordinate system. The second integral vanishes if the field is symmetric around the cell mid-plane and the origin is set accordingly. The integration boundaries are set to $\pm\infty$ to take into account the fields leaking out of the cavity cell. In case the fields are forced to zero by boundary conditions of the simulation tool, see chapter 4, the integration boundaries can be set to $\pm L_{\mathrm{c}}/2$, where L_{c} is the cavity length.

More common is the following notation

$$\Delta W = q V_0 T(\beta) \cos(\phi).$$
(3.42)

where an axial RF voltage is introduced as

$$V_0 = \int_{-L_{\mathrm{c}}/2}^{L_{\mathrm{c}}/2} E_{\mathrm{z}}(z) \neq 0$$
(3.43)

and where the velocity-dependent *transit time factor* T is defined as:

$$T(\beta) = \frac{\left| \int_{-L_{\mathrm{c}}/2}^{L_{\mathrm{c}}/2} E_{\mathrm{z}}(0, z) \mathrm{e}^{(i\omega \frac{z}{\beta c})} dz \right|}{\int_{-L_{\mathrm{c}}/2}^{L_{\mathrm{c}}/2} E_{\mathrm{z}}(0, z) dz}$$
(3.44)

In a pillbox cavity with a square field profile the transit time factor simplifies to

$$T(\beta) = \frac{\sin(\frac{\pi L_{\mathrm{c}}}{\beta \lambda})}{\frac{\pi L_{\mathrm{c}}}{\beta \lambda}}.$$
(3.45)

The transit time factor is essential in case the same accelerating structure is used for a wide velocity range. There the accelerating voltage changes with the particle velocity. In the past analytic models for the transit time factor were very important, because the numerical integration, calculating directly the energy gain, was

very difficult in terms of computing time. Nowadays this is not an issue any more and the energy gain is directly calculated by deriving the integral numerically. A more detailed discussion on this subject is given in chapter 7.2.1, where different field integration methods are introduced.

The maximum effective accelerating voltage is

$$V_{\mathrm{RF}} = V_0 T(\beta). \tag{3.46}$$

Taking into account the synchronous phase one gets

$$V_{\mathrm{acc}} = V_0 T(\beta) \cos(\phi). \tag{3.47}$$

Often the average accelerating field E_0 is quoted, given by

$$E_0 = \frac{V_0}{L_{\mathrm{c}}}. \tag{3.48}$$

The product $E_0 T(\beta)$ is called the *accelerating gradient* $E_{acc}(\beta)$.

Another characteristic value of a cavity is the *unloaded quality factor* Q_0, which is the number of oscillations the field performs inside the resonator until it is decayed. It is defined as the relationship between the power dissipation P_0 in the surface per oscillation and the stored energy U_0 of the accelerating mode in the structure

$$Q_{0,0} = \omega_0 \frac{U_0}{P_0} = \omega_0 \frac{\mu_0 \int_V \left|\vec{H}\right|^2 dv}{R_s \int_S \left|\vec{H}\right|^2 ds} = \frac{G_0}{R_s}, \tag{3.49}$$

where G_0 is the *geometry factor* and does only depend on the cavity shape and not on the surface resistance or the cavity size. It can be used to directly compare different cavity designs. The design goal is to maximise G to reduce the relative losses in the surface. R_s is the *surface resistance*. In case of SRF, R_s is very small, in the order of some tens of nΩ, and depends on the external parameters temperature, frequency and ambient residual magnetic field, as well as on the material surface properties. More details on this topic and present research activities in this field can be found in [52]. The quality factor of SRF cavities is typically four to six orders of magnitude better than in normal conducting cavities. Since the power is dissipated in the helium bath, the carnot efficiency has to be taken into account to calculate for overall power consumption.

The ratio of the square of the accelerating voltage V_0 and the dissipated power P_0 in the surface is the *shunt impedance*[15] r_s

$$r_{\mathrm{s}} = \frac{V_0^2}{P_0}. \tag{3.50}$$

---

[15]The linac definition is used here, while the definition $r_s^c = \frac{V_0^2}{2P_0}$ is used in circuit theory.

It is a measure of how much power is lost in the surface to reach a given acceleration voltage. The *effective shunt impedance* of a cavity takes the transit time factor into account and is defined as

$$r_a = \left(\frac{\Delta W_{\phi=0}}{q}\right)^2 \frac{1}{P_0} = \frac{(V_0 T(\beta))^2}{P_0} = r_s T(\beta)^2. \tag{3.51}$$

In linacs the shunt impedance is usually defined per unit length (meter) and not per cell

$$Z \equiv \frac{r_s}{L} = \frac{V_0^2}{P_0 L} = \frac{E_0^2 L}{P} \tag{3.52}$$

and the effective shunt impedance per unit length is then

$$ZT(\beta)^2 \equiv \frac{r}{L} = \frac{(V_0 T)^2}{P_0 L} = \frac{(E_0 T(\beta))^2 L}{P_0} \tag{3.53}$$

The ratio of shunt impedance and the quality factor, often referred to as "R over Q" value

$$(R/Q)_0 = \frac{r_a}{Q_0} = \frac{V_{\mathrm{acc}}^2}{\omega_0 U_0} \tag{3.54}$$

is independent of the surface resistance and depends only on the cavity geometry. It expresses how efficiently the energy stored in the cavity can be transferred to the beam and vice versa. Therefore, it is used to characterize the efficiency of a cavity geometry and is a common value to characterise SRF cavities. $(R/Q)_0$ depends on particle velocity, which is essential in the later discussion. Therefore the following notation is used: $(R/Q)_0(\beta)$, which will be also used for other properties such as $E_0 T$, V_{RF} and V_{acc}.

A cavity design goal is to maximise the $(R/Q)_0(\beta_{\mathrm{g}})$ for the accelerating mode and typical values are of the order of $100\,\Omega$ per cell for $\beta_{\mathrm{g}} = 1$ cavities. By maximising the (R/Q) value for the accelerating mode, the (R/Q) values for other modes in the cavity also becomes high, which can cause problems and is of particular interest for the analysis of HOMs, the new focus of this thesis. Some general rules how to optimise the shape of SRF elliptical cavities for different applications are given in [47, 58, 59].

3.5.2 Multicell Cavities

To increase the overall accelerating efficiency, multicell cavities are used in linacs. By increasing the number of accelerating cells per cavity the ratio between active acceleration length to total length improves, where the space between the cavities is included. On the other hand the transit time factor drops faster for cavities

with more cells [60], if the particle enter the cavity with different β than β_{opt}[16], as illustrated in Figure 3.6.
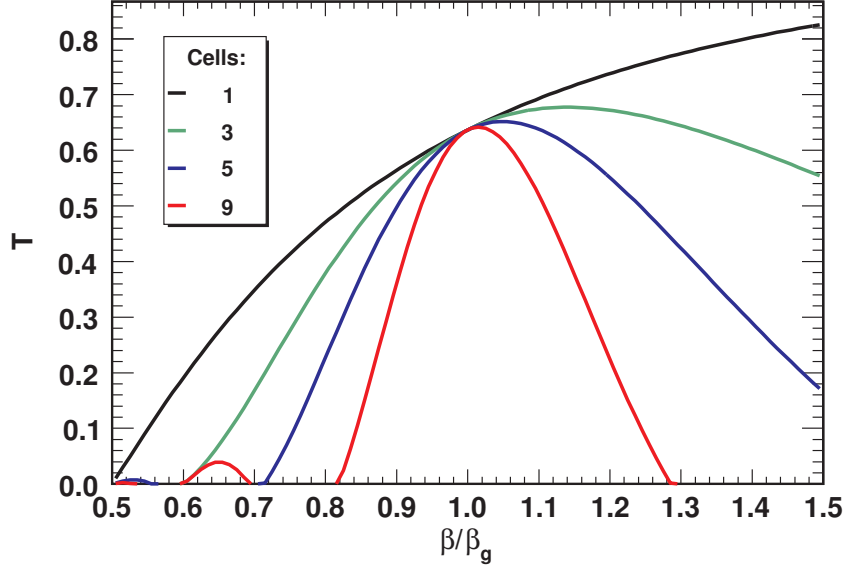
Figure 3.6: Transit time factor for cavities with different number of cells. The peak of the transit time factor is above β_{g} in all cavities. T drops faster for $\beta \neq \beta_{\mathrm{opt}}$ with increasing number fo cavity cells. The transit time factor model of [60] is used for this plot.

An elliptical cavity with five cells, illustrated in Figure 3.7, is assumed in the following and each cell is excited in the TM_{010} mode. If a cavity consists of N cells, there is a subset of N modes for each main mode, because the cells are coupled resonators. They behave like a coupled pendulum illustrated in Figure 3.8. The modes have different cell to cell phase relations as well as different frequencies, which can be expressed via the dispersion relation in case of electric coupling [44]

$$f_n = f_{\mathrm{zero}}\sqrt{1 + k_{\mathrm{cc,e}}(1 - \cos(n\pi/N))} \tag{3.55}$$

where n is the mode out of N modes, k_{cc} is the coupling constant between the cells and f_{zero} is the frequency of the zero mode, which has a cell to cell phase relation of zero. This is the resonance frequency of the single cell, which is not coupled to others. An example for frequencies in a five cell cavity is illustrated in Figure 3.9, called Brioullin diagram.

In case the phase relation from one cell to the next is π, the E-field changes its sign in each cell. This mode is typically used as accelerating mode in multicell

---

[16] β_{opt}: $\max(T(\beta))$; in genera is $\beta_{\mathrm{opt}} > \beta_{\mathrm{g}}$.
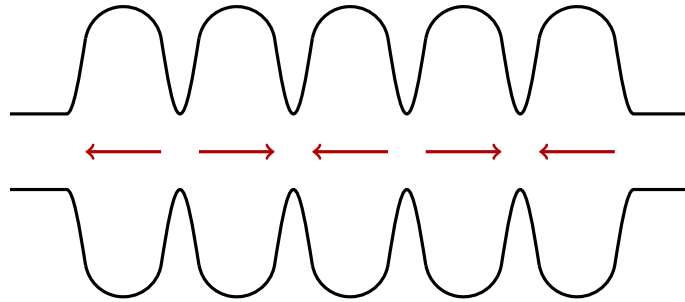
Figure 3.7: Schematic drawing of a five cell elliptical cavity. The phase difference from one cell to the next is 180° or π.
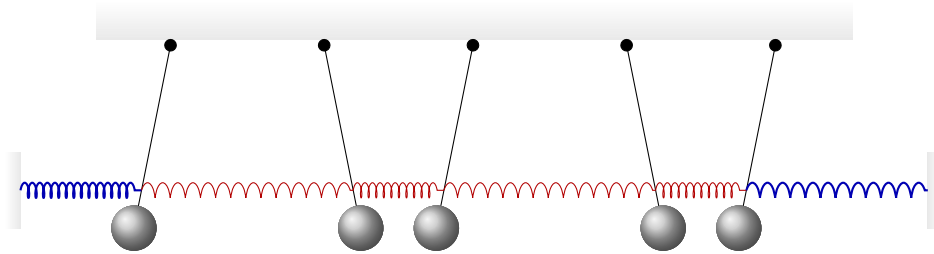
Figure 3.8: Sketch of a coupled pendulum. The outer most pendulums have a different coupling behaviour than the centre pendulums.
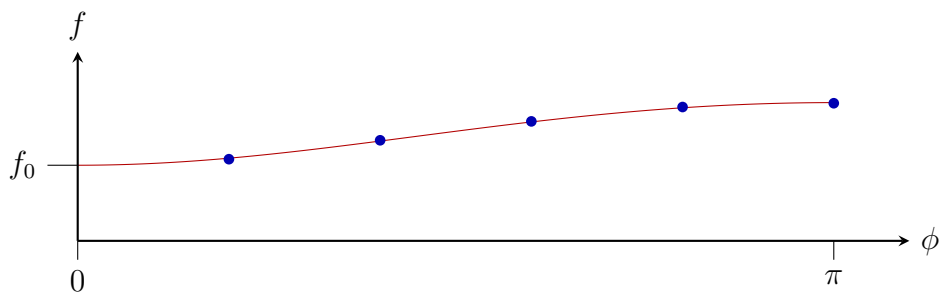
Figure 3.9: Brioullin diagram of a five cell cavity with electric coupling. The five modes are marked with blue dots and the red curve is obtained with (3.55). The lowest mode is the $1/5\pi$ mode and not the zero mode.

(a) 0-mode   (b) π-mode
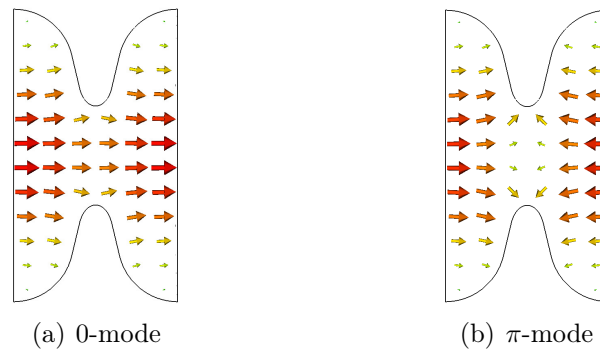
Figure 3.10: E-Field distribution of the 0- and π-mode in two coupled cells. The sign of the E-Field changes for the π-mode, which corresponds to a phase difference of 180°, while for the zero mode the sign is the same in both cells. Red correspond to high field and green to no field.

cavities. In case of magnetic coupling the π mode has a lower frequency than the zero mode.

The end cells have a different resonance frequency than the centre cells to compensate the different coupling behaviour to the beam pipe. Therefore the geometry of the half cells connected to the beam pipe is modified. This is necessary to reach the same field profile in all cells for the accelerating mode. The cell to cell variation in the peak E-Field on the beam axis is called field flatness and is typically a few per cent. In order to reach a good field flatness, the cavity cells have to be tuned for the acceleration mode after fabrication by inelastic deformation[17]. With this method fabrication tolerances are compensated. The same principal is also used in operation to compensate for effects such as Lorentz force detuning[18] [61].

The RF properties introduced for a single cell cavity can also be used for multicell cavities. Only (3.43) has to be modified taking into account that the particles need half an RF period to get from one cell to the next. Hence, the integration has to be done separately for each cell or the transit time factor has to be directly included into the calculation. All other relations can be adapted accordingly.

---

[17]The deformation changes the resonance frequency of the local cell, but effects the complete system in terms of resonance frequency and field profile.

[18]*Lorentz Force Detuning*: The pulsing RF power causes pulsing mechanical stress in the cavity due to Lorentz force that deforms slightly the cavity.

3.5.3 Characterisation of Higher Order Modes

All quantities introduced in the previous subsection were related to the accelerating monopole mode, but all of them are also valid for other TM_{0np} modes; similar methods can also be applied for multipole modes with particles off axis.

In order to characterise the influence of HOMs, they can be divided in two classes according to their field profile, the TM monopole modes with an E_z component on the beam axis and the multipole modes, which do not have an E_z component along the beam axis[19]. While the TM monopoles act in the longitudinal plane on the beam in terms of acceleration and deceleration, the other modes act in the transverse plane as deflecting forces.

As a quantity for the interaction of the mode and the beam the $(R/Q)(\beta)$ can be used. In order to have the same relation for multipole modes, the definition of $(R/Q)(\beta)$ has to be adapted, since they do not have a longitudinal field component on axis.

Multipole modes can only be excited by off axis particles, because they don't have any field component (E_z) along the beam axis. The following convention is used for multipole fields in this section: $E_z(x, y, z) = E_z(r, z)\cos(\phi)$ with $x = r\cos(\phi)$ and $y = r\sin(\phi)$. The polarisation axis is chosen such that the maximum electric field is along the x-axis and $\phi = 0$. E_z rises approximately with x^m as long as x is smaller than the cavity iris radius R_{iris}. A deviation from the x-axis can be neglected in a first order approximation because $\partial E_z/\partial y = 0$. The longitudinal voltage $V_{||,n}(r, \beta)$ induced by a charge q travelling with the speed βc parallel to the beam axis at distance r scales then as follows

$$V_{||,n}(r, \beta) = \left(\frac{r}{r_0}\right)^m V_{||,n}(r_0, \beta) \tag{3.56}$$

The particles get deflected in the field of a multipole mode inside a cavity. According to the *Panofski-Wenzel theorem* [62, 63] this can be expressed as

$$\Delta p_{\perp,n} = i\frac{e}{\omega_n}\frac{dV_{||,n}}{dr}, \tag{3.57}$$

where ω_n is the angular frequency of the mode n. A so-called "transverse voltage" $V_{\perp,n}$ can be defined and linked to the voltage $V_{||,n}(r, \beta)$

$$V_{\perp,n} = \frac{cp_\perp}{e} = i\frac{cr^{(m-1)}}{\omega_n r_0^m}V_{||,n}(x, \beta) \tag{3.58}$$

Similar to the longitudinal $(R/Q)_n(\beta)$ the same parameter can be introduced for multipole modes

$$(R/Q)_{\perp,n}(\beta) = \frac{|V_{\perp,n}(\beta)|^2}{\omega_n U_n} \tag{3.59}$$

---

[19]The TE monopoles are also treated like multipole modes.

with an integration path parallel to the beam axis at distance r_0 using relation (3.58)

$$V_{\perp,n} = i \left(\frac{c}{\omega_n r_0^m} \right) \int\limits_{-\infty}^{\infty} E_{n,z}(r = r_0, z) \mathrm{e}^{i\omega_n \frac{z}{\beta c}} dz. \tag{3.60}$$

$(R/Q)(\beta)$ and $(R/Q)_{\perp}(\beta)$ will be used in the beam dynamics simulations to model the beam-cavity interaction, which will be introduced in chapter 6.

3.5.4   Power Coupler

The power from the source is transported via the *fundamental power coupler* (FPC) into the cavity, which is either a wave-guide or a coaxial line with a impedance of $50\,\Omega$. The FPC and the cavity are a coupled system and the coupling is adjusted such that at nominal beam no transmitted RF power is reflected. The *external quality factor* Q_{ex} of the FPC is typically several orders of magnitude smaller than the $Q_{0,0}$ of the cavity and given by

$$Q_{\mathrm{ex}} = \omega_0 \frac{U_0}{P_{\mathrm{ex}}}, \tag{3.61}$$

where P_{ex} is the average power dissipation in the source load in case the RF power source is switched off. The quality factor of the complete system, called *loaded quality factor* Q_{L} is the inverse sum of all subsystems

$$\frac{1}{Q_{\mathrm{L}}} = \frac{1}{Q_{\mathrm{ex}}} + \frac{1}{Q_0}. \tag{3.62}$$

According to [63] the optimum Q_{ex} for the FPC in SRF cavities is given by

$$Q_{\mathrm{ex}} = \frac{V_{\mathrm{acc}}(\beta_{\mathrm{g}})}{(R/Q)_0 (\beta_{\mathrm{g}}) I_{\mathrm{b}} \cos(\phi_{\mathrm{s}})} \tag{3.63}$$

assuming $1/Q_0 << 1$.

This optimum value for the accelerating mode is reached by adjusting the FPC position. The FPC couples also to other modes and could in principle be used to reduce the Q_{ex} for these modes. Since the coupling is only optimised for the accelerating mode, the coupling is dependent on the frequency and the installed waveguide system. Hence, dedicated devices have to be introduced for HOM damping.

3.5.5 Higher Order Mode Damping

As shown in the last subsection, the Q_{L} of a mode can be reduced by coupling an additional load to the mode. This concept is also used for HOM damping. This requires that the HOMs must have field components which propagate out of the cavity into the neighbouring beam pipe. Experience has shown that coupling ports on the cells of SRF cavities introduce problems with multipacting and crossing of weldings, hence modern SRF cavities carry their HOM couplers on the cut-off tubes close to the endcells [64].

Today there are in principal two methods used for damping HOMs in superconducting cavities [65]. One solution is to add lossy material, such as for example ferrite, to the beam pipe [66]. The modes which propagate out of the cavity into the beam pipe are damped in this material. With this method a moderate damping is possible. The created heat has to be absorbed before it enters the He bath, hence requiring a specific distance between cavity and absorber, as well a special cooling circuit by for example He gas, liquid N_2 and even water for high-current machines. A big problem with this method is that the lossy material can contaminate the cavity, lead to field emission and reduce the maximum possible accelerating gradient. In addition the material is sensitive to all modes and thus also to the accelerating mode. Hence, the beam pipe has to be designed such that the fundamental mode is decayed already to a tolerable level at the position where the ferrite is located. This can also reduce the coupling to the other modes.

The other method is to use an antenna or loop which couples to the HOMs and which has a notch filter[20] to reject the accelerating mode. A strong HOM damping in the order of $Q_{\mathrm{ex}} = 10^4$ is possible with a broad-band coupler[21]. The mechanical design of such devices has to be done carefully to avoid multipactoring and coupling to the accelerating mode [69]. An example of an antenna type HOM coupler is shown in Figure 3.12, which is a first design model for the SPL $\beta_{\mathrm{g}} = 1$ cavity and is currently under development at the University of Rostock [70, 71]. Another advantage of a HOM coupler is that it can be used for beam diagnostics purposes [72].

So called "trapped" modes have most of their stored energy in the centre cells, which means that they do not or only very weakly couple to HOM couplers or the power coupler, which are placed before and/or after the cavity cells. In consequence trapped modes have generally a very high Q_{ex}. These modes have to be identified during the design and prototyping stage and eliminated by changing the cavity geometry. The probability of a trapped mode generally increases with the number of cavity cells [29]. Additionally the end cells, which are connected to the beam

---

[20] *Notch Filter*: is a band-stop filter with a narrow stopband (high Q factor).

[21] On the LHC SRF cavities resonant couplers have even stronger coupling [67, 68].
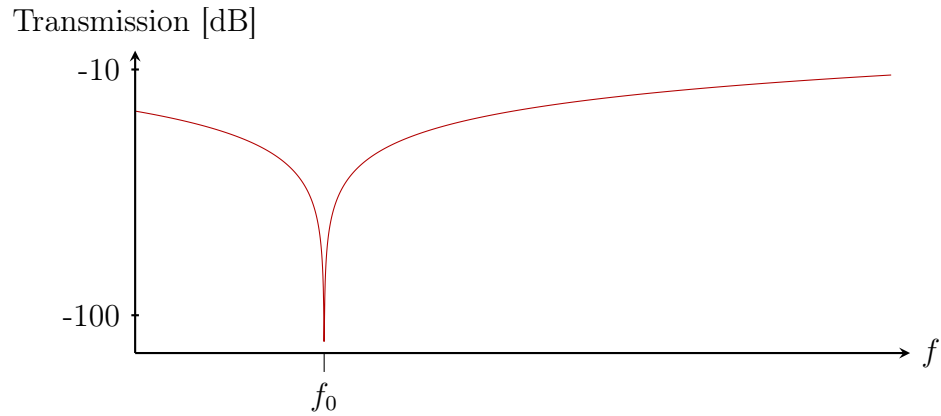
Figure 3.11: Transmission curve of a notch filter. At the rejection frequency f_0 the transmission is several orders of magnitude lower than at other frequencies.
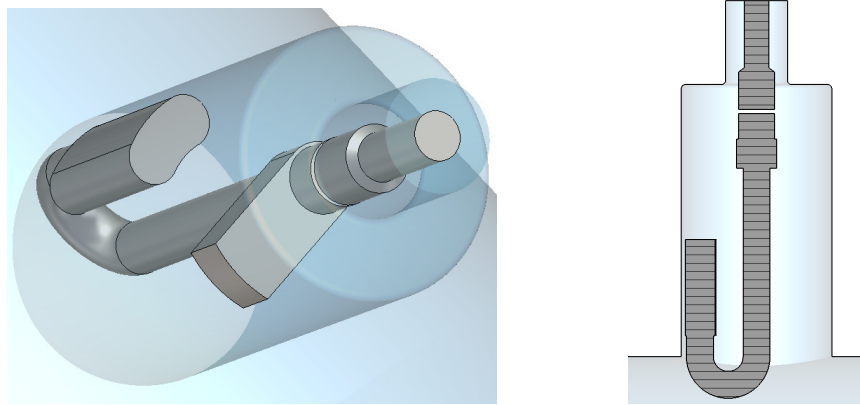
Figure 3.12: Hook type HOM coupler design study for the SPL [71, 73].

pipe, have a different resonance frequency to compensate for the coupling to the beam pipe in order to reach field flatness for the accelerating mode. This frequency difference increases with the number of cells and is even larger for HOMs. This can lead to the situation where a HOM cannot propagate out of the cavity because it is rejected from the end cell, due to the different mode frequency of that particular mode [47, 74].

Chapter 4

Radio Frequency Simulation Methods and Tools

Since the eigenmodes and field distributions in elliptical cavities cannot be solved analytically, numerical methods have to be used. First, the principal simulation methods and techniques for this task are introduced. After defining a list of requirements needed to do a full HOM spectrum analysis, three tools, which will be used for studies in the frame of this thesis are investigated in detail and their features are compared.

4.1 Simulation Methods

According to [75], the three different choices for the numerical solution of *Partial Differential Equations* (PDEs) are the *Finite Differential Method*, the *Finite Element Method* (FEM) and the *Finite Volume Method* (FVM). The basic concept of these methods is to discretise the area of interest in small cells and solve the PDE in these cells using the conservation law, which is the *Poynting theorem* in electro dynamics

$$\int_S (\vec{E} \times \vec{H}) \cdot d\vec{s} + \frac{\partial}{\partial t} \int_V \frac{1}{2}(\epsilon E^2 + \mu H^2) dv + \int_V \vec{E} \cdot \vec{J} dv = 0. \qquad (4.1)$$

The first term is the energy flux through the surface of the volume, the second the change of the stored energy in the electric and magnetic field, and the third one represents the rate at which the electric field does work on the electric charges within the volume V.

In the following, the principal concepts of the three solving methods following [75, 76] are introduced with a focus on the Maxwell's equations in a source free region (3.10). Different mesh types are discussed, which are used to approximate

the object of interest. Afterwards the role of boundary conditions and symmetry planes is explained.

4.1.1 Finite Difference Method (FDM)

The FDM is the oldest method to solve PDEs numerically and was introduced in a fundamental theoretical paper by R. L. Courant, K. O. Friedrichs, and H. Lewy [77, 78]. It is based on the Taylor expansion

$$f(x_{j+1}) = f(x_j) + f'(x_j)h + f''(x_j)\frac{h^2}{2} + \dots, \tag{4.2}$$

where

$$h \equiv x_{j+1} - x_j. \tag{4.3}$$

The problem is discretised with a mesh spacing h, assuming a 1D problem, and the derivatives can be written in terms of discrete points

$$f'(x_j) = \frac{f(x_{j+1}) - f(x_{j-1})}{2h} \tag{4.4}$$

$$f''(x_j) = \frac{f(x_{j+1}) - 2f(x_j) + f(x_{j-1})}{(2h)^2}. \tag{4.5}$$

These derivatives can be used to solve the wave equation at a discrete mesh point. This method is easy to implement and only a few calculations have to be done per mesh point, but a large number of mesh points are necessary to get a good approximation, especially if a Cartesian mesh with rectangular or , in the 3D case hexahedral mesh cells is used.

4.1.2 Finite Element Method (FEM)

The FEM, dated back to R. L. Courant [79, 80], is one of the standard techniques for many numerical applications. If the PDE is given in differential form as

$$\mathcal{L}(u) = s, \tag{4.6}$$

where $\mathcal{L}$ is a differential operator, the integral form is given by

$$\int_0^1 \mathcal{L}(u)w(x)dx = \int_0^1 sw(x)dx, \tag{4.7}$$

where the choice of the weight function $w(x)$ defines the type scheme. Discretising the region of interest $\Omega = \{x : 0 \leq x \leq 1\}$ into $N-1$ sub-domains or elements $\Omega_i = \{x : x_{i-1} \leq x \leq x_i\}$ and assuming that the approximate solution is represented by

$$u^\delta(x,t) = \sum_{i=1}^N u_i(t)N_i(x), \tag{4.8}$$

where the set of functions $N_i(x)$ is known as the expansion basis. Its support is defined as the set of points, where $N_i(x) \neq 0$. If the support of $N_i(x)$ is the whole interval, the method is called *spectral method*. In case of the *Galerkin* FEM the weight function $w(x)$ in (4.7) is the same as the basis function $N_i(x)$, i.e. $w(x) = N_i(x)$. This system can be represented as an eigenvalue problem of a spares matrix, which can be solved on a computer.

In case of the Maxwell's equations in a source free ($s = 0$) region u may stand for the vector $\vec{E}$ in the entire volume and $\mathcal{L}(u) = 0$ for

$$\nabla \times \left(\frac{1}{\mu} \nabla \times \vec{E} \right) - \omega^2 \epsilon \vec{E} = 0. \tag{4.9}$$

4.1.3 Finite Volume Method (FVM)

The FVM, often also called finite integration method (FIM), works similar to the FEM, but uses an integral representation of the problem, instead of a differential one. The PDE is solved stepwise on small volume elements.

In case of the Maxwell's equations, the finite integration technique (FIT), which is based on the *finite integration theory*, was developed by T. Weiland [81]. It is a consistent discretisation scheme for Maxwell's equations in their integral form using a dual grid $G, \tilde{G}$, illustrated in Figure 4.1.
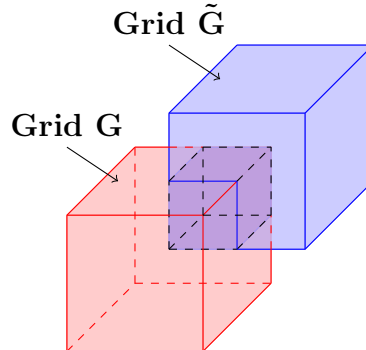
Figure 4.1: Scheme of two cells in the dual grid G and $\tilde{G}$. The edges of the cell in G represent the electric fields and the edges of cell in $\tilde{G}$ the magnetic fields.

The mesh points of one grid are centred in the cubical cells formed by the other. All the edges of a cell represent the electric respectively the magnetic fields or currents. This dual grid models the feature of the Maxwell's equations, that the spatial derivatives of the electric field are related to the magnetic field and vice versa. The resulting matrix equations called *Maxwell-Grid-Equations* can be processed efficiently. One other advantage of using this dual grid is, that the vector

identities $\nabla \times \nabla \phi \equiv 0$ and $\nabla \cdot \nabla \times \vec{A} \equiv 0$ become properties of the topological matrices representing the curl, grad and div operators. A detailed description is given in [82].

4.1.4   Mesh Types

In order to apply a numerical solver, the simulation object must be discretised. This is done by approximating the object by a mesh consisting of small primitive cells. A face of a cell is connected uniquely to a face of a neighbouring cell. These primitive cells have normally all the same basic shape in a mesh. According to the shape type of the primitive cell the mesh type is classified. In 2D problems typically rectangles or triangles are used as primitive cell shapes, but also curved elements can be used. An example of three different mesh types is shown in Figure 4.2, where a part of an elliptical cavity is meshed. The rectangles are less accurate than triangles and the curved elements approximate the structure best.

(a) rectangles (MWS)   (b) triangles (SF)   (c) curved elements (HFSS)
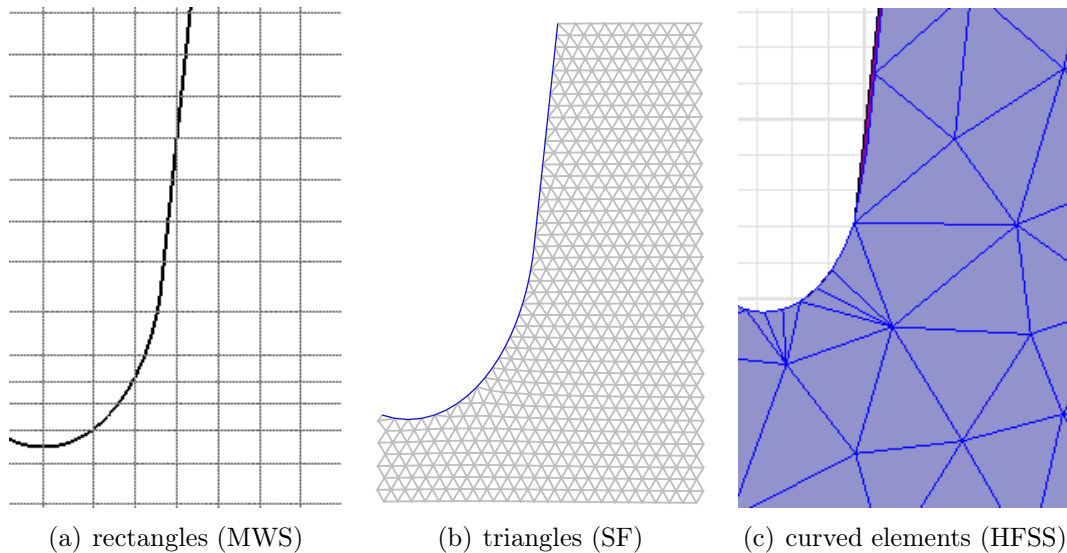
Figure 4.2: Different 2D mesh type representations of a part from an elliptical cavity. The meshes are screen shots from different simulation tools, which will be introduced in the next section.

In 3D models, the rectangles are replaced by hexahedral and the triangles by tetrahedral elements. Also curved elements exist based on tetrahedral. Three different 3D mesh cell shapes are illustrated in Figure 4.3.

While a hexahedral mesh is the easiest to generate, the tetrahedral mesh generation with curved elements is more complex, but the approximation to round

(a) hexahedral   (b) tetrahedral   (c) curved tetrahedral
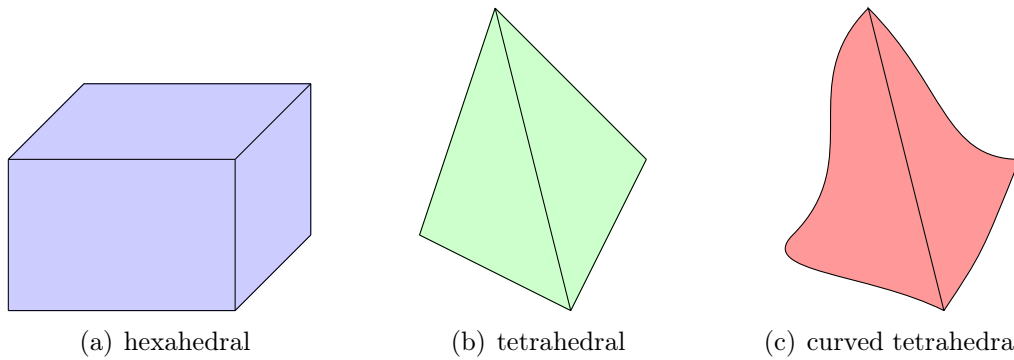
Figure 4.3: Different 3D mesh cell geometries used to approximate the model geometry.

structures is far better than with a hexahedral mesh. The accuracy of a mesh using only tetrahedral elements is between the other two types, if the same number of mesh cells is used. With tetrahedral or curved elements or triangles in two dimensions, it is simple to increase the number of mesh cells in a region without increasing the number mesh cells in the surrounding area, which is not possible with a basic hexahedral mesh. Increasing the mesh cells in a region also leads to an increase of the mesh cells in the neighbouring regions as illustrated in Figure 4.4. On solution of this problem is to introduce a sub-grid, where a mesh cell is split up in smaller cells. Then several mesh cell faces of the sub-grids' cells are connected to one face of the basic cell.

(a) initial mesh   (b) refined mesh   (c) sub-gridding
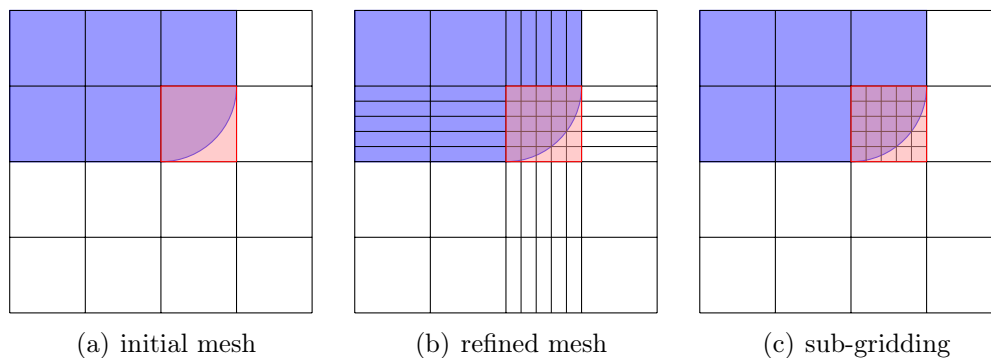
Figure 4.4: Illustration of the mesh refinement problem of a rectangular mesh and a solution by introducing sub-gridding.

The complexity for the mesh generator increases with the used cell shape. While a rectangular/hexahedral mesh is most easy and fast to generate, the reso-

lution is not that good compared to a triangle/tetrahedral mesh using also curved elements with the same number of mesh cells.

In the field of mesh generation and solving Maxwell's equations research is ongoing, also in the context of the SPL R&D [83]

4.1.5 Boundary Conditions and Symmetry Planes

The simulation model boundaries are a critical issue for all solver methods and have to be modelled carefully. In electro dynamics there are in principal two different boundary conditions used to describe a vector potential $\vec{A}$. The first one is the so called Dirichlet boundary condition, where the potential is specified everywhere at the boundary. The second one is the Neumann boundary condition, where $\vec{n} \cdot \nabla A$ is specified everywhere at the boundary. Typically, one of these two conditions is applied at the model boundary. In principal also a combination of the boundary conditions is possible. In RF simulations of a lossless cavity three elements are used: vacuum, *Perfect Electric Conductors* (PECs) and walls, which act as mirror either for electric field lines or magnetic field lines. The fields are only calculated inside the vacuum parts. The surface of a PEC corresponds to a Dirichlet boundary condition. There exist several acronyms in the different simulation tools for these boundary conditions, which are listed in Table 4.1. These boundary conditions can also be used to introduce symmetry planes in order to reduce the simulation effort significantly, because only a part of the entire object has to be simulated and the simulation time increases more than linear with the number of mesh cells, depending on the solver method.

Table 4.1: Simulation boundary conditions and names used in different simulations tools.

	Dirichlet	Neumann
$\vec{E}$	perpendicular ($E_\mathrm{t} = 0$)	parallel ($\vec{n} \cdot \vec{E} = 0$)
$\vec{H}$	parallel ($\vec{n} \cdot \vec{H} = 0$)	perpendicular ($H_\mathrm{t} = 0$)
Screens	electric	magnetic
Walls	Perfect E	Perfect H
Material	PEC	PMC[†]

[†] *Perfect Magnetic Conductor*

4.2 Simulation Tools

Over the last decades the CPU power has increased significantly and now 3D EM simulations can be carried out on desktop computers. There are a lot of 2D and 3D EM simulation tools available, which can be used to simulate elliptical cavities.

In order to do a HOM analysis the software must provide an eigenmode solver, which finds all modes in a cavity in a given frequency range. Furthermore several mode properties like mode type, mode frequency, $R/Q(\beta)$, stored energy, Q_0, damping, and the electric field profile along a predefined path is needed for beam dynamics simulations or power consumption estimations.

Three different tools are introduced in this section, which provide most of the needed features and will be used later to analyse different SC elliptical cavities.

4.2.1 Superfish

SUPERFISH (SF) [84] is one part of the Poisson/Superfish 2D FDM code, which is distributed for free by the Los Alamos Accelerator Code Group [85] and is one of the most popular 2D simulation tools for RF cavity design. While electro and magneto static problems, which are the solution of Poisson's equation, are covered by *Poisson*, Superfish is dedicated to RF field distributions in a resonant cavity or wave-guide with the two general solvers *FISH* and *CFISH* for lossless (vacuum) and lossy material. There are several packages available for different types of cavities, containing dedicated solver and tuning programs. The routines *ELCAV* and *ELFISH* form a package specialized in the design and optimisation of elliptical cavities and with BuildCavity [86] a GUI is available which provides further functions for this package.

The cavity structure is described by the contour line, which is modelled with a combination of straight lines, circle and ellipse parts. A triangular mesh is used afterwards to approximate the modelled structure. Dirichlet or Neumann boundary conditions can be used at the walls. A drive point has to be specified to excite the structure. This point must be located in an area where the mode has a non zero magnetic field. That is why the drive point has to be adopted to find all modes in a structure properly.

The solver is based on the method from Holsinger and Halbach [84] to solve the generalised Helmholtz equation

$$\nabla^2 \phi + k^2 \phi = S \tag{4.10}$$

for the eigenvalue k and the eigenfunction $\phi(x)$. The quantity S is called the source term. It focuses to solve RF wave-guides in two dimensions and cylindrical symmetric RF cavities in three dimensions with Dirichlet or Neumann boundary conditions.

The solver uses the Poynting theorem (4.1) and the fact, that the surface integrals must vanish in a closed cavity. Then the resonance finding problem can be reformulated as a root finding problem of the following function

$$D(k^2) = kc\frac{\int_V \vec{H}_t \cdot \vec{K}_t dv}{\int_V \epsilon H_t^2 dv} \equiv R(k^2) - k^2 c^2, \qquad (4.11)$$

where $\vec{H}_t$, $\vec{K}_t$ are the time independent parts of magnetic field $\vec{H}$ and the magnetic current density $\vec{K}$[1] and

$$R(k^2) = k^2 c^2 \frac{\int_V \epsilon E_t^2 dv}{\int_V \epsilon H_t^2 dv}. \qquad (4.12)$$

Resonances occur, when $D(k^2) = 0$ and $dD(k^2)/d(k^2) = -1$. There is no magnetic current required to maintain the fields in the cavity. This implies also that $R(k^2) = k^2 c^2 = \omega^2$, which means that the energy stored in the electric field is equal to the magnetic field.

Monopole modes can be found via a frequency scan to get a starting frequency. Then different iterative root finding methods can be used to get the exact resonance frequency. The field distribution of the accelerating mode in a medium beta cavity is shown in Figure 4.5. With SF only monopole modes can be found, because a rotational symmetry of the field is assumed, which is only valid for monopole modes. The method in general could also be used for other modes, but then different assumptions for the field symmetry in azimuthal direction have to be used.
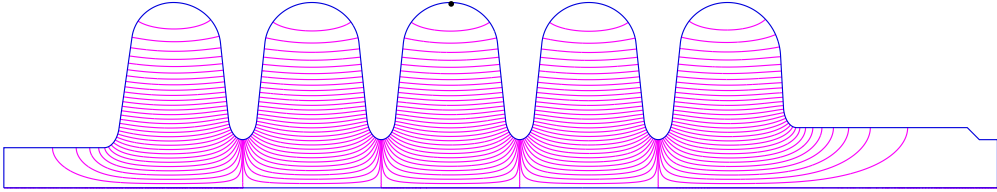
Figure 4.5: Plots of the E-field distribution in the accelerating mode in a 5 cell $\beta = 0.65$ cavity. The black dot in the centre cell is the driving point.

SF is written in Fortran and compiled with the Lahey LF95 compiler for MS Windows®. It runs on a Intel® Pentium® or equivalent processor. The memory usage depends on the problem size, but is very moderate, compared to the requirements of 3D codes. Solving an SPL cavity takes only a few seconds on a desktop computer and about 100 MB RAM are needed.

---

[1] In superfish a fictitious magnetic current density and magnetic charge density are introduced to "drive" the fields in the cavity. At resonance the current driving the cavity approaches zero.

4.2.2 CST Microwave Studio

Microwave Studio® (MWS) is a module of the *Computer Simulation Technology* (CST®) [87] software suite. MWS is a 3D FIT EDA tool, dedicated for RF design and simulation. Several solvers for frequency and time domain are available, which are not investigated further. Only the eigenvalue solver is discussed, which will be used for the HOM analysis. The software is widely used in the accelerator community to simulate cavities.

A cavity simulation model, shown in Figure 4.6, can be built up with the modeller or imported from another EDA or CAD tool. The model body is a cuboid consisting of *Perfect Electric Conductor* (PEC) material and the real simulation model is placed inside. Boundary conditions or ports can only be specified on the outer borders of the model body, which can be a problem in some cases. For example, it is not possible to simulate a 10° model of a rotational symmetrical cavity, which would be sufficient to get all monopole modes. Simulation symmetry planes can only be specified in the symmetry planes of the model body. A hexahedral mesh is produced inside the complete model body. To improve the geometric approximation a method called *Perfect Boundary Approximation*® (PBA) [88] is used. Other mesh types like tetrahedral or sub-griding are not available for the eigenmode solver. This leads to a very high number of mesh cells in the order of several million to model a complete SPL cavity.
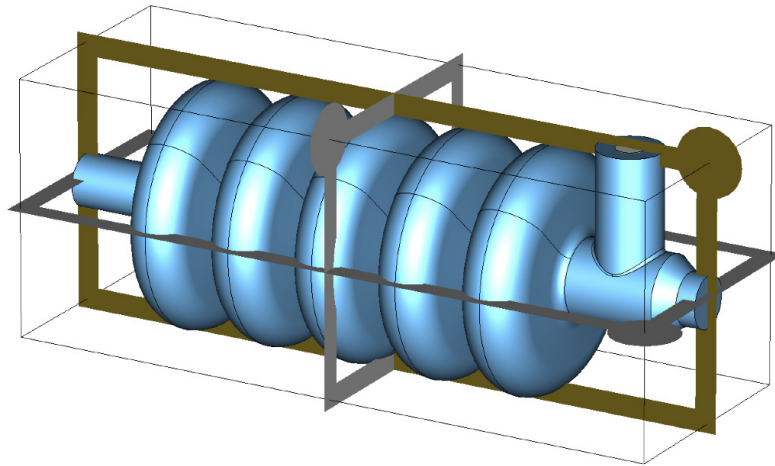
Figure 4.6: Cavity model of a medium β cavity in MWS. The simulation body (cuboid with black edges) and the possible symmetry planes are shown.

The Advanced Krylov Subspace method[2] (AKS) is used to find the n lowest eigenfrequencies of the model. For a good performance the highest mode frequency must be estimated for a proper construction of the AKS filter polynomial. It can only be used in lossless structures, hence in lossy structures another solver (JDM[3]) has to be used. All MWS simulation results presented in this thesis are produced with the AKS solver. The simulation time and memory requirements increase with the number of modes, which should be found. An adaptive mesh refinement can be used to increase the eigenmode frequency accuracy until the frequency deviation from step to step is less than a specified value. In each step the number of mesh cells is increased in general.

The modelling and post processing can be automated using VBA[4] macro scripts. It is also possible to build parameterised models, which can be tuned automatically. For most of the cavity performance parameters there are already predefined post processing macros.

The software runs under MS Windows® on 32 Bit or 64 Bit systems. The solvers are also available for Linux. Since the complete model is not needed to be in the memory during solving, the RAM requirements are less compared to FEM based solvers. The storage requirements on disk are higher, due to the large number of mesh cells. In case the model does not fit completely into the RAM, the solving time increases significantly, because of swapping.

4.2.3   Ansoft HFSS

The High Frequency Structure Simulator (HFSS™) is a commercial 3D Full-wave EM FEM tool for EDA from ANSOFT® [90], which is part of ANSYS®. It is primarily intended to analyse S-parameters and radiation problems, but it also provides an eigenmode solver, which will be used here.

The simulation model can either be imported from an EDA or CAD program or built directly in HFSS™. It is possible to construct parameterised models, which could be optimised by tuning the model parameters. The geometric model is divided into tetrahedral cells, where a single tetrahedron is a four-sided pyramid. In HFSS™ version 12 non-linear quadratic or cubic elements, so called curved elements, are introduced to represent the geometry. In each model object, different mesh constrains can be given to optimise the mesh or to increase the number of

---

[2] Krylov subspace methods are iterative conjugate gradient methods to find eigenvalues. They work by forming an orthogonal basis of the sequence of successive matrix powers times the initial residual (the Krylov sequence). The approximations to the solution are then found by minimizing the residual over the subspace [89].

[3] Jacobi-Davidson method

[4] Visual Basic for Applications

mesh cells in the area of interest. The mesh generated to analyse a five cell $\beta = 0.65$ cavity is shown in Figure 4.7
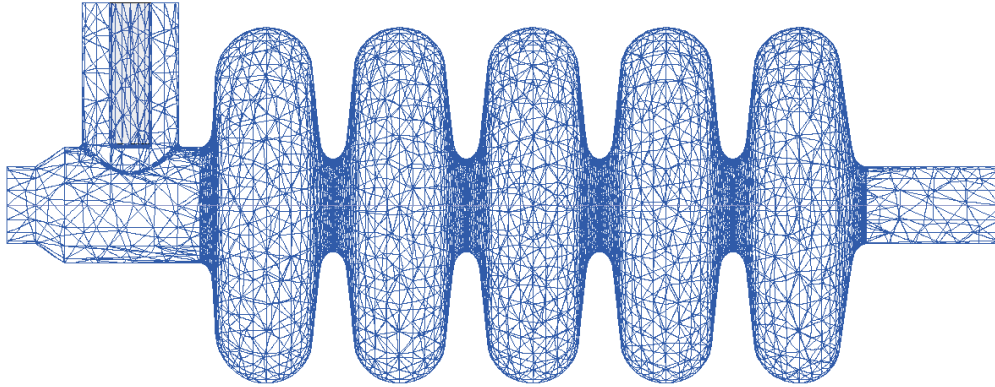
Figure 4.7: Surface mesh of a 5 cell $\beta = 0.65$ cavity. The curved elements reduce the number of mesh cells to approximate the round shapes.

Boundary conditions, such as perfect magnetic or electric walls, can be applied to each object face. So any kind of symmetry can be modelled. The default boundary condition, which is applied to all outer surfaces of the model is a perfect electric wall. HFSS uses an FEM based eigenmode solver, which can find up to 20 modes per simulation setup. A minimum frequency has to be defined as starting point. The adaptive mesh refinement can be used to improve the eigenmode frequency accuracy. It is an iterative process, refining the mesh in regions with high fields until the eigenmode frequency deviation from step to step is less than a specified value. For the post processing of the simulation several VBScript macros were developed by a summer student [91]. In this context a benchmark against an already build cavity structure was done.

The FEM needs an enormous amount of memory and the complete model must be located in the memory during the solving process. There are approaches for splitting up the model and solve it in a distributed way. Another limitation in HFSS is that no ports can be included in eigenmode problems. In order to simulate the influence of the FPC and HOM couplers, they have to be replaced by lumped circuit elements[5], which have a different frequency characteristics for the resistance compared to a wave-guide port. In HFSS versions earlier than 12 only a tetrahedral mesh without curved elements was available, which was a big limitation for modelling rounded structures such as elliptical cavities. The number

---

[5] A lumped circuit element consists of a resistor, a capacitor and an inductance, connected in parallel.

of mesh cells had to be increased enormously for curved structures to get the mode
frequencies with a sufficient accuracy.

The software runs under MS Windows® and Linux on 32 Bit or 64 Bit systems
and as scripting language VBScript is used, which is only available on Windows
systems. Solving a full 3D cavity model with a sufficient accuracy[6] more than
4 GB RAM are needed and requiring a 64 Bit OS. The CPU time is in the order
of several minutes to find a single mode in SPL cavity using symmetry conditions
on a single Intel® Xeon™ or AMD® Operon™ core.

4.2.4   Mesh Improvements by Using Curved Element

In HFSS v.12 a curved element mesh is introduced to better approximate round
structures. This feature is tested using a symmetrical, $10°$ model of the preliminary
$\beta = 1$ SPL cavity, illustrated in Figure 4.8. The simulation results are listed in
Table 4.2. This model is simulated using a pure tetrahedral mesh with and without
further mesh restrictions and compared with simulations where a curved element
mesh is taken. In all simulations the adaptive mesh refinement with a maximum
frequency deviation of 0.01% as convergence criteria is used. The simulations are
carried out specifying first or second order basis functions. Without any further
mesh restrictions the frequency calculated using curved elements is at least one
order of magnitude more precise than the best result without curved elements and
is found using a factor of 10 less mesh cells. The best result is obtained by using
curved elements together with the second order basic function where the frequency
error is in the order of $4 \cdot 10^{-5}$ compared to the frequency obtained with SF for
the same geometry. In this simulation also the smallest number of mesh cells
is used. All further HFSS simulations are carried out with the same simulation
options. The simulations carried out with HFSS v.11 lead to the same results as
with version 12, not using curved elements.

4.2.5   Software Features Comparison

The basic features, advantages, and drawbacks of the introduced simulation codes
are summarised in Table 4.3. All three of them will be used to analyse different
cavities in the next chapters. 2D simulations are much faster than 3D simulations
and provide a better accuracy, if the influence of asymmetric parts like the FPC
or other ports are not of interest. Hence, Superfish will be used for most of the
EM simulations.

---

[6] Frequency erro of 10^{-3}.

Table 4.2: HFSS simulation results of the accelerating mode frequency. Evaluation of the curved mesh option and different order of the basis function.

Type	Restriction	Order	Cells	RAM [MB]	f [MHz]	$\Delta f / f_0$
tetrahedral	no	1	907	30.5	709.499	$7 \cdot 10^{-3}$
tetrahedral	no	2	794	51.4	709.705	$8 \cdot 10^{-3}$
tetrahedral	yes	1	9352	98.2	706.437	$3 \cdot 10^{-3}$
tetrahedral	yes	2	14754	434.0	705.682	$2 \cdot 10^{-3}$
curved	no	1	1150	32.8	704.234	$3 \cdot 10^{-4}$
curved	no	2	603	44.1	704.385	$4 \cdot 10^{-5}$
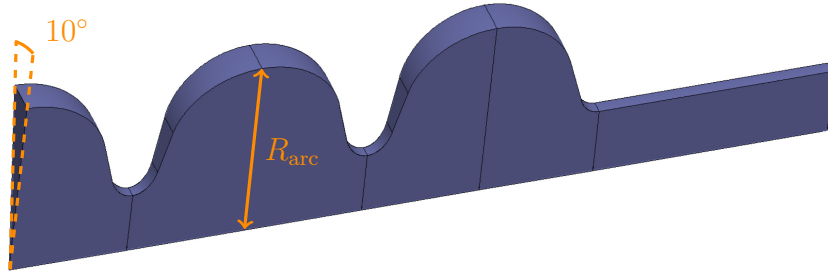
Figure 4.8: HFSS: $10°$ simulation model of preliminary symmetrical $\beta = 1$ SPL cavity. Due to the symmetry, only $\frac{1}{72}$ of the cavity volume is modelled.

Table 4.3: Simulation code features

	SF	MWS	HFSS
Dimensions	2	3	3
Mesh	triangles	hexahedral	tetrahedral, curved elements
Solver method	FDM	FIT	FEM
Advantage	very fast	arbitrary modes per simulation	very flexible
Drawback	only monopole modes	no arbitrary boundary conditions	only 20 modes per simulation

Chapter 5

SPL Baseline Cavities

Beginning of 2010 the design of the SPL cavities [92, 93] has been frozen for prototyping[1]. The HOM of these cavities is analysed in detail in this chapter, which is needed for beam dynamics studies. First the centre cells of both cavities are analysed to get an overview of the HOM spectrum. Then the modes in 2D and 3D models are analysed using the tools introduced in chapter 4.2. The cavity shape parameters of the baseline cavities are listed in Table 5.1.

For the beam dynamics studies, discussed in chapter 8, not the baseline cavity design is used, because it was not yet available, when the simulations started. Preliminary cavity shapes are used for the studies. Also beam dynamics simulations, using the HOM spectrum of the baseline cavities, are carried out [95] with the same general results as with the preliminary cavity shapes. Hence, only the beam dynamics simulation results of the preliminary shapes are discussed in this thesis.

Table 5.1: Shape parameters of the SPL baseline cavities. All sizes are in mm.

Cell	$\beta_\mathrm{g} = 0.65$ cavity			$\beta_\mathrm{g} = 1$ cavity		
	centre	left	right	centre	left	right
R_arc	185	185	185	191	191	191
R_iris	48	40	60	65	70	65
l	69	69	69	106	103	103
A	47	42	53	78	74	74
B	45	40	56	78	77	83
a	14	15	13	22	19	19
b	24	25	22	35	25	25

---

[1] In case of the $\beta_\mathrm{g} = 0.65$ cavity, modifications have been made to use the same equipment and interfaces as for the $\beta_\mathrm{g} = 1$ cavity [94]. These changes are not considered here.

5.1   Centre Cell Analysis

In order to get an overview of the HOM spectrum the centre cells of the $\beta_\mathrm{g} = 0.65$ and $\beta_\mathrm{g} = 1$ cavities are analysed using MWS 2010. The simulations are carried out with different boundary conditions to obtain the 0- and π-mode. The lowest modes, found in both cavities, are listed in Table 5.2. Looking at the mode frequencies one finds, that the order is not the same in which the different modes appear in the two cavities. For example the first higher order monopole mode in the $\beta_\mathrm{g} = 0.65$ cavity is the TM_{020} mode, but the TM_{011} in the $\beta_\mathrm{g} = 1$ cavity, which can be explained by the different cell length.

At low frequencies the modes are clearly separated, while for higher frequencies the frequency band between the 0- and π-mode configuration of a mode start to overlap with the band of other modes. Going from a single cell to a multi cell cavity, the number of sub-modes increases linear with the number of cells. The identification of the modes becomes more difficult because different sub-modes of different modes start to merge and create hybrid modes, which can look completely different from cell to cell. In the $\beta_\mathrm{g} = 1$ cavity there are 20 modes below $2\,\mathrm{GHz}$, hence one has to expect about 100 modes in a five cell cavity for this frequency range.

Table 5.2: Lowest TE and TM modes in the centre cell of the SPL baseline cavities. Different boundary conditions at the cavity iris are used to obtain the 0 and π mode. The modes are sorted by their names, all frequencies are stated in MHz.

Mode	$\beta_\mathrm{g} = 0.65$		$\beta_\mathrm{g} = 1$	
	0	π	0	π
TE_{011}	1766	1763	1355	1352
TE_{021}	2347	2336	2048	2021
TE_{022}	2964	2910	2027	2014
TE_{111}	1432	1227	988.3	875.7
TE_{112}			1689	1337
TE_{121}	2028	2012	1665	1641
TE_{211}	1707	1691	1256	1244
TE_{212}	2894	2654	1992	1860
TE_{221}	2309	2292	1973	1956
TE_{311}	1936	1935	1508	1507
TE_{411}	2160	2160	1757	1757

Mode	$\beta_\mathrm{g} = 0.65$		$\beta_\mathrm{g} = 1$	
	0	π	0	π
TM_{010}	694.9	704.9	691.1	704.2
TM_{011}	1741	1772	1288	1331
TM_{020}	1387	1564	1446	1501
TM_{021}	2219	2337	1834	1982
TM_{110}	1040	1009	1022	970
TM_{120}	1880	1707	1808	1817
TM_{121}	1912	1808	1524	1395
TM_{210}	1040	1383	1348	1336
TM_{211}			1793	1736
TM_{310}	1719	1719	1660	1658
TM_{410}	2038	2038	1960	1959
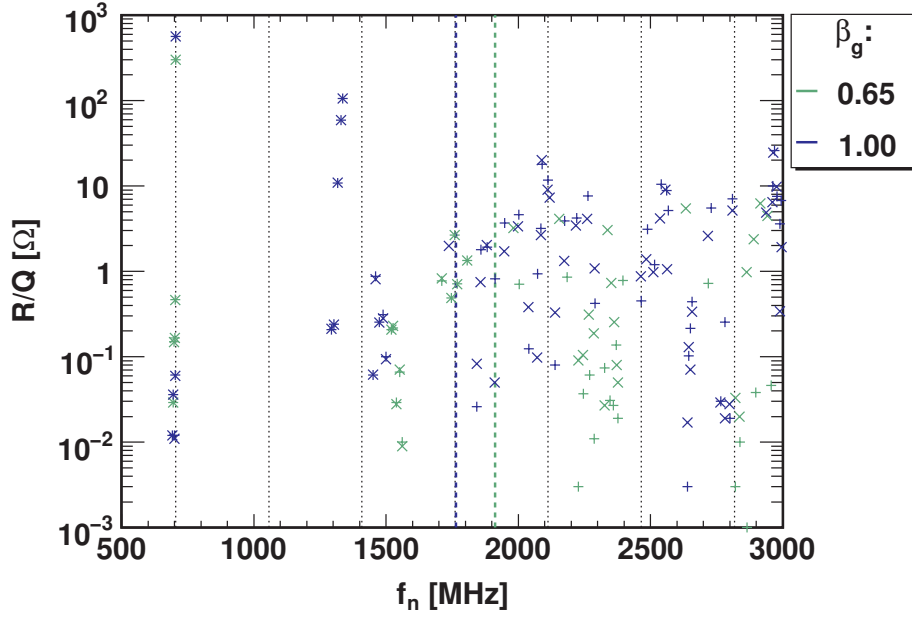
Figure 5.1: Maximum $(R/Q)(\beta)$ value in the used velocity range for all monopole modes in both cavities up to $3\,\text{GHz}$. The results for different boundary conditions are indicated with different markers (plus, cross) and merge to a star, if the values agree. The $(R/Q)(\beta)_{\text{max}}$ values start to deviate above the beam pipe cutoff frequency, indicated by the dashed lines, for the different boundary conditions and are about one order of magnitude higher in the $\beta_{\text{g}} = 1$ cavity. There are several modes close to fundamental machine lines, which are indicated by the black dashed lines.

5.2 2D Monopole Analysis

2D models assuming a rotational symmetry of the baseline cavities are analysed using superfish. The impact of the fundamental power coupler cannot be modelled in such simulation. Two different boundary conditions (electric and magnetic wall) are applied at the beam pipe ends. A frequency scan is then performed to find all modes up to a frequency of $3\,\text{GHz}$. The monopole modes found in both cavities and both boundary conditions are summarised in Figure 5.1.

In the $\beta_{\text{g}} = 1$ cavity, the highest $(R/Q)(\beta)_{\text{max}}$ values are about one order of magnitude higher as compared to the $\beta_{\text{g}} = 0.65$ cavity. There are several modes close to fundamental machine lines, which have to be carefully checked in prototype cavities.

At low frequency the identified modes with both boundary conditions agree very well and the 'plus' and 'cross' markers merge to a star. They are located at the frequency expected from the single cell analysis. For higher frequencies the

modes diverge, especially above the beam pipe cutoff frequencies, which are listed in Table 5.3 for different beam pipe radii. At high frequencies the modes depend on the beam pipe geometry and couple via the beam pipe with the modes in the neighbouring cavities. The mode coupling inside an SPL cryo-module is currently under investigation [96] and will not be discussed further here. Hence, the HOM analysis in the 3D model will focus on the modes below the cutoff frequency of the FPC beam pipe.

Table 5.3: Beam pipe cutoff frequencies

Position	$\beta_{\mathrm{g}} = 0.65$ cavity			$\beta_{\mathrm{g}} = 1$ cavity		
	r [mm]	TM_{01} [MHz]	TE_{11} [MHz]	r [mm]	TM_{01} [MHz]	TE_{11} [MHz]
FPC side	60	1912	1464	65	1765	1352
Opposit	40	2869	2196	70	1639	1255
After taper	48	2390	1830	40	2869	2196

5.3   HOM Analysis in the 3D Model

3D cavity models including the fundamental power coupler are analysed for both cavities, see Figure 5.2 and Figure 5.3. Simulations are carried out using MWS 2010 and HFSS v12. To reduce simulation time and required computing resources, a symmetry plane (perfect magnetic wall) in the y-plane is used. By introducing this symmetry plane no TE monopole modes can be found and only multi-pole modes of one polarity. These modes can be found by applying a perfect electric wall on the symmetry plane. To simulate 180° models about 1.5 Million mesh cells are needed in MWS and about $40,000$ in HFSS.

First, the fundamental passband modes are analysed before other monopole and dipole modes below the beam pipe cutoff frequency are cowered.

5.3.1   Fundamental Passband Modes

The modes in the fundamental passband beside the $\mathrm{TM}_{010,\pi}$ have to be studied carefully, because of their small frequency spread and their significant $(R/Q)(\beta)$ values for relative particle velocities different from the geometrical β of the cavities. In order to estimate the Q_{ex} provided by the fundamental power coupler to the fundamental passband modes, 3D EM simulations with HFSS v.12 and MWS 2010 are carried out. The coaxial power coupler is designed to have an impedance of
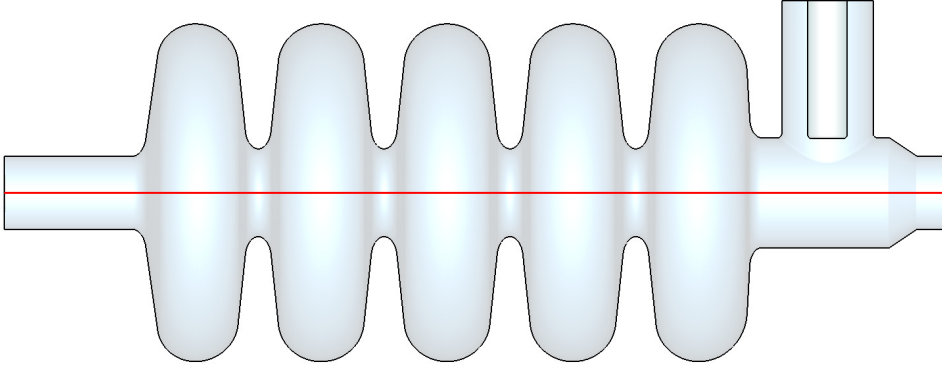
Figure 5.2: Cut along the beam axis in the 3D simulation model of the medium β cavity including the FPC but no HOM couplers. The beam axis is indicated by the red line.
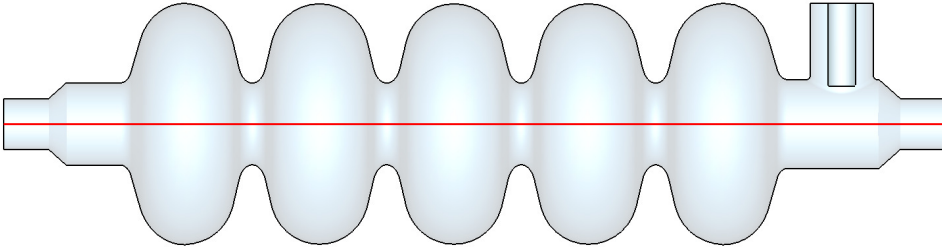
Figure 5.3: Cut along the beam axis in the 3D simulation model of the high β cavity including the FPC but no HOM couplers. The beam axis is indicated by the red line.

$50\,\Omega$ and provide a $Q_{ex} = 1.2 \cdot 10^6$ for the accelerating mode. It is connected to a wave guide. This port is modelled with a wave guide port in MWS and a lump circuit in HFSS. The resulting frequencies and Q_{ex} are listed in Table 5.4. 2D Superfish results without a fundamental power coupler are added for comparison.

The frequencies found with HFSS are always higher than the ones found with MWS. In case of the $\beta_\mathrm{g} = 1$ cavity the difference is only about $200\,\mathrm{kHz}$ and the results agree very well with the 2D simulations, where the deviation is the same order of magnitude as comparing the 3D results. In the $\beta_\mathrm{g} = 0.65$ cavity the differences are slightly higher, but still below $1\,\mathrm{MHz}$. Comparing the values with Superfish simulations, there is a good general agreement with the MWS results, but the HFSS values are all about $500\,\mathrm{kHz}$ higher. Looking at the Q_{ex} values, the maximum difference ($|(Q_{\mathrm{ex,MWS},n} - Q_{\mathrm{ex,HFSS},n})/(Q_{\mathrm{ex,HFSS},n})|$) for the $\beta_\mathrm{g} = 1$ cavity is only $\sim 4\%$, but up to 13% for the $\beta_\mathrm{g} = 0.65$ cavity.

The $(R/Q)(\beta)$ dependency of the modes in the used β range, based on the MWS simulation results, is shown in Figure 5.4. Only the $\mathrm{TM}_{010}, 4/5\pi$ mode has

Table 5.4: Mode frequencies and Q_{ex} of the fundamental passband modes in the $\beta_g = 0.65$ and $\beta = 1$ cavities.

β_g	Mode	SF f_n [MHz]	HFSS f_n [MHz]	Q_{ex} [10^6]	MWS f_n [MHz]	Q_{ex} [10^6]
0.65	$TM_{010,1/5\pi}$	695.4	696.0	6.46	695.2	5.73
0.65	$TM_{010,2/5\pi}$	697.9	698.5	1.78	697.8	1.60
0.65	$TM_{010,3/5\pi}$	701.0	701.6	0.91	700.9	0.81
0.65	$TM_{010,4/5\pi}$	703.5	704.1	0.61	703.4	0.57
0.65	$TM_{010,\pi}$	704.4	705.0	1.10	704.4	1.03
1	$TM_{010,1/5\pi}$	692.5	692.5	6.32	692.3	6.07
1	$TM_{010,2/5\pi}$	695.7	695.7	1.73	695.5	1.67
1	$TM_{010,3/5\pi}$	699.8	699.7	0.91	699.6	0.88
1	$TM_{010,4/5\pi}$	703.1	703.1	0.65	703.0	0.63
1	$TM_{010,\pi}$	704.4	704.4	1.17	704.3	1.15

[†] linac definition; [‡] maximum value in used velocity range

high $(R/Q)(\beta)$ values for β values different to β_g. This mode has an even higher $(R/Q)(\beta)$ value than the accelerating π-mode at the beginning and end of the medium β section. Hence, high HOM voltages can build up in this mode, which can influence the beam and lead also to an additional heat load. This effect can only be avoided by reducing the velocity range in which the cavity is used or by reducing the number of cavity cells.

5.3.2   Higher Order Modes

MWS 2010 is used to find at least the first 100 modes in the 3D model. A symmetry plane is used to reduce the number of mesh cells. The simulation execution time was about one week each on a desktop PC for both models. All found modes and their $(R/Q)(\beta_g)$ value are shown in Figure 5.5 and Figure 5.6.

The found monopole and dipole modes up to the beam pipe cutoff frequency on the FPC side are listed in Table 5.5 and Table 5.6 for the $\beta_g = 0.65$ cavity and in Table 5.7 and Table 5.8 for the $\beta_g = 1$ cavity. Additionally, simulations with HFSS v12 are carried out to cross-check the MWS results. In the HFSS simulations a lumped circuit element with a resistance of $50\,\Omega$ is present at the FPC port. The resulting Q values are also listed in the table. For the monopole modes, the Superfish simulation results from section 5.3.1 are added.

The simulation results are in good agreement for the first modes, where the
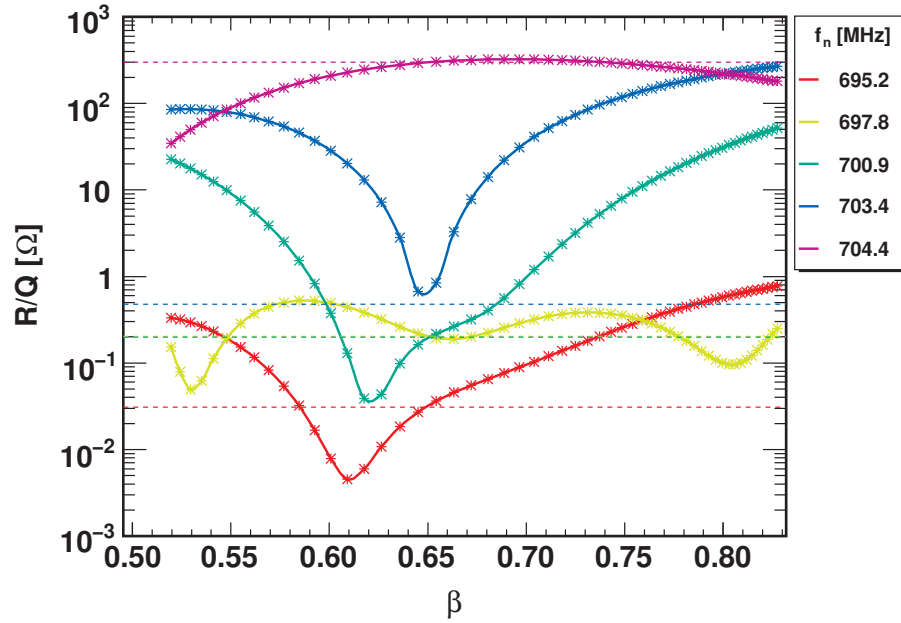
(a) $\beta_g = 0.65$
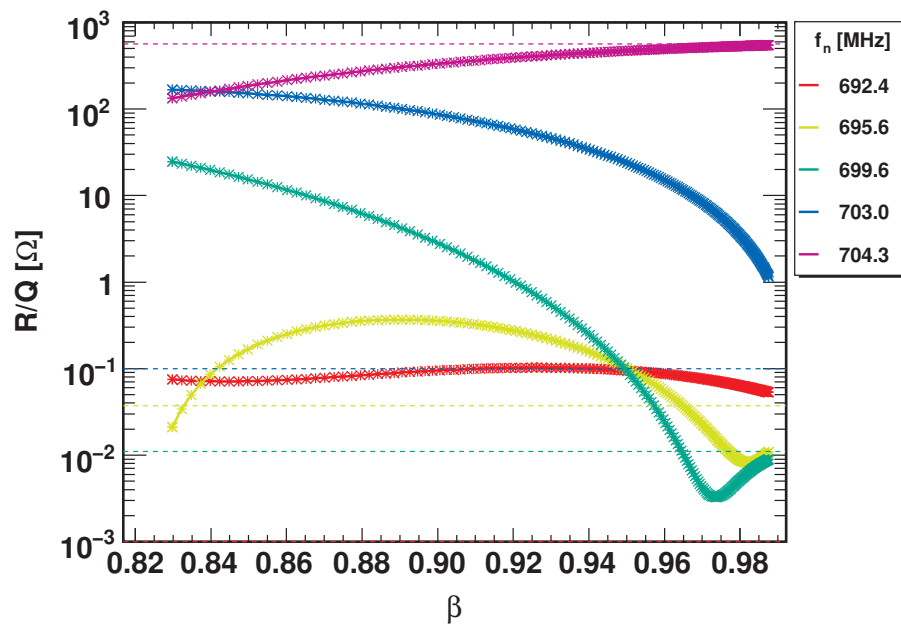
(b) $\beta_g = 1$

Figure 5.4: $(R/Q)(\beta)$ dependency of the TM_{010} modes. The dashed lines indicate the $(R/Q)(\beta_g)$ value. In the $\beta_g = 0.65$ cavity, the $TM_{010}, 4/5\pi$ mode has a higher $(R/Q)(\beta)$ value than the π-mode at the beginning and the end of the $\beta_g = 0.65$ cavity section.
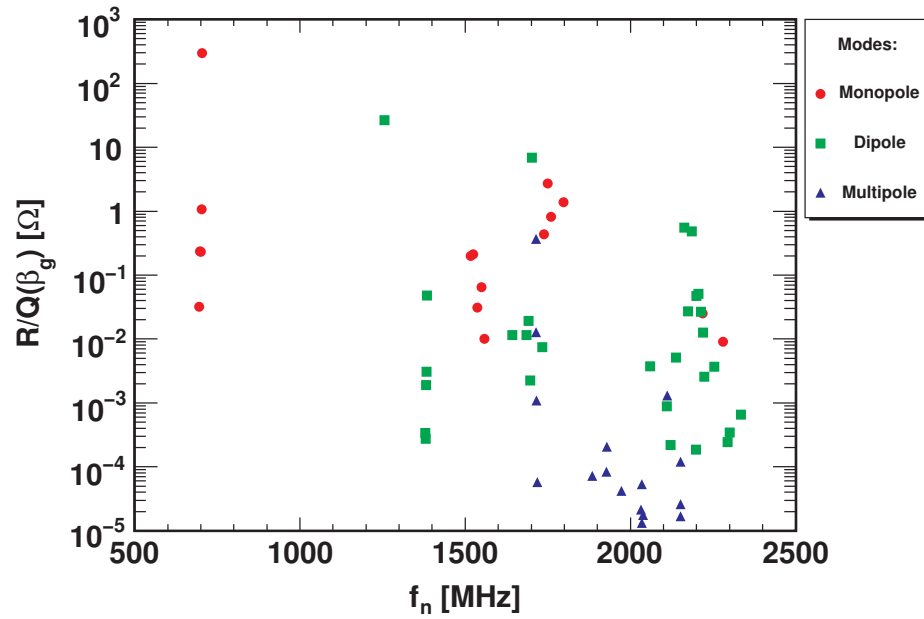
Figure 5.5: First 100 modes found in the $\beta_g = 0.65$ cavity and their $(R/Q)(\beta_g)$ value. The modes are divided into monopole, dipole and multipole modes.
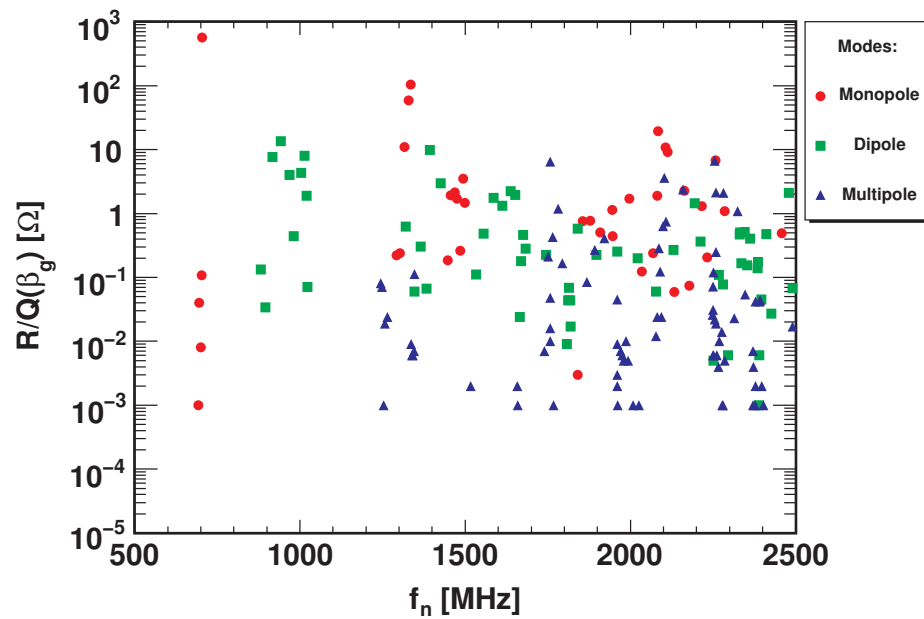
Figure 5.6: First 200 modes found in the $\beta_g = 1$ cavity and their $(R/Q)(\beta_g)$ value. The modes are divided into monopole, dipole and multipole modes.

Table 5.5: First two higher order monopole passbands in the $\beta_\mathrm{g} = 0.65$ cavity.

Mode	MWS		SF		HFSS	
	f_n [MHz]	$(R/Q)_n(\beta_\mathrm{g})$ [Ω]	f_n [MHz]	$(R/Q)_n(\beta_\mathrm{g})$ [Ω]	f_n [MHz]	Q_ex [10^3]
$\mathrm{TM}_{020}, 1/5\pi$	1516	0.2	1520	0.2	1521	43
$\mathrm{TM}_{020}, 2/5\pi$	1524	0.2	1527	0.2	1528	9
$\mathrm{TM}_{020}, 3/5\pi$	1536	0.03	1539	0.03	1540	4
$\mathrm{TM}_{020}, 4/5\pi$	1549	0.07	1551	0.07	1553	3
$\mathrm{TM}_{020}, 5/5\pi$	1558	0.01	1561	0.01	1562	5
$\mathrm{TM}_{011}, 4/5\pi$	-	-	1711	0.8	1712	2
$\mathrm{TM}_{011}, 3/5\pi\mathrm{a}$	1739	0.4	-	-	-	-
$\mathrm{TM}_{011}, 3/5\pi\mathrm{b}$	1750	2.7	1748	0.5	1749	300
$\mathrm{TM}_{011}, 2/5\pi$	1760	0.8	1759	2.7	1760	315
$\mathrm{TM}_{011}, 1/5\pi\mathrm{a}$	1797	1.4	1769	0.7	1770	1418
$\mathrm{TM}_{011}, 1/5\pi\mathrm{b}$	-	-	1807	0.7	1808	$3.43 \cdot 10^9$

Table 5.6: First two dipole passbands in the $\beta_\mathrm{g} = 0.65$ cavity.

Mode	MWS		HFSS	
	f_n [MHz]	$(R/Q)_{\perp,n}$ [Ω]	f_n [MHz]	Q_ex [10^3]
$\mathrm{TM}_{110}, 5/5\pi$	1007	0.8	1011	189
$\mathrm{TM}_{110}, 3/5\pi$	1012	8.5	1015	63
$\mathrm{TM}_{110}, 2/5\pi$	1019	10.6	1022	52
$\mathrm{TM}_{110}, 2/5\pi$	1028	2.5	1031	83
$\mathrm{TM}_{110}, 1/5\pi$	1036	0.3	1039	414
$\mathrm{TE}_{111}, 1/5\pi$	1214	2.5	1225	3
$\mathrm{TE}_{111}, 2/5\pi$	1249	2.7	1260	6
$\mathrm{TE}_{111}, 3/5\pi$	1303	1.5	1314	5
$\mathrm{TE}_{111}, 3/5\pi$	1328	3.6	-	-
$\mathrm{TE}_{111}, 4/5\pi$	1370	0.1	1377	6
$\mathrm{TE}_{111}, 5/5\pi$	1419	0.1	1426	21
$\mathrm{TE}_{111}, 5/5\pi$	1475	0.1	1483	0.02

Table 5.7: First two higher order monopole passbands in the $\beta_\mathrm{g} = 1$ cavity.

Mode	MWS		SF		HFSS	
	f_n [MHz]	$(R/Q)_n(\beta_\mathrm{g})$ [Ω]	f_n [MHz]	$(R/Q)_n(\beta_\mathrm{g})$ [Ω]	f_n [MHz]	Q_ex [10^3]
TM_{011}, π	1292	0.2	1293	0.2	1294	1017
$\mathrm{TM}_{011}, 4/5\pi$	1303	0.2	1304	0.2	1304	215
$\mathrm{TM}_{011}, 3/5\pi$	1317	10.9	1317	10.9	1318	71
$\mathrm{TM}_{011}, 2/5\pi$	1329	58.6	1330	58.8	1330	10
$\mathrm{TM}_{011}, 2/5\pi$	1335	104.7	1336	105.7	1336	92
$\mathrm{TM}_{020}, 1/5\pi$	1448	0.2	1451	0.1	1451	3
$\mathrm{TM}_{020}, 2/5\pi$	1457	1.9	1460	0.9	1460	1
$\mathrm{TM}_{020}, 3/5\pi$	1469	2.1	1474	0.3	1474	1
$\mathrm{TM}_{020}, 4/5\pi\mathrm{a}$	1476	1.7	-	-	-	-
$\mathrm{TM}_{020}, 4/5\pi\mathrm{b}$	1485	0.3	1489	0.3	1484	0.01
$\mathrm{TM}_{020}, 4/5\pi\mathrm{c}$	1494	3.5	-	-	1488	1
TM_{020}, π	1497	1.5	1499	0.1	1499	5

Table 5.8: Lowest dipole modes in the $\beta_\mathrm{g} = 1$ cavity. The modes are a combination of TE and TM modes, so called hybrid modes, and cannot be classified as in a pillbox cavity.

Mode	MWS		HFSS	
	f_n [MHz]	$(R/Q)_{\perp,n}$ [Ω]	f_n [MHz]	Q_ex [10^3]
Hybrid:	880.9	0.1	882.4	180
TE_{111}&	895.7	0.03	897.0	47
TM_{110}	917.3	7.7	918.7	24
	942.2	13.5	943.6	182
	968.6	4.0	969.9	110
	981.7	0.4	983.0	35
	1004	4.3	1004	75
	1015	8.0	1015	145
	1020	1.9	1021	338
	1022	0.1	1023	1266
	1320	0.6	1333	0.1
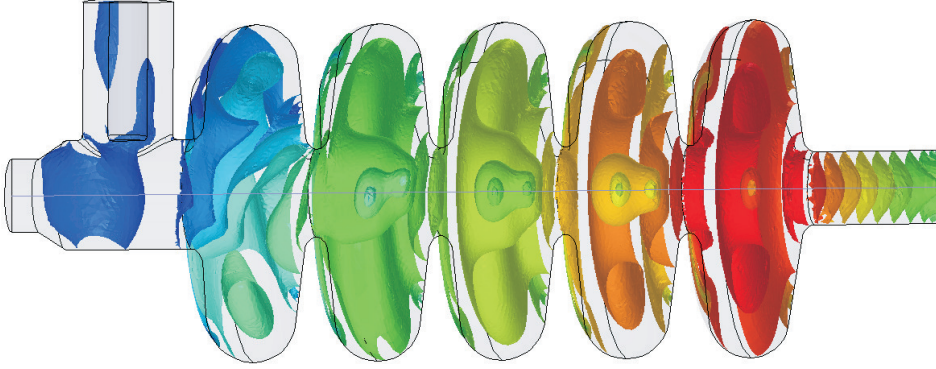
Figure 5.7: E-Field distribution of the $TM_{011}, 1/5\pi b$ mode in the $\beta_g = 0.65$ cavity. The iso spheres of the E-Field magnitude are shown with a logarithmic scaling and a total dynamic range of six orders of magnitude. Red corresponds to a high field and blue to a low field. The mode is located at the opposite site of the FPC and therefore is only weakly damped by the FPC.

deviation is in the per million level, but deviate with increasing frequency. Especially the MWS monopole results deviate from the HFSS and Superfish results, which are in good general agreement.

Looking at the Q_{ex} values obtained from HFSS across all frequencies one finds, that most of the modes have a strong coupling to the FPC. Only the $TM_{011}, 1/5\pi b$ monopole mode in the $\beta_g = 0.65$ cavity has a weak coupling. This can be seen from the field distribution of this mode, shown in Figure 5.7. The mode is located on the opposite side of the FPC and has almost no field in the FPC region. The same can also happen to an antenna HOM coupler. In order to avoid such situations, two HOM couplers are mounted per cavity, one on either side and at different angles to couple to both polarities of a mulit-pole mode. Based on these simulation results the FPC could be used as HOM damper. But in this context other effects have to be considered as well. In the simulation a resistance of $50\,\Omega$ is present for each mode, which in reality is only the case for the accelerating mode. The load is not matched for other frequencies and hence reflections can occur. In principal the complete power transmission line has to be simulated to validate that the HOMs are really propagating through the transmission line, damped there and not reflected into the cavity. At the moment studies on this subject are ongoing at the University of Rostock [97].

Comparing the results with data from the preliminary shapes introduced in appendix B and which will be used in the beam dynamics studies in chapter 8, no significant deviations are observed. The $(R/Q)(\beta_g)$ values are of the same order of magnitude and the beam dynamics simulation results obtained will not be affected significantly from the changes in the cavity geometry.

The simulation results have to be benchmarked against measurement data from actual cavities. This is planned in 2011, when a copper model of the $\beta_\mathrm{g} = 1$ cavity will be available for measurements.

Chapter 6

Beam Dynamics in a Linear Accelerator with Higher Order Modes

The analysis of charged particle dynamics in electromagnetic fields is usually based on the *Lorentz force equation*

$$\frac{d\vec{p}}{\mathrm{d}t} = q(\vec{E} + \vec{v} \times \vec{B}) \tag{6.1}$$

In this chapter the influence of HOMs on the beam dynamics is introduced. A short summary of general beam dynamics in an ion linear accelerator is given in Appendix C. A more general introduction into the beam dynamics in accelerators can be found in various textbooks such as for example [5, 6, 98–100].

The effects of HOMs can be split into two classes: accelerating and deflecting modes. The accelerating modes are the monopole modes, while the deflecting modes are the modes with two and more poles. In the following the monopole and dipole modes will be discussed in detail, since these have the highest impact on the beam.

6.1   Monopole Modes

In this subsection a brief summary is given of the basics of higher order mode excitation and beam interaction, based on [44, 46, 101, 102]. For simplification, a complex notation for the voltage is used. By convention, the observable physical quantities are real and the sign of the imaginary phase is positive ($e^{+i\omega t}$). Compared to the considered HOM wavelength, the bunch length in the SPL is very short, meaning that bunches can be treated as point-like charges. The coordinate

system is chosen such that the beam always travels along the z-axis (beam axis) in positive direction. The electrical z-axis in the cavity is assumed to be identical with the geometrical z-axis.

6.1.1   Monopole Mode Excitation

A point charge, travelling along the beam axis, excites all monopole modes inside a cavity. Since all modes are orthogonal to each other, they can be discussed separately. The mode-specific voltage induced by a point-charge q is according to the *fundamental theorem of beam loading* given by [103]

$$\Delta V_{\mathrm{q},n} = -q\frac{\omega_n}{2}\left(R/Q\right)_n(\beta),\tag{6.2}$$

where ω_n is the angular frequency of mode n, β the relativistic factor $\frac{v}{c}$ and $(R/Q)_n(\beta)$ as introduced in (3.54):

$$\left(R/Q\right)_n(\beta) = \frac{\left|\int\limits_{-\infty}^{\infty} E_{\mathrm{z},n}(r=0,z)\mathrm{e}^{i\omega_n\frac{z}{\beta c}}dz\right|^2}{\omega_n U_n},\tag{6.3}$$

where U_n is the stored energy in the mode and $E_{\mathrm{z},n}(r=0,z)$ the electric field along the beam axis. The integration limits are set to infinity to include the field leaking out of the cavity.

The voltage induced by the bunch starts oscillating at $t=0$ when the bunch passes the cavity mid plane. This assumes that there is no voltage present in the cavity before the bunch enters the cavity. Due to losses, the amplitude decays according to

$$V_n(t) = \Delta V_{\mathrm{q},n}\mathrm{e}^{-t/T_{\mathrm{d},n}}\mathrm{e}^{i\omega_n t}.\tag{6.4}$$

Since the stored energy is proportional to V_n^2, the cavity voltage decays with time constant $T_{\mathrm{d},n}$ that is twice the (energy) filling time $\tau_n = Q_{\mathrm{L},n}/\omega_n$, hence

$$T_{\mathrm{d},n} = \frac{2Q_{\mathrm{L},n}}{\omega_n},\tag{6.5}$$

with $Q_{\mathrm{L},n}$ as the quality factor of the complete system, including all couplers for this mode, see (3.62). The natural Q_0 of a superconducting cavity is in the order of 10^{10}. So Q_{L} is dominated by Q_{ex} and the simplification $Q_{\mathrm{L}} \approx Q_{\mathrm{ex}}$ can be made. $Q_{\mathrm{ex},n}$ depend on the coupling efficiency to the particular mode and can vary over several orders of magnitude from mode to mode.

The transit time of the bunch through the cavity is several orders of magnitude smaller than the decay time $T_{\mathrm{d,n}}$. Hence the voltage does not decay during the

bunch passage and the cavity-bunch interaction can be assumed to be instantaneous. The voltage induced in the same mode by the next bunch arriving after the time T_b is added as vector sum to the voltage present in the cavity.

$$V_{2,n} = \Delta V_{\mathrm{q},n} \left\{ 1 + e^{i\omega_n T_\mathrm{b}} e^{-\frac{T_\mathrm{b}}{T_{\mathrm{d},n}}} \right\} \tag{6.6}$$

is the voltage present in the cavity directly after the second bunch, if no voltage was present before the first bunch passed the cavity. Under the assumption that the time between bunches is constant and that there is no charge scatter the equilibrium HOM voltage in CW operation can be derived by evaluating the sum of the induced voltage directly

$$V_{\mathrm{cw},n} = \Delta V_{\mathrm{q},n} \sum_{k=0}^{\infty} e^{-kT_\mathrm{b}/T_{\mathrm{d},n} + ik\omega_n T_\mathrm{b}} = \frac{\Delta V_{\mathrm{q},n}}{1 - e^{-T_\mathrm{b}/T_{\mathrm{d},n} + i\omega_n T_\mathrm{b}}}. \tag{6.7}$$

From this formula one can easily see that a HOM with $f = k/T_\mathrm{b}, k \in \mathbb{N}$ will be resonantly excited by the fundamental machine lines. In this case, when additionally $T_\mathrm{b} << T_{\mathrm{d},n}$, (6.7) can be simplified by a Tailor expansion to

$$V_{\mathrm{res},n} = \Delta V_{\mathrm{q},n} \frac{T_{\mathrm{d},n}}{T_{\mathrm{b},n}} = \frac{\omega_n}{2}(R/Q)_n(\beta) I_\mathrm{b} T_{\mathrm{d,n}} = (R/Q)_n(\beta) I_\mathrm{b} Q_{\mathrm{L,n}}, \tag{6.8}$$

where $I_\mathrm{b} = |q|/T_\mathrm{b}$ is the average beam current. In the anti-resonance case ($\omega_n T_\mathrm{b} = (2k+1)\pi, k \in \mathbb{N}$) (6.7) and again assuming $T_\mathrm{b} << T_{\mathrm{d,n}}$ can be simplified to

$$V_{\mathrm{anti},n} = \frac{1}{2}\Delta V_{\mathrm{q},n} = \frac{\pi}{2}(R/Q)_n(\beta) I_\mathrm{b}. \tag{6.9}$$

In pulsed operation the voltage after one pulse with N bunches and no HOM voltage present before the arrival of the first bunch, is then given by

$$V_{\mathrm{p},n} = \Delta V_{\mathrm{q},n} \sum_{k=1}^{N} e^{-kT_\mathrm{b}/T_{\mathrm{d},n} + ik\omega_n T_\mathrm{b}} = \Delta V_{\mathrm{q},n} \frac{1 - e^{-NT_\mathrm{b}/T_{\mathrm{d},n} + iN\omega_n T_\mathrm{b}}}{1 - e^{-T_\mathrm{b}/T_{\mathrm{d},n} + i\omega_n T_\mathrm{b}}}. \tag{6.10}$$

After m pulses the voltage

$$V_{\mathrm{p},n}^m = \Delta V_{\mathrm{q},n} \frac{1 - e^{-NT_\mathrm{b}/T_{\mathrm{d},n} + iN\omega_n T_\mathrm{b}}}{1 - e^{-T_\mathrm{b}/T_{\mathrm{d},n} + i\omega_n T_\mathrm{b}}} \frac{1 - e^{-mT_\mathrm{p}/T_{\mathrm{d},n} + im\omega_n T_\mathrm{p}}}{1 - e^{-T_\mathrm{p}/T_{\mathrm{d},n} + i\omega_n T_\mathrm{p}}} \tag{6.11}$$

is present in the cavity, where T_p is the pulse period. If there are sub-structures in the pulse train the formula can be extended to

$$V_{\mathrm{p},n} = \Delta V_{\mathrm{q},n} \prod_{j=0}^{M} \frac{1 - e^{-k_j T_j/T_{\mathrm{d},n} + ik_j\omega_n T_j}}{1 - e^{-T_j/T_{\mathrm{d},n} + i\omega_n T_j}}, \tag{6.12}$$

where k_j is the number of repetitions, T_j the period length of the sub-structure and M the number of structure elements. $M = 0$ corresponds to CW operation, $M = 1$ to pulsed operation, and $M > 1$ to pulsed operation with further sub-structures. Due to the chopping of the regular bunch sequence, additional weaker machine lines appear at

$$f_n = k/T_j, \quad k \in \mathbb{N}, \tag{6.13}$$

which can also excite a HOM resonantly. These resonances, created by the pulse sub-structure, are referred to as *chopping machine lines* in this thesis. The smaller T_j, the stronger the resonance, which can be seen from the Fourier components of the excitation. The most dangerous resonances are the fundamental machine lines. This is illustrated in Figure 6.1, where the HOM voltage spectrum with different pulse sub-structures is shown. In this thesis the following notation for the chopping patterns is used:

$$N_\text{c} = N_\text{ci}/N_\text{cb}, \tag{6.14}$$

where N_ci bunches out of N_cb bunches stay in the pulse train as shown in Figure 6.2. This leads to a repetition rate of

$$f_\text{c} = \frac{1}{T_\text{c}} = \frac{1}{N_\text{cb}T_\text{b}}. \tag{6.15}$$

Furthermore the abbreviation ML and CML will be used to indicate the fundamental machine lines created by the bunch repetition rate and chopping machine lines created by the pulse sub-structure.

6.1.2   Monopole Mode Beam Interaction

A particle with charge q passing the cavity excites all modes as described before, but is also subject to an energy change caused by an excited HOM

$$dU_n = q \left(\Re(V_n) \cos(\omega_n dt) - \Im(V_n) \sin(\omega_n dt) \right) - \frac{1}{2}\Delta V_{\text{q},n}, \tag{6.16}$$

where $\Re(V_n)$ and $\Im(V_n)$ are the real and imaginary part of the HOM voltage, present during transit of the cavity's mid plane taking into account the arrival time error dt with respect to the synchronous particle. In addition, half of the HOM voltage $\Delta V_{\text{q},n}$ induced by the particle itself acts back on it, which is known as the fundamental theorem of beam loading [103].

HOM voltage spectrum
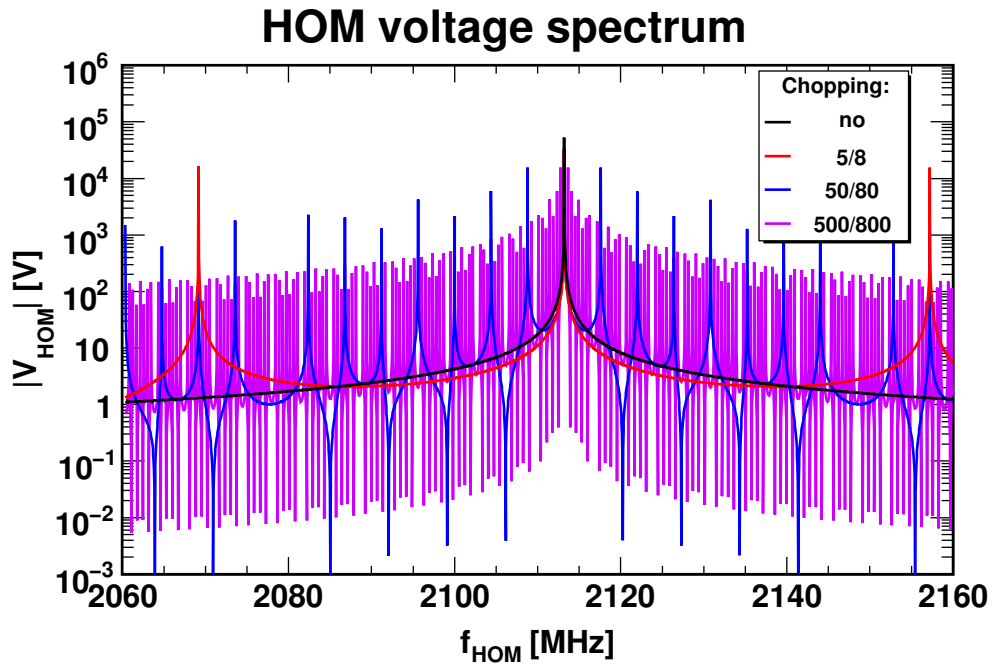
Figure 6.1: HOM voltage present in a cavity after 100 pulses for different pulse sub-structures (chopping patterns) around the 6th fundamental machine line, where f_n is varied continuously. Further calculation settings: $R/Q = 1$, $\langle I_{\text{b}} \rangle = 40\,\text{mA}$, $Q_{\text{ex}} = 10^6$.
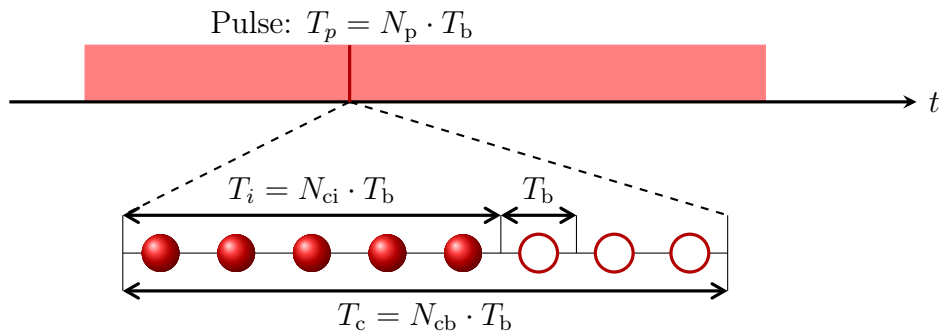
Figure 6.2: Illustration of the used chopping nomenclature. The period length of the chopping pattern defines the chopping machine line.

6.2   Dipole Modes

The same basic constraints as introduced for monopole modes are also used for
dipole modes. First, the excitation of a dipole mode is discussed before the beam
interaction is analysed.

6.2.1   Dipole Mode Excitation

A point-like bunch of charge q, passing the cavity off axis at distance x, induces
in a dipole mode with an angular frequency ω_n a purely imaginary[1] transverse
voltage given by

$$\Delta V_\perp = \frac{1}{2} i x q \frac{\omega_n^2}{c} (R/Q)_{\perp,n}(\beta). \tag{6.17}$$

where $(R/Q)_{\perp,n}(\beta)$ was defined in (3.59).

   If a pulse consisting of several bunches passes a cavity, one has to sum up the
induced voltages taking into account their phase relationship and their exponential
decay. Concerning the induced longitudinal voltages, equations (6.7) - (6.12) are
also valid for dipole modes under the assumption that x is constant.

6.2.2   Dipole Mode Kicks

The particles get deflected in the field of a dipole mode inside a cavity, where the
deflection is, to very good approximation, independent of the transverse position
(x,y), at which the particle passes the cavity. Using to the *Panofski-Wenzel theorem*
[62, 63], a complex voltage $V_\perp$ yields a transverse momentum kick

$$\Delta p_x = q \frac{\Re(V_\perp)}{c}, \tag{6.18}$$

which gives rise to a change of the transverse trajectory inclination for small angles
of

$$\Delta x' = \Delta p_x / p_\parallel = q \frac{\Re(V_\perp)}{c p_\parallel}, \tag{6.19}$$

where $p_\parallel$ is the longitudinal momentum and $\Re(V_\perp)$ the real part of the HOM
voltage. There is no direct interaction between the voltage induced by a particle
and the particle itself, since there is a phase difference of 90° between them for
dipole modes.

---

[1] 90° out of phase

6.3 Beam Dynamics in a Drift Kick Simulation Model

The formulae (6.7) - (6.12) for the HOM voltage development as function of time can be used for first estimates of the expected HOM voltage in resonant excitation. Away from the machine lines, destructive interference occurs. In a real machine, bunch noise, such as arrival time errors, energy errors, transverse displacement and tilt, as well as charge jitter, has to be considered, leading to a much higher voltage than one would expect from the assumption of a perfect beam off resonance. This can even drive instabilities as shown in [101]. That is why numerical studies have to be performed to estimate the effect of HOMs.

Based on general beam dynamics considerations, a linac simulation model is built with a special focus on the beam-HOM interaction in an ion linac. In the model the cavities are compressed to a plane located at the cavity mid-plane, where the particle cavity interaction takes place instantaneously. The acceleration kick is derived for a particle travelling with a constant velocity through the complete cavity. Then there are drift spaces between the cavity mid-planes according to the linac layout. A schematic drawing is shown in Figure 6.3.
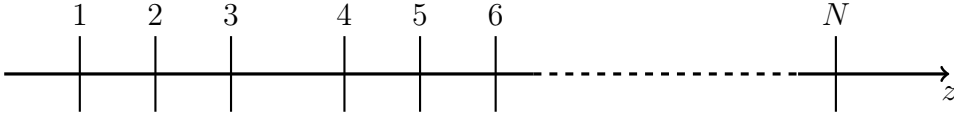
Figure 6.3: Drift kick schema. The particles get a kick at each cavity mid-plane and drift with constant velocity in between. The drift spaces are not necessarily identical between the cavities. They are based on the actual linac geometry.

The charge to mass ratio is the same for a single particle and a bunch of particles of the same kind. Hence, all following equations are also valid for a point-like bunch of particles. In contrast to electron linacs, particles with a velocity well below the speed of light typically enters a proton linac. In this case the change of the particle velocity along the linac has various consequences, such as for example a velocity dependent time of flight, which have to be included in the simulation.

An energy error leads to a transit time factor change from cavity to cavity and additionally a change of the maximum accelerating voltage V_{RF} in a cavity. This, together with the phase error of the particle, leads to a different energy gain in the cavity as compared to the synchronous particle. Due to errors in the RF system, an additional phase and amplitude error of the accelerating mode has to be considered. The error in the energy gain per cavity is then

$$dU_{\mathrm{RF}} = qV_{\mathrm{RF}}^* \cdot \cos(\phi_{\mathrm{s}}^* + \omega_{\mathrm{RF}}dt) - \Delta U \tag{6.20}$$

where V_{RF}^* is the maximum accelerating voltage including transit time factor correction and amplitude errors. ϕ_{s}^* is the effective operation phase ($\phi_{\mathrm{s}}^* = \phi_{\mathrm{s}} + \phi_{\mathrm{RF\ Error}}$) of the cavity and $\omega_{\mathrm{RF}} dt$ is the arrival phase error of the particle. ΔU is the energy gain of the synchronous particle without RF errors

$$\Delta U = qV_0 \cos(\phi_{\mathrm{s}}) = qE_0 T(\beta_{\mathrm{s}}) l \cos(\phi_{\mathrm{s}}). \tag{6.21}$$

A charged particle passing the cavity is subject to an additional energy change caused by an excited HOM (6.16). Summing up all these effects leads to a total energy error evolution in cavity m of

$$dE^{(m+1)} = dE^{(m)} + dU_{\mathrm{RF}}^{(m)} + dU_n^{(m)} \tag{6.22}$$

where $dE^{(m)}$ is the energy error in front of the cavity m. This energy error dE translates into an arrival time error when passing through the drift space between two cavities

$$dt^{(m+1)} = dt^{(m)} + (dt/dE)_{\mathrm{E}} \cdot dE. \tag{6.23}$$

The slope depends on the drift length L, the mass m_0 and relativistic γ of the synchronous particle

$$(dt/dE)_E^m = -\frac{L^{(m)}}{c \cdot m_0 c^2 \cdot (\gamma^2 - 1)^{3/2}}. \tag{6.24}$$

The longitudinal beam dynamics along a linac can be fully described by equations (6.22) and (6.23).

The same model can also be applied in the transverse plane. There transfer matrices are used to transport the beam from cavity mid-plane to cavity mid-plane. There the dipole kick is applied and the induced HOM voltage is added to the already present HOM voltage as for the longitudinal plane.

Chapter 7

Beam Dynamics Code: Simulation of Higher Order Mode Dynamics (SMD)

One of the main tasks in this thesis was the development and implementation of a new beam dynamics code, specialised to analyse the beam-HOM interaction in a linear accelerator with a focus on $\beta < 1$ beams. In this chapter the simulation concept and general implementation of SMD is introduced. Afterwards, the performance of different simulations routines is discussed. The reference system used for performance tests is a desktop PC with an Intel® Core™ 2 Duo E6750 processor, 4 GB RAM and Windows XP® 32 Bit as operating system. Only one core and about 250 MB RAM is used per simulation.

The complete code and all scripts are available in the CERN SVN repository [104].

7.1 Simulation Concept of SMD

A linac containing different sections and periodic sub-structures with a given cavity spacing is modelled using a drift-kick approach introduced in the last chapter 6.3. Point-like bunches or single particles are tracked through the complete linac. The particle velocity is assumed to be constant inside the cavity and the interaction between particle and cavity takes place in the cavity mid-plane. Further, it is assumed that there is no coupling between the longitudinal and the transverse plane so they can be treated independently. Space charge effects are neglected in all simulations, because they don't effect the beam significant in the used focusing lattice. Hence, they have to considered in the lattice design to avoid instabilities.

The simulation code can be split up into two logical modules: One for the

longitudinal plane and one for the transverse plane.

7.1.1   Longitudinal Module

Field maps of the $TM_{010,\pi}$-mode in the different cavities are used to derive the $E_0T(\beta)$ for the synchronous particle in each cavity. A two point linear interpolation is used for all other particles. The fields in the cavities are normalized to the design E_0T, taking into account a phase advance limitation per period and the synchronous phase ϕ_s. Furthermore, amplitude and phase errors can be applied individually to each cavity. A bunch is defined as lost, if its absolute phase ϕ is outside the limits

$$2\phi_s < \phi < -\phi_s, \tag{7.1}$$

where ϕ_s is the synchronous phase, which is negative in the linac convention.

Longitudinal beam dynamics simulations are carried out to study effects of input errors in terms of energy and phase errors, as well as cavity gradient or RF errors. In addition, one HOM with individual characteristic values per cavity is applied, which can be excited by a pulsed beam. It is also possible to preserve the induced voltage per cavity or set it to a certain value in order to perform studies with a fixed HOM voltage. The action back on the beam can also be considered individually for each cavity.

7.1.2   Transverse module

The transverse plane is modelled by 2×2 transfer matrices in the inter cavity drift space. For simplicity no explicit focusing lattices are modelled. Instead, the transverse focusing profile of multi particle simulations is used to generate the transfer matrices, assuming a smooth focusing.

In the initial transverse beam dynamics model the following basic assumptions and simplifications are made:

- No alignment errors exist in the focusing elements

- The cavities have no transverse displacement

- The beam is injected on axis with a normal distributed spread in position and transverse momentum

- One dipole mode is considered per cavity with its maximum field in the simulated plane

- The beam is longitudinally matched and there are no HOM monopoles

- All errors are Gaussian distributed.

A simplified model of transversely displaced cavities is implemented to study alignment issues in the context of dipole modes. Therefore, a Gaussian distributed transverse position offset is used in all cavities. This affects only the HOM excitation, but not the transverse focusing. A bunch is defined as lost, if the transverse displacement is larger than a defined threshold value.

7.1.3 Modelled effects

In the modules a variety of effects is implemented. They can be divided into machine and beam related effects. The modelled machine effects are first of all the impact of different HOM parameters such as for example HOM frequency, frequency spread, $(R/Q)(\beta)$, and Q_{ex}. Each cavity has its own set of independent parameters. Secondly, RF errors and cavity gradient errors can be applied individually to each cavity. This opens a wide range of scenarios which can be investigated. In the case of beam based effects the influence of the basic beam parameters like current and different pulse sub-structures can be studied as well as beam injection noise in terms of energy, phase, position, momentum, and bunch charge jitter. For the noise generation independent Mersenne Twistor [105] random number generators are used for each quantity.

7.2 Code Implementation

SMD is written in C++ using the ROOT framework [106] to allow for a fast, compiled program core and to use the framework data analysis routines. One big advantage of ROOT is its integrated C++ interpreter. The scripts can then also be compiled to speed up the execution time.

The logical modules, introduced in the section before, are not represented in the implementation. There, the key functions are provided by the two classes `TCavity` and `TCavityPeriod`. The preparation, execution and analysis of a simulation is realised with scripts. The basic features of the two classes are introduced in the following subsections, after a discussion the field integration methods used.

7.2.1 Field Integration Methods

The energy gain of a particle in a cavity depends strongly on its velocity and its arrival time. The dependency on the velocity is expressed by the transit time factor (3.44). In this section the energy gain in a cavity with multiple cells is calculated. First, methods assuming a constant particle velocity are discussed. They can be divided into methods using symmetry conditions and general methods. Second, the field integration in the time domain is introduced, which takes into account

the velocity change inside the structure. Finally, all methods are compared to each other.

Symmetric Cavity Fields

If the cavity has a symmetry plane[1] in the cavity mid-plane (x,y-plane), the origin is set to this plane and the reference phase is also set to this origin. The field integration can then be simplified and the accelerating voltage is

$$V_{\mathrm{acc}} = 2 \int_0^{L/2} E_{\mathrm{z}}(z,0) \cos(kz)dz, \quad \text{odd number of cells} \tag{7.2}$$

$$V_{\mathrm{acc}} = 2 \int_0^{L/2} E_{\mathrm{z}}(z,0) \sin(kz)dz, \quad \text{even number of cells} \tag{7.3}$$

where $k = \omega/\beta c$ and L the total cavity length including beam pipes. To treat fields leaking out of the cavity correctly, the integration limits would have to be set to infinity. In the model considered in this thesis are forced to be zero at the end of the cavity. The integration path the is equal to half the cavity length due to the symmetry.

Equivalent Field Method

Another way to calculate the accelerating voltage in a cavity containing several gaps and no symmetry around a mid-gap plane is to compute the 'equivalent field', which is illustrated in [45]. First, the origin of the coordinate system is placed outside the accelerating element. Then the unnormalised transit time coefficients are calculated

$$T(k) = \int_0^L E_{\mathrm{z}}(z,0) \cos(kz)dz \tag{7.4}$$

$$S(k) = \int_0^L E_{\mathrm{z}}(z,0) \sin(kz)dz \tag{7.5}$$

and the accelerating voltage is

$$V_{\mathrm{acc}}(k,\phi_0) = [T(k)\cos(\phi_0) - S(k)\sin(\phi_0)] \tag{7.6}$$

where ϕ_0 is the phase of the particle in the origin of the coordinate system and $k = \omega/\beta c$. The phase $\phi_0 = \phi_c$ must satisfy

$$\tan(\phi_c) = -\frac{S(k)}{T(k)} \tag{7.7}$$

---

[1] The TM_{010}, π is assumed, which has a symmetric field profile per cell.

to obtain the maximum accelerating voltage of

$$V_{\mathrm{acc,c}}(k) = \sqrt{T^2(k) + S^2(k)} = T_0(k), \tag{7.8}$$

where $T_0(k)$ corresponds to a transit time factor of an equivalent symmetric field with the origin in the middle of the symmetry.

$$T_0(k) = V_0 \frac{\sin(\vartheta/2)}{\vartheta/2} \tag{7.9}$$

with $V_0 = E_0 L_e$, where E_0 is the average accelerating field over an equivalent distance L_e and $\vartheta = (k - \hat{k})L_e$ is the phase slip, where $\hat{k}$ corresponds to a travelling wave velocity, for which the energy gain is maximum. The distance l between the origin and the centre of symmetry of the equivalent field is found from

$$\phi_c = -lk + n\pi \rightarrow l = -\frac{\partial \phi_c}{\partial k} = -\frac{S'(k)T(k) - S(k)T'(k)}{T(k)^2 + S(k)^2} \tag{7.10}$$

Time Domain Integration

In all other methods it is assumed that the velocity change inside the cavity is too small to affect the transit time significantly. The velocity change can be considered in the field integration

$$V_{\mathrm{acc}} = \int_0^L E_{\mathrm{z}}(z, 0)e^{(\omega/v(z)z + \phi_0)} dz, \tag{7.11}$$

where ϕ_0 is the phase at the cavity entrance and $v(z)$ is

$$v(z) = \frac{\sqrt{(1 + (W_0 + V(z))/(mc^2))^2 - 1}}{(1 + (W_0 + V(z))/(mc^2))}. \tag{7.12}$$

W_0 is the energy of the particle before entering the cavity and mc^2 its rest mass. The time of flight from the cavity entrance to the cavity mid-plane has to be calculated to synchronise the phase and adopt the start phase accordingly. To calculate the start phase, the optimum phase obtained from the equivalent field method can be used.

Comparing Different Integration Methods

For a direct comparison of the different methods the field profile of a medium beta ($\beta_{\mathrm{g}} = 0.65$) cavity is used and the maximum energy gain as a function of the particle energy at the entrance of the cavity is plotted in Figure 7.1. All methods show the same energy gain profile, with no significant differences. From this point

of view the constant velocity approach, which is the fastest method for calculating the energy gain, is fine in the investigated energy range and needed accuracy. The deviation introduced by field imperfections and errors in the EM simulation tools to generate the field profile is larger than the systematic error introduced by the integration method.
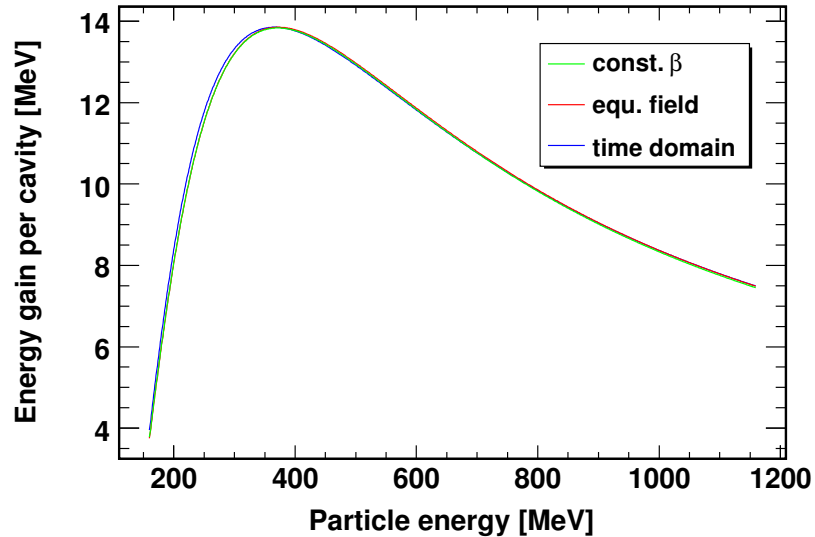
Figure 7.1: Maximum energy gain per cavity as a function of the injection energy. The field profile of a medium beta $(\beta_g = 0.65)$ cavity is used together with different field integration methods.

7.2.2   Class TCavity

In this class, all basic data of a cavity is stored such as for example the field map of the accelerating mode, design beta, length, operation frequency and phase. All field integration methods introduced before are implemented using the E-field map of the accelerating mode along the beam axis. This data is imported from one of the RF simulation tools introduced in chapter 4.2. The field map must consist of equidistant points to allow a simple integration with a fixed step size using the trapeze formula. Symmetry conditions at the cavity mid plane can be used to speed up the integration further. Before the field map can be used for particle tracking, it has to be normalised to the designed accelerating gradient.

(a) Accelerating mode field profile

(b) Effective field $E_0T(\beta)$
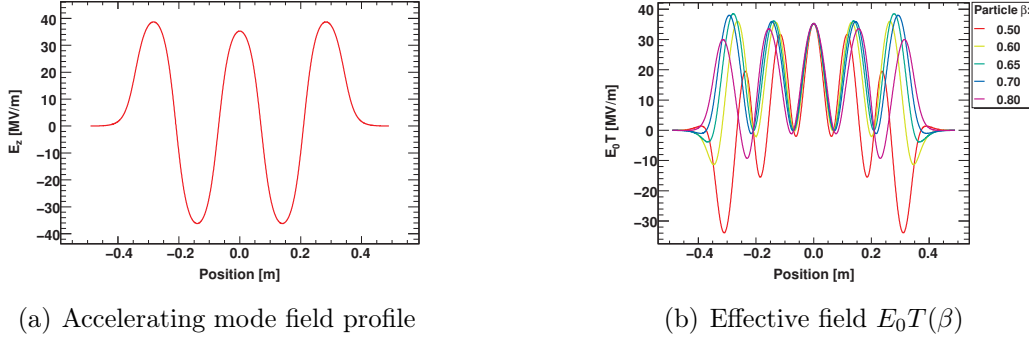
Figure 7.2: Field map of the accelerating mode E_z component in the SPL $\beta_g = 0.65$ cavity (a) and the effective field taking into account the transit time factor (b).

The correction factor for the E-field values is calculated by

$$k_{\text{corr}} = \frac{V_{\text{ref}}(\beta_g)}{V_{\text{map}}(\beta_g)}, \tag{7.13}$$

where $V_{\text{map}}(\beta_g)$ is the accelerating voltage at the geometrical β using the field map. V_{ref} is the design voltage given by

$$V_{\text{ref}} = E_0T(\beta_g)L_{\text{active}}, \tag{7.14}$$

where $L_{\text{active}} = n\frac{\beta\lambda}{2}$ is the active cavity length of an n cell cavity. The E-field integration is realised over the complete cavity including the beam pipes at either end. Thereby the fields leaking out into the beam pipe are taken into account. In Figure 7.2 the imported and normalised field map of a medium beta cavity is shown together with the effect of the transit time factor.

The field integration methods can also be used for particle tracking. This however, is very time consuming, because the field integration is done for each particle in each cavity. For example, tracking 10,000 particles through 250 cavities takes about 30 s on a desktop PC. Hence only the synchronous particle is tracked once through the linac using a field integration method. The energy gain per cavity is stored and is used for all other particles in the simulation later on, which is implemented in `TCavityPeriod`.

7.2.3 Class TCavityPeriod

The class `TCavityPeriod` is an inheritance from `TCavity` and implements all extensions needed to simulate a complete linac section. `TCavityPeriod` holds lists for all parameters, which vary from cavity to cavity, such as HOM frequencies, (R/Q) values, accelerating voltage or RF phase. Also layout information of the

linac section such as for example the cavity spacing is stored in this class. In the following the initialisation process and the tracking functions are introduced.

First, the number of cavities per section and the section layout has to be specified, including focusing periods and cavity positions. During this process also the transverse focusing along the linac is defined. In order to do bunch tracking simulations and to identify the influence of a HOM, a reference orbit is introduced by tracking the reference particle without injection noise and RF errors through the linac, using a field integration method. The kinetic energy at the entrance of each cavity is stored, as well as the time of fight and energy gain per cavity, which is needed for the fast tracking later on. A maximum phase advance per focusing period can be specified. This value is calculated for each period during the initialisation process and the accelerating gradient in all cavities of this period is reduced, if the maximum value is exceeded. Then the particle is tracked again through this period and the phase advance per period is recalculated. This process is repeated until the phase advance per period meets the specified maximum value.

Finally, all other simulation specific parameters such as for example HOM properties, RF errors or alignment errors are configured. The properties of one monopole mode or one dipole mode which are needed for the simulations are stored individually for each cavity. A fixed (R/Q) value can be specified or a $(R/Q)(\beta)$ map can be imported, which was generated before. The $(R/Q)(\beta)$ map generation is realised by importing the field map of the HOM to an instance of `TCavity` and calculating the induced HOM voltage for the synchronous energy in each cavity. For the complete section the same HOM damping value in each cavity is used.

The root random number generator `TRandom3` based on [105] is used to generate different HOM frequency distributions, the RF phase error and the RF amplitude error. For each parameter a separate instance of the random number generator is generated.

Since the charge to mass ratio is the same for a single particle and a complete bunch, the tracking functions can be used either for bunches or single particles, if space charge effects are not considered. The only difference is the HOM loading, which is proportional to the charge. This problem can be solved by controlling the HOM loading individually.

Fast tracking functions in the longitudinal plane

All longitudinal tracking functions have in common that the energy and phase error at each cavity mid-plane along the linac is calculated using (6.22) and (6.23). They can be divided into the field integration methods introduced in the last section and methods which use the $E_0T(\beta_{s,n})$ of the synchronous particle to calculate the energy gain and will be called *fast methods* in the following. Their execution time is about two orders of magnitude faster compared to the field integration
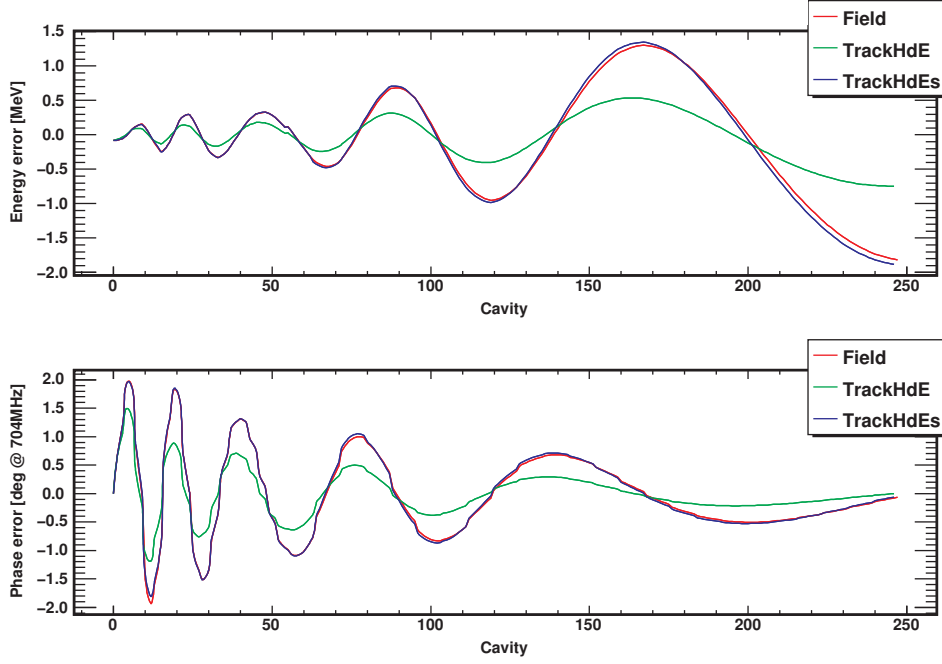
Figure 7.3: Energy and phase error evolution along the linac for different tracking functions, where a particle is injected with a energy error. The particle performs oscillations in the longitudinal phase space around the orbit of the synchronous particle. The field integration function is chosen as reference, because the synchronous orbit was also calculated with this function. `TrackHdEs` show only minor deviations introduced by interpolation errors at the period borders, while the oscillations of `TrackHdE` are about a factor two smaller.

methods. The basic tracking function (`TrackHdE`) uses only $E_0T(\beta_{s,n})$ to calculate the energy gain for all particles neglecting their energy deviation. To reduce the introduced $E_0T(\beta)$ error a three point linear interpolation is used in `TrackHdEs` and `TrackHdE2`. This improves the tracking accuracy significantly as illustrated in Figure 7.3, where the results of three tracking functions are compared. A field tracking method is used as reference. `TrackHdEs` shows only a minor deviation, introduced by the discontinuities at the transitions from one focusing period to the next, while the oscillation amplitude of `TrackHdE` is about a factor two smaller as compared to the reference track. The drawback of the interpolation is the increase of the simulation time of up to a factor of four, but it is still almost two orders of magnitude faster than the field integration methods. The RF error is implemented by modulating the phase and the accelerating voltage in each cavity. The beam-HOM interaction is divided into two features, the pure effect of a HOM acting on

the beam[2] and the HOM excitation by the beam. By splitting these two effects, it is possible to study a well defined HOM voltage distribution along the linac with different beam injection noise or RF errors. All fast tracking methods are listed in Table 7.1 together with their features. The execution time for all methods without $E_0T(\beta)$ interpolation is about $11\,\mathrm{s}$ for $700,000$ bunches and about $45\,\mathrm{s}$ for the methods with $E_0T(\beta)$ interpolation and HOM beam interaction. The HOM voltage present in the cavity after tracking two pulses through the linac is shown in Figure 7.4 and additional the voltage evolution during one pulse in a single cavity. In Figure 7.5 the track of a particle in the longitudinal phase space is illustrated, where different effects are present. If no disturbing effects are present, the energy and phase error is zero along the linac.

Table 7.1: Longitudinal fast tracking functions and their implemented features.

Function	E_0T interpolation	RF erros	HOM to beam	HOM loading
TrackHdE	n	n	n	n
TrackHdEk	n	y	n	n
TrackHdEt	n	y	y	n
TrackHdEh	n	y	y	y
TrackHdEs	y	y	y†	n
TrackHdE2	y	y	y	y

$\dagger$ can be activated by a function parameter.

Tracking functions in the transverse plane

The implementation of the tracking in the transverse plane is much simpler than in the longitudinal plane at the considered level of detail. Only one dimension is implemented, since there are no major differences in the two transverse planes and the coupling between the planes can be neglected for this kind of simulations. A 2×2 transfer matrix is used to transport the particles from cavity mid-plane to cavity mid-plane and the four matrix elements are stored individually for each inter cavity space. Thus any focusing scheme can be applied by using the corresponding transfer matrix which can be exported from lattice design or simulation tools such as for example *MAD-X* [107], *GenLinWin* [108] or *TranceWin* [109]. Energy and

---

[2] The voltage induced by the bunch itself, which also acts back to the bunch is taken into account. Only the change in the HOM voltage is deactivated.
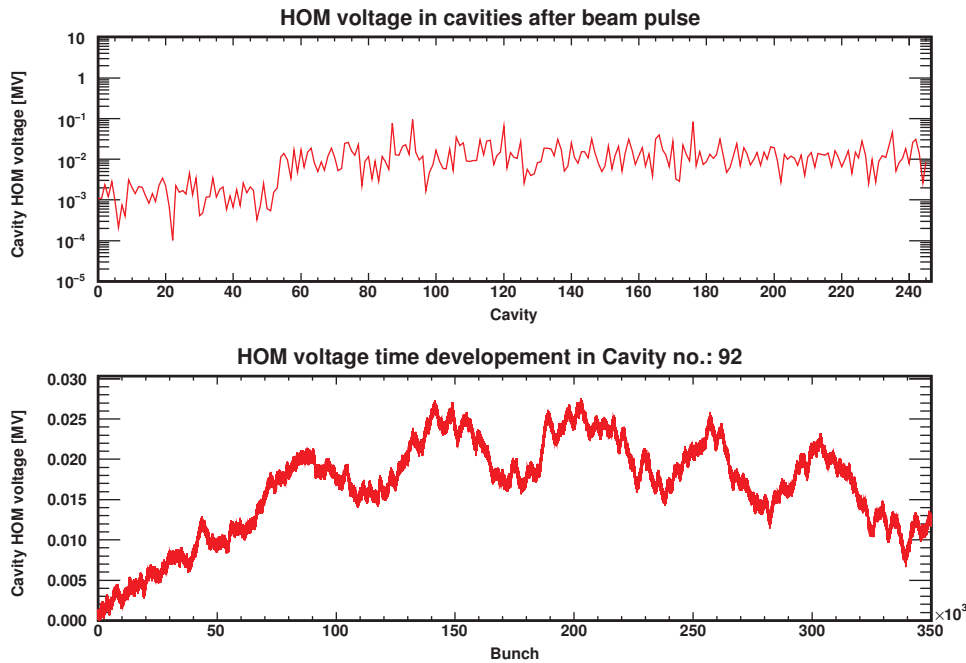
Figure 7.4: The monopole HOM voltage present in each cavity along the linac after two pulses is shown (top). A constant $(R/Q)(\beta)$ (10/100) is used in both linac sections. The ten times higher (R/Q) in the high beta section lead to higher HOM voltages, which vary from cavity to cavity about two orders of magnitude. The voltage evolution during a pulse in the cavity with the highest voltage present at the end of the pulse is illustrated as well (bottom). After a rise time very noisy oscillations are observed.

phase deviation are not considered in the transverse plane, which would affect the energy dependent transverse quadrupole focusing.

Similar to the studies in the longitudinal plane, several tracking functions with different features are implemented and listed in Table 7.2. The transverse cavity displacement is realised by adding a cavity specific offset to the particle position, for the interaction with the HOM, which is implemented using (6.19) and (6.17). Tracking 700,000 bunches through the linac takes about 10 s for all functions on the reference system. The trajectory of a particle along the linac in the transverse phase space using different tracking features is shown in Figure 7.6. The HOM voltage map is plotted in Figure 7.7, where also the voltage evolution is shown in the cavity with the highest HOM voltage. Over the pulse the HOM voltage rises roughly linear and causes a significant transversal kick, which is clearly visible as a jump in x' in the trajectory plot. In general the particle performs betatron oscillations due to the focusing.
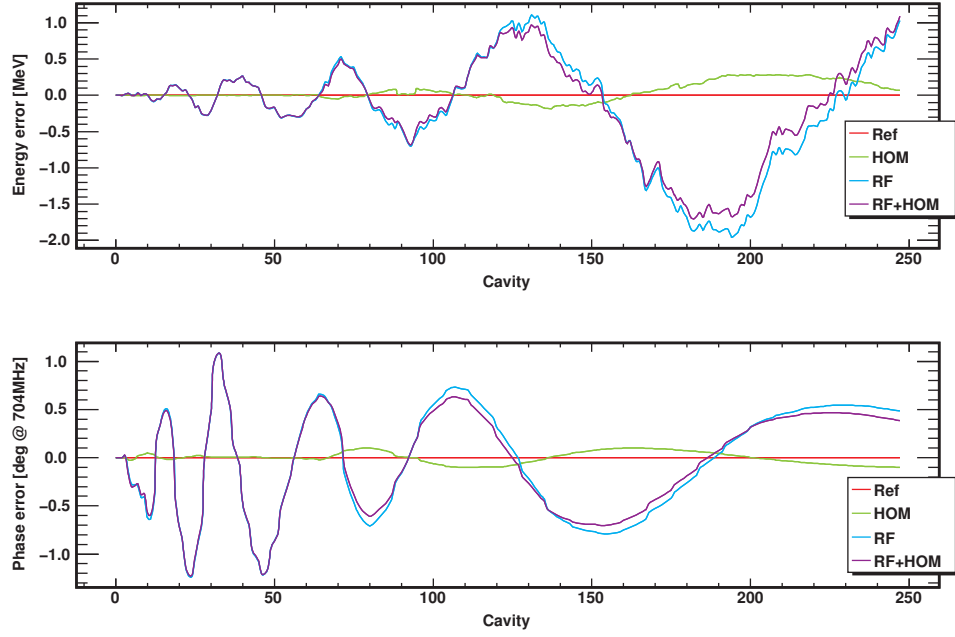
Figure 7.5: Track of a particle with no injection errors and different effects. The reference particle shows no energy and phase error (reference orbit). The other particles oscillate around the reference orbit. The influence of RF errors is dominant over the influence of the HOM in this simulation. There is only a minor deviation in the case where RF errors and a HOM are present, compared to the simulations with RF errors. The deviations starts to rise in the high beta section, where the HOM voltage is a factor 10 higher due to the higher (R/Q) value. The oscillation period is about the same in all simulations, but the amplitude varies significantly.

Table 7.2: Transverse tracking functions and their implemented features.

Function	Cavity alignment	HOM to beam	HOM loading
TrackHdEh	n	n	n
TrackHdEs	y	y[†]	n
TrackHdE2	y	y	y

[†] can be activated by a function parameter.
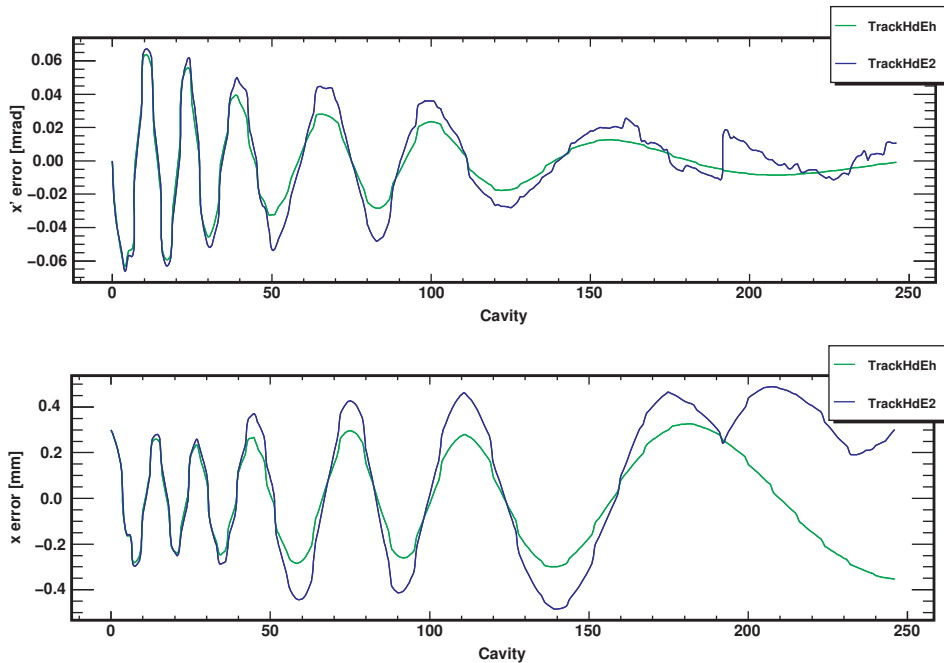
Figure 7.6: A particle with an injection position error of 0.3 mm is tracked through the linac with (blue) and without (green) HOM interaction. In the absence of HOMs a stable betatron oscillation is observed. The discontinuities are due to the different inter cavity distances. Activation of the HOM interaction leads to an oscillation around the reference orbit. The huge momentum kick at cavity 190 is caused by the high HOM voltage in this cavity, see Fig 7.7.

7.3 Code Benchmark

In order to verify the simulation results, a benchmark in the longitudinal plane against other codes [101, 110] was realised. All codes use the same drift kick approach, but the other codes do not include all effects modelled in SMD. 50,000 bunches were tracked through a generic linac and the different results were compared. The results agree perfectly within the numerical errors and a detailed discussion can be found in [111]. It has to be stated that in this benchmark only the same features as implemented in the other codes are used. In other words the transit time dependency of the acceleration kick is not considered in the benchmark. In case of the SPL the other codes would lead to the results obtained with the tracking function `TrackHdEh` without RF error.
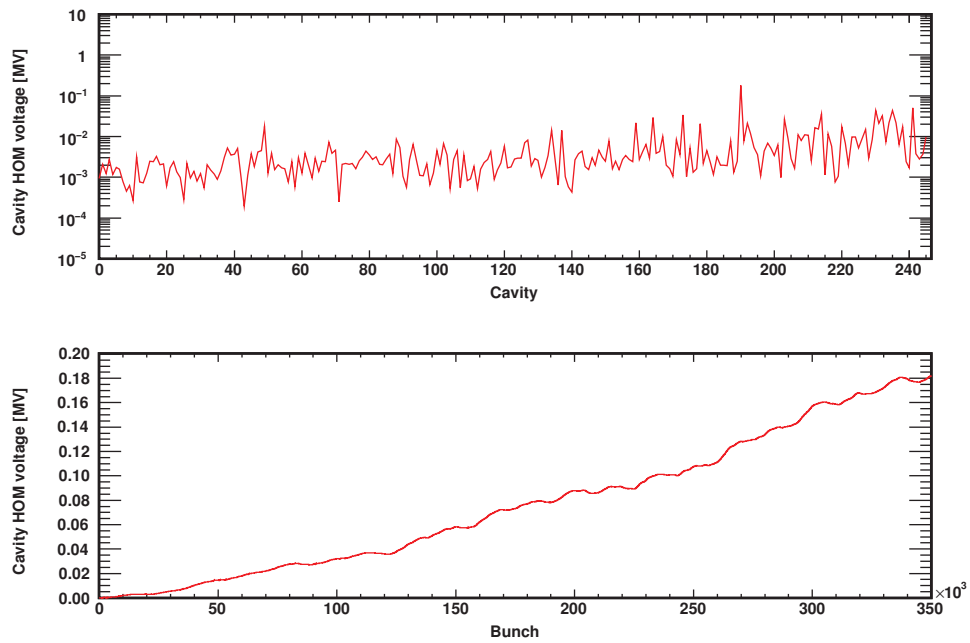
Figure 7.7: HOM voltage present in the cavities along the linac after the pulse (top) and the voltage development during the pulse in cavity number 190 (bottom), where the highest HOM voltage is induced. A constant $(R/Q)(\beta)$ value is used in all cavities. On average the HOM voltage increases along the linac. In the monitored cavity the voltage increases roughly linear due to a resonance condition.

Chapter 8

SPL Beam Dynamics Studies with HOMs

The general influence of HOMs on the beam is discussed in this chapter as a function of several parameters such as the damping, beam current, sub-structured pulses, RF or alignment errors. But first of all the simulation input parameters and and used assumptions are introduced. Then simulations are carried out separately in the longitudinal and transverse plane. Based on the simulation results HOM damping requirements can be defined in dependency of the machine's operation parameters.

8.1 Simulation Input Parameters

In order to run beam dynamics simulations, cavity HOM data and beam input parameters are needed. They are introduced in this section. All parameters are based on results from the SPL HOM workshop [112] held at CERN in 2009. Linac4 [34, 35], presently under construction at CERN, will be used as injector front end for all simulations.

8.1.1 Cavity Modelling

Since the baseline cavity geometries, introduced in chapter 5, were not yet available when the beam dynamics studies started, preliminary symmetrical cavity shapes, discussed in the appendix B, are used. Simulations have also been carried out with the SPL's baseline geometry HOM data, which shows no significant differences to the results obtained with the preliminary shapes. Hence, for consistence reasons only simulation results base on the preliminary cavity geometry are discussed in this thesis.

The HOM with the highest overall $(R/Q)(\beta)$ below the beam pipe cutoff frequency in each linac section is chosen as default for all simulations. A Gaussian HOM frequency spread of $\sigma_{f_{\mathrm{HOM}}} = 1\,\mathrm{MHz}$ is assumed for all modes based on the experience at DESY [113] and Jefferson Laboratory [114]. The HOM frequency spread is introduced by manufacturing tolerances, which is compensated for the accelerating TM_{010}, π mode by tuning. This tuning process does not affect all modes in the same manor. Hence, the HOM frequency spread for non TM_{010} modes is in the order of MHz, while the spread for the TM_{010}, π mode is below $1\,\mathrm{kHz}$.

In the analysis the focus is set to modes below the beam pipe cutoff frequency with artificially high (R/Q) values. However, there are also potentially dangerous modes above the cutoff frequency. Their frequency and $(R/Q)(\beta)$ values depend strongly on the inter cavity section and the cavity-to-cavity coupling. Hence, the complete cryomodule has to be simulated as it is done in [115]. With these simulations trapped modes can be identified and the cavity and/or cryomodule design will then have to be adapted, if necessary. The influence on the beam of a mode with moderate $(R/Q)(\beta) \sim 1$, weak damping and resonantly excited will be discussed in section 8.2.7.

Introducing mechanical imperfections, the (R/Q) and the Q_{ex} of a HOM in a cavity can change significantly, as shown in [116]. This effect has to be taken into account when specifying the HOM damping requirements. One can try to quantify the effect by studying the influence of mechanical tolerances on $(R/Q)(\beta)$ and Q_{ex}. Instead of performing a statistical study, simulations with very conservative assumptions and large safety margins (e.g. on the beam current) are carried out to account for these effects.

8.1.2   Beam Input Parameters

Simulation values based on Linac4 beam dynamics studies [117] are used as beam input parameters. The relevant values for the bunch energy and phase jitter in the longitudinal plane, as well as the position and momentum spread in the transverse plane, are listed together with all other beam parameters in Table 8.1. In the default simulation settings, a $1\,\mathrm{ms}$ pulse with no sub-structure is used and the beam current is set to $\langle I_{\mathrm{b}} \rangle = 400\,\mathrm{mA}$, which corresponds to ten times the nominal current, as a safety margin.

Besides the position/momentum or the energy/phase jitter, a bunch to bunch charge jitter of $\sigma_{\mathrm{q}} = 3\,\%$ is used as a very conservative value[1]. All input noise is considered as independent and Gaussian distributed. Focusing in the longitudinal plane is achieved by the RF, which operates at $\phi = -15\,^\circ$ and the maximum zero current phase advance per period is limited to $75\,^\circ$. In order not to exceed this limit,

---

[1] Ten times higher then measured at SNS [112, 118]

Table 8.1: Beam input parameters and assumed variation based on Linac4 beam dynamics simulations and SNS data [117, 118].

Parameter		Value	σ
E_{Input}	[MeV]	160	0.078
ϕ	[deg at 704 MHz]	-15	0.4
x	[mm]	0.0	0.3
x'	[mrad]	0.0	0.3
I_{b}	[mA]	40	3%

the gradient in some cavities has to be reduced accordingly. A smooth focusing based on the phase advance per period for zero current in the transverse plane is used. Along the linac the phase advance per period decreases from $13.3\,°/m$ to $1.1\,°/m$ according to the used lattice design [119].

8.1.3   Simulation Execution

The beam and HOM configuration, introduced before, is used to perform bunch tracking simulations in the longitudinal and transverse plane. Always at least two consecutive pulses are simulated. If the HOM voltage decay time T_{d} gets longer than the period length ($T_{\text{r}} = 20\,\text{ms}$) due to a high Q_{ex}, the number of simulated pulses is increased until a steady state situation is reached, assuming an ideal loading curve from pulse to pulse. This is the case for $Q_{\text{ex}} > 10^7$. The number of simulated pulses is calculated using (6.10) and a theoretical load level of 99%

$$n_{\text{pulse}} > -\frac{T_{\text{d}}}{T_{\text{r}}} \ln(0.01) + 1. \tag{8.1}$$

All results shown refer always to the last simulated pulse, if not stated differently.

8.2   Longitudinal Plane

Before looking at the effects of HOMs, the nominal beam according to Table 8.1, with injection energy and phase jitter is tracked through the linac without HOM interaction. The resulting energy and phase error distribution is plotted in a 2D phase space histogram, see Figure 8.1. It shows no filamentation and a relatively sharp border contour line.

A set of default simulation values, listed in Table 8.2, is defined based on the data introduced before and will be used in all longitudinal beam dynamics simulations, if nothing different is stated.
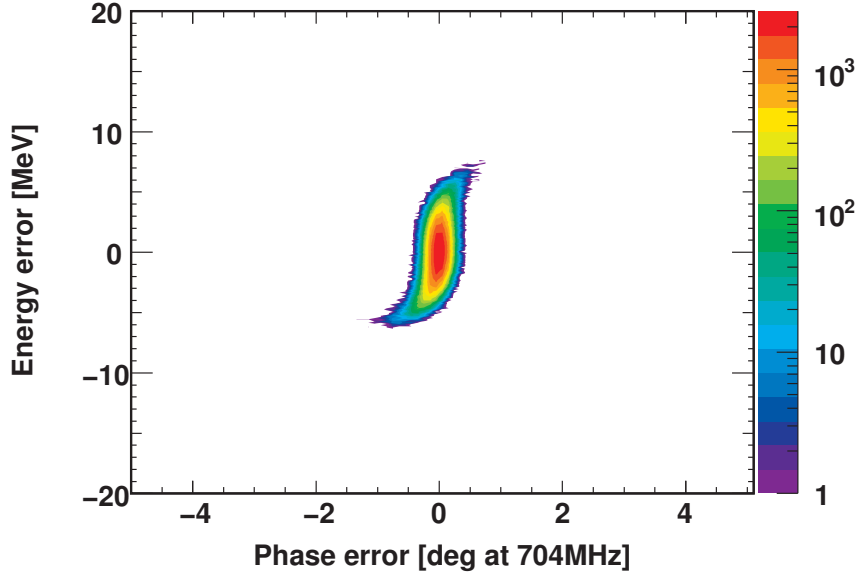
Figure 8.1: 2D phase space histogram of one pulse at the end of the linac, which is not disturbed by HOMs. This distribution will be used as reference for HOM simulation in this section. Settings: No HOM, $N = 1$, see Tab. 8.2.

8.2.1   Initial Simulation with a HOM

The same bunch pattern as before is used, but an additional HOM monopole far away from any machine line is present in each cavity, see Table 8.2. The case where a HOM falls on a machine line will be discussed in subsection 8.2.7. The beam current is $\langle I_b \rangle = 400\,\text{mA}$, the charge scatter $\sigma_q = 3\,\%$, the HOM frequency spread $\sigma_{f_{\text{HOM}}} = 1\,\text{MHz}$, and $Q_{\text{ex}} = 10^7$. The simulation is repeated for 1,000 linacs, which means that each time a different seed for the HOM frequency spread generator is used. All other parameters stay the same. In Figure 8.2 the resulting phase space histogram is shown. The mean values in both planes show only minor deviations in the order of 10^{-3} compared to the situation without HOM. Only slight changes are visible in the border area.

The average and maximum HOM voltage, present in the cavities after the second pulse, is illustrated in Figure 8.3. The voltage changes along the linac according to the $(R/Q)(\beta)$ change. The maximum values are about 5 times higher than the average values.

In order to compare the results obtained with different input parameters and to identify easily the impact of the HOM, a figure of merit has to be defined. The phase space area created by all bunches in a pulse at the end of the linac

$$\epsilon = \pi \sqrt{\langle dE^2 \rangle \langle d\phi^2 \rangle - \langle dEd\phi \rangle^2}, \tag{8.2}$$
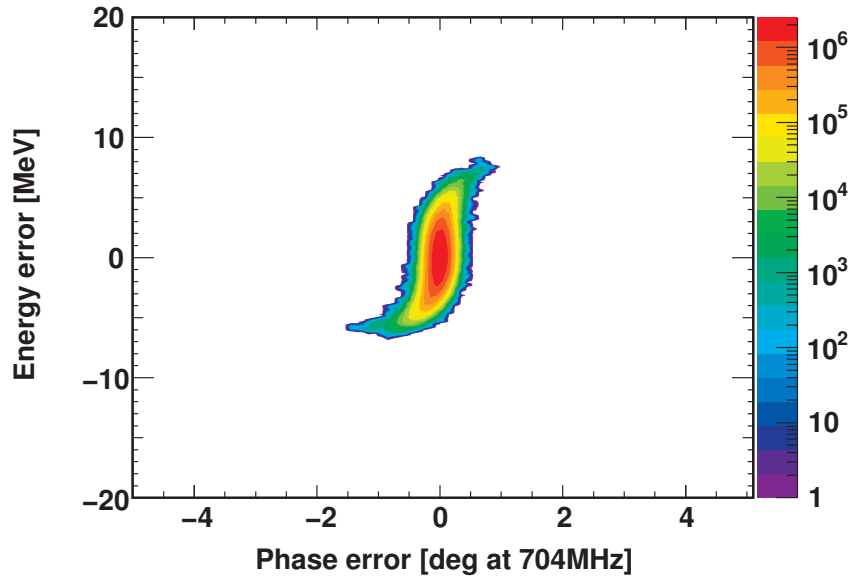
Figure 8.2: 2D phase space histogram of one pulse at the exit of 1,000 linacs, where always the same pulse was tracked through but different seeds for the HOM frequency pattern is used. Settings: $N = 1,000$, see Tab. 8.2.
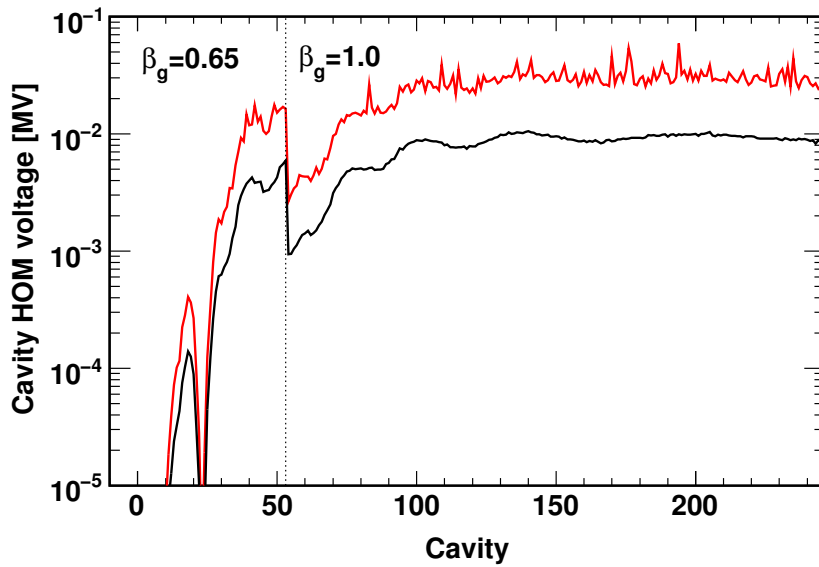
Figure 8.3: Average (black) and maximum (red) HOM voltage present in the cavities after two pulses. The $(R/Q)(\beta)$ dependency is clearly visible in the medium beta section. Settings: $N = 1,000$, see Tab. 8.2.

Table 8.2:   Default settings used in all longitudinal beam dynamics simulations.

Injected beam		Mean	σ
E_{Input}	[MeV]	160	0.078
ϕ	[deg at 704MHz]	-15	0.4
x	[mm]	0.0	0.0
x'	[mrad]	0.0	0.0
I_{b}	[mA]	400[†]	3%
Pulse structure			
T_{b}	[ps]	2.84	
T_{p}	[ms]	1.00	
T_{r}	[ms]	20.0	
Monopole mode $\beta_{\text{g}} = 0.65$ cavity			
f_n	[MHz]	1783	1
$(R/Q)(\beta)$	[Ω]	$6 \cdot 10^{-5}$ - 44	
Q_{ex}		10^7	
Monopole mode $\beta_{\text{g}} = 1.0$ cavity			
f_n	[MHz]	1331	1
$(R/Q)(\beta)$	[Ω]	10 - 140	
Q_{ex}		10^7	

[†] ten times nominal current as safety margin.

where dE is the energy error of a bunch and $d\phi$ its phase error, is used for this purpose. This value is rotation but not displacement invariant, which means the energy and phase oscillations along the linac have no effect on ϵ but a general energy or phase offset increases it.

A growth $\epsilon_{\text{HOM}}/\epsilon$ with a growth rate $\epsilon_{\text{HOM}}/\epsilon - 1$ is then defined as the effective ratio of a HOM disturbed pulse over an undisturbed pulse. This can be used to measure the influence of HOMs or RF errors.

8.2.2   RF Errors without HOMs

One of the main sources of energy and phase jitter are the RF power sources [95]. The SPL design aims for RMS errors below $0.5°$ in phase and 0.5% in amplitude. With these errors and assuming a uniform distribution, 1,000 different linacs are simulated. The phase space distribution at the exit of the linac is shown in Figure 8.4(a). A significant phase space area increase can be observed

as compared to the case, where no RF errors are present. The distribution of ϵ is normalised to the case, where no RF errors are present.

The peak of the resulting histogram in Figure 8.4(b) is at ~ 3 times the nominal effective longitudinal ϵ and the average value is at ~ 3.8. In the following simulations, this 3.8-fold increase in effective longitudinal ϵ is used as the tolerable limit for HOM induced beam degradation.

(a) 2D phase space histogram   (b) ϵ distribution
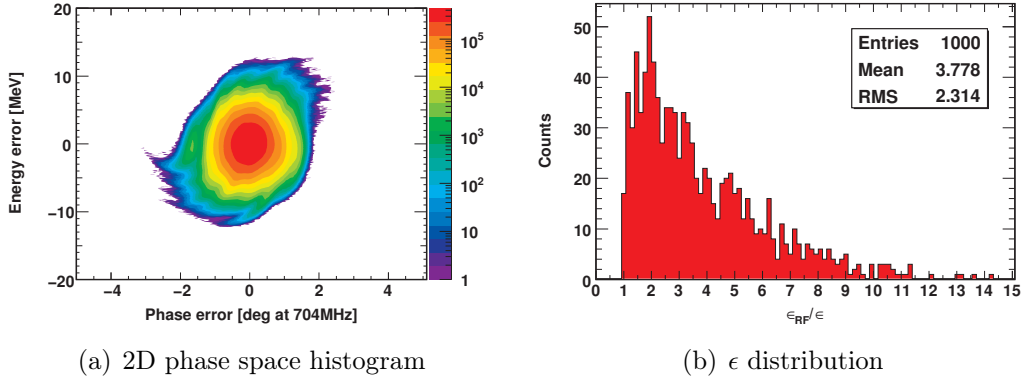
Figure 8.4: 2D phase space histogram at the exit of 1,000 linacs with RF errors, but no HOM is present and the ϵ distribution of the single pulses. The phase space area is increased significantly compared to Figure 8.2. On average ϵ is ~ 3.8 times higher. Settings: uniform distributed RF errors ($0.5°$ in phase and 0.5% in magnitude), no HOM, $N = 1000$, see Tab. 8.2.

The values of the energy and phase error at the end of the linac are about a factor of two larger as compared to the values in [29]. This difference can be explained with a different energy gain per cavity due to energy error caused transit time factor changes. This effect was not included in the previous study. To confirm this explanation, simulations using the energy gain of the synchronous particle per cavity for each particle are executed and lead to the expected energy and phase error as stated in [29]. Further simulations with different RF errors and the influence of HOMs will be shown later in subsection 8.2.9.

8.2.3 Current and Damping Sweeps

The first two parameters which are investigated in detail are the beam current I_b and the external damping Q_ex. Figure 8.5 shows a parameter sweep, where $\langle I_\mathrm{b} \rangle$ is varied between $40\,\mathrm{mA}$ and $400\,\mathrm{mA}$ and Q_ex between 10^4 and 10^8. Each set is simulated for 100 linacs. At nominal current, no obvious change is visible. At $Q_\mathrm{ex} = 10^7$, $\epsilon_\mathrm{HOM}/\epsilon - 1$ is about 0.2‰. Increasing the beam current by a factor of 10 leads to an increase of $\epsilon_\mathrm{HOM}/\epsilon - 1$ by a factor 100, but only $\sim 3\%$ in absolute terms. Below $Q_\mathrm{ex} = 10^5$ even at $400\,\mathrm{mA}$ $\epsilon_\mathrm{HOM}/\epsilon - 1$ is less than 1‰.
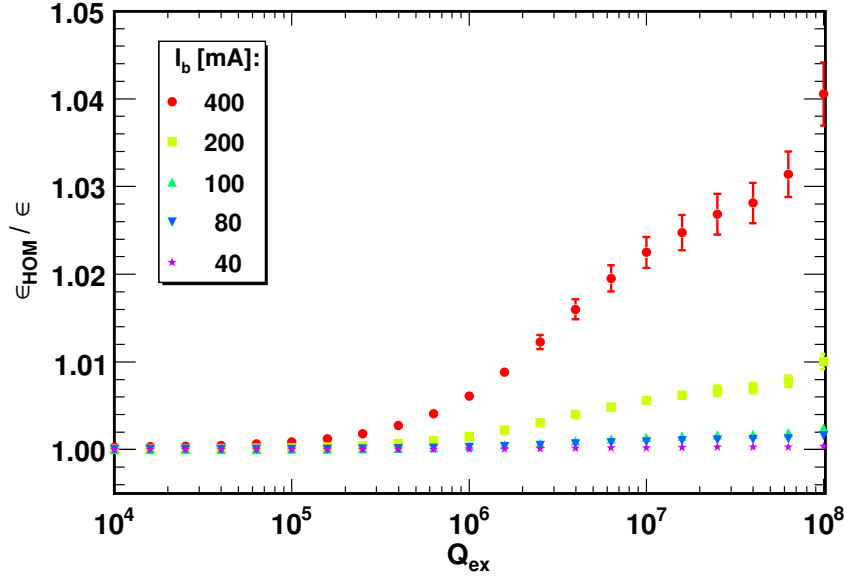
Figure 8.5: Average longitudinal phase space increase and deviation of 100 linacs against the damping Q_{ex} for different I_{b}. $\epsilon_{\mathrm{HOM}}/\epsilon$ is proportional to $\langle I_{\mathrm{b}}\rangle^2$. The plateau around $Q_{\mathrm{ex}} \approx 4 \cdot 10^7$ is due to the pulse period structure. Settings: $N = 100$, see Tab. 8.2.

In general $\epsilon_{\mathrm{HOM}}/\epsilon$ is proportional to $\langle I_{\mathrm{b}}\rangle^2$, while the HOM voltage increase is proportional to $\langle I_{\mathrm{b}}\rangle$. This is because the HOM voltage induced by a single bunch is proportional to the charge per bunch, see Eq. 6.2 and is no contradiction, since ϵ is the correlated product of the energy and phase error. The mean value of both quantities increases linear with $\langle I_{\mathrm{b}}\rangle$.

Investigating the Q_{ex} dependency the plot can be divide into three regions: $Q_{\mathrm{ex}} < 4 \cdot 10^6$, $4 \cdot 10^6 < Q_{\mathrm{ex}} < 6 \cdot 10^7$, and $6 \cdot 10^7 < Q_{\mathrm{ex}}$. In the second region around $Q_{\mathrm{ex}} \approx 4 \cdot 10^7$ a plateau is visible. This can be explained by the fact that the rise time to reach the maximum HOM voltage is longer than the beam pulse, but the decay time is shorter than the period length. So the voltage decays completely before the next pulse arrives. In the first region the maximum HOM voltage is reached during the pulse. If Q_{ex} increases further (third region), the decay time gets longer than a period length and the HOM voltage can increase from pulse to pulse. This damping regime should be avoided to prevent long term instabilities. This characteristic curve of the Q_{ex} dependency shows the same qualitative behaviour as the square of the voltage calculated with Eq. 6.12, taking only the real part and neglecting the oscillations introduced by the imaginary part.

In all further simulations ten times the nominal beam current $\langle I_{\mathrm{b}}\rangle = 400\,\mathrm{mA}$ is used as safety margin and $Q_{\mathrm{ex}} = 10^7$ is assumed.

8.2.4 Beam Injection Noise

The excitation of a HOM far from a resonance depends strongly on the beam noise. In order to verify, that the used injection beam noise patten is a representative sample, 1,000 simulations are carried out, where all machines parameters stay the same, but the injection beam noise pattern is varied. Then the simulations are repeated, where additionally the HOM frequency pattern is varied. All simulations show a deviation in the order of 10^-3, which is not significant. Hence, the same injection beam noise pattern is used in all further simulations and only the HOM frequency pattern is varied.

8.2.5 Charge Scatter

The number of particles per bunch is not constant over time and so there is a bunch to bunch charge scatter, which is assumed to be Gaussian distributed with a sigma of a few per cent. This scatter has an impact on the HOM excitation and induces a beam blow up as shown in Figure 8.6, where σ_q is varied between 0 and 10%. For each σ_q 100 different linacs with a $\sigma_{f_{HOM}} = 1\,\text{MHz}$ are simulated. A change in the used charge scatter pattern has only a minor influence in the order of 10^{-3} and can be neglected in further discussion. The observed increase in ϵ_{HOM}/ϵ is proportional to σ_q^2.
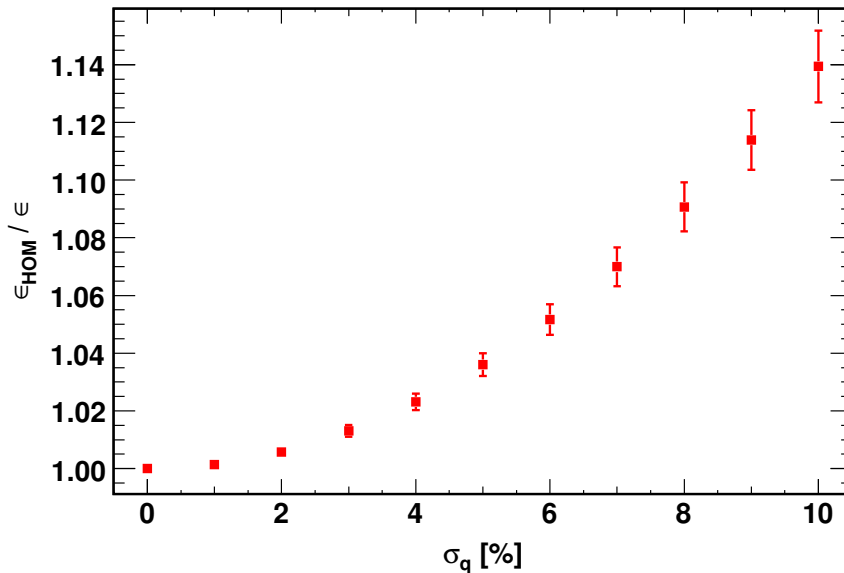
Figure 8.6: Average longitudinal phase space increase and deviation as a function of the Gaussian bunch to bunch charge scatter. The phase space increases approximately with $\approx \sigma_q^2$. Settings: $N = 100$, see Tab. 8.2.

8.2.6   HOM Frequency Spread

Past studies [101, 110] have shown that the HOM frequency spread plays an important role in building up beam instabilities. In this thesis the parameters listed in Table 8.2 are used with the width of the Gaussian distributed HOM frequency spread $\sigma_{f_{\mathrm{HOM}}}$ being varied in the range between 10^4 - 10^7 Hz around the nominal HOM frequencies. In total 100 linacs are simulated in each step.

The average and maximum value of $\epsilon_{\mathrm{HOM}}/\epsilon$ is plotted in Figure 8.7, where a growth is observed for $\sigma_{f_{\mathrm{HOM}}} < 100\,\mathrm{kHz}$. A larger HOM frequency spread leads to less beam perturbation and reaches a minimum level for $\sigma_{f_{\mathrm{HOM}}} > 1\,\mathrm{MHz}$. In this regime, the HOM in a cavity does not drive the HOM excitation in further downstream cavities.
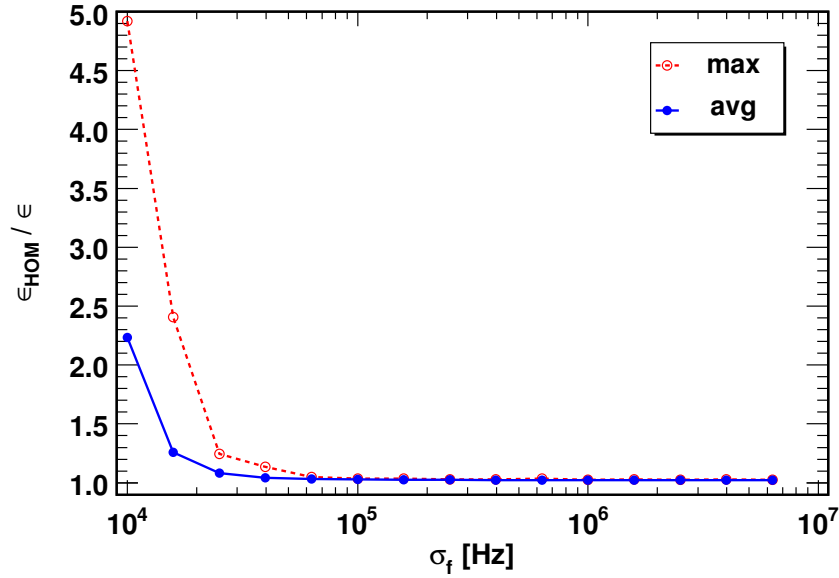
Figure 8.7: Average (solid, blue) and maximum (dashed, red) longitudinal phase space increase against the HOM frequency spread for 100 linacs. Settings: $N = 100$, see Tab. 8.2.

At nominal beam current, the impact of the HOM is less than 1‰ at $\sigma_{f_{\mathrm{HOM}}} = 10\,\mathrm{kHz}$. The expected HOM frequency spread in the SPL cavities is assumed to be greater than $1\,\mathrm{MHz}$ for all modes beside the fundamental passband and is thus well above the threshold.

The simulations are also carried out for stronger damping. This leads to a shift of the HOM frequency spread threshold to lower $\sigma_{f_{\mathrm{HOM}}}$. For higher Q_{ex} the threshold moves to larger $\sigma_{f_{\mathrm{HOM}}}$. A comparison with analytic results is done in section 8.3.5.

8.2.7 Machine Lines

The most dangerous situation in terms of beam instabilities is a HOM which falls on a machine line (ML). In this case a resonance excitation from bunch to bunch occurs and a significant HOM voltage can be built up in the cavities. The minimum distance of a HOM to a machine line is estimated in this subsection, where machine operation is possible with no essential impact by HOMs. Two sets of simulations are carried out. First, the mean HOM frequency $\langle f_{\mathrm{HOM}} \rangle$ is set on a machine line and the HOM frequency spread $\sigma_{f_{\mathrm{HOM}}}$ is increased. Second, $\langle f_{\mathrm{HOM}} \rangle$ is shifted away from the machine line with a constant $\sigma_{f_{\mathrm{HOM}}}$. Additionally, the effect of strong HOM damping is analysed. In both linac sections the $(R/Q)(\beta)$-maps of the monopole modes listed in Table 8.1 are used as, but the HOM frequency is shifted to a machine line. The beam current is reduced to the nominal $40\,\mathrm{mA}$, because the beam is lost immediately at $400\,\mathrm{mA}$ in almost all cases. All other simulation parameters are the default parameter listed in Table 8.2

HOM Frequency Spread at a Machine Line

The mean HOM frequency is set to the 4th machine line at $1408.8\,\mathrm{MHz}$ and the HOM frequency spread is varied from $10\,\mathrm{kHz}$ to $10\,\mathrm{MHz}$. In order to have enough statistics, 100 linacs are simulated in each step and the resulting $\epsilon_{\mathrm{HOM}}/\epsilon$ against $\sigma_{f_{\mathrm{HOM}}}$ is shown in Figure 8.8, where the beam is strongly disturbed and beam losses occur for $\sigma_{f_{\mathrm{HOM}}} < 400\,\mathrm{kHz}$. Even for a large HOM frequency spread of $10\,\mathrm{MHz}$ there is still a significant impact. One cavity with a HOM at the machine line can drive instabilities as already shown earlier in this chapter. Hence, the occurrence of a HOM with a high $(R/Q)(\beta)$ sitting directly on a machine line, has to be excluded during the cavity design phase.

HOM Frequency Distance to a Machine Line

The HOM frequency spread is fixed to $1\,\mathrm{MHz}$ and $\langle f_{\mathrm{HOM}} \rangle$ increased in $1\,\mathrm{MHz}$ steps starting at the 4th machine line. The results are shown in Figure 8.9. Outside the 3σ area which correspond to $3\,\mathrm{MHz}$, there is no impact from the machine line any more and normal off-resonance growth is observed. Since the machine line resonances are very sharp, only very few cavities with a HOM in this small bandwidth are needed to drive beam instabilities. The following criteria can be used to exclude frequency bands around machine lines during the design phase, where no HOM with high $(R/Q)(\beta)$ is allowed:

$$| \langle f_{\mathrm{HOM}} \rangle - f_{\mathrm{ML}} | > 3\sigma_{f_{\mathrm{HOM}}} \tag{8.3}$$
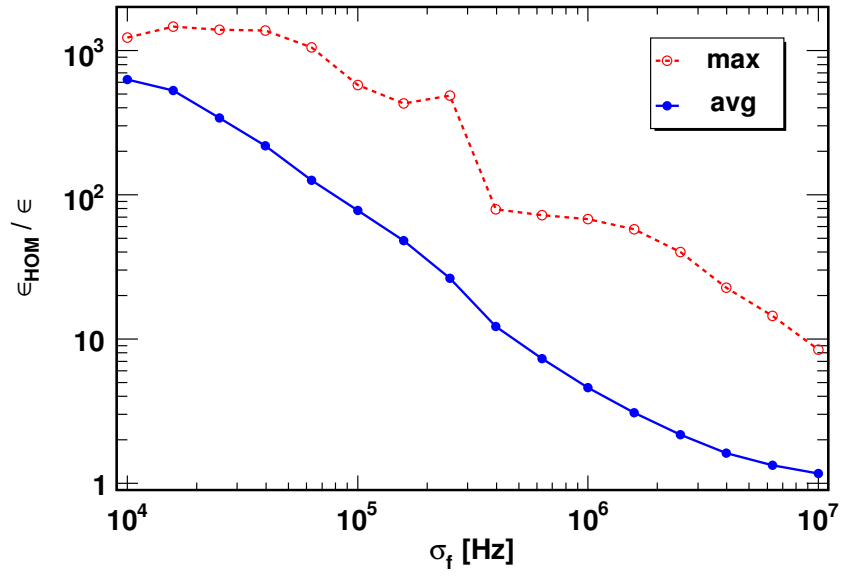
Figure 8.8: Average (solid, blue) and maximum (dashed, red) longitudinal phase space increase as function of the HOM frequency spread at the 4th machine line. Losses occur in case of $\epsilon_{\text{HOM}}/\epsilon > 100$. Settings: $\langle f_{\text{HOM}} \rangle = 1,408.8\,\text{MHz}$, $\langle I_{\text{b}} \rangle = 40\,\text{mA}$, $N = 100$, see Tab. 8.2.
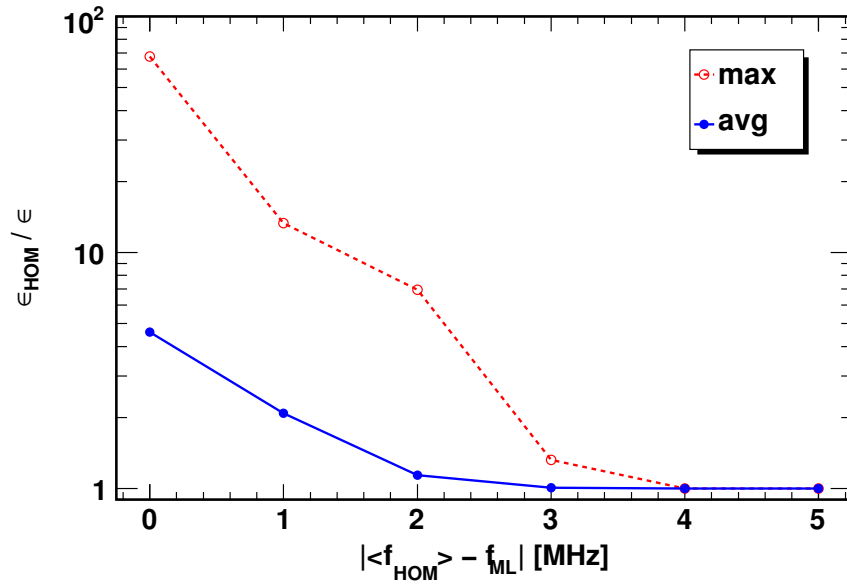
Figure 8.9: Average (solid, blue) and maximum (dashed, red) longitudinal phase space increase as function of the distance to 4th machine line. Settings: $\langle f_{\text{HOM}} \rangle$ shifted, $\langle I_{\text{b}} \rangle = 40\,\text{mA}$, $N = 100$, see Tab. 8.2.

Strong Damping

The dependency on Q_{ex} in case of a resonance excitation is investigated. The average and maximum phase space increase in simulations of 100 linacs is shown in Figure 8.10, where the damping and the current is varied. At $400\,\mathrm{mA}$ the phase space increase is always higher than the increase due to RF errors. Decreasing the current to the nominal $40\,\mathrm{mA}$ relaxes the situation, but even there the maximum phase space increase exceeds the average phase space increase due to RF errors above $Q_{\mathrm{ex}} = 10^5$. Even with strong HOM damping, operation is critical from a beam dynamics point of view if a HOM falls on a principal machine line. In this case also the power dissipated in the HOM coupler is significant and has to be considered and will be addressed in chapter 9.
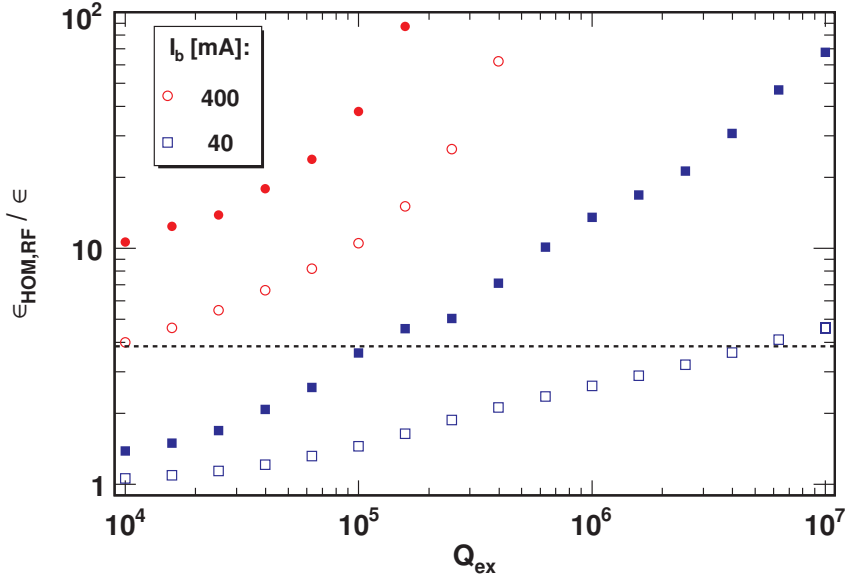
Figure 8.10: Average (hollow dots) and maximum (solid dots) longitudinal phase space increase as function of the damping, where a HOM is resonantly excited. The average increase due to RF errors is indicated with the dashed line. Settings: $\langle f_{\mathrm{HOM}} \rangle = 1,408.8\,\mathrm{MHz}$, $N = 100$, see Tab. 8.2.

Resonance in a Single Cavity

In the previous subsections the mean HOM frequency was set to a machine line. Now only one cavity in the linac shall be considered that has a HOM directly at the 8th machine line with an $(R/Q) = 1\,\Omega$. In all other cavities, the nominal HOM with a frequency spread of $1\,\mathrm{MHz}$ is present. A sweep is performed where the resonant HOM is put in each cavity in the linac with a $Q_{\mathrm{ex}} = 10^8$. Four

consecutive pulses are simulated to take into account the long rise time at that damping level. For comparison also the voltages and the phase space increase after the first pulse is recorded. The HOM voltage present in the resonantly excited cavity is about $336\,\mathrm{kV}$ after the first pulse and $405\,\mathrm{kV}$ after the last pulse, which is in good agreement with the analytical value obtained by Eq. 6.12. There is only a minor deviation ($\sim 10^{-3}$) in the resonance HOM voltage along the linac due to the arrival time error.

In Figure 8.11 the resulting phase space increase is shown as a function of the cavity number where the HOM at the machine line is located. The strongest influence is observed if the resonant HOM is at the beginning of the linac. In this case the relative deceleration kick[2] caused by the HOM is highest there compared to the particle energy. Oscillations in phase space growth along the linac are observed. Bunches with an energy and phase error perform oscillations in phase space travelling along the linac due to the RF focusing. The used injection pattern causes a characteristic oscillation with peaks in phase and energy error at certain points along the linac. If the resonant HOM is at a position with a low energy error, the impact is strongest than at positions with high energy error. The period length of the observed phase space increase oscillations fits with the phase error oscillation. In a real machine these peaks in energy and phase error are not fix due to a changing injection distribution. Hence the envelope of the oscillation should be taken as measure of the phase space increase. The influence at the first pulse is smaller, because no HOM voltage is present in the cavity at the start. At $Q_{\mathrm{ex}} = 10^{8}$ the decay time is larger than the repetition period and the HOM voltage cannot decay completely between two pulses. Hence, the HOM voltage increases from pulse to pulse and causes a larger phase space increase.

The total phase space increase due to a resonant HOM with a low (R/Q) (< 1), can be tolerated at a damping of $Q_{\mathrm{ex}} = 10^{8}$ in the high beta section, without any major influence at the beam. There the influence of RF errors is still dominant. In the beginning of the medium beta section the phase space increase is significantly larger than the increase due to RF errors. This situation improves, if a higher damping is present or the mode is detuned. Detuning the resonant mode leads also to a decrease of the maximum HOM voltage and causes less beam disturbance. The HOM voltage is reduced by about a factor of ten, if the mode frequency is shifted by $1\,\mathrm{kHz}$ at $Q_{\mathrm{ex}} = 10^{8}$. A cavity in operation is tuned each pulse to compensate for the Lorentz force detuning. It is very unlikely that a HOM stays over several pulses exactly on a machine line. Hence the most critical case is the HOM voltage build up during one pulse. The HOM voltage induced during one

---

[2] The induced HOM voltage is opposite in sign from the acceleration voltage and the HOM frequency is an integer multiple of the bunch frequency. Therefore the HOM acts always as decelerating kick.
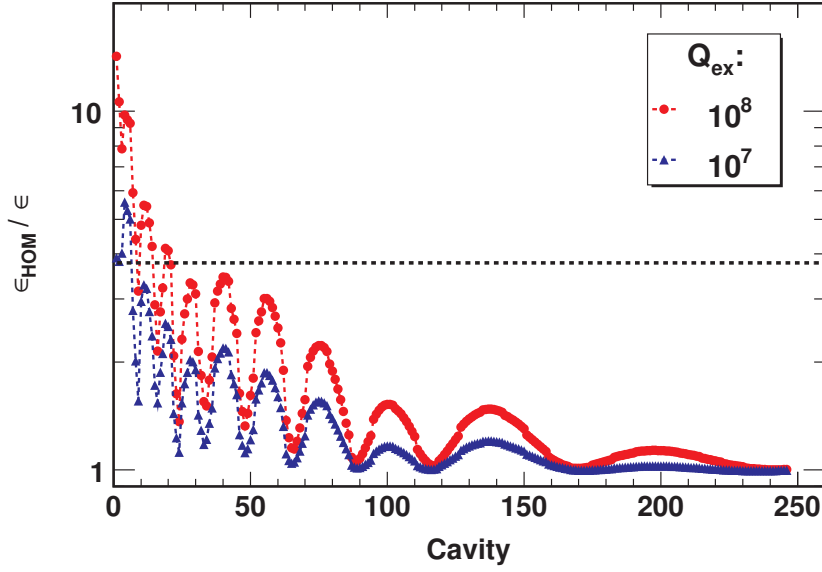
Figure 8.11: Longitudinal phase space increase as function of the cavity number, where the HOM at the 8th machine line is located for different damping. The average increase due to RF errors is indicated with the dashed line. An oscillating phase space increase is observed, which decreases further downstream the linac. The oscillation is due to the used injection noise pattern. Settings: $f_{\text{ML}} = 2,817.6\,\text{MHz}$, $(R/Q)_{\text{ML}} = 1\,\Omega$, $N = 1$, other cavities use default HOM configuration, see Tab. 8.2.

pulse saturates above $Q_{\text{ex}} = 10^8$ due to the long filling time. From this point of view a trapped mode with an $(R/Q) < 1$ is only a concern for the beam stability, if it appears in the beginning of the medium beta section and its frequency hits exactly a machine line. The width of the resonance decreases with increasing Q_{ex}. Hence, the needed detuning decreases as well. The exact limits for $(R/Q)(\beta)$ as function of the resonance frequency can be calculated analytically using Eq. 6.12. This way the HOM voltage can be limited to a value smaller than the accelerating voltage error caused by the RF system.

8.2.8 Sub-structured Pulses

Any sub-structure in the beam pulse, created by chopping, introduces new spectral lines in addition to the machine lines created by the bunch spacing ($nf_{\text{b}}, n \in \mathbb{N}$). The chopping frequency $f_{\text{c}} = f_{\text{b}}/N_{\text{cb}}$ is defined by the periodicity of the sub-structure, where N_{ci} out of N_{cb} bunches are used. Stable operation with a resonant HOM excitation must be guaranteed if the SPL wants to provide any pulse substructure to various user facilities. Therefore, three different $(N_{\text{ci}}/N_{\text{cb}})$ patterns

with the same ratio and a bunch repetition frequency of 352.2 MHz are investigated in more detail and listed in Table 8.3. The charge per bunch is increased by a factor 8/5 to keep the total charge per pulse constant.

A frequency scan between the 3rd and 4th machine line is performed, where the mean HOM frequency with a $\sigma_{f,HOM} = 1\,\mathrm{MHz}$ is set to a chopping machine line and the $(R/Q)(\beta)$-maps of the monopole modes listed in Table 8.1 are used.

Table 8.3: Chopping patterns used in the beam dynamics simulations.

Chopping pattern $(N_{\mathrm{ci}}/N_{\mathrm{cb}})$	f_c [MHz]
5/8	44.025
50/80	4.4025
500/800	0.44025

The longitudinal phase space increase of one simulated pulse at nominal beam current and $Q_{\mathrm{ex}} = 10^7$ versus the frequency is shown in Figure 8.12, where also the simulated TM_{011} monopole frequencies of the $\beta_{\mathrm{g}} = 1$ cavity are indicated along with the phase space increase due to RF errors. Away from the principal machine lines only the 5/8 pattern triggers a certain growth of about a factor of two. One of the 5/8 chopping resonance lines is close to the expected frequency of the $TM_{011,3/5\pi}$ mode, which has a maximum (R/Q) value of about $5\,\Omega$. In general, the impact of the chopping machine lines on beam degradation increases with the repetition rate, which can be explained by looking at its Fourier components. At $Q_{\mathrm{ex}} = 10^5$ no growth due to the chopping machine lines is observed in Figure 8.13 for all chopping patterns at nominal current, which ensures stable operation for any chopping pattern. At this damping level only principal machine lines can cause beam blow up.

The pulse sub-structure used at SNS [102] corresponds to a 260/378 chopping pattern. Such repetition rate is too small to create any potentially dangerous chopping machine lines. Hence, only the principal machine lines can drive significant instabilities. Since all monopole modes in the SNS cavities [120] are far away from these resonance lines, no resonant HOM excitation is observed during operation [112].

8.2.9   RF Errors and HOMs

As shown earlier in this chapter, RF errors lead to a significant longitudinal phase space increase of about a factor of four. Repeating the 1,000 simulations with an equal distributed RMS RF error of $0.5°$ in phase and $0.5\,\%$ in amplitude, but additionally with a HOM present, no changes are observed as compared to
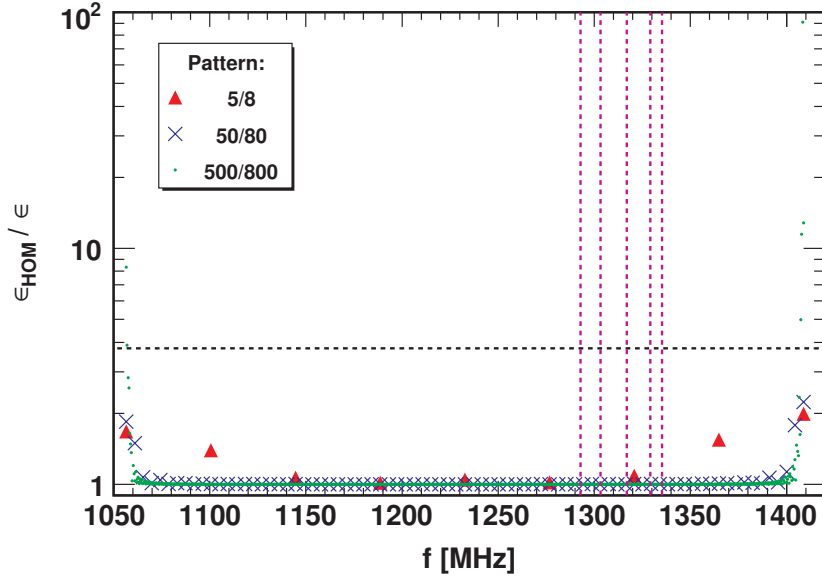
Figure 8.12: Longitudinal phase space increase against the HOM frequency where a HOM falls on a chopping machine line at nominal current and $Q_{ex} = 10^7$ for different chopping patterns. The RF induced growth (black dashed line) is indicated together with the identified monopole modes (violet dashed lines) in the investigated frequency range. Settings: Chopping, $\langle f_{HOM} \rangle$ shifted, $\langle I_b \rangle = 40\,\mathrm{mA}$, $N = 1$, see Tab. 8.2.

Figure 8.4. Increasing the RF error leads to a further increase in ϵ, as shown in Figure 8.14. Also in this case there is no deviation observed, if additionally a HOM is present.

The effect of a HOM at a machine line on the beam together with RF errors dependent on the damping is studied as well. To better illustrate the effect of a HOM at a machine line in combination with RF errors (RF+ML) the following additional cases are simulated: only a HOM at a machine line (ML), only RF errors (RF) and RF errors with a HOM not resonantly excited (RF+HOM) are plotted together in Figure 8.15. There the average and maximum values of 100 simulations per damping value are shown, where the HOM frequency pattern and the RF error pattern are both varied. An equal distributed RMS RF error of $0.5\,°$ in phase and $0.5\,\%$ in amplitude is used in all simulations with RF errors. At $Q_{ex} = 10^4$ the HOM at a machine line is damped strong enough not to cause an additional phase space increase. Between $10^4 < Q_{ex} < 10^5$ the influence of the HOM starts to rise and the maximum values of ϵ increase slightly, while the average values are still the same as for the other cases. Above $Q_{ex} = 10^5$ the effective phase space starts to increase and the HOM at the machine line becomes the main source of beam
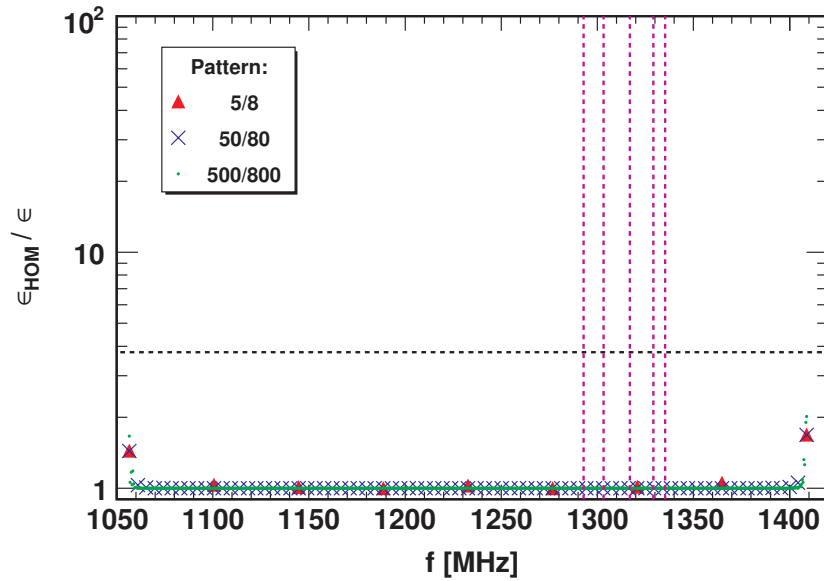
Figure 8.13: Same as Figure 8.12, but with strong HOM damping. Settings: Chopping, $\langle f_{\text{HOM}} \rangle$ shifted, $\langle I_{\text{b}} \rangle = 40\,\text{mA}$, $Q_{\text{ex}} = 10^5$, $N = 1$, see Tab. 8.2.
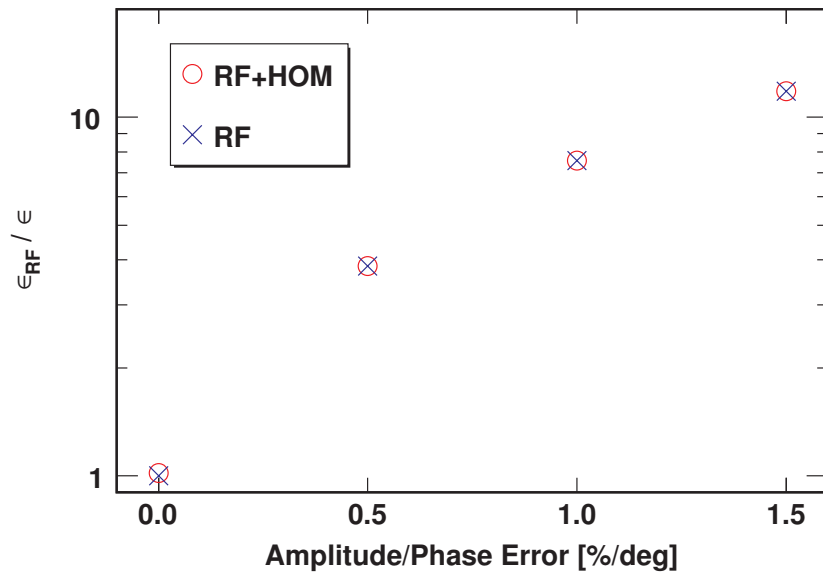
Figure 8.14: Average longitudinal phase space increase as function of the RF error with and without a HOM. Settings: uniform distributed RF errors, $N = 1000$, see Tab. 8.2.

blow up, if the damping is less than $Q_{ex} = 5 \cdot 10^6$.
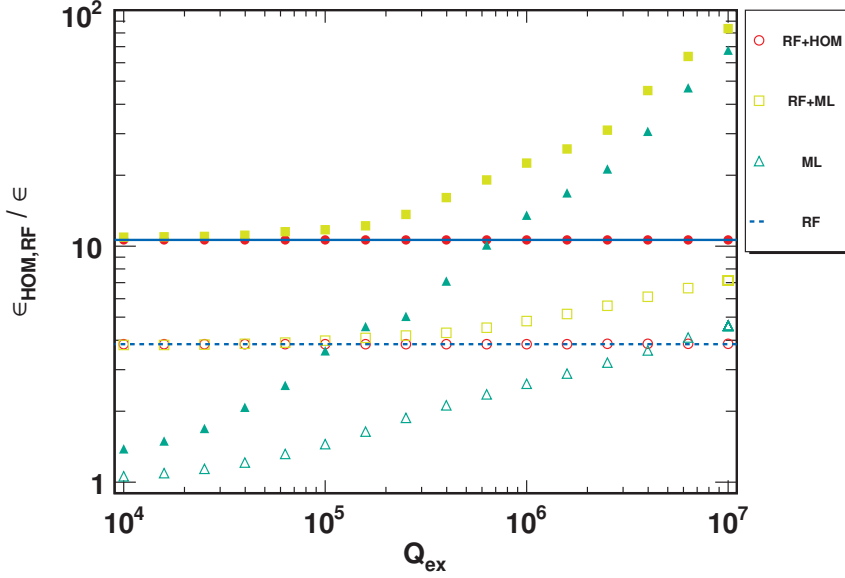
Figure 8.15: Average (hollow dots) and maximum (filled dots) phase space increase against the damping Q_{ex} at nominal current for different cases, where RF errors (RF) and/or a HOM at a machine (ML) or off resonance (HOM) is present. The average (dashed line) and maximum (solid line) increase due to RF errors is also shown. Settings: uniform distributed RF errors ($0.5\,°$ in phase and $0.5\,\%$ in magnitude), $\langle I_b \rangle = 40\,\mathrm{mA}$, $\langle f_{HOM,ML} \rangle = 1,408.8\,\mathrm{MHz}$, $N = 1,00$, see Tab. 8.2.

8.2.10 Fundamental Passband Modes

In the 5 cell SPL cavities, the four additional modes of the fundamental passband can drive beam instabilities, because their $(R/Q)(\beta)$ values can be significant at certain particle velocities as shown in Figure B.2. The mode frequencies and the $(R/Q)(\beta)$ obtained with SUPERFISH are listed in Table B.4.

The $TM_{010,4/5\pi}$ modes, which have the highest $(R/Q)(\beta)$ values, are used in both cavities for further beam dynamics studies. The mode frequency spread is significantly lower for these modes as compared to other HOMs. In all simulations a frequency spread of $10\,\mathrm{kHz}$ is used.

In the first configuration the $TM_{010}, 4/5\pi$ modes are excited by the nominal pulse structure for five different beam currents, as shown in Figure 8.16(a), and 10 linacs are simulated for each step. Above $Q_{ex} = 5 \cdot 10^4$ the average effective longitudinal ϵ as well as its deviation increases significantly for $\langle I_b \rangle = 400\,\mathrm{mA}$ and losses in some simulation runs occur if $Q_{ex} > 5 \cdot 10^5$. The rate of runs with

losses increases to 47% at $Q_{\mathrm{ex}} = 10^7$. At $\langle I_{\mathrm{b}}\rangle = 200\,\mathrm{mA}$ the influence of the $\mathrm{TM}_{010}, 4/5\pi$ modes starts to rise above $Q_{\mathrm{ex}} = 10^5$ and no significant effects occur at $\langle I_{\mathrm{b}}\rangle = 100\,\mathrm{mA}$ and lower currents. The strong influence of the $\mathrm{TM}_{010,4/5\pi}$ is due to the high $(R/Q)(\beta)$ values at the beginning and end of the medium beta section. This effect can only be reduced by changing the energy range, which is covered by the medium beta cavity.
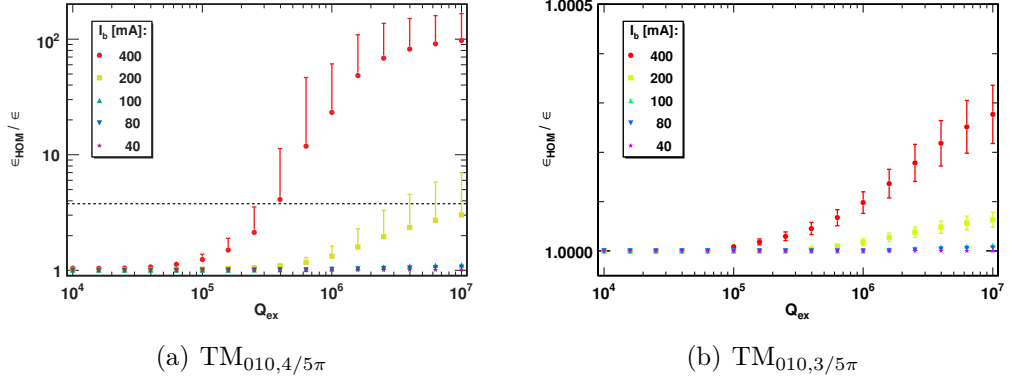
(a) $\mathrm{TM}_{010,4/5\pi}$ (b) $\mathrm{TM}_{010,3/5\pi}$

Figure 8.16: Average longitudinal phase space increase and upper RMS error against the damping Q_{ex} caused by the $\mathrm{TM}_{010,4/5\pi}$ modes in (a) and by the $\mathrm{TM}_{010,3/5\pi}$ in (b) for different beam currents. Above the RF-limit (dashed line) lossy runs occur in (a), while the phase space increase in (b) is insignificant. Settings: $\mathrm{TM}_{010,4/5\pi}$ and $\mathrm{TM}_{010,3/5\pi}$ mode, $\sigma_{f_n} = 10\,\mathrm{kHz}$, $N = 10$, see Tab. 8.2.

The $\mathrm{TM}_{010}, 3/5\pi$ mode in the high beta cavity and the $\mathrm{TM}_{010}, 2/5\pi$ mode in the medium beta cavity are close to a chopping machine line at 699.998 MHz created by a 50/80 chopping pattern. A worst case scenario would be, if the mean mode frequency in both cavities is identical with the chopping machine line, which is simulated and shown in Figure 8.17(b). For comparison the simulation is repeated with the mode frequencies obtained from SUPERFISH, see Figure 8.17(a), and with the nominal pulse structure, see Figure 8.16(b). All simulations are done for 10 linacs.

If the mean mode frequency falls directly on that chopping machine line, ϵ increases significantly. At 400 mA the beam exceeds the RF growth limit above $Q_{\mathrm{ex}} = 5 \cdot 10^4$. At nominal beam current the beam stays stable, but ϵ starts to grow above $Q_{\mathrm{ex}} = 10^4$. All simulations away from the resonance show no significant longitudinal phase space increase even when using ten times the nominal current. A distance of a few 100 kHz to the chopping machine line is sufficient to avoid resonance excitation and a significant longitudinal phase space increase.

In [95] the damping provided by the fundamental power coupler is estimated for the fundamental passband modes and is found to be between $Q_{\mathrm{ex}} = 10^5$ and
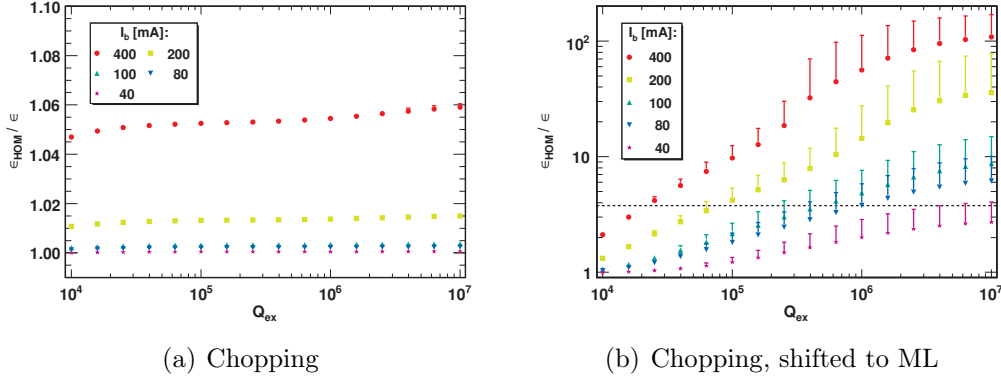
(a) Chopping   (b) Chopping, shifted to ML

Figure 8.17: Average longitudinal phase space increase and upper RMS error against the damping Q_{ex} caused by the $\mathrm{TM}_{010,3/5\pi}$ mode and $\mathrm{TM}_{010,2/5\pi}$ mode and a chopped beam (a). In (b) additionally the mode frequency is shifted to the chopping machine line. The phase space increase due to RF errors is indicated with the dashed line. Settings: Passband modes, $\langle f_{\mathrm{CML}} \rangle = 699.998\,\mathrm{MHz}$, $\sigma_{f_n} = 10\,\mathrm{kHz}$, chopping pattern: 50/80, $N = 10$, see Tab. 8.2.

$Q_{\mathrm{ex}} = 10^6$ depending on the mode. This damping is sufficient for all scenarios as long as the beam current does not exceed $100\,\mathrm{mA}$. At $400\,\mathrm{mA}$ ϵ exceeds the RF growth limit at the expected Q_{ex} in the worst case chopping scenario and for the excitation of the $\mathrm{TM}_{010}4/5\pi$ mode.

8.3 Transverse Plane

In contrast to the longitudinal plane, a HOM that affects the transverse plane can only be exited by an off axis beam, because $E_z(0, \phi, z)$ is zero for all non monopole modes. First, the parameters and assumptions needed to execute simulations in the transverse plane are summarised. Then, effects such as beam break up threshold current, beam noise, alignment errors, and sub-structured pulses are investigated in detail.

8.3.1 Simulation Input Parameters

It is assumed for the SPL, that the beam enters the linac on axis with a Gaussian position and momentum spread listed in Table 8.4 together with all other default simulation settings used in the transverse plane. An explicit study of off axis injected beams is done as well and will be discussed later in this section.

A bunch is defined as lost if the transverse displacement at the end of a section is larger than the iris radius of the cavity, which is a very optimistic value. The aim

Table 8.4: Default settings used in all transverse beam dynamics simulations.

Injected beam		Mean	σ
E_{Input}	[MeV]	160	0.0
ϕ	[deg at 704MHz]	-15	0.0
x	[mm]	0.0	0.3
x'	[mrad]	0.0	0.3
I_{beam}	[mA]	400	3%
Pulse structure			
T_{b}	[ps]	2.84	
T_p	[ms]	1.00	
T_r	[ms]	20.0	
Dipole mode $\beta_{\mathrm{g}} = 0.65$ cavity			
f_n	[MHz]	1020	1
$(R/Q)_\perp(\beta)$	[Ω]	$8 \cdot 10^{-3}$ - 103	
Q_{ex}		10^7	
Dipole mode $\beta_{\mathrm{g}} = 1.0$ cavity			
f_n	[MHz]	915	1
$(R/Q)_\perp(\beta)$	[Ω]	38 - 57	
Q_{ex}		10^7	

of this study is not to monitor losses, but to limit the maximum induced voltage by an off axis bunch. For precise loss studies the beam halo has to be modelled as well as the exact linac layout including magnet and alignment errors.

8.3.2   Initial Simulation

Before looking at the impact of dipole modes, a simulation limited to injection beam noise, including charge jitter, transverse displacement and tilt is carried out and used as reference. The resulting phase space distribution at the end of the linac is shown in Figure 8.18(b). Repeating the simulations with one dipole mode present in each cavity, a HOM frequency spread of 1 MHz, a beam current of 400 mA and a $Q_{\mathrm{ex}} = 10^7$, leads only to modest changes in the phase space distribution, as illustrated in Figure 8.18(a).

As in the longitudinal plane an effective transverse phase space area, created by one pulse and calculated by

$$\epsilon = \pi\sqrt{\langle x^2\rangle\langle x'^2\rangle - \langle xx'\rangle^2}, \tag{8.4}$$

can be used. By normalising it to a reference area, which is the effective phase space area without HOM impact, it can be used as measure for HOM influence.

(a) HOM

(b) Reference phase space
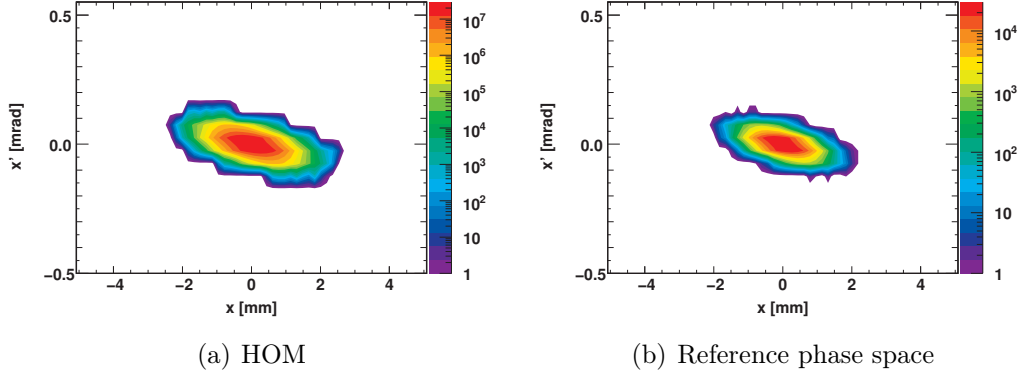
Figure 8.18: 2D phase space plot of the second pulse at the exit of the linac with and without dipole modes present. 1,000 linacs are simulated in case HOMs are present. The distribution in (b) is used as reference for subsequent studies. Settings: (No) HOM, $N = 1,000$ ($N = 1$), see Tab. 8.4.

The average and maximum HOM voltage along the linac after the second pulse for 1,000 different linacs, using the same settings as before, are shown in Figure 8.19. The oscillations observed in the average HOM voltage in the high beta section are due to the betatron oscillations along the linac. Looking at the maximum HOM voltage, an increase along the high beta section is observed while the $R/Q_\perp(\beta)$ decreases. This result is consistent with analytical studies [121].

8.3.3 Current and Damping Sweeps

The upper limit for Q_{ex} is set to 10^8 as in the longitudinal plane. This is the damping level where the influence of pulse-to-pulse coupling starts to rise.

The beam current I_b is varied between the nominal current and a maximum of $400\,\text{mA}$. 100 different linacs are analysed for each combination of Q_{ex} and I_b and the resulting average transverse phase space increase and its variance is illustrated in Figure 8.20.

At a Q_{ex} of 10^4, no growth is observed for all currents. In case of $\langle I_b \rangle = 400\,\text{mA}$, the influence starts to rise at $Q_{ex} = 10^5$ and reaches a plateau level around $Q_{ex} = 10^7$ before starting to rise further above $Q_{ex} = 4 \cdot 10^7$ due to pulse-to-pulse coupling. Also the spread in the single simulation results increases significantly. At nominal current below $Q_{ex} = 4 \cdot 10^7$ no effect is visible. In general the phase space increase is quadratic with the beam current and the dependency on Q_{ex} is the same as in the longitudinal plane.
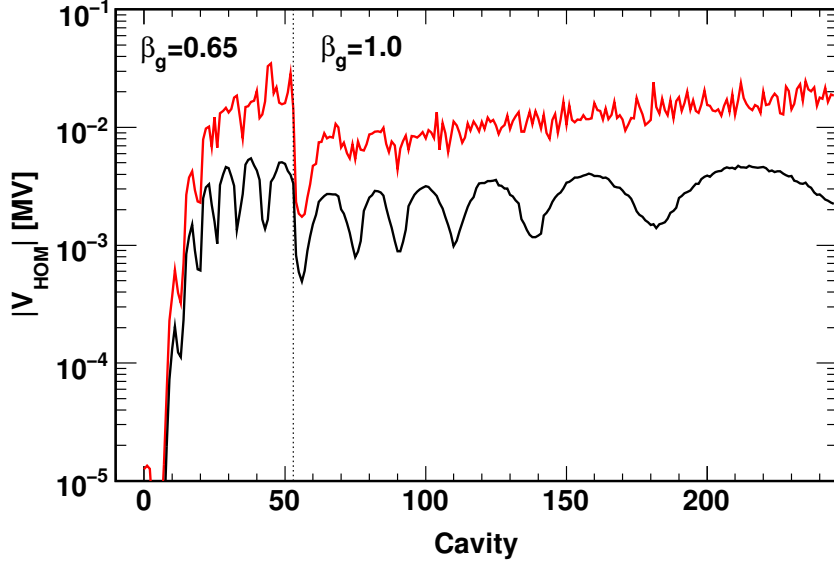
Figure 8.19: Average (black) and maximum (red) transverse HOM voltage present in the cavities after two pulses for 1,000 linacs. Settings: $N = 1,000$, see Tab. 8.4.
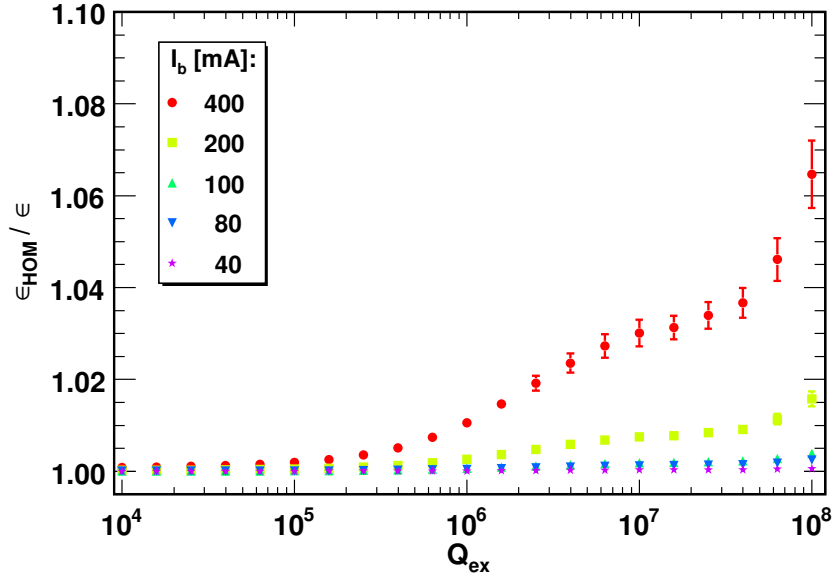
Figure 8.20: Average transverse phase space increase of the beam against the damping Q_{ex} and different beam currents $\langle I_{\mathrm{b}} \rangle$ where one HOM per cavity is present for 100 linacs. The influence of the HOM rises above $Q_{\mathrm{ex}} = 10^5$ and is proportional to $\langle I_{\mathrm{b}} \rangle^2$. The plateau around $Q_{\mathrm{ex}} = 10^7$ is due to the pulse period structure. Settings: $N = 100$, see Tab. 8.4.

Based on these results all further studies are carried out with $Q_{ex} = 10^7$ and $\langle I_b \rangle = 400\,\text{mA}$. At this damping level the pulses are still independent from each other and the HOM voltage history does not have to be taken into account.

8.3.4 Injection Beam Noise

Injection beam noise is essential to excite dipole modes, because the beam on axis has no effect. Following the logic applied in the longitudinal plane simulations with different beam noise patterns are executed to define a representative sample, which is used in the subsequent studies. 1,000 simulations are carried out in each case, where the following parameters are varied:

- injection noise pattern

- HOM frequency pattern

- injection noise and HOM frequency pattern.

The deviation in all cases is around $0.3\,\%$ and all mean values deviate less than $1\,\sigma$. Based on these results, the effect of different injection noise patterns is not considered in further simulations and only the HOM frequency pattern will be varied.

In Figure 8.21 the effect of the charge scatter is shown, which is smaller than in the longitudinal plane. The observed increase in ϵ is proportional to σ_q^2 and scales with the beam current in the same manner. Even for a charge scatter of 10% the phase space increase is of the same order of magnitude as the deviation due to different injection noise or HOM frequency patterns.

8.3.5 HOM Frequency Spread

The HOM frequency spread is important in building up instabilities. Below a certain frequency spread threshold level, the beam position modulation induced by a dipole mode in a cavity is constructively increased in further downstream cavities. In order to find this threshold level, the HOM frequency spread is varied between $10\,\text{kHz}$ and $10\,\text{MHz}$.

The average and maximum transverse phase space increase for 100 linacs is shown in Figure 8.22. No values are plotted for $10\,\text{kHz}$ because beam losses occurred there. The threshold level, below the transverse phase space increase start to rise, is in the order of some $100\,\text{kHz}$, much smaller than the HOM frequency spread in the SPL cavities, which is expected to be around several MHz.

Simulations carried out with the nominal beam current indicate the same threshold level. The transverse phase space increase is smaller due to the reduced current.
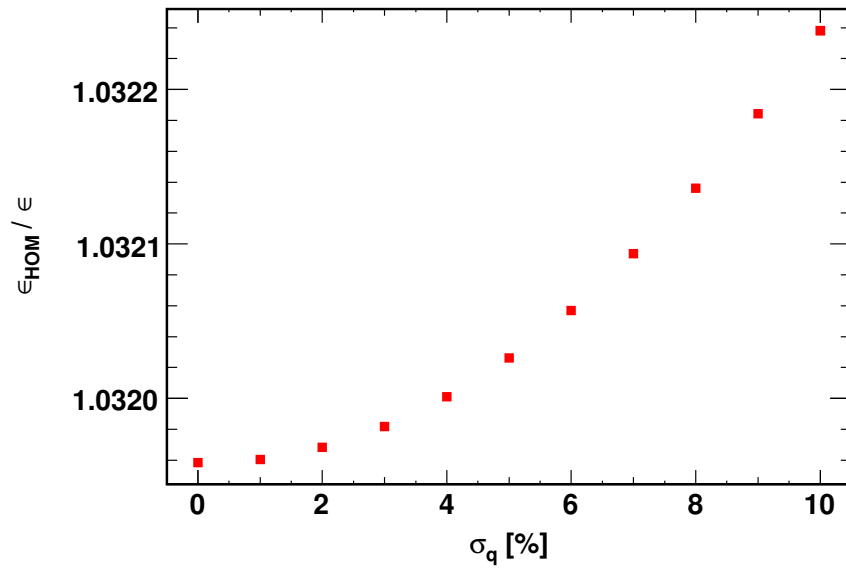
Figure 8.21: Average effective transverse phase space growth of the beam as function of the Gaussian bunch to bunch charge scatter. Settings: $N = 100$, see Tab. 8.4.
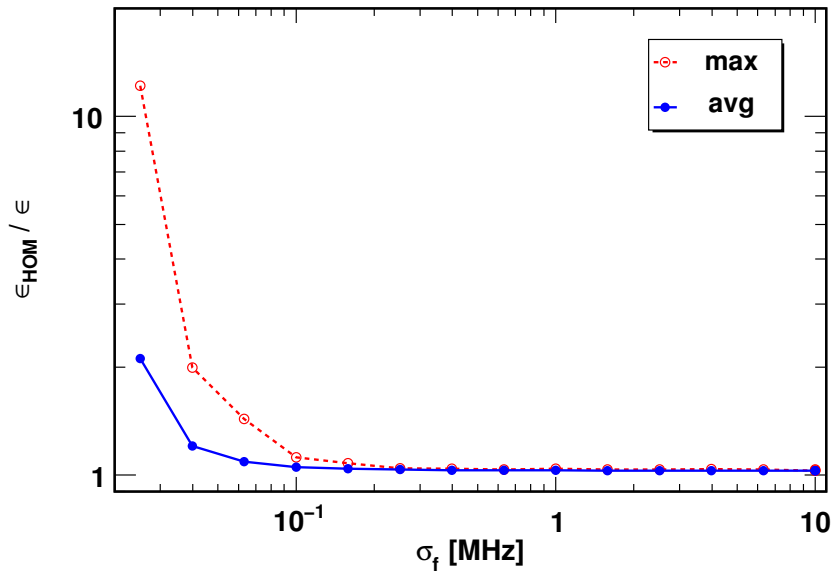
Figure 8.22: Average and maximum transverse phase space increase dependency on the HOM frequency spread. Settings: $N = 100$, see Tab. 8.4.

Table 8.5: Chopping patterns and used resonance frequencies for dipole modes in both linac sections.

Mode	Chopping pattern ($N_{\mathrm{ci}}/N_{\mathrm{cb}}$)	f_{ML} [MHz]
1	no chopping	1056.60
2	5/8	1012.58
3	50/80	1016.98
4	500/800	1018.30

This confirms the analytical work on transverse beam break up of transient beams in [121], which describes the HOM frequency spread as an additional HOM damping. Repeating the simulation with lower Q_{ex} values leads to a shift of the threshold value to lower frequency spread values. A higher HOM frequency spread is needed for higher Q_{ex} to sufficiently reduce the HOM excitation and the caused phase space increase.

8.3.6   Sub-structured Pulses

The influence of the pulse sub-structure is investigated in detail in the transverse plane, too. Therefore, the same chopping patterns are used as in the longitudinal plane, but different resonance frequencies, which are listed in Table 8.5. The integrated charge per pulse is kept constant, which means an increase of the bunch current in case of chopping. The increase in phase space at the exit of the linac for different chopping patterns, off and on resonance, as function of the damping is shown in Figure 8.23. For each configuration 100 linacs with different HOM frequency patterns are simulated.

Introducing chopping leads to an increase in ϵ due to the increased bunch charge. This can be validated by repeating the simulation with increased beam current but without chopping. Shifting the HOM frequency to a chopping machine line causes a further increase in the phase space area. In this context it should be stated that the induced transverse HOM voltage scales with ω_n^2. A chance of the HOM frequency leads to a change in the transverse phase space increase, which is roughly proportional to ω_n. Hence, the observed phase space increase is only partly due to the resonance condition.

The characteristic Q_{ex} dependency is the same as in the nominal case. The difference between the different chopping patterns is relatively small and the mean values are all inside an error of one sigma.

In general the effect of chopping in the transverse plane is far less dramatic than in the longitudinal plane and has the same effect as shifting a dipole mode to a machine line. At ten times the nominal current the phase space increase is
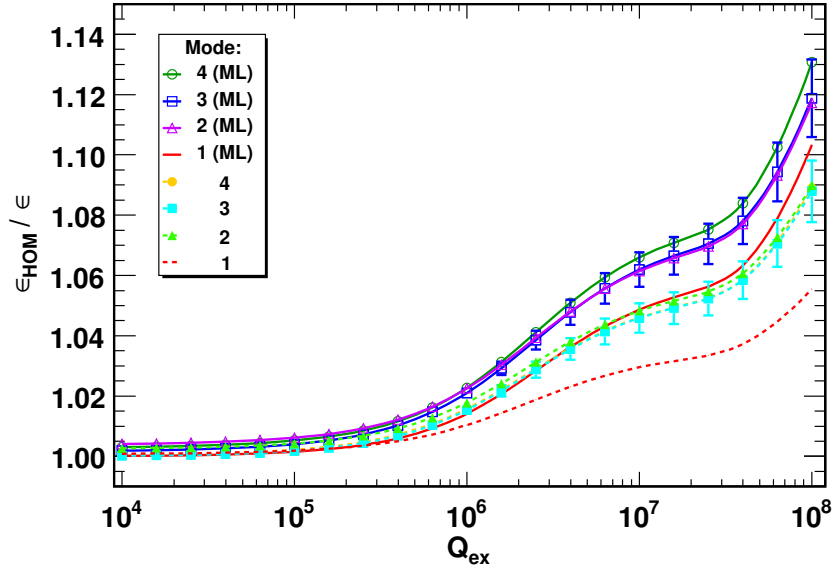
Figure 8.23: Average transverse phase space increase against the damping Q_{ex} and for different chopping patterns on (ML) and off a resonance. The error bars are only plotted for the 50/80 chopping pattern and about the same for the other cases. Settings: Chopping, $\langle f_{\mathrm{HOM}} \rangle$ partly shifted (see Tab. 8.5), $N = 100$, see Tab. 8.4.

less than 10%, even for $Q_{\mathrm{ex}} = 10^7$.

8.3.7   Alignment Errors

Displaced beams and cavities can drive dipole modes, as the beam passes the cavities off axis. There is no additional first order effect on the monopole modes, because a longitudinally displaced cavity causes the same effect as a phase error, which can be treated as a klystron error. Hence, alignment errors are only treated in the transverse plane in this study. First, the cavities are displaced inside the cryo-module and second the effect of off axis injection is analysed.

Cavity Alignment

The cavities are randomly displaced transversely around the beam axis. A Gaussian distribution with a deviation of σ_{dx} is considered. The magnets are assumed not to be affected. Additional transverse RF kicks, introduced by the accelerating mode in a displaced cavity, are also not considered in this simulation[3]. The

---

[3] Transverse RF focusing is included in the smooth focusing data obtained from general beam dynamics simulations, where a perfectly aligned linac is assumed.

σ_{dx} is varied in the range from $0.1\,\mathrm{mm}$ to $10\,\mathrm{mm}$ and for each σ_{dx} 100 linacs are simulated, where only the cavity displacement is varied. All other parameters are the default ones. Figure 8.24 shows the phase space increase at the end of the linac. The average increase in ϵ is proportional to σ_{dx}^2 and starts to rise above $\sigma_{\mathrm{dx}} = 1\,\mathrm{mm}$ compared to the simulation result without cavity displacement. This result agrees with the analytic predictions in [122]. For smaller displacements no significant phase space increase is observed. Even for $\sigma_{\mathrm{dx}} = 10\,\mathrm{mm}$ and $400\,\mathrm{mA}$ the additional phase space increase is only about 3‰ and in the same order of magnitude as the variation due to different HOM frequency patterns.

From experience at other labs, it is expected that the cavities can be aligned with a precision of about $1\,\mathrm{mm}$. At that level, dipole modes do not affect the beam more than in the case of a perfect cryo module. Therefore cavity alignment errors are no concern for HOM excitation in the SPL, within the simulation limitations. The influence of magnet displacement errors has been studied for different focusing schemes in [40].
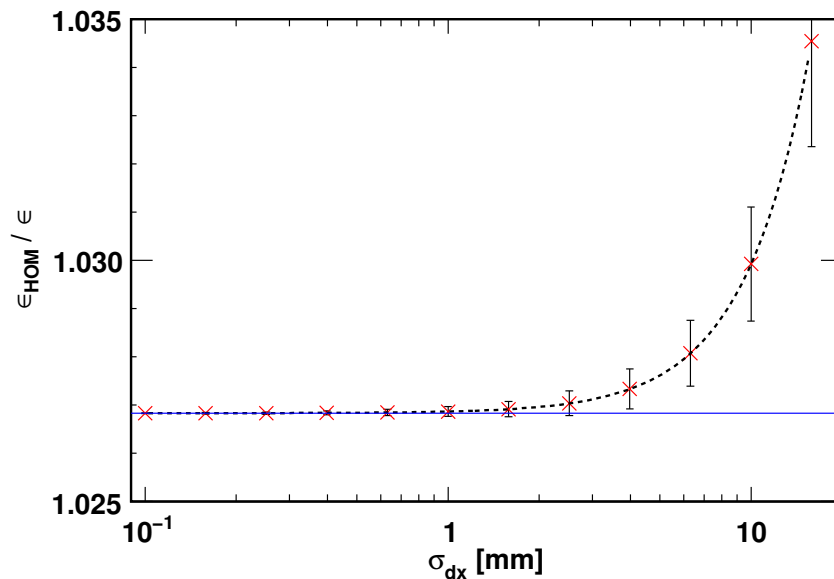
Figure 8.24: Average transverse phase space increase against cavity alignment errors (red crosses with error bars). A second order polynomial is fitted through the data (dashed line). For comparison the phase space increase without cavity displacement (blue line) is added. Settings: $N = 100$, see Tab. 8.4.

Off Axis Injection

The beam is injected off axis into the linac. All further downstream cryo-modules are assumed to be perfectly aligned with the first one. ϵ is not translation invariant and a mean off axis extraction position leads to an increase of ϵ.

To get rid of this effect, the following translation invariant formula is used to calculate the phase space area in this subsection

$$\epsilon^* = \pi\sqrt{\langle x^2\rangle\langle x'^2\rangle - \langle xx'\rangle^2 - 2\overline{x}\cdot\overline{x}' + \overline{x}'^2\langle x^2\rangle + \overline{x}^2\langle x'^2\rangle} \qquad (8.5)$$

where $\overline{x}$ and $\overline{x}'$ are the mean values of the position and momentum distribution. Using (8.5) instead of (8.4) the phase space increase is then only due to the effect of the dipole mode and shown in Figure 8.25(a). There the phase space increases with the injection offset approximately quadratically. The mean extraction position as well as the extraction declination increases linear with the injection offset, which is also reflected in the HOM voltage, shown in Figure 8.25(b), because the bunch induced voltage in a dipole mode is proportional to the off axis position x. This result is in good agreement with [123], where the effect of off-axis injection is discussed analytically.

(a) Phase space increase   (b) Max. HOM voltage
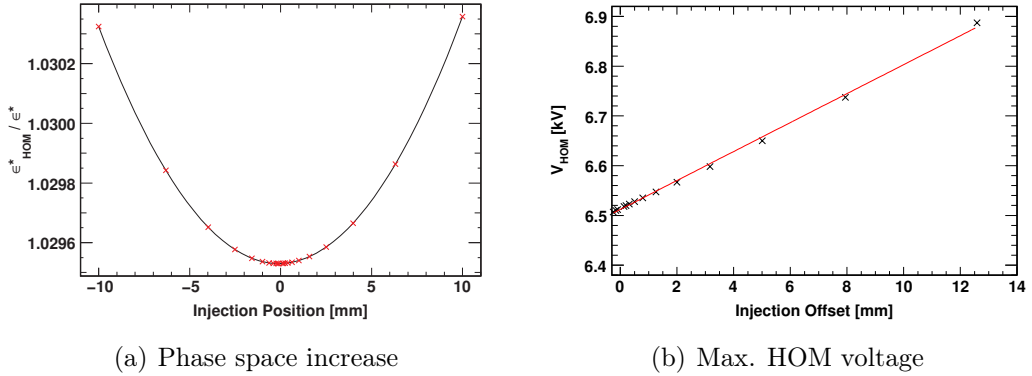
Figure 8.25: Average ϵ^* growth in case of an off axis injected beam with a HOM present and normalised with same off axis beam without HOMs (a) and the maximum HOM voltage in the high beta section (b). The phase space increases with the injection offset approximately quadratically and the HOM voltage approximately linearly with the injection offset. Settings: $N = 100$, see Tab. 8.4.

In case of off axis injection the influence of the dipole mode increases slightly. The additional increase is less than 1‰ in case of injection 10 mm away from the beam axis and a beam current of 400 mA. The deviation in the phase space area due to different HOM frequency patterns is 2.8‰ and so much higher than the influence of an off axis injected beam. Hence, alignment errors are no concern in the context of HOMs for the SPL.

8.4   Conclusion

It was shown in this chapter, that dipole modes do not affect a proton beam significantly as it is the case for electrons. In the longitudinal plane the influence of injection beam noise, HOM frequency spread, RF errors, machine lines and sub-structured pulses were investigated in detail as a function of beam current and HOM damping. Using the SPL design parameters and estimated errors, it was shown that only resonance lines are critical for a stable operation. The principal machine lines are known and can be taken into account in the cavity design, so that no HOM hit such a resonance. However, machine lines created by the pulse sub-structure depend on the chopping pattern and can occur at any frequency. A strong HOM damping of $Q_{\mathrm{ex}} = 10^5$ is recommended to allow any possible pulse sub-structure. In the absence of any pulse sub-structure only a moderate damping in the order of $Q_{\mathrm{ex}} = 10^7$ is needed. In the transverse plane the influence of beam injection noise, HOM frequency spread, resonances and cavity alignment was investigated in detail and no instabilities have been found at a moderate HOM damping level of $Q_{\mathrm{ex}} = 10^7$.

The variety in the pulse sub-structure is the main difference between the SPL and other high power superconducting proton linacs such as SNS or ESS and causes stricter HOM damping requirements in the order of $Q_{\mathrm{ex}} = 10^5$ as compared to for example SNS, which will discussed in detail in chapter 11. In Project X also high frequent chopping patterns are foreseen, but with an average beam current that is a factor of 40 smaller than in the SPL. Hence, resonant HOM excitation is substantially less critical there.

Chapter 9

Power Dissipation by HOMs

A cavity can be seen as a power transformer. The power from the power source such as for example a klystron is transferred to the beam by the accelerating mode, which is usually the $\mathrm{TM}_{010,\pi}$ mode in superconducting elliptical cavities. This works also in the other direction. A bunch passing through a cavity excites all modes in the cavity, as shown in chapter 6. This has consequences for the beam stability and power dissipation in the cavity. The power transferred back to the cavity has to be dissipated either in the cavity walls or has to be extracted via HOM couplers. Some of the power is also transferred back to the beam and can excite beam instabilities. In case of superconducting cavities the heat load is an important design parameter for the cryostat. Depending on the design of the HOM couplers the power is transferred to room temperature or dissipated in the helium bath, which has an impact on the cryo capacity needed. The additional heat load should not exceed a few Watts per cavity to keep the overall cryo power needs within reasonable limits.

First, some basic formulae for the power dissipation are introduced in the next section. Then, the HOM power dissipation per cavity is calculated with an analytical model and benchmarked against data obtained from beam dynamics simulations. Finally, various SPL operating conditions and their influence on the HOM power are analysed.

9.1 Power Dissipation - Analytic Model

The actual power dissipated by mode n in the cavity walls can be directly calculated from the voltage present in the cavity at time t

$$P_{\mathrm{c},n}(t) = \frac{|V_n(t)|^2}{R_{\mathrm{a},n}(\beta)} = \frac{|V_n(t)|^2}{(R/Q)_n(\beta)Q_{0,n}}. \tag{9.1}$$

125

In CW operation the power dissipation can be assumed to be constant after the system has reached an equilibrium state. In pulsed operation the average power dissipation can be calculated by integrating over one pulse period T_{p}

$$\langle P_{\mathrm{c},n} \rangle = \frac{1}{T_{\mathrm{p}}} \int_{t_1}^{t_1+T_{\mathrm{p}}} P_{\mathrm{c},n} dt. \tag{9.2}$$

Only a small fraction of the power is dissipated in the cavity and most of the power goes into the load, which is in general the HOM coupler. The power dissipated in a load with a coupling strength $\bar{\beta} = \frac{Q_0}{Q_{\mathrm{ex}}}$ is then

$$P_{\mathrm{ex},n}(t) = \bar{\beta} P_{\mathrm{c},n}(t) = \frac{|V_n(t)|^2}{(R/Q)_n(\beta) Q_{\mathrm{ex},n}}. \tag{9.3}$$

A worst case power dissipation in the load can be estimated using (6.8)

$$\tilde{P}_{\mathrm{ex},n} = (R/Q)_n(\beta) I_{\mathrm{b}}^2 \frac{Q_{\mathrm{L},n}^2}{Q_{\mathrm{ex},n}} \approx (R/Q)_n(\beta) I_{\mathrm{b}}^2 Q_{\mathrm{ex},n} \tag{9.4}$$

and for the cavity

$$\tilde{P}_{\mathrm{c},n} = (R/Q)_n(\beta) I_{\mathrm{b}}^2 \frac{Q_{L,n}^2}{Q_{0,n}} \approx (R/Q)_n(\beta) I_{\mathrm{b}}^2 \frac{Q_{\mathrm{ex},n}^2}{Q_{0,n}}. \tag{9.5}$$

The same can be done for a best case estimation using (6.9). The total power dissipated in HOMs is the sum over all modes since the modes are orthogonal

$$\langle P_{\mathrm{tot}} \rangle = \sum_{n}^{\infty} \langle P_{\mathrm{c},n} \rangle. \tag{9.6}$$

The voltage as well as the power are proportional to (R/Q). Hence, the voltage and power can be normalised to (R/Q), which is used in general for an (R/Q) independent analysis. For large Q_{ex} values the decay time gets longer than the gap between two pulses in case of pulsed operation. The voltage increases from pulse to pulse until a steady state is reached. In order to calculate the average HOM power dissipation correctly, the limit of infinite pulses has to be used.

All the formulae above are only valid under the assumption of a perfect beam without any variations in bunch charge and arrival time. Applying beam noise, the analytic formulae can no longer be used reliably to calculate the HOM voltage. The induced voltage has to be summed up explicitly, considering phase, energy and charge variations, even in case of a Gaussian distribution because of the non linearity of the voltage decay between the bunches and the phase deviation, which introduces also a non linearity.

9.2 Boundary Conditions of the Analytic Model

Using the analytic expressions to calculate the HOM power dissipated in the system is much more convenient than first performing beam dynamics simulations and from where the power dissipation data can be derived. In this section, conditions under which the analytic formulae can still be used without systematic errors are analysed. All simulated and calculated values for the dissipated power are the average values over one pulse period. In case of beam dynamics simulation the average value of all simulations results is used, where a single result is the average value over one pulse period.

At the fundamental machine lines a perfect beam without phase jitter is the best driver for HOMs. The effect of charge jitter can be neglected because on average the same voltage is induced by each bunch and the phase of the HOM voltage is always the same modulo 2π at the bunch arrival time. The difference in the voltage decay between the bunches is zero in first order at the investigated damping regime. Off resonance, especially at anti resonances ($f_n = \frac{2k+1}{2} f_{\mathrm{b}}, k \in \mathbb{N}$), the voltage induced by a perfect beam cancels itself out via destructive interference. This condition is not fulfilled any more, when phase and charge jitter are present.

9.2.1 Test Scenario

The HOM power dissipation is calculated using the analytical formulae (9.2),(9.3). Additionally, a semi analytic approach is used, where a Gaussian distributed charge scatter is applied. These results are compared with data obtained from end to end beam dynamics simulations of the complete SPL using SMD where HOM voltage development during a pulse of one cavity in the linac is recorded. Afterwards the average HOM power dissipation in this monitored cavity is calculated. One HOM is present per cavity in all simulations and the general simulation parameters are listed in Table 9.1. In the monitoring cavity different HOM settings are applied to study the HOM power dissipation for a HOM close to the 6$^{\text{th}}$ fundamental machine line ($2113.2\,\mathrm{MHz}$) with an (R/Q) value of $100\,\Omega$.

9.2.2 Analysis

Simulations are executed where the damping Q_{ex} and the HOM frequency is varied. A system check is done using no beam noise and monitoring the first cavity, which should give the same result as the analytic calculation. No HOM voltage is present in the cavity at simulation start. One pulse is simulated and the resulting $\langle P_{\mathrm{c},n} \rangle$ (crosses) perfectly agree with the analytic values (solid lines) as shown in Figure 9.1.

Table 9.1: Simulation input parameters for HOM power estimation.

Parameter	Unit	Value	RMS-Error
E_{Input}	[MeV]	160	0.078
ϕ_{sync}	[deg]	-15	0.4
$\langle I_{\text{b}} \rangle^{\dagger}$	[mA]	40	1%
Cavities (β_{g}=0.65/1.0)		54/192	
Design gradient $E_0 T(\beta_{\text{g}})$	[MV/m]	19.5/25	
$(R/Q)(\beta_{\text{g}})$	$[\Omega]^{\ddagger}$	290/570	
ϕ_{rf}	[deg]	-15	0.5
V_{rf}	[MV]	$E_0 T(\beta)L$	0.5%
Bunch frequency f_b	[MHz]	352.2	
Pulse length T_p	[ms]	1.00	
Pulse repetition rate	[Hz]	50	
HOM frequency f_n	[MHz]	1783/1331	1.0
$(R/Q)_{\text{max},n}$	$[\Omega]^{\ddagger}$	44/140	
$Q_{0,n}$		10^{10}	

† Average pulse current; peak current of 64 mA in case of chopping to
keep the charge per pulse constant
‡ linac definition

(a) Coupler

(b) Cavity ($Q_{0,n} = 10^{10}$)
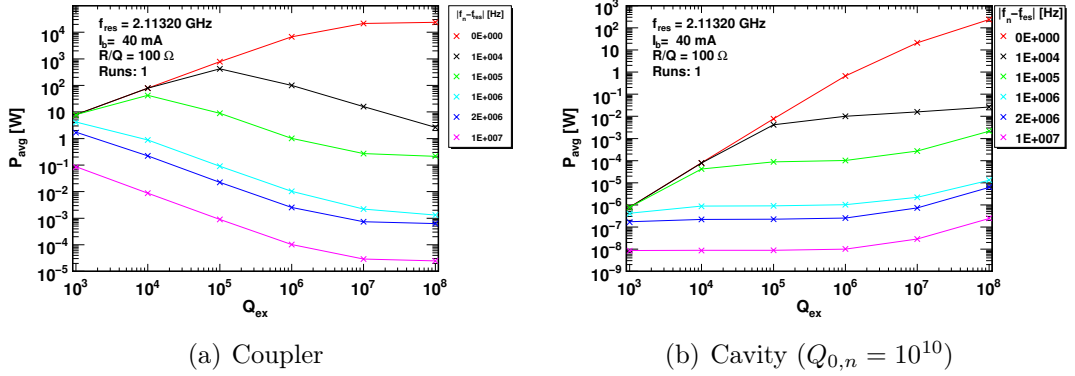
Figure 9.1:   HOM power dissipation in the HOM coupler and cavity wall for
different distances of f_n to the 6$^{\text{th}}$ fundamental machine line and different damping.
Simulated (crosses) and calculated (solid lines) values perfectly agree in the absence
of beam noise.

In a next step beam noise is added and cavity number 100 in the $\beta = 1$ section is chosen as monitoring cavity. 100 simulations with different noise patterns are executed for each damping and HOM frequency value. The power dissipation in the cavity ($Q_{0,n} = 10^{10}$) and the HOM coupler is shown in Figure 9.2, where the simulated values (cross) are directly compared with the analytic values (solid lines). Additionally, a semi analytic approach where only a Gaussian charge jitter is used is shown (circles).

(a) Coupler

(b) Cavity ($Q_{0,n} = 10^{10}$)
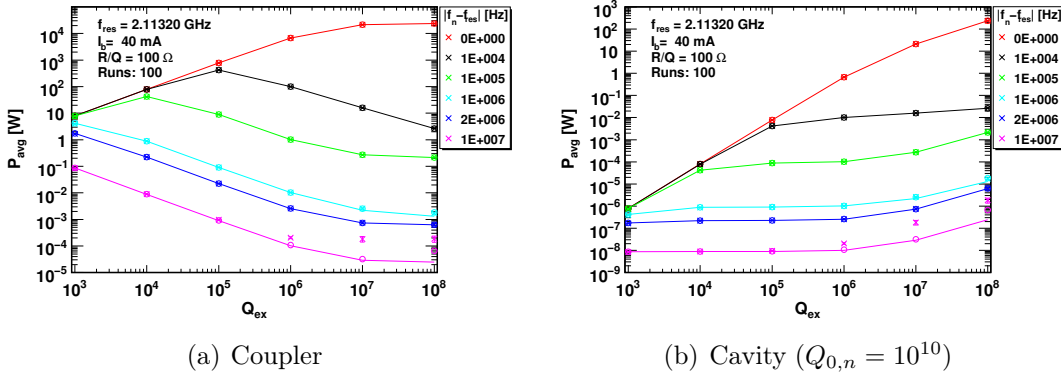
Figure 9.2: HOM power dissipation in the HOM coupler and cavity walls as function of the damping and different distances of f_n to the 6th machine line, calculated with different methods: simulation (crosses), semi analytic (circles) and analytic (line). Only at low damping ($Q_{ex} > 10^5$) and away from the machine line ($|f_n - f_{res}| \geq 10\,\text{MHz}$) a deviation between the simulated and analytic values is observed. The simulation values are averaged over 100 different pulses.

At resonance the dissipated power increases with Q_{ex} and seems to saturate at $Q_{ex} = 10^8$, which is an effect of the pulse structure. Increasing Q_{ex} further would lead to a pulse to pulse coupling and the HOM voltage does not decay completely between two pulses any more. In that regime the used simulation configuration would lead to a systematic error, because the HOM voltage increases from pulse to pulse and the assumption that at the beginning of the pulse no HOM voltage is present is not valid any more. The power dissipated in the HOM coupler exceeds $10\,\text{kW}$ beyond $Q_{ex} = 10^7$ and is more than $1\,\text{W}$ in the cavity wall. Off resonance there is a peak in the power dissipation of the HOM coupler around $Q_{ex} = 10^5$. The values in the cavities are several orders of magnitude lower.

Simulation and analytic values agree on resonance and close to the resonance. At low damping and away from the machine line the analytic values decrease further, while the simulated values seem to saturate at a level of $2 \cdot 10^{-4}\,\text{W}$. The semi analytic value follows directly the analytic value with minor deviation. Only

one charge pattern is used for the calculation. Repeating the calculation with 100 different charge patterns at $Q_{ex} = 10^8$ and $10\,\text{MHz}$ distance to the 6th fundamental machine line leads to an average value of $29 \pm 16\,\mu\text{W}$, which is slightly higher than the analytic value ($24.5\,\mu\text{W}$) but still almost one order of magnitude lower than the simulation value ($187 \pm 48\,\mu\text{W}$). The distributions for the semi analytic and simulated values are shown in Figure 9.3.


(a) Semi analytic model   (b) Beam dynamics simulation
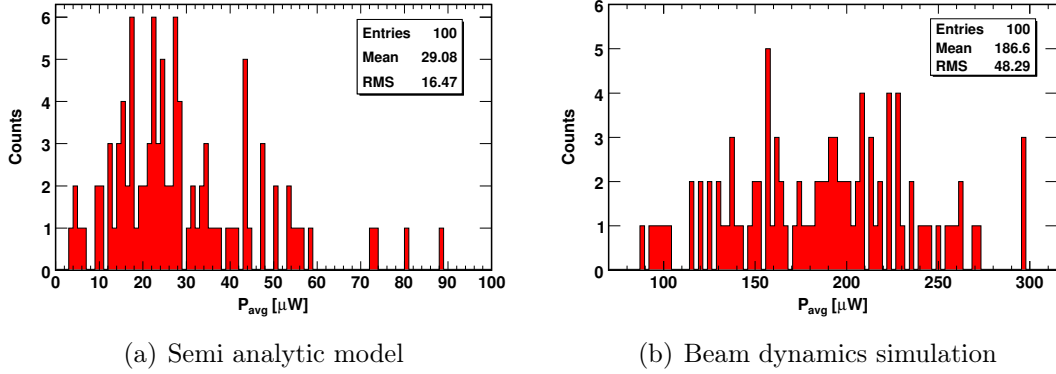
Figure 9.3: Average HOM power dissipation in the HOM coupler with the following settings: $Q_{ex} = 10^8$, $|f_n - f_{res}| = 10\,\text{MHz}$, $(R/Q) = 100$, $I_b = 40 \pm 0.4\,\text{mA}$. The semi analytic values are closer to the analytic values than to the simulated ones.

From this result one can conclude that the charge jitter is not solely responsible for the saturation of the simulation value, but that also the phase jitter has to be included. Adding also a Gaussian phase jitter to the semi analytic model leads to slightly higher values but they are still below the simulation values. Repeating the beam dynamics simulation only with phase jitter and monitoring the first cavity the values of the semi analytic model can be reproduced. This leads to the conclusion that the complete bunch to bunch phase modulation including all effects such as for example energy error, arrival time errors and impact of HOMs has to be considered for the off-resonance condition with a frequency distance of more than $1\,\text{MHz}$ to a machine line.

Further simulations in the middle of two fundamental machine lines ($f_n = 6.5 \cdot f_b$) are carried out to confirm the mismatch between simulation and analytic approach. The results are shown in Figure 9.4. Only at $Q_{ex} = 10^3$ analytic and simulated values are identical. The values decrease with increasing Q_{ex}, but the simulation values only gently decline while the analytic values drop by several orders of magnitude. However, these discrepancies are only of academic interest since they occur only off resonance where the HOM power dissipation is very low. The methods are in good agreement close to resonances where the power

dissipation is significant.
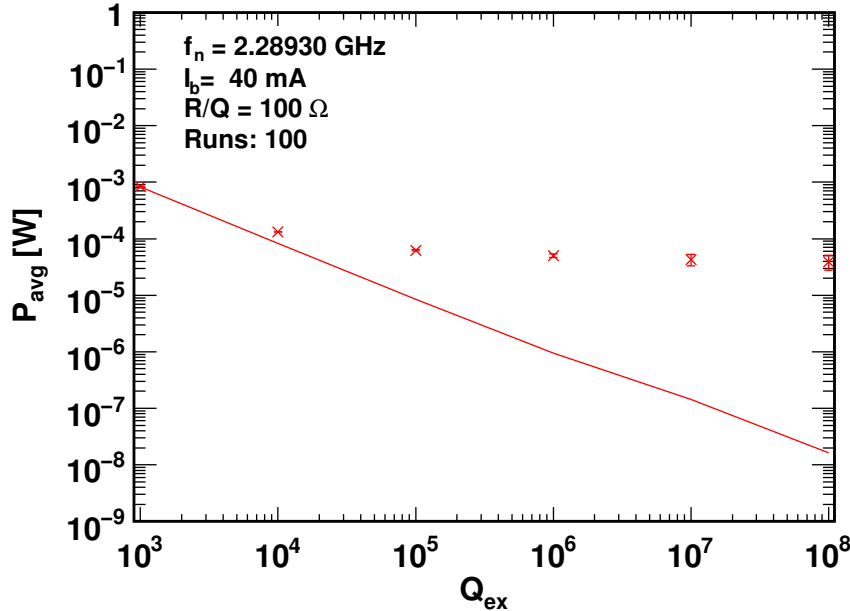
Figure 9.4: Normalised average HOM power dissipation in the HOM coupler in the middle between the 6th and 7th fundamental machine line as function of Q_{ex} for the nominal beam (40 mA) without chopping calculated analytically (solid line) and in simulations (cross).

Not only fundamental machine lines are evaluated, but also resonant lines introduced by chopping are investigated. There the same configuration as before is used, but the resonance frequency is adapted. The used chopping patterns and the distance between two resonances are listed in Table 9.2.

Table 9.2: Chopping patterns used in HOM power simulation

Pattern ($N_{\mathrm{ci}}/N_{\mathrm{cb}}$)	f_c [MHz]
5/8	44.025
50/80	4.4025
500/800	0.44025

Since the chopping resonance frequencies are closer together only frequency detuning steps are done until the same order of magnitude as the distance between

two resonances is reached. This means for the 500/800 chopping pattern the simulations are carried out until the detuning is 100 kHz. The power dissipation in the cavity and the HOM coupler for different chopping patters is shown in Figure 9.5 - 9.7.

(a) Coupler   (b) Cavity ($Q_{0,n} = 10^{10}$)
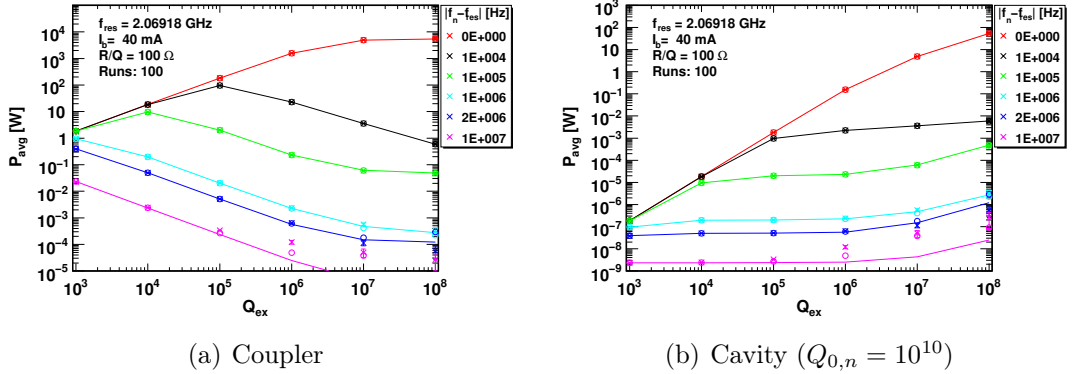
Figure 9.5: Average HOM power dissipation in the HOM coupler and cavity walls as function of the damping and different distances to a 5/8 chopping machine line is calculated in simulations (crosses) and analytically (line). Only at low damping ($Q_{\mathrm{ex}} > 10^5$) and away from the machine line a deviation between the simulated and analytic values is observed.

The same general behaviour is observed as for the fundamental machine lines but the power dissipation is much less in case of resonant lines introduced by chopping. Here also a deviation of analytic and simulated values in case of high Q_{ex} and off resonance is observed.

9.2.3   Results

Both power calculation methods introduced agree very well, as long as the distances to a resonance line is not larger than 1 MHz. Off-resonance and at high Q_{ex} the values obtained with the different methods deviate. In that regime the power dissipation is less than 1 mW and thus far below any critical value.

From this comparison one can conclude that the analytic model can be used to estimate the maximum power dissipation due to HOMs without considering beam noise. Off resonance, a threshold value of 1 mW can be used.

(a) Coupler

(b) Cavity ($Q_{0,n} = 10^{10}$)

Figure 9.6: Average HOM power dissipation in the HOM coupler and cavity walls as function of the damping and different distances to a 50/80 chopping machine line is calculated with different methods: simulation (crosses) analytic (line). Only at low damping ($Q_{ex} > 10^5$) and away from the machine line a deviation between the simulated and analytic values is observed.

(a) Coupler

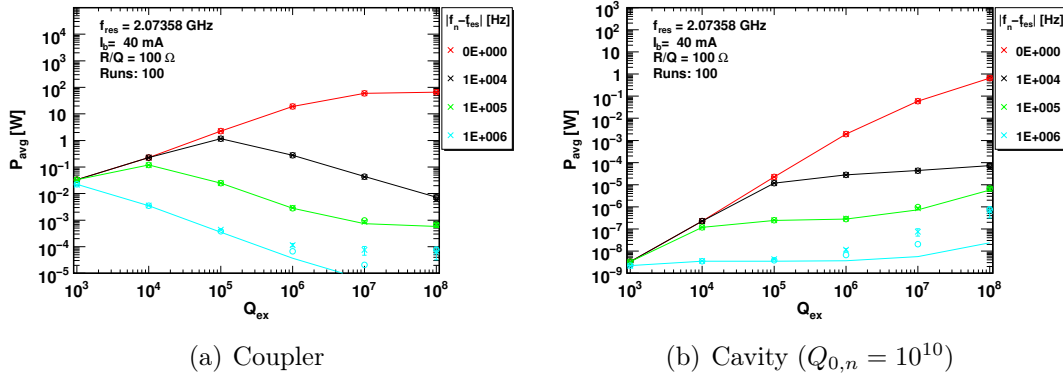(b) Cavity ($Q_{0,n} = 10^{10}$)
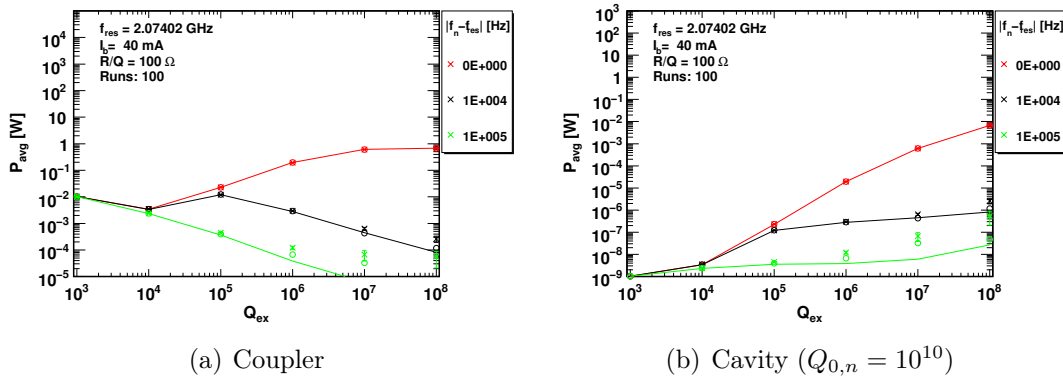
Figure 9.7: Average HOM power dissipation in the HOM coupler and cavity walls as function of the damping and different distances to a 500/800 chopping machine line is calculated with different methods: simulation (crosses) analytic (line). Only at low damping ($Q_{ex} > 10^5$) and away from the machine line a deviation between the simulated and analytic values is observed.

9.3 General Analysis

The analysis is divided in two subsections. First, the HOM power dissipation in the cavity wall is calculated and then the power extracted by the HOM coupler is analysed.

9.3.1 HOM Power Dissipation in the Cavity Walls

A fraction of the HOM power is dissipated in the cavity walls. From the results obtained in the last section, one can see directly that only in case of the fundamental machine line resonance a significant amount of power is dissipated in the cavity. In that regime the analytic model can be used for a further analysis. A $Q_{0,n} = 10^{10}$ is assumed for all HOMs. Figure 9.8 shows the normalised average equilibrium HOM power dissipation in the cavity at the 6$^{\text{th}}$ fundamental machine line as function of Q_{ex} for the nominal beam (40 mA) without chopping. There is a linear increase in the log-log scale above $Q_{\text{ex}} = 10$. The dip around $Q_{\text{ex}} = 10^7$ is due to pulsed operation. If the power dissipation should be less than 1 W, a damping in the order of $Q_{\text{ex}} = 10^6$ is needed for HOMs with (R/Q) values of $\sim 100\,\Omega$.

Including additionally a pulse sub-structure by chopping, the plot in Figure 9.8 would only change very little below $Q_{\text{ex}} = 10^4$ and above $Q_{\text{ex}} = 10^7$ and does not change the general result. Different fundamental machine lines have a minor effect on the dip area around $Q_{\text{ex}} = 10^7$, and do not influence the defined Q_{ex} limit.

9.3.2 Power Dissipation in the HOM Coupler

Only resonances are critical for the HOM power dissipation. Far from resonance the dissipated HOM power in the HOM coupler is not a concern as already illustrated in Figure 9.4. Hence, the area around the fundamental machine lines is investigated in more detail. Additionally the effect of the the chopping machine lines between the 6$^{\text{th}}$ and 7$^{\text{th}}$ fundamental machine line is analysed. The power dissipation for different Q_{ex} values is shown in Figure 9.9 - 9.11.

Without chopping only a very narrow band (less than 1 MHz) around the fundamental machine line has to be taken into account at $Q_{\text{ex}} = 10^7$. The peak value is more than $100\,\text{W}/\Omega$ but decreases fast down to less than $100\,\text{mW}/\Omega$. Decreasing Q_{ex} leads to a broadening of the resonance but also to a decrease of the peak value down to $0.1\,\text{W}/\Omega$ in case of $Q_{\text{ex}} = 10^3$. At the distance of 10 MHz to the machine line the level of $1\,\text{mW}/\Omega$ is reached.

Introducing chopping causes an increase of the resonances. The peak values for the 5/8 pattern are all above $1\,\text{W}/\Omega$ at $Q_{\text{ex}} = 10^7$ and some reach almost the same value as the fundamental machine lines. The other patterns have more
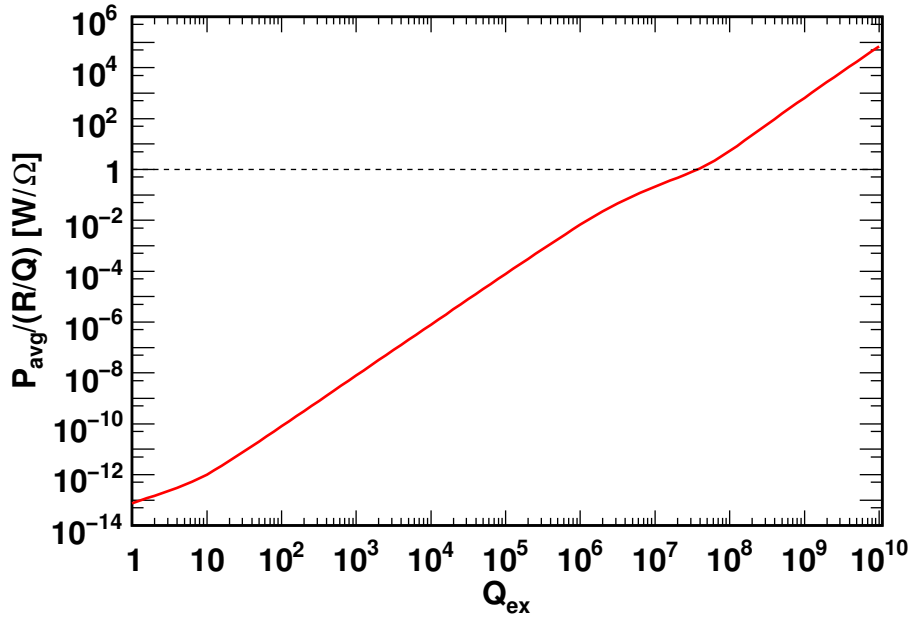
Figure 9.8: Normalised average HOM power dissipation in the cavity at the 6$^\text{th}$ fundamental machine line as function of Q_ex for the nominal beam (40 mA) without chopping and a $Q_{0,n} = 10^{10}$ of the cavity.

(a) 6$^\text{th}$ ML

(b) CML between 6$^\text{th}$ and 7$^\text{th}$ ML
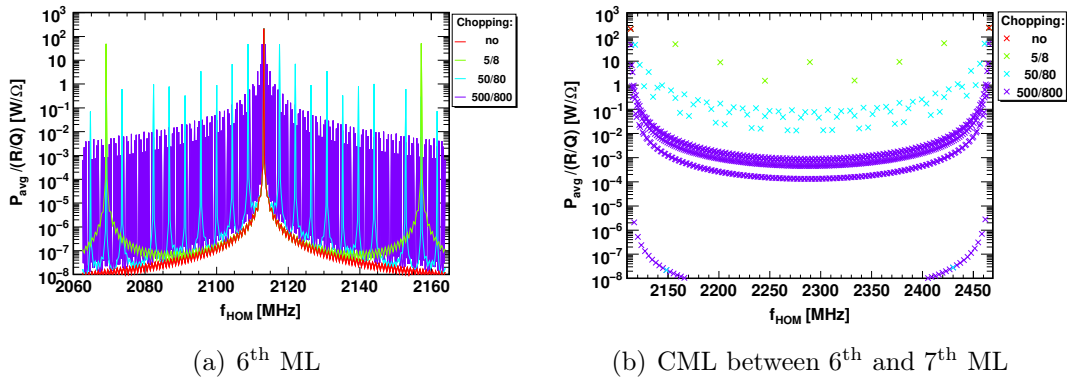
Figure 9.9: Normalised average HOM power dissipation in the HOM coupler at $Q_\text{ex} = 10^7$ for different chopping patterns and nominal beam current around the 6$^\text{th}$ fundamental machine line (a) and at resonances between 6$^\text{th}$ and 7$^\text{th}$ fundamental machine line (b).

(a) 6$^{\text{th}}$ ML
(b) CML between 6$^{\text{th}}$ and 7$^{\text{th}}$ ML
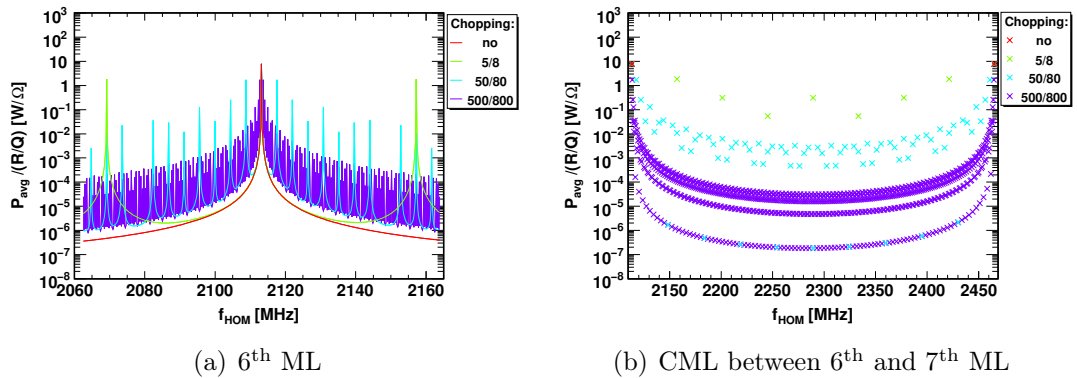
Figure 9.10: Normalised HOM power dissipation in the HOM coupler at $Q_{\text{ex}} = 10^5$ for different chopping patterns and nominal beam current around the 6$^{\text{th}}$ fundamental machine line (a) and at resonances between 6$^{\text{th}}$ and 7$^{\text{th}}$ fundamental machine line (b).

(a) 6$^{\text{th}}$ ML
(b) CML between 6$^{\text{th}}$ and 7$^{\text{th}}$ ML
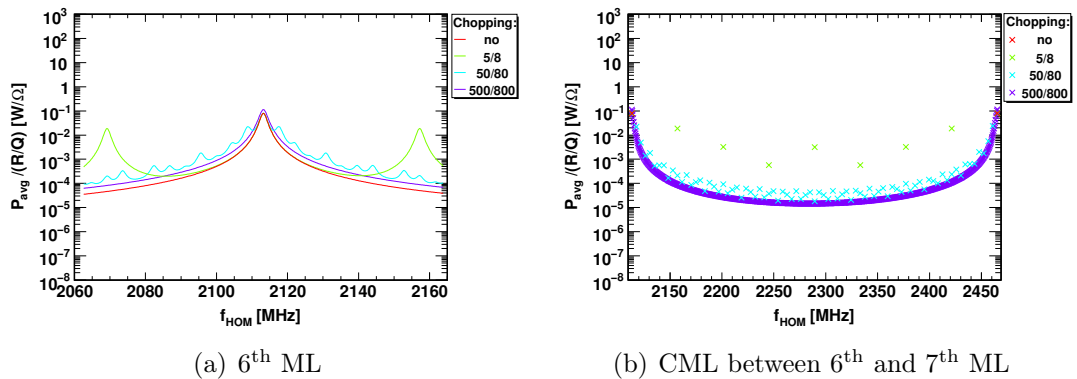
Figure 9.11: Normalised HOM power dissipation in the HOM coupler at $Q_{\text{ex}} = 10^3$ for different chopping patterns and nominal beam current around the 6$^{\text{th}}$ fundamental machine line (a) and at resonances between 6$^{\text{th}}$ and 7$^{\text{th}}$ fundamental machine line (b).

resonances but significantly lower peak values. In case of the 500/800 pattern the peak values drop fast below $0.1\,\mathrm{W}/\Omega$ with increasing distance to the fundamental machine line. The chopping resonances are very sharp. A detuning of a few kHz is sufficient to drop the power by several orders of magnitude.

Decreasing the Q_{ex} to 10^3 leads to a significant decrease in the dissipated HOM power. For the 50/80 and 500/800 pattern dissipated power is below $1\,\mathrm{mW}/\Omega$, only the 5/8 pattern shows higher peak values. The drawback of this is the broadening of the resonance.

9.4 Discussion

Detuning the HOM frequency from the resonance showed a peak in the power dissipation around $Q_{\mathrm{ex}} = 10^5$, which is the recommended damping value from the beam dynamics studies done in this thesis. Increasing the Q_{ex} leads to HOM power drop in the off resonant case, but an increase on resonance. Detuning of HOMs away from machine lines is possible in principal [124], but not suitable for the large number of resonances to deal with in case of the SPL. At moderate damping $Q_{\mathrm{ex}} = 10^7$ the dissipated HOM power at a chopping resonance line can easily exceed $10\,\mathrm{W}/\Omega$. This is an enormous load for the cryogenic system, if the power is dissipated at $2\,\mathrm{K}$. This damping is expected when using slightly lossy material between cavities as the only HOM damping mechanism. Instead, a dedicated HOM coupler can reduce the Q_{ex} further and decreases the dissipated HOM power on resonance. On the other hand it increases the width of the resonance and the power dissipation close to a resonance. Nevertheless, this situation is preferable, because it enables the operation with HOMs at chopping machine lines and does not limit the operation to low frequency chopping patterns. In the situation without any chopping, a higher Q_{ex} is preferable as already discussed in [125] to reduce the overall power dissipation and have no complicated HOM coupler design, which can also cause problems. There HOMs at fundamental machine lines have to be expelled from machine lines in the cavity design stage.

9.5 Conclusion

It is shown that analytic calculations without beam noise can be used to estimate the HOM power dissipation close to resonances, which are the areas of interest. A strong damping below $Q_{\mathrm{ex}} = 10^5$ is recommended to limit the HOM power dissipation to the Watt level and to enable operation with arbitrary chopping patterns.

Chapter 10

A Case Study for the European Spallation Source - HOM Issues in 704 MHz and 1.3 GHz Cavities

In the current design stage of the *European Spallation Source (ESS)* linac [17, 126, 127] the question was raised, why not to choose 1.3 GHz as operation frequency for the main linac to profit from developments for the *International Linear Collider* (ILC) [8]. This question with similar frequencies is discussed in [29] for the SPL, but there no dedicated beam dynamics simulations with HOMs are included. Hence, in this chapter the influence of HOMs in cavities, operating at 704.4 MHz and 1.3 GHz, is compared using SMD.

Therefore a set of two cavities was designed for both frequencies [128] and one basic linac layout for each frequency [119]. First, the two linac layout options and the used cavity designs are introduced. Then, different beam dynamics scenarios are studied, where the effect of monopole modes is investigated in detail.

10.1 ESS Linac Layout Options

The two linac layout options [119, 127], illustrated in Figure 10.1, are compared against each other. In both cases a normal conducting front end is used up to 50 MeV followed by a section of SRF spoke cavities. Afterwards two families of SRF elliptical cavities accelerate the beam up to an energy of 2.5 GeV. All relevant layout parameters are summarised in Table 10.1. The main difference between the two options is the operation frequency in the elliptical cavities and the number of cells per cavity, which are in the focus of this chapter. HOM effects are only studied in the SRF elliptical cavity sections between 380 MeV and 2.5 GeV. The starting energy is set to 380 MeV which is the injection energy of the SRF elliptical

cavity sections of the 1.3 GHz option for comparison reasons.

(a) 704 MHz linac

(b) 1.3 GHz linac
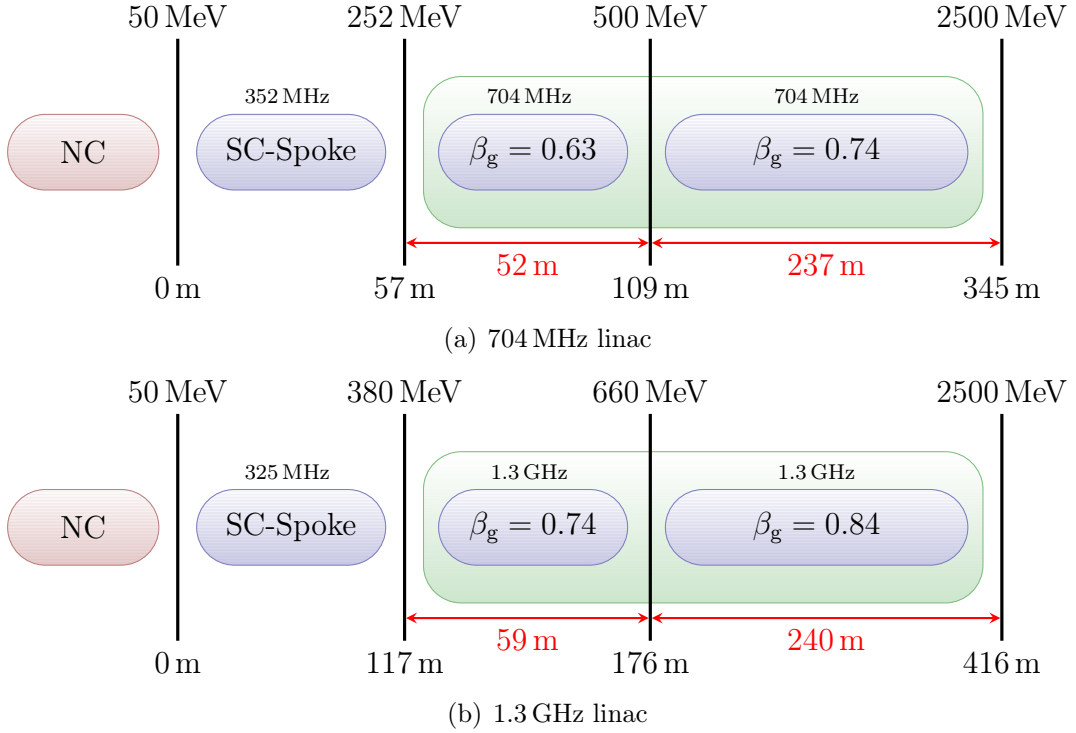
Figure 10.1: Schematic layout of the ESS linac options used in this study. The 1.3 GHz option is about 70 m longer, due to the smaller energy acceptance range of its nine cell cavities. This is compensated by a longer SRF Spoke cavity section.

Table 10.1: Section parameters of the studied linac options.

Option	Section	β_g	cells	f [MHz]	E_in [MeV]	length [m]	cavities
704 MHz	Spoke			352.2	50	57	42
	Medium β	0.63	5	704.4	225	52	36
	High β	0.74	5	704.4	500	237	168
1.3 GHz	Spoke			325	50	117	81
	Medium β	0.74	9	1300	380	59	40
	High β	0.84	9	1300	660	240	160

In Figure 10.2 the effective accelerating voltage V_acc (3.47) and synchronous phase ϕ_s in all superconducting structures are shown. The power per cavity is limited to 0.9 MW, which leads to a maximum effective accelerating voltage of

about 12 MV at a beam current of 75 mA. ϕ_s is reduced for longitudinal beam matching after the SRF Spoke cavity section due to the frequency jump. In the 1.3 GHz option this is very important because the natural bucket size decreases by a factor of four in phase due to the four time higher operation frequency.

(a) Effective accelerating voltage (b) Synchronous phase
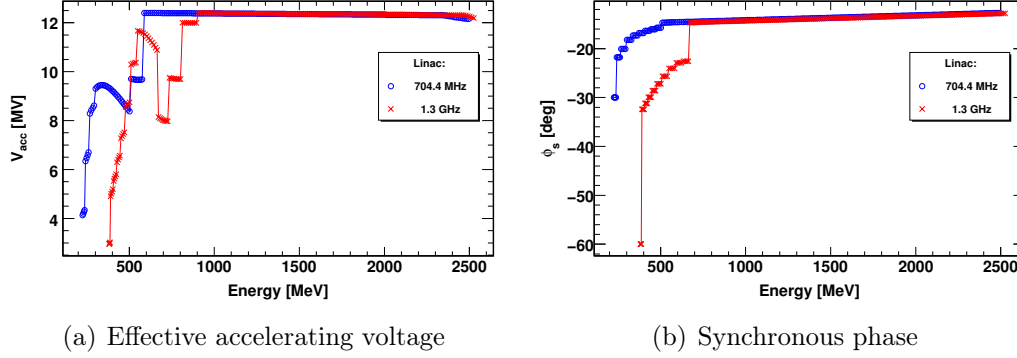
Figure 10.2: Effective accelerating voltage (a) and synchronous phase (b) along the linac with a power limitation of 0.9 MW per cavity for both options. The phase is reduced at the frequency jump to longitudinally match the beam.

10.2 Elliptical Cavities

The SRF elliptical cavities were designed by R. Calaga (BNL) [58, 128] and analysed with SUPERFISH. Some of the cavity parameters are listed in Table 10.2 and the monopole spectrum is shown in Figure 10.3. In all cavities there are 3 frequency bands of interest, each containing 5 or 9 modes (TM_{010}, TM_{011}, TM_{020}), respectively below the beam pipe cutoff frequency which is a function of the beam pipe radius. All HOMs are far away from machine lines and resonant excitation should not be an issue as long as no pulse substructure is introduced. In case of the 1.3 GHz cavities, there are more modes with high (> 1) $(R/Q)(\beta)$ values and the values itself are, as expected from the frequency scaling, about a factor two higher than in the 704 MHz cavities.

Table 10.2: Cavity parameters

	704.4 MHz		1.3 GHz	
β_{g}	0.63	0.74	0.74	0.84
Cells	5	5	9	9
L (l_{active}) [m]	0.99 (0.67)	1.11 (0.79)	1.09 (0.77)	1.19 (0.87)
R_{iris} [cm]	5.5	6.2	3.5	3.5
$(R/Q)(\beta_{\mathrm{g}})$ [Ω][†]	238	307	513	715
$E_0 T(\beta_{\mathrm{g}})$ [MV/m]	14	20	15	21
f_{cutoff} [GHz]	2.09	1.85	3.28	3.28

[†] linac definition
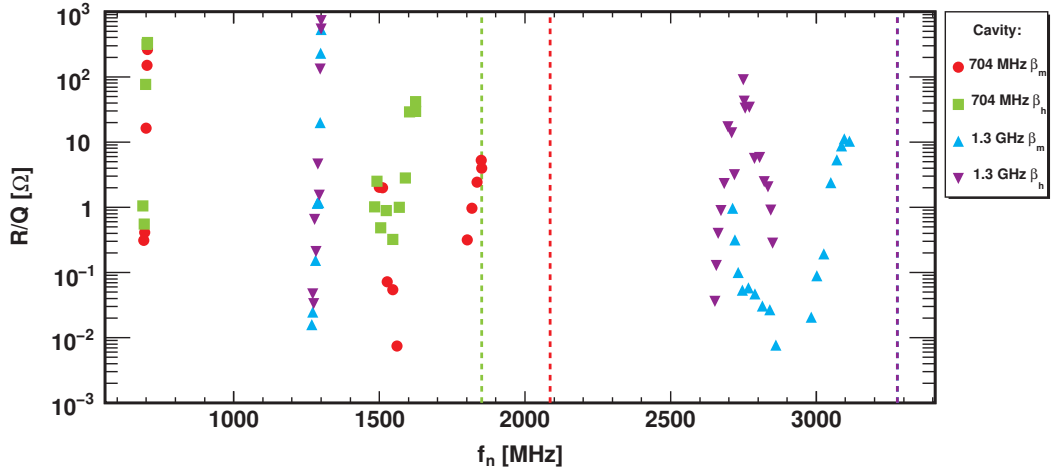
Figure 10.3: Monopole spectrum and maximum $(R/Q)(\beta)$ value in the used energy range for all four cavities. The beam pipe cutoff frequencies are marked with dashed lines and are the same for both 1.3 GHz cavities, due to the same beam pipe radius.

Increasing the frequency leads to a decrease in cavity cell length. In order to keep the ratio between the effective acceleration length and the total length small, the number of cells has to be increased. In general $(R/Q)/L$ scales linear with the frequency. Thus a higher frequency and number of cells lead to a higher acceleration efficiency at the cavity geometrical beta β_{g}. The drawback is that the transit time factor $T(\beta)$ drops faster for a higher number of cells, if the particle β differs from the geometrical β and so also $(R/Q)(\beta)$ drops. This significantly reduces the energy range where the cavity efficiently accelerates the beam. This is illustrated in Figure 10.4, where $(R/Q)(\beta)$ dependency of the $\beta_{\mathrm{g}} = 0.75$ cavities is

shown. The used velocity range, indicated by the vertical dashed lines, is smaller in the 1.3 GHz cavity. Also the number of HOMs and their $(R/Q)(\beta)$ values increases with the number of cells, which is clearly shown in Figure 10.3, where $(R/Q)(\beta)_{\mathrm{max}}$ values of the HOMs in the 1.3 GHz cavities are at least a factor two higher than in the 704.4 MHz cavities. The $(R/Q)(\beta)$ of $\mathrm{TM}_{010}, 4/5\pi$ mode in the 704.4 MHz cavity and the $\mathrm{TM}_{010}, 8/9\pi$ mode in the 1.3 GHz cavity have a pole at the β_{g} and rise fast for higher and lower β values and even exceed the $(R/Q)(\beta)$ values of the accelerating mode for certain β values. In the nine cell cavity the $(R/Q)(\beta)$ of the $\mathrm{TM}_{010}, 8/9\pi$ mode rises faster than the $\mathrm{TM}_{010}, 4/5\pi$ mode in the five cell cavity. In general at β_{g} all non TM_{010}, π modes have a very low $(R/Q)(\beta)$ compared to the accelerating mode, hence these modes are less critical in electron machines, where the electrons always travels with β_{g}. Further frequency scaling laws, also in the context of HOMs are discussed in [29].

Looking at the $(R/Q)(\beta)$-map of the modes with the highest (R/Q) values in all cavities within their energy range (see Figure 10.5 and Figure 10.6) one observes that in both high β cavities the fundamental passband mode next to the accelerating mode has a higher (R/Q) value than the accelerating mode towards the end of the linac. Hence, it has a high potential to drive instabilities and beam losses. A special focus is set to this mode in the beam dynamics study. All other modes have at least a factor of two smaller $(R/Q)(\beta)$ values.

10.3 Beam Dynamics Simulations

In order to directly compare both linac options all simulations start at 380 MeV and go up to 2.5 GeV. All relevant beam parameters are listed in Table 10.3. The injection noise is extrapolated from Linac 4 [34, 117]. The two times higher injection phase jitter in the 1.3 GHz option is caused by the higher operation frequency and the 2 times higher frequency jump at the beginning of the SRF elliptical cavity section. It is assumed that the front-end delivers the same beam quality in both options.

10.3.1 Reference Simulations Without HOMs

Before looking at the impact of HOMs, simulations without HOMs are carried out in order to check the beam noise parameters at injection. The resulting phase space distributions of the nominal injection beam jitter, which will be used for comparison in the following HOM simulations, is shown in Figure 10.7, where the phase error in the 1.3 GHz linac is normalised to the unit of the 704 MHz linac. No filamentation is observed at the end of both linacs. The phase spread is less in the 1.3 GHz linac due to the higher operation frequency.
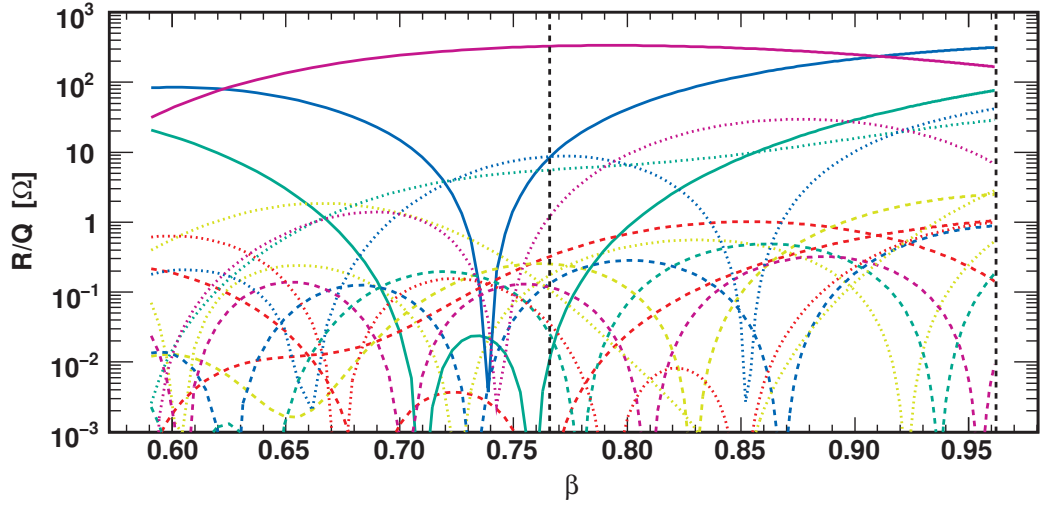
(a) $(R/Q)(\beta)$-map 704.4 MHz $\beta_{\mathrm{g}=0.74}$ cavity
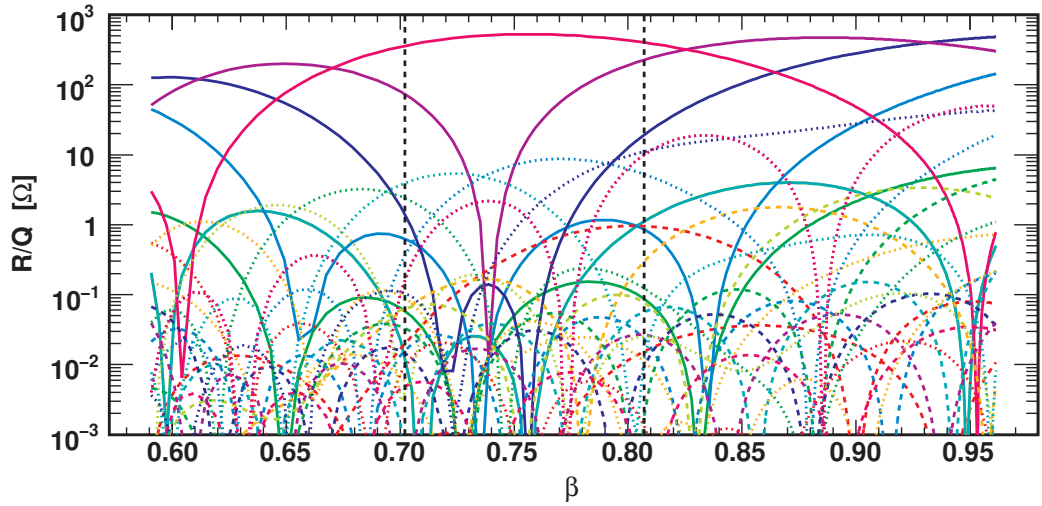
(b) $(R/Q)(\beta)$-map 1.3 GHz $\beta_{\mathrm{g}=0.74}$ cavity

Figure 10.4: $(R/Q)(\beta)$-maps of the first 3 monopole bands in both $\beta_{\mathrm{g}} = 0.74$ cavities.   The solid curves are the TM_{010} modes.   The dashed and doted curves are the TM_{011} and TM_{020} modes.   The vertical dashed lines mark the beta range where the cavity is used.   There are more modes in the 9 cell 1.3 GHz cavity and the maximum $(R/Q)(\beta)$ of the TM_{010}, π mode (purple) is higher, but drops faster beside the β_{g} as in the 5 cell 704.4 MHz cavity (violet) with the same β_{g}. Hence, the beta range in which the 704.4 MHz cavity can be used efficiently is much larger.

(a) 704.4 MHz $\beta_{\mathrm{g}=0.63}$ cavity

(b) 704.4 MHz $\beta_{\mathrm{g}=0.74}$ cavity
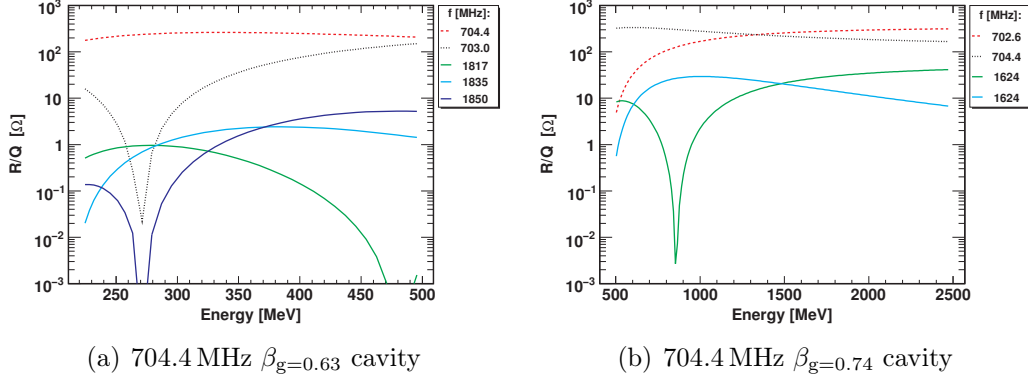
Figure 10.5: $(R/Q)(\beta)$-map of the monopole modes in the used energy range in both 704.4 MHz cavities, which are used in the beam dynamics simulations. The $TM_{010,4/5\pi}$-mode (red, dashed) overshoots the accelerating mode (black, dotted) above 1.5 GeV. Several HOMs (solid lines) are used in the simulations, where the HOM with the highest $(R/Q)(\beta)$ is present in each cavity along the linac.

(a) 1.3 GHz $\beta_{\mathrm{g}=0.74}$ cavity

(b) 1.3 GHz $\beta_{\mathrm{g}=0.84}$ cavity
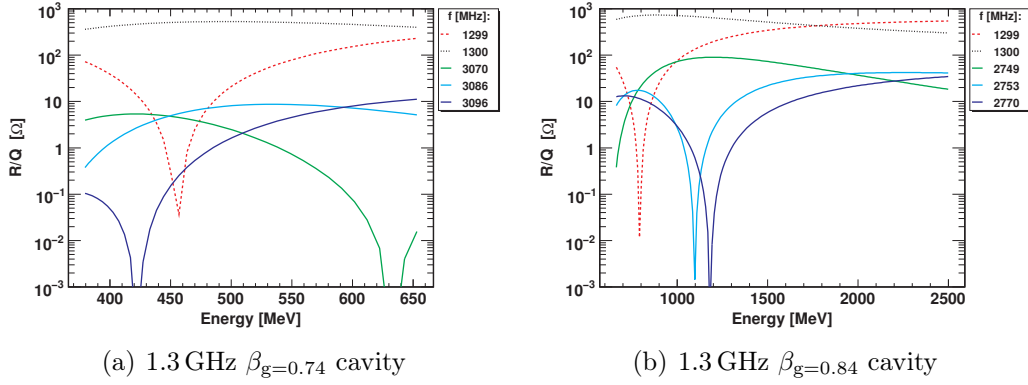
Figure 10.6: $(R/Q)(\beta)$-map of the monopole modes in the used energy range in both 1.3 GHz cavities, which are used in the beam dynamics simulations. The $TM_{010,8/9\pi}$-mode (red, dashed) overshoots the accelerating mode (black, dotted) above 1.75 GeV. Several HOMs (solid lines) are used in the simulations, where the HOM with the highest $(R/Q)(\beta)$ is present in each cavity along the linac.

Table 10.3: Simulation parameters used in the the beam dynamics simulations. Errors are estimated from Linac 4 simulation data.

Parameter	Unit	704.4 MHz		1.3 GHz	
		Mean	Variance	Mean	Variance
Bunch frequency	[MHz]	352.2		325	
Pulse length	[ms]	$\sim 2^{\dagger}$		$\sim 2^{\dagger}$	
Period length	[ms]	50		50	
Beam current	[mA]	50...400	1%	50...400	1%
Injection energy	[MeV]	380	0.2	380	0.2
Injection phase	[deg]‡	-16	0.2	-60	0.4

† 700,000 bunches

‡ at the operation frequency

(a) 704 MHz linac
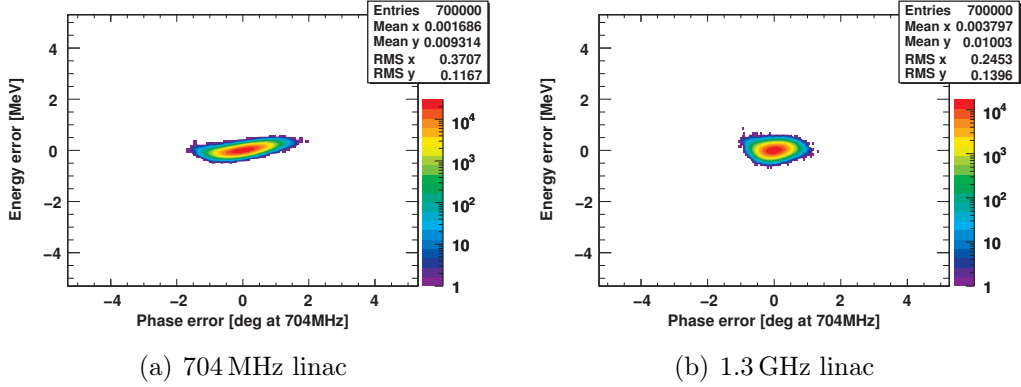
(b) 1.3 GHz linac

Figure 10.7: Phase space distribution of one pulse at the end of both linacs with the nominal injection energy and phase jitter. In the 1.3 GHz linac the phase error is normalised to 704 MHz for comparison reasons. The phase error is smaller in the 1.3 GHz linac due to the higher operation frequency.

Increasing the injection energy and phase jitter by a factor of two leads to a phase space increase as shown in Figure 10.8, where a starting filamentation is observed in both linac options. The resulting output energy and phase errors are as expected about twice the values of the simulation with nominal injection jitter.

As a measure of the influence of various effects such as injection noise, RF errors or HOMs the effective phase space area of a pulse is calculated by (8.2) and compared to the nominal simulation. The phase space area increases by a factor 4.65 in the 704 MHz linac and 4.27 in the 1.3 GHz linac in the simulations with

(a) 704 MHz linac
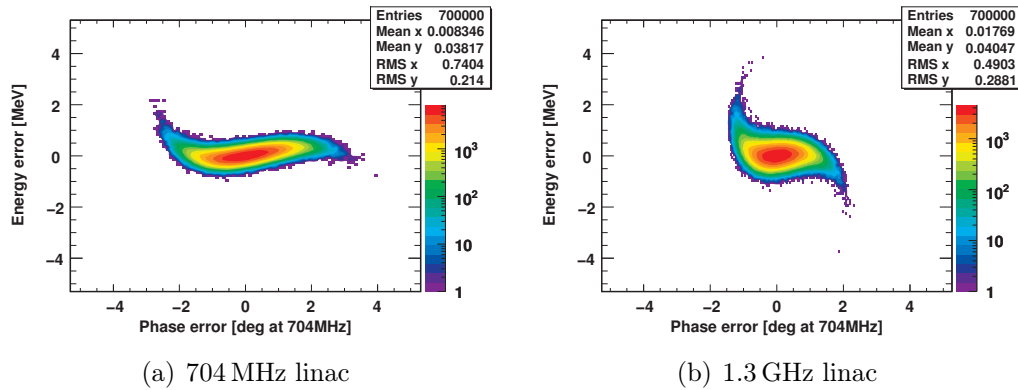
(b) 1.3 GHz linac

Figure 10.8: Phase space distribution of one pulse at the end of both linacs with a two times higher injection energy and phase jitter. In the 1.3 GHz linac the phase error is normalised to 704 MHz for comparison reasons. The phase space distribution shows a starting filamentation.

increased injection noise.

The effect of RF-errors originating from the RF system is analysed for both linacs assuming an error of $0.5\,°$ in phase and $0.5\,\%$ in amplitude. Both errors have a uniform distribution along the linac. The phase space distribution resulting from 1,000 different errors is shown in Figure 10.9. An increase in the occupied phase space area is observed due to the RF errors. The energy error is about the same in both options, while the phase error is almost twice as large in the 704 MHz linac compared to the 1.3 GHz linac. As a consequence the calculated phase space area is roughly five times higher in the 704 MHz linac but only three times higher in the 1.3 GHz linac. The impact of RF errors seems to be less significant in the 1.3 GHz linac.

The effect of RF errors will be compared later to the effect of HOMs to judge their impact on the beam. The phase space increase due to RF errors can be used as upper tolerable limit for the phase space increase caused by HOMs.

10.3.2   HOMs With High $(R/Q)(\beta)$ Values

The HOM with the highest $(R/Q)(\beta)$ value is chosen individually in each cavity for the corresponding β, see Table 10.4. A HOM frequency spread of 1 MHz in the 704 MHz option and 2 MHz in the 1.3 GHz option is used. In order to avoid pulse to pulse coupling the HOM damping in terms of Q_{ex} is set to 10^8 in all cavities for both options. The beam current is varied between the nominal 50 mA and 400 mA to explore the safety margin.

First, it is validated that at $Q_{\mathrm{ex}} = 10^8$ no pulse to pulse coupling occurs by

(a) 704 MHz linac
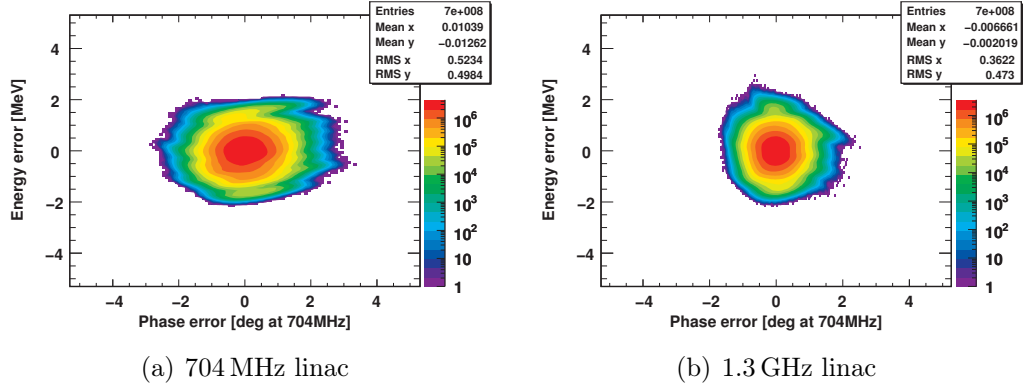
(b) 1.3 GHz linac

Figure 10.9: Phase space distribution of one pulse at the end of 1,000 linacs with an uniformly distributed RF-error (0.5% in amplitude and 0.5° in phase) for both options. In the 1.3 GHz linac the phase error is normalised to 704 MHz for comparison reasons. An increase in phase space, especially in the energy error, is observed in both options.

Table 10.4: HOMs used in the simulations. The $(R/Q)(\beta)$ map of the modes is shown in Fig. 10.5 and Fig. 10.6.

Section	704 MHz			1.3 GHz		
	f_n [MHz]	σ_{f_n} [MHz]	$(R/Q)(\beta)_{\max}$ $[\Omega]^\dagger$	f_n [MHz]	σ_{f_n} [MHz]	$(R/Q)(\beta)_{\max}$ $[\Omega]^\dagger$
Medium β	1817.37	1	0.964124	3070.12	2	5.38
	1835.18	1	2.4	3085.97	2	8.7
	1849.61	1	5.2	3096.47	2	11.1
High β	1623.77	1	36.1	2749.17	2	90.1
	1623.84	1	30.3	2752.79	2	42.1
				2769.63	2	34.5

† linac definition

simulating 100 consecutive pulses with a beam current of 400 mA. In Figure 10.10 the maximum observed cavity HOM voltage in the linac is plotted at the end of each pulse for both options. It shows a completely random distribution and no correlation between pulses is observed. The induced voltages in the 1.3 GHz case are significantly higher than for the 704 MHz case. At weaker damping (higher Q_{ex}) an increase of cavity HOM voltage over the pulses is observed due to pulse to pulse coupling.

(a) 704 MHz linac

(b) 1.3 GHz linac
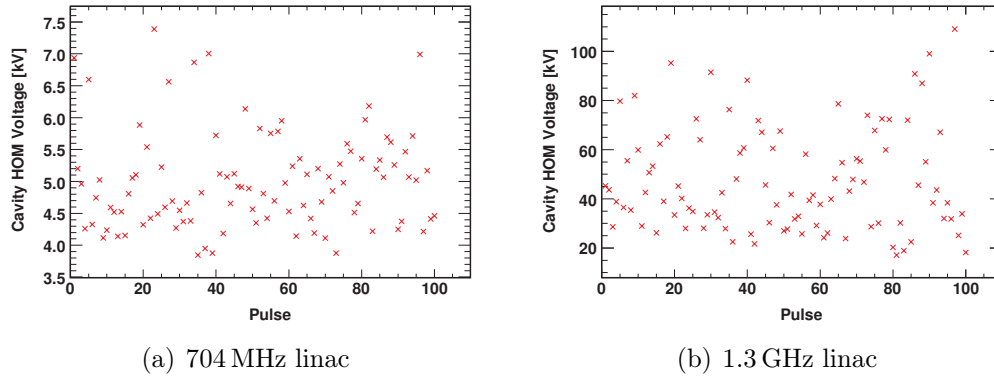
Figure 10.10: Maximum HOM voltage in the linac after each pulse for 100 consecutive pulses at 400 mA, with $Q_{ex} = 10^8$ and for the HOMs listed in Tab 10.4. No systematic pattern is observable in both linacs. The voltage in the 1.3 GHz option is significantly higher.

Based on this result, only one pulse is simulated with no HOM voltage present in each cavity at the start of the simulation. 100 different error sets for the HOM frequency distribution along the linac are simulated for different beam currents. The average HOM voltage, present at the end of the pulse in each cavity is shown in Figure 10.11 for both linacs. In addition, the maximum observed HOM voltages are plotted for 400 mA.

The HOM voltage scales linear with the beam current and the variations along the linac are due to the $(R/Q)(\beta)$ change. In the 1.3 GHz option the voltages are on average about one order of magnitude higher than in the 704 MHz option and the observed peak voltages at 400 mA overshoot 100 kV, while in the 704 MHz linac the maximum is about 10 kV. This result can be explained by the higher HOM frequencies and $(R/Q)(\beta)$ values in the 1.3 GHz linac. Both lead to a higher induced HOM voltage by each bunch. At nominal current the HOM voltage is at a very moderate level in both options and causes no significant growth in the energy and phase spread at the end of the linac compared to RF-errors.

In Table 10.5 the average change in energy and phase error as well as the phase

(a) 704 MHz linac   (b) 1.3 GHz linac
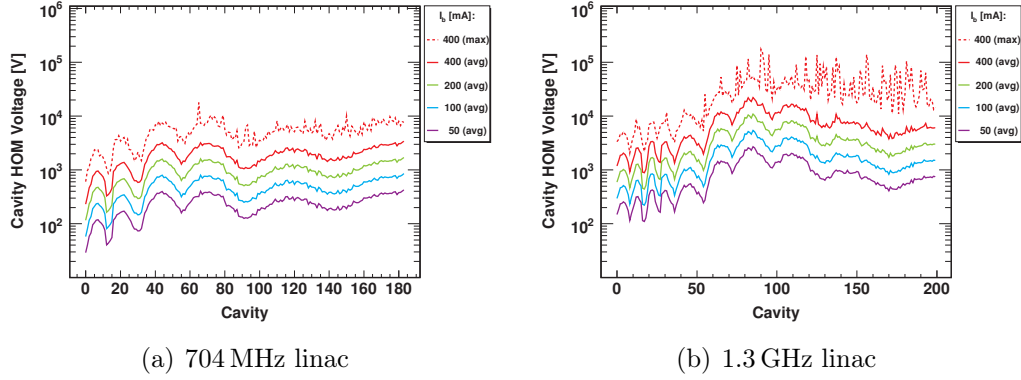
Figure 10.11: Average and maximum HOM voltage after one pulse for 100 linacs (different HOM frequency patterns) and different beam currents where one HOM per cavity is present. The maximum observed HOM voltage at 400 mA is about 10 kV in the 704 MHz linac and exceeds 100 kV in some cavities in the 1.3 GHz linac.

space increase, caused by HOMs, is shown. Additionally, the data from initial simulations without HOMs are added for better comparison. Even at 400 mA the influence of HOMs in both options is small compared to the impact of RF errors. Comparing the two linacs one finds that at 400 mA the influence of HOMs is higher in the 1.3 GHz linac.

In the next scenario, the same HOM configuration as before is used and a sweep of the HOM damping (Q_{ex}) is done for different beam currents. Two pulses are simulated and the phase space area increase of the second pulse is compared with the case where no HOMs are present (Figure 10.7). The results for both linacs are shown in Figure 10.12. Here, only one HOM frequency pattern is simulated to get a qualitative overview, where operational boundaries are located. Further simulations with different HOM frequency pattern should be carried out to quantify these results. At 400 mA, the HOM influence starts to rise above $Q_{ex} = 10^6$ and reaches a plateau around $Q_{ex} = 10^8$. If Q_{ex} increases further, a steep increase in phase space area is observed due to pulse to pulse coupling. The plateau is shifted to a higher Q_{ex} in the 1.3 GHz linac because of the shorter decay time T_d at higher frequencies ($T_d \propto 1/\omega_n$). In general, the phase space increase is about a factor of ten higher in the 1.3 GHz linac as in the 704 MHz linac, caused by the higher HOM voltages and shorter fill time ($\propto \omega_n$). At nominal current no influence is observed below $Q_{ex} = 10^8$ in both linacs.

Table 10.5: Average energy and phase error deviation as well as the phase space increase at the end of the linacs for injection beam jitter, RF-errors and HOMs.

	704 MHz			1.3 GHz		
	σ_{E} [MeV]	σ_ϕ [deg]†	$\epsilon/\epsilon_{\mathrm{Norm}}$	σ_{E} [MeV]	σ_ϕ [deg]†	$\epsilon/\epsilon_{\mathrm{Norm}}$
nominal	0.113	0.370	1	0.137	0.245	1
more inj. jitter[2]	0.214	0.740	4.65	0.288	0.490	4.27
RF errors[3]	0.498	0.523	4.76	0.473	0.362	3.18
HOM[4] 50 mA	0.113	0.415	1.0003	0.137	0.245	1.002
HOM[4] 400 mA	0.114	0.370	1.02	0.155	0.247	1.15

† degree at 704 MHz; all values are normalised to this unit

[1] Reference simulation with nominal injection noise, see Fig. 10.7.

[2] doubled injection energy jitter and doubled injection phase jitter in the 704 MHz linac, see Fig. 10.8..

[3] Average of 1,000 simulations, see Fig. 10.9.

[4] Average of 100 simulations, $Q_{\mathrm{ex}} = 10^8$, see Tab. 10.4.
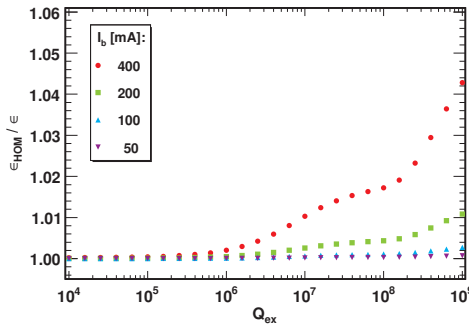
(a) 704 MHz linac
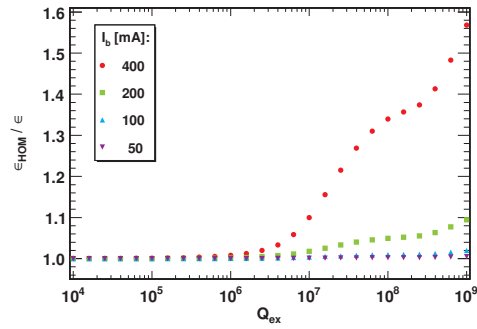
(b) 1.3 GHz linac

Figure 10.12: Phase space area increase of a pulse in both linacs under the influence of HOMs for different beam currents and damping values. At nominal current no effect is observed below $Q_{\mathrm{ex}} = 10^8$. Different scales for the y-axis are used, because the phase space increase is about one order of magnitude higher in the 1.3 GHz linac due to the higher HOM voltages, as illustrated in Fig. 10.11.

10.3.3   Machine Lines

The HOM frequencies found by SUPERFISH are all far from machine lines. However, the effect of a HOM with a moderate (R/Q) value $(1\,\Omega)$ falls in one cavity on a machine line is analysed. The 5th fundamental machine line $(1.761\,\text{GHz})$ is used for the $704\,\text{MHz}$ linac and the 9th $(2.925\,\text{GHz})$ for the $1.3\,\text{GHz}$. These are the machine lines, which are closest to any HOMs in the cavities. For this kind of simulation the same HOM settings as before and the nominal current are used, but one cavity is modified. In all simulations the HOM voltage in the complete linac after one pulse is shown in Figure 10.13–10.15, and the HOM voltage development during the pulse in the modified cavity is shown in Figure 10.16–10.18.

(a) $704\,\text{MHz}$ linac: 5th machine line   (b) $1.3\,\text{GHz}$ linac: 9th machine line

Figure 10.13:   HOM voltage distribution along the linacs at $50\,\text{mA}$, where a HOM with $R/Q = 1$ in cavity 100 falls direc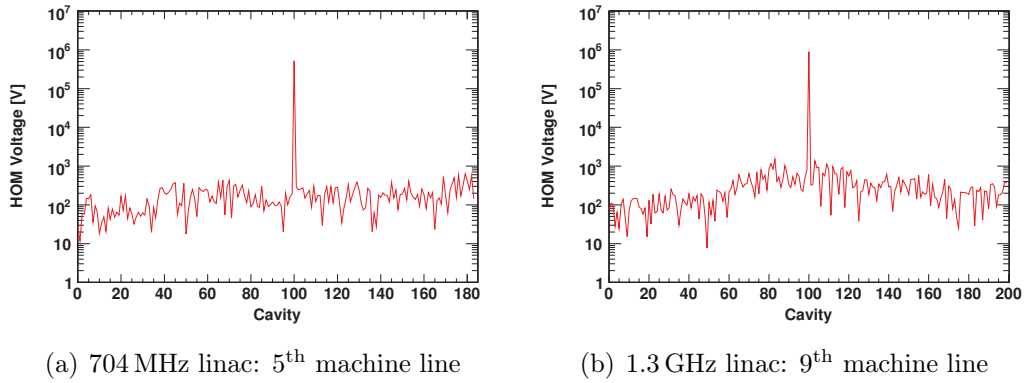t on a machine line. All HOMs are only weakly damped $(Q_{\text{ex}} = 10^8)$. The HOM voltage in the resonantly excited cavity is three orders of magnitude higher than in the other cavities.

First the HOM meets a resonance and is only weakly damped $(Q_{\text{ex}} = 10^8)$, see Figure 10.13 and Figure 10.16. The HOM voltage increases linear over the pulse, because of the weak damping and reaches almost $1\,\text{MV}$ at the end of the pulse in the $1.3\,\text{GHz}$ linac. The voltage in the $704\,\text{MHz}$ linac is only half due to the lower frequency. This high voltage disturbs the beam and causes a significant load for the cryogenic systems due to the power dissipation in the cavity walls and interconnections. The peak power dissipation (CW) in the cavity walls for $1\,\text{MV}$ would be $100\,\text{W}$ assuming $Q_0 = 10^{10}$. In the second simulation the HOM is still in resonance, but moderately damped $(Q_{\text{ex}} = 10^6)$, see Figure 10.14 and Figure 10.17. There the HOM voltage saturates at a level of $50\,\text{kV}$ in both linacs, which is not a problem from the beam dynamics point of view and also not for the cryogenic system. In the $1.3\,\text{GHz}$ linac the saturation value is reached faster due to the higher frequency. Finally the weakly damped HOM is detuned by $10\,\text{kHz}$
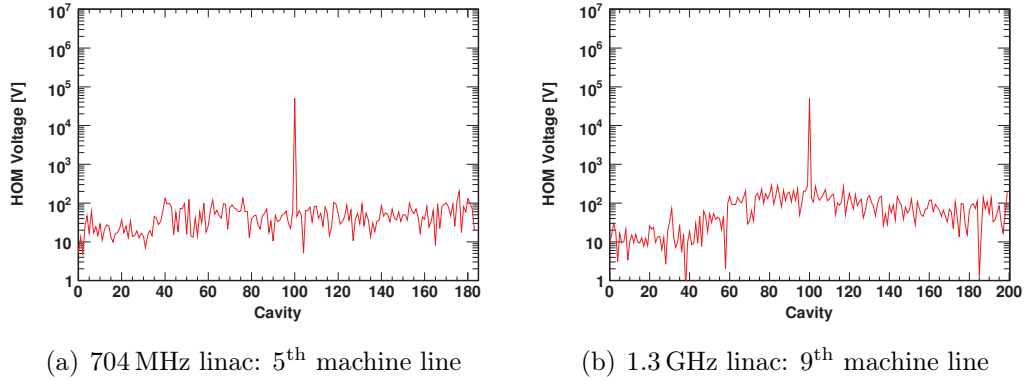
(a) 704 MHz linac: 5th machine line

(b) 1.3 GHz linac: 9th machine line

Figure 10.14: Same as Fig. 10.13, but moderate damping ($Q_{\mathrm{ex}} = 10^6$).
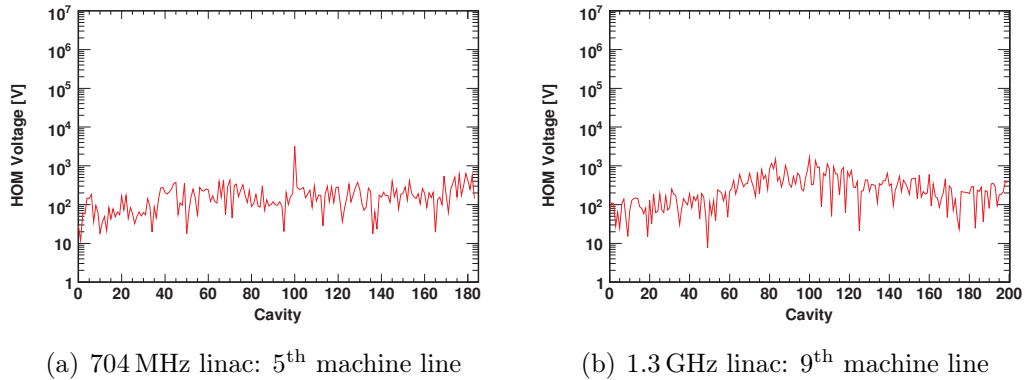
(a) 704 MHz linac: 5th machine line

(b) 1.3 GHz linac: 9th machine line

Figure 10.15: Same as Fig. 10.13, but the HOM frequency is detuned by 10 kHz in the 704 MHz cavity and 20 kHz in the 1.3 GHz cavity.

in the 704 MHz linac and by 20 kHz in the 1.3 GHz linac, see Figure 10.15(a) and Figure 10.18(a). In this case the HOM voltage oscillates with a frequency of 10 kHz or 20 kHz, which correspond to 35,200 Bunches in the 704 MHz linac and 16,250 Bunches in the 1.3 GHz linac. The maximum amplitude is about 7 kV in the 1.3 GHz linac and 9 kV in the 704 MHz linac.

Only in the case, where the HOM falls directly on a machine line and is weekly damped, a significant influence on the beam is observable. This is illustrated in Figure 10.19, where the energy error evolution of one pulse along the linacs is shown. The HOM leads to deceleration kick, which is observable as sudden increase in the energy error.

(a) 704 MHz linac: 5$^{\text{th}}$ machine line   (b) 1.3 GHz linac: 9$^{\text{th}}$ machine line
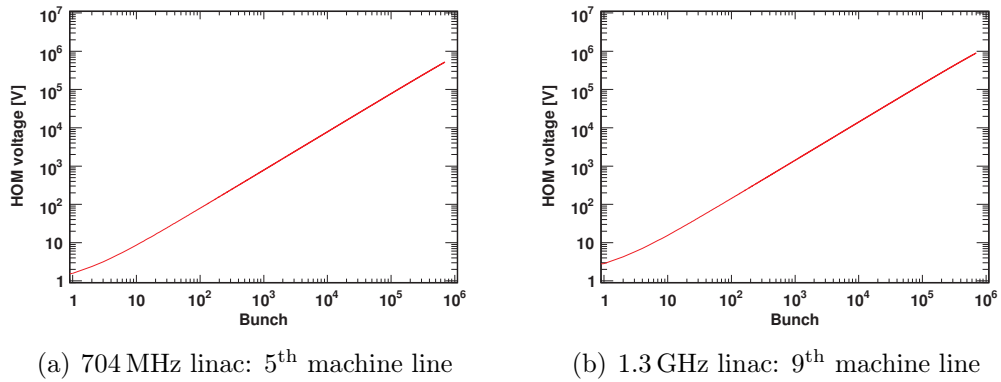
Figure 10.16:   Time development of the cavity HOM voltage during a pulse in the cavity with a HOM ($R/Q = 1$) directly at a machine line and a weak HOM damping ($Q_{\text{ex}} = 10^8$) at beam current of 50 mA. The HOM voltage rises linear in time until the end of the pulse and it increases in the 1.3 GHz cavity about a factor two faster.
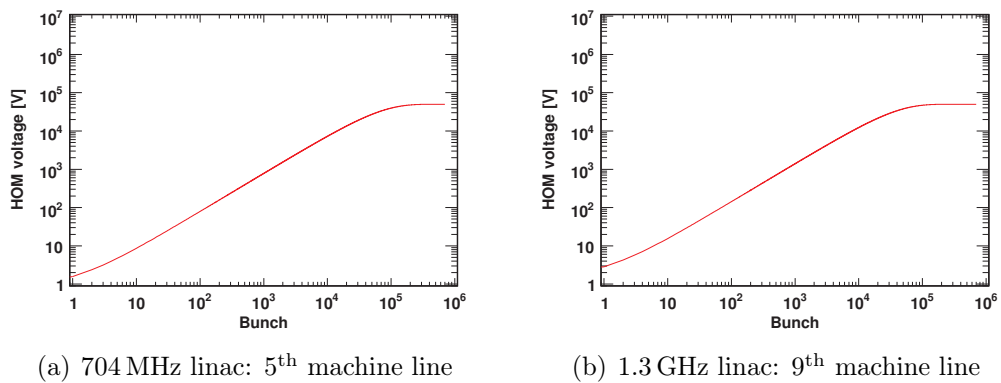

(a) 704 MHz linac: 5$^{\text{th}}$ machine line   (b) 1.3 GHz linac: 9$^{\text{th}}$ machine line

Figure 10.17:   Same as Fig. 10.16, but moderate damping ($Q_{\text{ex}} = 10^6$). The HOM voltage saturates at the same value in both cavities, but in the 1.3 GHz cavity the rise time is about a factor two faster.

(a) 704 MHz linac: 5$^{\text{th}}$ machine line

(b) 1.3 GHz linac: 9$^{\text{th}}$ machine line
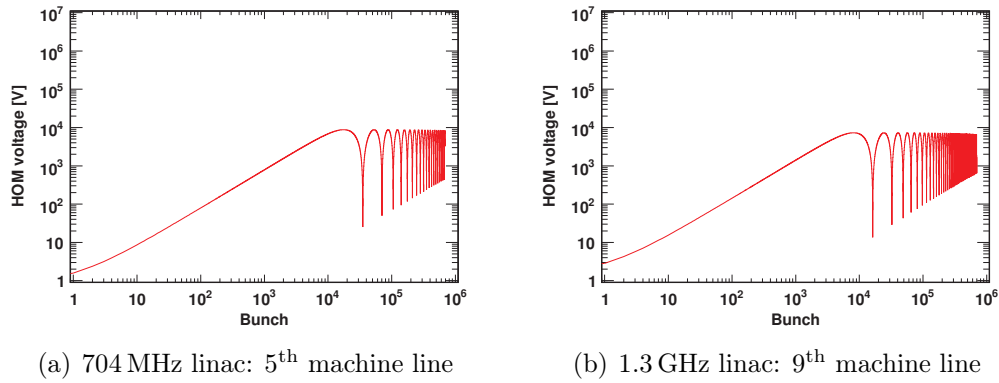
Figure 10.18: Same as Fig. 10.16, but with HOM frequency detuned by 10 kHz in the 704 MHz cavity and 20 kHz in the 1.3 GHz cavity. The HOM voltage oscillates in both cavities with the detuning frequency and the maximum amplitude is about two orders of magnitude lower as in 10.16. In the 1.3 GHz cavity the amplitude and the oscillation frequency are about a factor two higher due to the higher frequency.

(a) 704 MHz linac: 5$^{\text{th}}$ machine line

(b) 1.3 GHz linac: 9$^{\text{th}}$ machine line
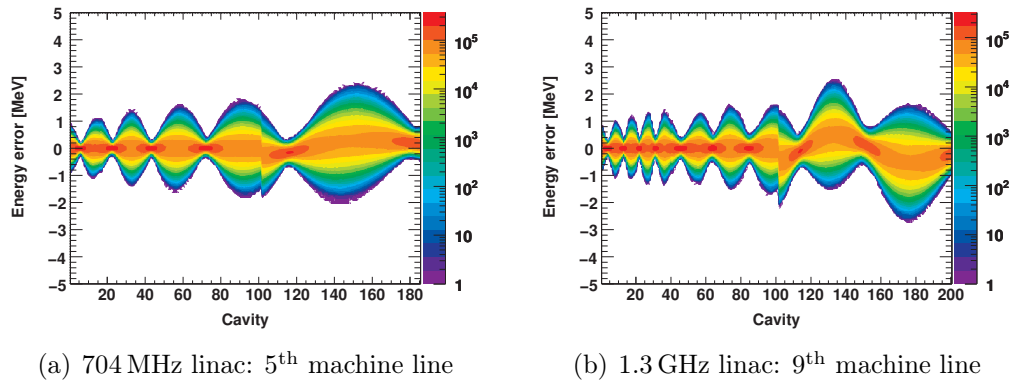
Figure 10.19: Energy error evolution of one pulse along the linac, where a HOM with $(R/Q) = 1\,\Omega$ falls directly on a machine line in cavity 100 and is only weakly damped ($Q_{\text{ex}} = 10^8$). The beam gets a significant kick from the HOM, which leads to a sudden increase in the energy error.

10.3.4   Fundamental Passband Modes

The $TM_{010,4/5\pi}$ mode in the 704 MHz cavities and the $TM_{010,8/9\pi}$ mode in the 1.3 GHz cavities have a significant $(R/Q)(\beta)$, see Table 10.6, which is even higher than the $(R/Q)(\beta)$ of the accelerating mode at certain β values.

Table 10.6: Fundamental passband modes used in the simulations. The $(R/Q)(\beta)$ map of the modes was shown in Fig. 10.5 and Fig. 10.6.

Section	704 MHz			1.3 GHz		
	f_n [MHz]	σ_{f_n} [kHz]	$(R/Q)(\beta)_{\mathrm{max}}$ $[\Omega]^\dagger$	f_n [MHz]	σ_{f_n} [kHz]	$(R/Q)(\beta)_{\mathrm{max}}$ $[\Omega]^\dagger$
Medium β	702.98	10	155.1	1298.91	20	230.30
High β	702.63	10	314.76	1299.27	20	545.35

† linac definition

Beam dynamics simulations are executed with these particular modes using a frequency spread of 10 kHz in the 704.4 MHz linac and 20 kHz in the 1.3 GHz linac. The fundamental power coupler provides a certain damping to these modes which corresponds to a $Q_{\mathrm{ex}} = 10^6$. This is about a factor of ten higher than the Q_{ex} of the accelerating mode. 100 linacs are simulated with different beam currents. The average and maximum HOM voltage in all cavities is shown in Figure 10.20.

(a) 704 MHz linac
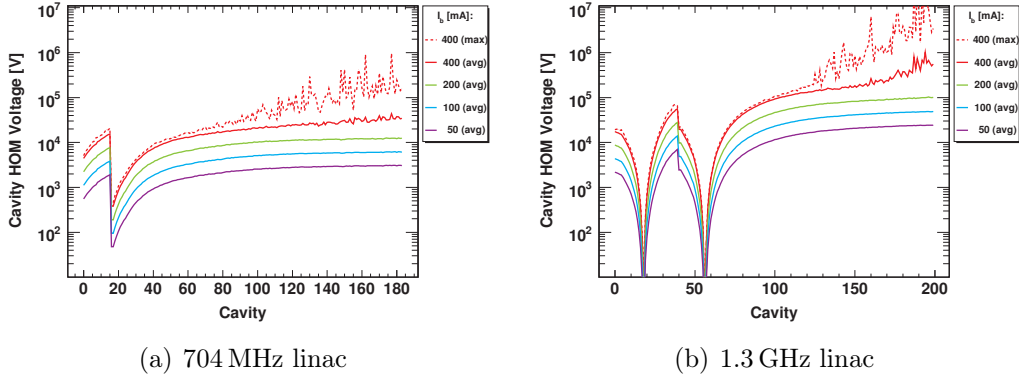
(b) 1.3 GHz linac

Figure 10.20: Average and maximum cavity HOM voltage in the TM_{010}-mode closest to the accelerating mode, see Tab. 10.6, after one pulse for 100 linacs with different beam currents. Instabilities occur at the end of the 1.3 GHz linac operating with 400 mA, where HOM voltages in the same order as the accelerating voltage are present.

Significant HOM voltages are observed for 400 mA in both linacs. A strong self amplifying effect is observed at the end of the linacs, especially in the 1.3 GHz case. In this situation a HOM in one cavity drives HOMs in further downstream cavities. This is possible, because the cavity to cavity HOM frequency spread is sufficiently small. HOM voltages at that level can cause significant beam losses, which are a major concern in the operation of such linacs. Even at nominal current the HOM voltages are about 0.1% of the accelerating voltage in the 1.3 GHz option and start to be comparable to the RF errors which are typically about 0.5% of the accelerating voltage.

For these modes a sweep of Q_{ex} and I_b is done and and the phase space increase is illustrated in Figure 10.21 for both linacs. One simulation is executed for each combination and simulations are stopped for higher Q_{ex} values in case the resulting phase space area is a factor 100 higher than the reference area.

(a) 704 MHz linac   (b) 1.3 GHz linac
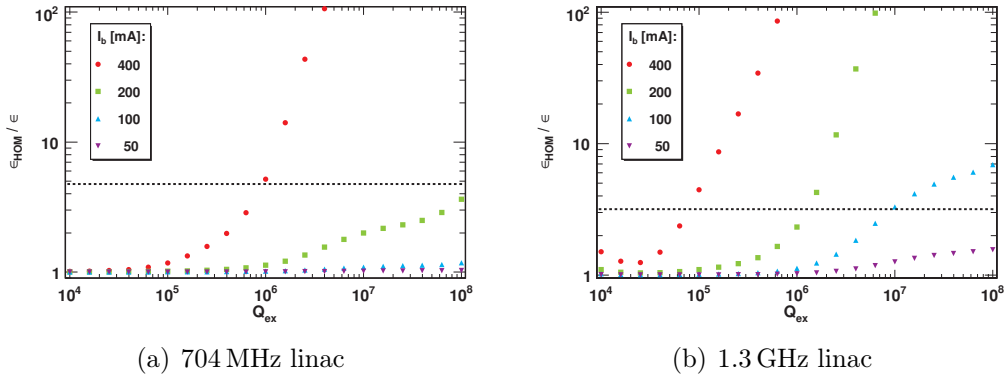
Figure 10.21: Phase space area increase of one pulse under the influence of non accelerating TM_{010}-modes for different beam currents and damping. The phase phase increase due to RF errors is indicated with the dashed line. No significant influence is observed at nominal current. Increasing currents lead to a strong phase space increase. At 400 mA the phase space more than a factor 100 larger for $Q_{ex} > 10^6$ and in the 1.3 GHz linac even at 200 mA for $Q_{ex} > 10^7$.

At nominal beam current the effect is still small, but increases above 100 mA in the 1.3 GHz linac and 200 mA in the 704 MHz linac. The fundamental power coupler should provide a damping in the order of some 10^5. At that damping level, the phase space increase in the 704 MHz linac is tolerable for all simulated currents, while in the 1.3 GHz linac the phase space increase exceeds the value which is caused by RF errors in case of 400 mA. The safety margin therefore is about a factor two higher in the 704 MHz linac option. In general the β_g should be reconsidered to reduce the $(R/Q)(\beta)$ values of the fundamental passband modes beside the accelerating mode.

10.4   Conclusion

Comparing directly the cavity properties one finds that the $(R/Q)(\beta)$ increases with the number of cells for all modes while the energy acceptance decreases with the number of cells. Hence, the high $(R/Q)(\beta_g)$ of the accelerating mode drops fast for velocities different from β_g. From this point of view a lower number of cells is preferable for $\beta < 1$ particles, which implies the use of a lower operation frequency in order to keep a high real estate gradient. In the investigated case the $(R/Q)(\beta)$ are about a factor two higher in the 1.3 GHz cavities as compared to the 704 MHz cavities.

The phase space increase due to HOMs at nominal current is negligible compared to the effect of RF errors if they are not excited resonantly. Based on the discussed scenarios a weak HOM damping in the order of $Q_{ex} \sim 10^8$ is fine in both linacs, if there is no HOM with high $(R/Q)(\beta)$ close to fundamental machine lines. The fundamental passband modes are critical in both options, because of the high $(R/Q)(\beta)$ at the end of both linacs. This can cause a phase space increase especially in the 1.3 GHz linac for high currents. For a final conclusion on HOM damping requirements a more detailed study has to be performed with the final cavity design and linac layout. Furthermore dipole modes should be considered, which are not discussed here.

Both designs are not yet fully optimised and need further improvements. Especially the choice of the geometrical β in the high β sections should be revised in order to avoid the unfavourable case, where other TM_{010} modes have higher $(R/Q)(\beta)$ values than the accelerating mode.

Chapter 11

The Spallation Neutron Source Superconducting Proton Linac

The accelerator-based *Spallation Neutron Source* (SNS) [15] at the Oak Ridge National Laboratory, Tennessee, USA provides the most intense pulsed neutron beams in the world for scientific research and industrial development. It consists of a linear accelerator and an accumulator ring, which is designed to deliver a 1 GeV proton beam with about 1 MW beam power on a liquid mercury target, where the neutrons are produced for the experimental beam lines. The linac is the first high intensity pulsed SRF proton linac in the MW class. It was commissioned in 2005 [129] and started operation in 2006.

At design stage, beam dynamics simulations [110] and HOM power estimations [102] showed no HOM caused effects for $Q_{ex} < 10^8$. This weak damping can be provided by the steel bellows in the inter cavity connection and the fundamental power coupler. Nevertheless, it was decided to install HOM couplers to provide safety margins. During commissioning and operation no HOM caused instabilities or any HOM excitation was measured. But several cavities could not be operated or only at lower gradient due to HOM coupler caused faults [69, 129–132]. This limits the output energy to 930 MeV at the moment[1]. The risk of HOM-caused instabilities is reanalysed using the available cavity measurement data and statistics for the HOM frequencies [133]. Based on this and the experience gained during operation, the decision was taken not to use HOM couplers in the additional high beta cavities of the *Power Upgrade Program* (*PUP*) [134] and take out the HOM coupler feed through in all cavities with HOM coupler problems during maintenance periods.

In the following section the linac, cavity, and beam parameters are introduced. Then the monopole modes are identified and SMD is used to analyse the linac,

---

[1] 1 GeV has been reached, but not in regular operation mode.

relying mostly on design data but using also measurement such for example the HOM frequencies and deviation. In a second step, the SNS linac is compared to the SPL design.

11.1 SNS Linac Design and Operation Parameters

The SNS linac consist of a H^- source, a normal conducting front-end up to 185 MeV and a SRF linac with two families of elliptical cavities ($\beta_g = 0.61$ and $\beta_g = 0.81$) with a design output energy of 1 GeV. The schematic layout of the linac and the period layout of the two SRF linac sections are illustrated in Figure 11.1 and Figure 11.2. All linac, section, and cavity parameters are summarised in Table 11.1, which are used in SMD to model the SRF linac sections. There are gaps for the kicker magnets with a fixed structure in the beam pulse, which introduces weak chopping resonance lines at a distance of 1 MHz. This structure is included in all simulations.
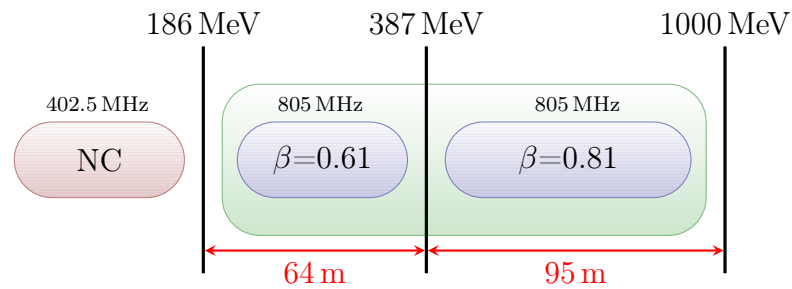
Figure 11.1: Schematic layout of the SNS linac without the PUP section.
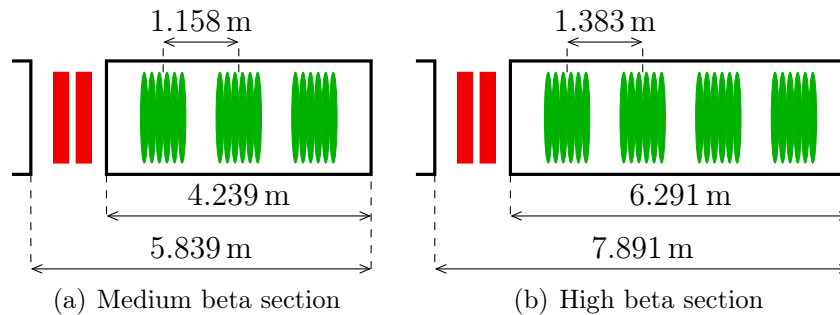
Figure 11.2: Period layout and cavity spacing of the medium (a) and high (b) beta section of the SRF linac. In the warm section between the cryostats, a quadrupole doublet is installed.

Table 11.1: SNS linac and beam parameters used in this study. Based on [133, 135–137].

Parameter	Unit	Value
Beam power	[MW]	1.0
Repetition rate	[Hz]	60.0
Average pulse current	[mA]	26
Peak pulse current	[mA]	38
Beam pulse length	[ms]	1
Sub-pulse length	[μs]	645
Sub-pulse repetition rate	[MHz]	1.059
Bunch frequency	[MHz]	402.5

Sections		$\beta_\mathrm{g} = 0.61$	$\beta_\mathrm{g} = 0.81$
Output energy	[MeV]	379	1,000
Number of cavities		33	48
Cavities per cryostat		3	4
Period length	[m]	5.839	7.891
Operation phase	[deg]	-20.5	-19.5
Q_ex Power Coupler		$7.3 \cdot 10^5$	$7.0 \cdot 10^5$
Q_ex HOM Coupler		10^4	10^4
Length	[m]	64	95

Cavities		$\beta_\mathrm{g} = 0.61$	$\beta_\mathrm{g} = 0.81$
Cells		6	6
Frequency	[MHz]	805	805
Geometrical beta β_g		0.61	0.81
$(R/Q)(\beta_g)$	[Ω]	279	483
$E_0T(\beta_g)$	[MV/m]	10.1	15.8

Beam	Unit	Value	Variation
Injection energy	[MeV]	185.6	0.07
Injection phase	[deg @ 805 MHz]	-20.5	0.225
Beam current	[mA]	0.26-0.4	0.3%

RF Errors			
Amplitude			0.5%
Phase	[deg @ 805 MHz]		0.5

11.2   Cavity Monopole Analysis

The cavity monopole modes are analysed using SUPERFISH models of the cavities
[138]. In Figure 11.3 the maximum $(R/Q)(\beta)$ values in the used energy range are
shown for all found modes up to $3\,\mathrm{GHz}$ in both cavity families. The $(R/Q)(\beta)$
map of the modes, which will be used in the beam dynamics study, are plotted
in Figure 11.4 and listed in Table 11.2, where also reference values from [120] are
included.
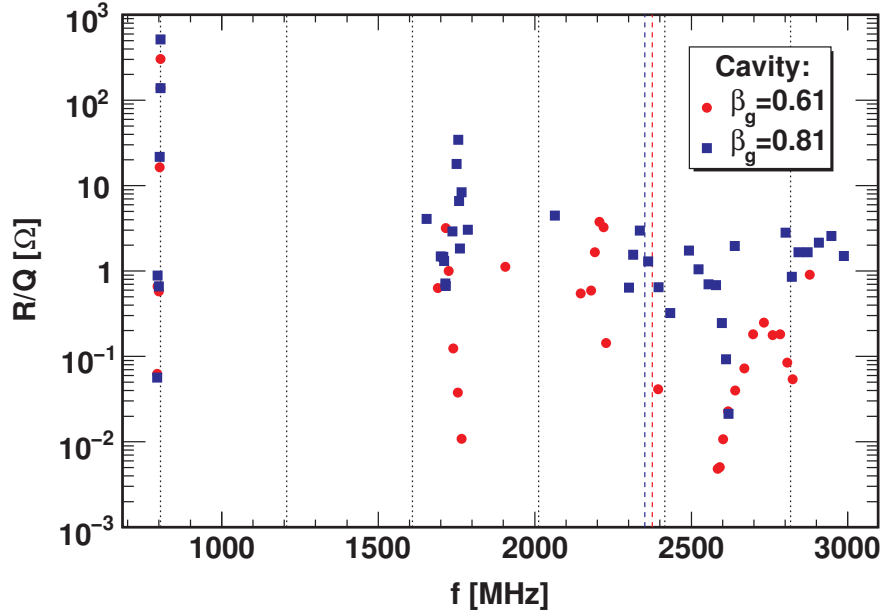
Figure 11.3: Map of the maximum $(R/Q)(\beta)$ values in the used energy range versus
the mode frequency in the SNS cavities up to $3\,\mathrm{GHz}$. The dashed lines indicate the
TM_{01} cutoff frequencies and the dotted lines the fundamental machine lines. The
maximum values for non TM_{010} modes are $4\,\Omega$ in the medium beta cavity and $35\,\Omega$
in the high beta cavity. There are some modes close to the 6th and 7th fundamental
machine line.

The results agree well with [120] for all modes below the TM_{01} cutoff frequency,
which is $2.37\,\mathrm{GHz}$ in the medium beta cavity and $2.35\,\mathrm{GHz}$ in the high beta cavity.
Above cutoff the results diverge due to the influence of the beam pipe geometry
and simulation boundary conditions, which is modelled differently. These modes
have very moderate (R/Q) values and can be dumped sufficiently with the steel
bellows in the cavity interconnection. Only the modes very close to the funda-
mental machine lines are of concern. Additionally, measurement data from [133]
is included in the beam dynamics study for these modes.

(a) Medium beta cavity   (b) High beta section
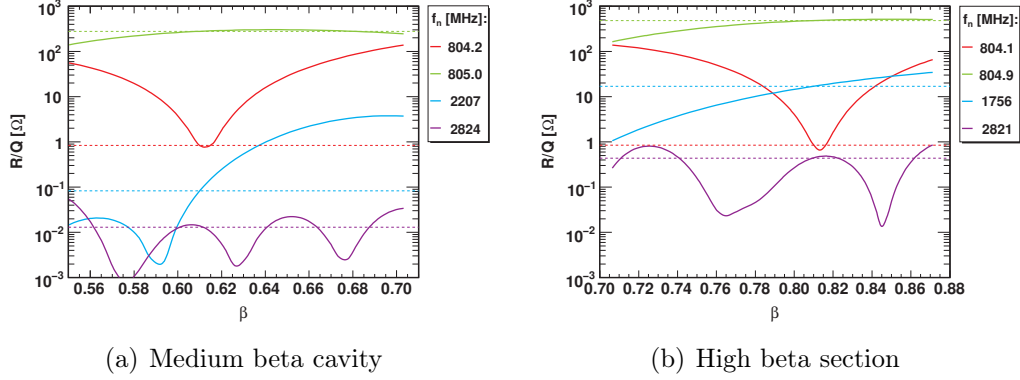
Figure 11.4: $(R/Q)(\beta)$ map of the used modes in the medium (a) and high (b) beta cavity. The dashed lines are the $(R/Q)(\beta_{\mathrm{g}})$ values of these modes.

Table 11.2: List of monopole modes in SNS cavities found with SUPERFISH and [120] as reference.

	SUPERFISH		Reference	
Mode	f_n [MHz]	$(R/Q)(\beta)_{\mathrm{max}}[\Omega]$	f_n [MHz]	$(R/Q)(\beta)_{\mathrm{max}}[\Omega]$
Medium beta cavity				
$\mathrm{TM}_{010}, 5/6\pi$	804.2	138.5	804.2	130.6
TM_{010}, π	805.0	303.0	805.0	303.9
$\mathrm{TM}_{011}, 4/6\pi$	2,207.0	3.8	2,206.0	3.6
TM_{021}, π	2,823.7	0.1	2,820.7	0.2
High beta cavity				
$\mathrm{TM}_{010}, 5/6\pi$	804.1	138.6	804.2	145.5
TM_{010}, π	804.9	516.3	805.0	516.4
$\mathrm{TM}_{011}, 4/6\pi$	1,755.7	34.5	1,754.7	37.2
TM_{022}	2,821.3	0.9	2,828.9	1.2

11.3 HOM Simulations

A simulation model using the data introduced before is implemented in SMD. The phase space distribution at the end of the linac with and without RF errors is shown in Figure 11.5. In both cases injection beam noise is present. Due to RF errors, the phase space increases roughly by a factor of five. The energy deviation at the end of the linac is $0.46\,\mathrm{MeV}$, which is comparable to the measured spread of $1\,\mathrm{MeV}$.

In the following, always two consecutive sub-structured $1\,\mathrm{ms}$ pulses are simulated, using a fixed but different beam noise pattern for each pulse. Three different

(a) Injection beam noise   (b) RF errors
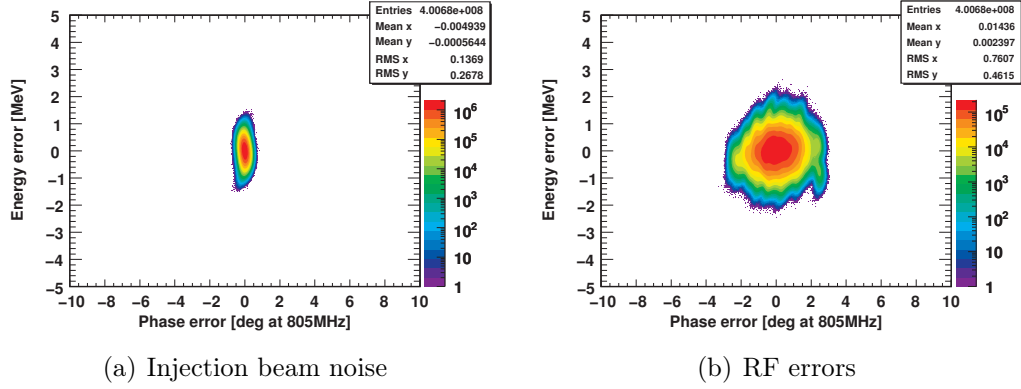
Figure 11.5: 2D phase space histogram at the exit of the SNS linacs with a colour coded density distribution. In (a): only injection noise of 1,000 pulses. (b): 1,000 linacs including RF errors using always the same pulse with injection noise.

scenarios are investigated. First, the HOM with the highest $(R/Q)(\beta)$ value in each section is chosen. Second, the influence of the fundamental passband modes is analysed and third, the modes close to the 7th fundamental machine line are investigated.

In the 2D phase space histograms the bin content is colour coded and colour matching is done individually for each histogram in order to get a high dynamic resolution. The phase space plots are only used to get a qualitative overview. A second class of histograms, illustrating the HOM voltage distribution in the linac, will be used to compare the influence of different effects.

11.3.1 HOMs with high $(R/Q)(\beta)$ Values

The modes found with high $(R/Q)(\beta)$ values are far from fundamental machine lines. Hence, they can only be excited by beam noise and chopping machine lines. This is analysed in beam dynamics simulations, where the damping, the bunch to bunch charge scatter and the mean HOM frequency are varied. The configuration of each set is listed in Table 11.3 and the average and maximum HOM caused phase space increase without RF errors for 100 linacs is shown in Figure 11.6. As reference phase space, the simulation result of the initial simulation without RF errors is used. In the SNS power upgrade program the beam current will increase from nominal 28 mA to 40 mA. Therefore these two currents and additionally ten times these currents are used in the simulations. 1 MHz is used as HOM frequency spread in all simulations.

If there is strong HOM damping (Set 5), no phase space increase is observed for all currents. Reducing the damping in the high beta section (Set 4), which

Table 11.3: HOM simulation parameters

|	Q_{ex}			
Set	$\beta_{\mathrm{g}} = 0.61$	$\beta_{\mathrm{g}} = 0.81$	σ_{q} [%]	comment
1	10^8	10^8	1	f_n shifted to chopping machine line
2	10^8	10^8	1	
3	10^8	10^8	0.3	
4	10^4	10^8	0.3	
5	10^4	10^4	0.3	
6	10^8	10^8	1	SPL 5/8 chopping and f_n shifted to chopping machine line

corresponds to demounting the HOM couplers, leads to a longitudinal phase space increase at high currents. The longitudinal phase space increases slightly more, if the damping is also reduced in the medium beta section (Set 3). Increasing the bunch to bunch charge scatter to 1% (Set 2) has a negative impact, too. In the worst case scenario (Set 1) the mean HOM frequency is shifted to the next chopping resonance line, which leads on average to longitudinal phase space increase of 2.1% at 400 mA. This is completely insignificant as compared to the effect of RF errors. For comparison with the SPL also a high frequent chopping pattern and shifted HOM frequencies to such a resonance is simulated (Set 6). There, an average longitudinal phase space increase of 2.6% at 26 mA is observed, which is already higher than in the SNS worst case scenario at 400 mA. This shows the danger potential of high frequent chopping patterns resonant HOM excitation.

Additionally, simulations including RF errors at 400 mA are executed for Set 1. 1,000 linacs are analysed and it can be seen that the phase space distribution does not change as compared to Figure 11.5(b), where only RF errors are present. Figure 11.7 shows the histograms of the HOM voltages present in all medium and high beta cavities after the second pulse. The peak is around 1 kV in the high beta cavities and even lower for the medium beta cavities. These voltages are insignificant as compared to accelerating voltage variations due to RF errors, which is up to 72 kV, and cannot cause a significant increase in the energy and phase error.

At nominal current the HOM voltage is about a factor 10 lower and no influence on the beam is observable. It can be seen that the beam noise is too low, the $(R/Q)(\beta)$ too low, the HOM frequency spread too high, and the chopping resonance not strong enough to drive beam instabilities in the SNS SRF linac, even with weak HOM damping. The additional heat load is negligible as well, even at a beam current of 400 mA.
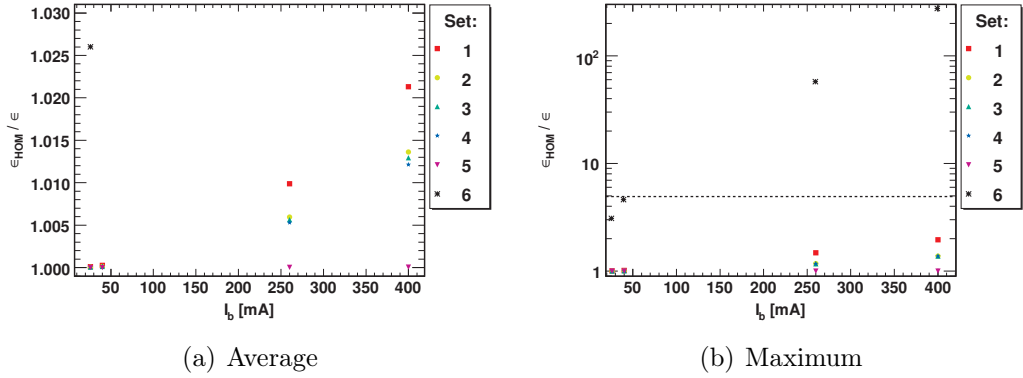
(a) Average

(b) Maximum

Figure 11.6: Average (a) and maximum (b) longitudinal phase space increase due to HOMs with high $(R/Q)(\beta)$ values for 100 linacs. The phase space increase due to RF errors is indicated by the dashed line in (b). An insignificant increase is observed in all SNS scenarios, compared to the influence of RF errors. In the SPL scenario the increase at nominal current is already higher than for the worst case SNS scenario at 400 mA. Settings: $\sigma_{f_n} = 1\,\mathrm{MHz}$, $N = 100$, see Tab. 11.3.

(a) Medium beta cavity

(b) High beta cavity
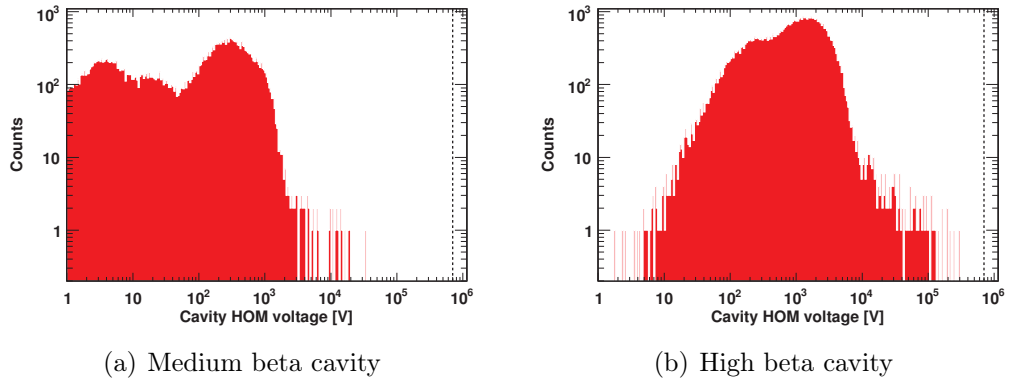
Figure 11.7: Histogram of the HOM voltage present after the second pulse for 1,000 linacs, where the HOM frequency and RF error pattern are varied. In the medium beta section 10% of the cavities have voltages below 1 V. In total there are only a few cavities in the high beta section, which have higher voltages than the maximum voltage amplitude error of the RF system (dashed line). Settings: HOM with the highest $(R/Q)(\beta)$ in each section, $\sigma_{f_n} = 1\,\mathrm{MHz}$ $I_\mathrm{b} = 400\,\mathrm{mA}$, $\sigma_{I_\mathrm{b}} = 0.3\%$, RF errors, $N = 1,000$.

11.3.2 Fundamental Passband Modes

The TM_{010} passband modes beside the accelerating π mode have a low frequency spread and considerably high $(R/Q)(\beta)$ values for $\beta \neq \beta_g$, which can cause significant HOM voltages. The most dangerous one is the $TM_{010}, 5/6\pi$ and its impact is investigated into detail. A damping of $Q_{ex} = 10^6$ is assumed, based on [133, 139]. Simulations are carried out with a mode frequency spread of $1\,kHz$ and $10\,kHz$, as well as different currents, see Figure 11.8. For $10\,kHz$ the average phase space increase is only about the same as for pure RF errors even at a high beam current of $400\,mA$. If the mode frequency spread is only $1\,kHz$, instabilities occur in the two simulations with currents above $100\,mA$.
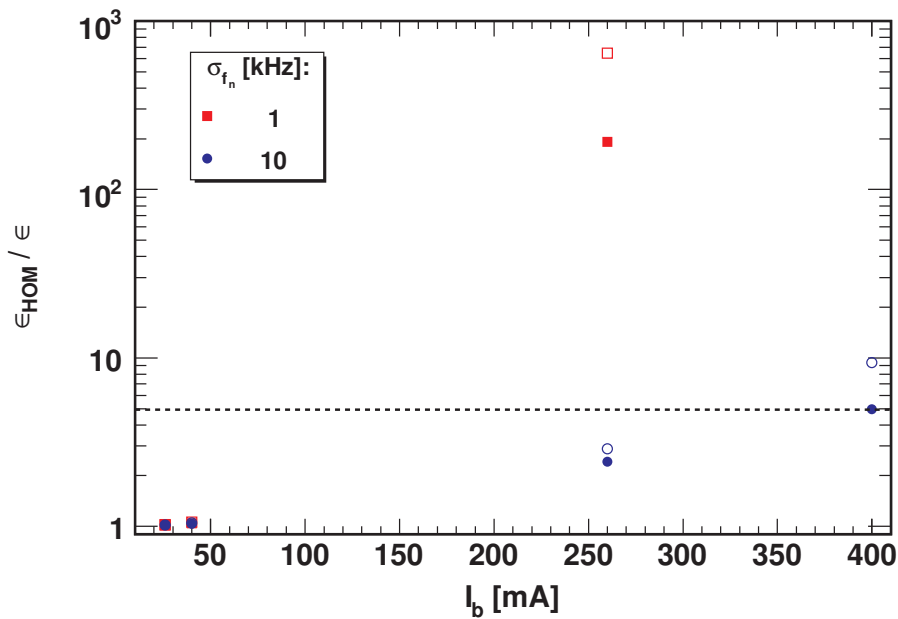
Figure 11.8: Average (filled dots) and maximum (hollow dots) longitudinal phase space increase due to $TM_{010}, 5/6\pi$ mode for 100 linacs. The longitudinal phase space increase due to RF errors is indicated by the dashed line. In case of a mode frequency spread of $1\,kHz$ a strong impact on the beam is observed for high currents and no stable simulations are possible at $400\,mA$. Settings: $TM_{010}, 5/6\pi$ mode, $\sigma_{I_b} = 0.3\%$, $Q_{ex} = 10^6$, $N = 100$.

Comparing the HOM voltage in the high beta cavities for $1\,kHz$ and $10\,kHz$ at a beam current of $260\,mA$, one finds a significant increase in HOM voltage for $\sigma_{f_n} = 1\,kHz$, see Figure 11.9. In this case the HOM voltage exceeds the RF amplitude error level in many cavities and cause beam blow up. This is shown in the corresponding phase space histograms in Figure 11.10.

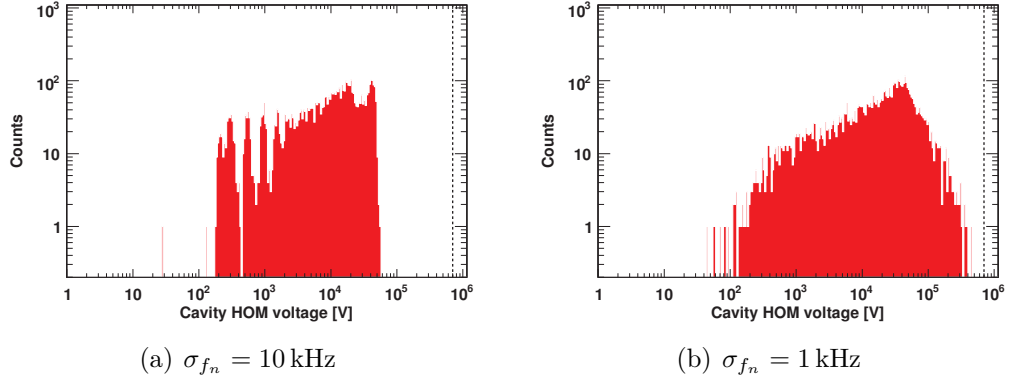(a) $\sigma_{f_n} = 10\,\mathrm{kHz}$ (b) $\sigma_{f_n} = 1\,\mathrm{kHz}$

Figure 11.9: Histogram of the HOM voltage present in the high beta cavities after the second pulse for 100 linacs without RF errors and different HOM frequency spreads. The maximum voltage amplitude error due to RF errors is indicated by the dashed line. Settings: $\mathrm{TM}_{010}, 5/6\pi$, $I_\mathrm{b} = 260\,\mathrm{mA}$, $\sigma_{I_\mathrm{b}} = 0.3\%$, $Q_\mathrm{ex} = 10^6$, $N = 100$.

(a) $\sigma_{f_n} = 10\,\mathrm{kHz}$ (b) $\sigma_{f_n} = 1\,\mathrm{kHz}$
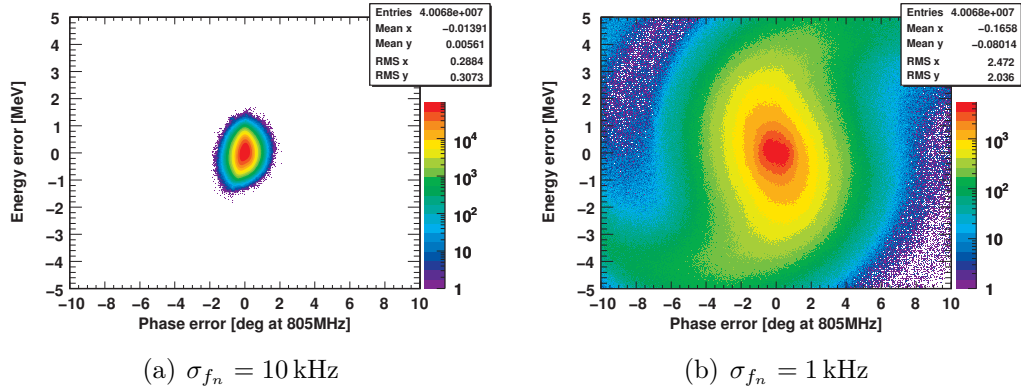
Figure 11.10: 2D phase space histogram at the exit of 100 linacs, where the $\mathrm{TM}_{010}, 5/6\pi$ mode is excited. Settings: $I_\mathrm{b} = 260\,\mathrm{mA}$, $\sigma_{I_\mathrm{b}} = 0.3\%$, $Q_\mathrm{ex} = 10^6$, $N = 100$.

Additional simulations with RF errors are executed for $40\,\mathrm{mA}$. The phase space increase is similar to the simulation where only RF errors are considered.

The $\mathrm{TM}_{010}, 5/6\pi$ mode has high potential to drive beam instabilities but the nominal beam current is too low for a critical excitation. Also the next chopping machine line is too far away and cannot cause resonant excitation. It is difficult to damp this mode by HOM couplers, since the HOM coupler must have a notch filter for the accelerating mode, which has a certain width. Therefore the $\mathrm{TM}_{010}, 5/6\pi$ mode must be damped by the fundamental power coupler and the steel bellows and does not need to be considered in the HOM coupler analysis.

11.3.3 Modes Close to Machine Lines

The second class of potentially dangerous HOMs are those which are close to fundamental machine lines. In both cavity families modes close to the 7th fundamental machine line were found, see Figure 11.3, and are used for beam dynamics simulations. In all SNS cavities modes close to fundamental machine lines have been measured at room temperature [133]. No cavity was found where a HOM falls directly on a machine line. This is true also when taking the frequency change after cool down into account. Additionally, simulations are carried out using this measurement data in terms of mean HOM frequency and deviation. All HOM simulation parameters are listed in Table 11.4 for two sets.

Table 11.4: Simulation parameters for HOMs close to the 7th fundamental machine line.

Set	Medium beta cavity			High beta cavity		
	f_n [MHz]	σ_{f_n} [MHz]	$(R/Q)(\beta)_{max}$ [Ω]	f_n [MHz]	σ_{f_n} [MHz]	$(R/Q)(\beta)_{max}$ [Ω]
1	2817.5[†]	2	0.03	2817.5[†]	2	0.86
2	2811.97	3.2	0.3[‡]	2813.83	2.1	0.4[‡]

[†] mean frequency is shifted to the 7th machine line
[‡] constant value assumed

For both sets simulations are executed for different currents and damping. Each configuration is repeated for 100 linacs. The average and maximum phase space increase is shown in Figure 11.11, where at nominal current no significant effective longitudinal phase space growth is observed. At high currents and low damping, instabilities occur in Set 1, while in Set 2 no instabilities are observed in all simulations. With strong damping present no effect is observed in both sets.

This small change in the mean HOM frequency, as done in Set 1, leads significant change in the results for high currents. It shows clearly the risk potential of machine lines in combination with high current beams.

Additional simulations are carried out with 400 mA and RF errors for both sets. The resulting phase space distribution is shown in Figure 11.12. In set 2 no significant changes are observed but in set 1, a tail becomes visible, caused by high HOM voltages at the end of the beam pulse. Also the HOM voltages in the high beta section of both sets are plotted in Figure 11.13. The distribution of both histograms is very broad and the longitudinal phase space increase is caused by some resonantly excited cavities with very high HOM voltages above 100 kV.

(a) Set 1   (b) Set 2
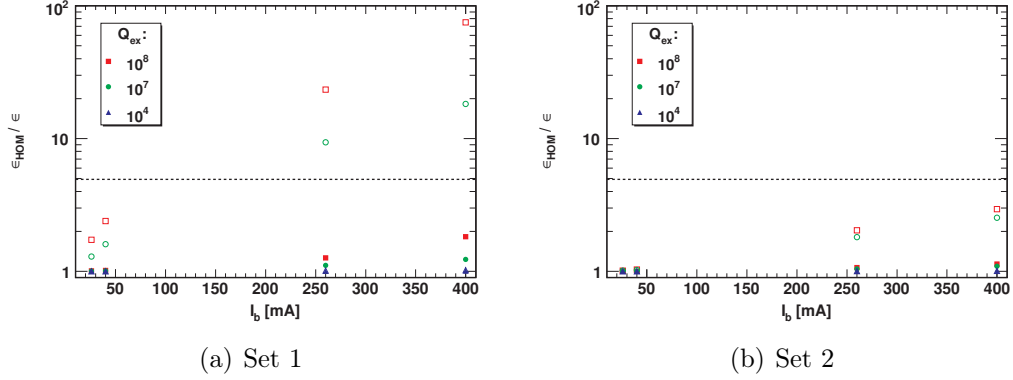
Figure 11.11: Average (filled dots) and maximum (hollow dots) longitudinal phase space growth due to modes close to fundamental machine lines. No significant increase is observed at nominal current in both sets, but at high current the maximum values in set 1 are more than one order of magnitude higher. Settings: $N = 100$, see Tab. 11.4.

(a) Set 1   (b) Set 2
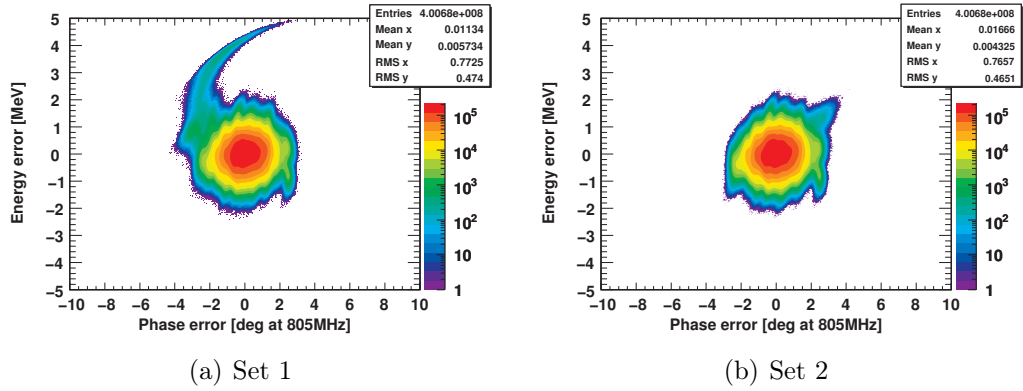
Figure 11.12: 2D phase space histogram at the exit of 1,000 linacs, where the modes are close to fundamental machine lines and RF errors are present. A tail is visible in set 1.

11.4 A Comparison between SNS and SPL

Based on the detailed analysis of both, the SNS linac and the SPL, in this thesis a direct comparison can be carried out.

In both linacs, the initial energy and injection beam noise is similar. The output energy is four to five times higher in the SPL and the number of cavities is three times higher. Since two cavity families are used in both linacs, the SPL cavities must cover a wider velocity range. Therefore the $(R/Q)(\beta)$ of the accelerating mode drops significantly at the beginning of both sections and at the end of the

(a) Set 1 (b) Set 2
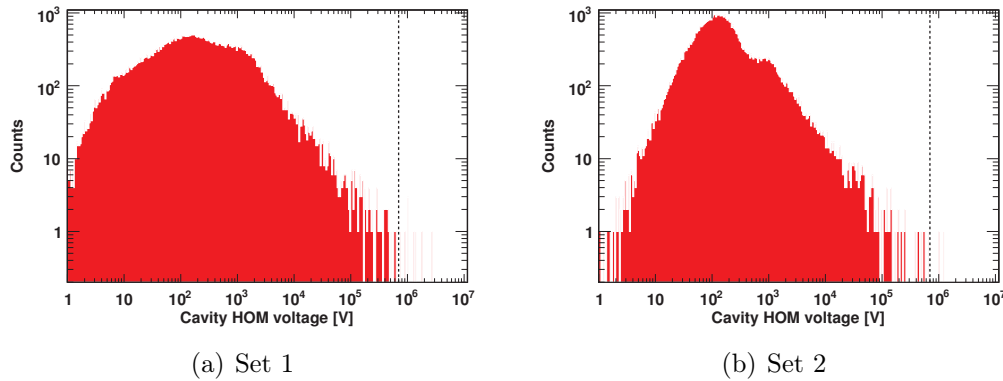
Figure 11.13: Histogram of the HOM voltage present in all high beta cavities after the second pulse for 1000 linacs, where the mode frequency and RF error pattern are varied. The maximum RF amplitude voltage error is indicated by the dashed line. Settings: $I_b = 400\,\text{mA}$, $Q_{\text{ex}} = 10^8$, $N = 1,000$, see Tab.11.4.

medium beta section, where the other fundamental passband modes have a high $(R/Q)(\beta)$. With an increasing number of cells the transit time factor drops faster for velocities below and above the design β and the number of modes per passband increases with the cell number. On the other hand, the real estate gradient increases, too. The SPL aims with five as compared to six cells at a higher real estate gradient than SNS to meet the length constraints. This is only possible by maximising the (R/Q) value for the accelerating mode, by reducing the cavity iris radius and minimising the inter cavity distance. This leads to a significant increase of the HOM's (R/Q), too. The ratio of highest $(R/Q)(\beta)$ values of a HOM to the $(R/Q)(\beta)$ value of the accelerating mode is 19% for the high beta cavity in the SPL and only 6.5% for the high beta cavity at SNS, which is about a factor of three lower for the SNS cavity. In this context the larger energy range also counts, which must be covered by one cavity family in the SPL. The difference in the operating frequency can be neglected. One may therefore conclude that the SNS cavities are better optimised than the SPL cavities with regard to HOMs with high $(R/Q)(\beta)$ values.

Looking at the bunch current and pulse structure, one finds a significant difference in the pulse substructure. In the SPL, high frequent ($\sim$30 MHz) chopping operation mode options are foreseen. This introduces spectral lines with a high danger potential. Since the chopping patterns are not fixed to keep the flexibility of providing any pulse substructure to the users, the case has to be taken into account, where a HOM with a high $(R/Q)(\beta)$ is resonantly excited by such a high frequent chopping machine line. At SNS the machine lines created by the pulse substructure have only a repetition rate of about 1 MHz, which has almost no im-

pact on the beam as shown earlier in this chapter. Also the $TM_{010}, 5/6$ is too far away to get resonantly excited by the chopping pattern. The chopping pattern is fixed, because only an accumulator ring has to be supplied and the flexibility that SPL provides is not needed.

The biggest advantage of the SNS PUP linac design is that measurement data with statistics and long term experience with the cavities exists, which was evaluated through further beam dynamics studies. Based one these results, the decision was taken not to equip the PUP cavities with HOM couplers and remove the feedthroughs in the others. Up to now only simulation data exists for the SPL, which cannot be benchmarked against experimental results. Thus a larger safety margin must be used to ensure stable operation. The measurement data from the test cryo module, which is currently under construction, will not provide enough statistics to reduce the safety margin significantly.

In summary, the simulation carried out as set of this project explain why the SNS linac can operate without HOM couplers. They also indicate why these are required in the SPL to provide beams with various pulse substructures.

Chapter 12

Electrons in the SPL - Recirculating Linac Option

12.1   Motivation

The LHeC[140] is an upgrade scenario of the LHC, where an additional electron accelerator is used to study proton electron collisions. There exist several design studies for this upgrade. One is to add an additional electron storage ring in the LHC tunnel [141]. It is under discussion, if the SPL could be used as an injector for this electron ring. To reach the injection energy of about $10\,\mathrm{GeV}$ [142] the high beta section of the SPL could be used as a recirculating electron linac (eSPL).

A potential bottleneck in operating the SPL as a re-circulating electron linac is HOM caused beam break up. Therefore HOM damping requirements have to be defined to design a damping system which can also meet the requirements for electron beams. In this chapter, results basic beam dynamics studies are presented that estimate if the HOM damping requirements for protons are also sufficient for electrons.

12.2   Simulation Input Parameters

Previous beam dynamics simulations [119] indicate a minimum injection energy of $35\,\mathrm{MeV}$ for the eSPL, if the lattice is not modified. Five acceleration cycles bring the electrons up to an energy of $24\,\mathrm{GeV}$. The quadrupole gradients stay constant during these cycles. This leads to a reduction of the phase advance per period from $3\,°/\mathrm{m}$ in the first turn to $0.6\,°/\mathrm{m}$ in the fifth turn. The total length is estimated as three times the acceleration length. At the present stage there is no arc design available. That is why a simple drift space in the longitudinal plane is used as transfer function. In the transverse plane the same smooth focusing as in

Table 12.1: Simulation input parameters and assumed variation for eSPL.

Parameter		Value	σ
Length re-ciculator	[km]	1.192	
Turns		5	
E_{Out}	[GeV]	24	
Cavities		192	
V_{acc}	[MV]	25	0.5%
ϕ_{RF}	[deg]	-4	0.1
E_{Input}	[MeV]	35	0.0035
ϕ	[deg@704MHz]	0	0.4
x	[mm]	0.0	0.1
x'	[mrad]	0.0	0.1
I_{b}	[mA]	40	1%
T_b	[ps]	2.84	
T_p	[ms]	1.00	
T_r	[ms]	20.0	
Bunches per Batch		1400	
Batches per pulse		50	

HOMs Typ	f_n [MHz]	σ_{f_n} [MHz]	R/Q [Ω]
Monpole	1331	1	140
Dipole	815	1	60

the accelerator section is assumed for the re-circulator part. The injection noise is estimated from the XFEL electron source [143]. All parameters are listed in Table 12.1. The HOMs with the highest (R/Q) values are chosen in both planes. Effects such as Landau damping or synchrotron radiation in the arcs is not considered in the simulation.

12.3   Simulations

In SMD core classes itself nothing had to be changed. Only the control scripts had to be adapted. Even at injection energy, the electrons can be treated as $\beta = 1$ particles, which leads to several simplifications, because all transit time dependent parameters such as V_{acc} and (R/Q) stay constant along the linac.

A batch of bunches is traced through the linac and the output values are
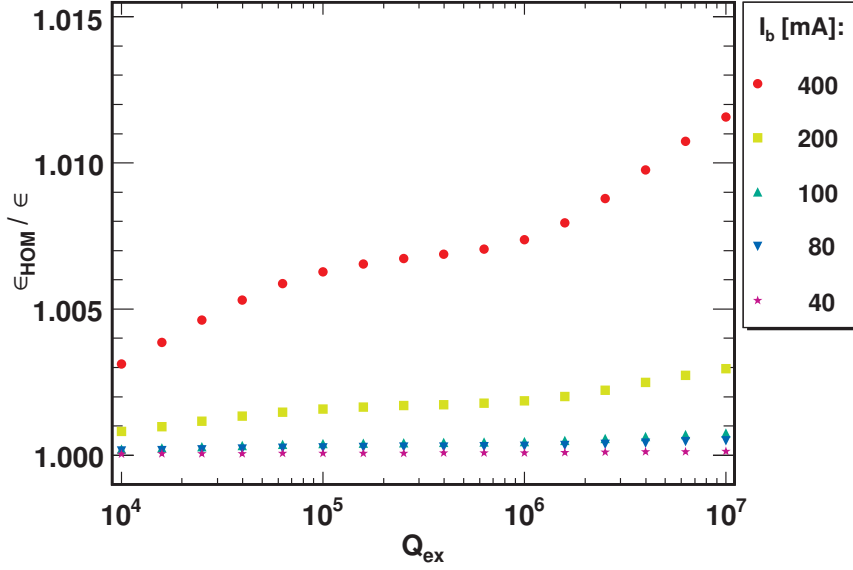
Figure 12.1: Plot of the longitudinal phase space growth versus Q_{ex} and different currents. No significant impact is observed.

used as input values for the next cycle, where the number of bunches in a batch is defined by the length of the re-circulator. The focusing and the longitudinal momentum values have to be updated between the turns. After n turns the batch is extracted and the next batch is injected. This is repeated until the end of the RF pulse is reached. In this scenario only one batch with the same energy level is in the re-circulator. One could also think of other scenarios, where several batches interleave each other. But then the necessary control logic of the simulation execution script gets significantly more complex and also changes in the core beam dynamics routines in SMD have to be applied to deal with changing energies on a bunch to bunch basis as compared to a batch to batch basis. On the physics side there should be no significant change in the HOM damping requirements for these bunch train scenarios. Hence, they are not considered here.

12.4 Results

Simulations are carried out in both planes, where current and Q_{ex} are varied. Figure 12.1 shows the phase space increase in the longitudinal plane after five turns. Even at $400\,\mathrm{mA}$ the phase space growth is only about 1% and is no issue for beam instabilities. TM_{010} modes are no concern because their R/Q values are at least three orders of magnitude lower.
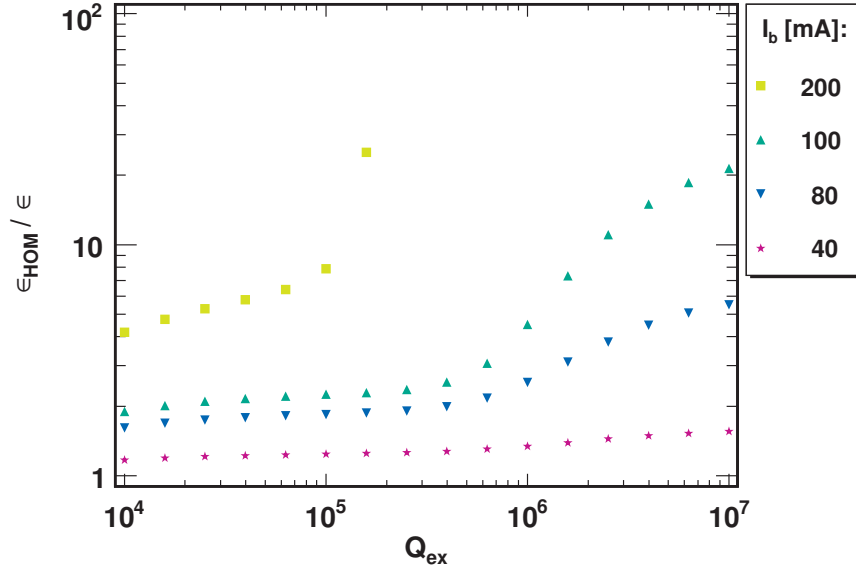
Figure 12.2:   Plot of the transverse phase space growth versus Q_{ex} and different currents. Above 200 mA no stable operation is possible and for lower currents the phase space increases significantly in case of $Q_{ex} > 10^5$.

The situation changes completely in the transverse plane as illustrated in Figure 12.2. At 400 mA no stable operation in the investigated damping regime is possible. The beam becomes unstable above $Q_{ex} = 10^5$ for 200 mA. At nominal current the ϵ_{HOM}/ϵ increases from 1.2 up to 1.5 and the slope gets steeper above $Q_{ex} = 10^5$.

12.5   Conclusion and Outlook

Based on the simulations carried out so far, there is no concern in the longitudinal plane, but very tight HOM damping requirements are needed for dipole modes. With a $Q_{ex} = 10^5$ proposed for the protons stable operation is also possible for electrons in the discussed configuration. Further simulation have to be carried out including real return arcs to model correctly the traverse motion considering resonances created by the orbit. With a return arc design other effect such as for example high current chopped beams, RF errors, and off axis injection can then also be studied in detail which can have an impact on the HOM damping requirements.

Furthermore, it was shown that SMD can also be used for electron machines and recirculating linacs and is not limited to ion linacs.

Chapter 13

Summary

This work was motivated by the question if dedicated higher order mode couplers were needed in superconducting radio-frequency proton linacs in general and in particular for the SPL at CERN. This thesis provides a guideline how to answer this question and which HOM damping is needed to ensure stable operation in this accelerator type. SMD, a dedicated simulation code to investigate into the HOM-beam interaction, focusing on $\beta < 1$ beams, has been developed and implemented in ROOT. This new code takes into account important effects, such as RF errors, or cavity misalignment and was successfully benchmarked against other existing codes. Applying SMD to the SPL machine indicated that the acceleration voltage dependency on the energy error is essential, which is in contrast to the results from earlier studies with other codes.

SMD was used to analyse the risk potential of HOMs in the SPL in detail. Simulations were carried out in both the longitudinal and transverse plane. One of the key results was that dipole modes do not affect a proton beam significantly, in contrast to the case of an electron beam. In the longitudinal plane, the influence of injection beam noise, HOM frequency spread, RF errors, machine lines, and sub-structured pulses were all investigated in detail as a function of beam current and HOM damping. Using the SPL design parameters and estimated errors, it was found that only resonance lines are critical for stable machine operation. The principal machine lines are well known and can therefore be taken into account in the cavity design, so that no HOM hits such a resonance. However, machine lines created by the pulse sub-structure depend on the chopping pattern and can thus occur at any frequency. It was found that a strong HOM damping in the order of $Q_{\mathrm{ex}} = 10^5$ should be used to allow all possible pulse sub-structures. In the absence of any pulse sub-structure only moderate damping in the order of $Q_{\mathrm{ex}} = 10^7$ is needed. In the transverse phase space plane the influence of beam injection noise, HOM frequency spread, resonances, and cavity alignment was studied in detail and no instabilities were found at a moderate HOM damping level of $Q_{\mathrm{ex}} =$

10^7. Furthermore it was confirmed that the bunch-to-bunch charge scatter is the main driver for longitudinal instabilities off-resonance and that the HOM frequency spread acts as additional damping in both phase space planes.

Furthermore, the power dissipation in HOMs has been analysed and the additional heat load in the cryogenic system has been calculated as a function of the damping and the distance to machine lines, using analytic and simulation-based methods. One of the findings is that the damping requirements from a cryogenic point of view are even more demanding than from the beam dynamics. This is mainly because the additional heat load in the HOM damper at moderate damping exceeds the possible cooling capacity significantly in the case where a HOM is resonantly excited. This must be taken into account when HOM damping requirements are defined. A distance of a few kHz to a machine line is enough to reduce the additional heat load by several orders of magnitude. This load reduces even further for weak HOM damping, because the width of the resonance is inversely proportional to the damping.

The influence of different operation frequencies and number of cavity cells has been evaluated in detail for the European Spallation Source. Two reference designs have been compared with each other with emphasis on the impact of HOMs. The results led to the conclusion that cavities with less cells and lower operation frequency are the preferable choice when the comparison is centred around HOMs. By doubling the number of cavity cells and the operation frequency, the impact of the HOMs on the beam increases by approximately one order of magnitude.

Finally, the Spallation Neutron Source linac, which is already in operation, has been analysed to understand why this machine can be operated with moderate HOM damping and in particular without dedicated HOM couplers. The obtained simulation results agree with previous, more limited, studies and are consistent with measurement data. In direct comparison to the SPL studies, no high frequency chopping pattern is present in the SNS bunch trains and the HOM frequencies are measured in all cavities. Hence, the risk of having a HOM at a fundamental machine line can be estimated more precisely and was found not to be an issue for machine operation. In this case, the HOM damping requirements are entirely defined by the HOM power dissipation.

In the SRF community two philosophies are presently under discussion: Using strong HOM damping to tolerate the case of a resonant HOM excitation or relying on weak HOM damping to reduce the theoretical risk of resonant HOM excitation and detuning the cavity in case a resonance condition is met. Using SMD it was found that for the SPL strong damping is essential, because the resonance spectrum for chopped beams is too narrow to avoid any resonant HOM excitation.

In the future, the code developed in the frame of the project can be used for superconducting proton linac projects such as Project X, ESS, EURISOL or

MYRRHA, which are currently in the design and R&D stages. In addition, SMD can also be used for electron machines such as ILC or CLIC, since the case of $\beta = 1$ is not excluded in the code. Normal conducting structures can also be simulated, because only the Q value changes in this case. Finally, the code itself is not even limited to linac structures and it is for example possible to simulate recirculating electron linacs such as the LHeC ring-linac option, without changing the core functions. First proof of principal tests have already been successfully done using the $\beta_{\mathrm{g}} = 1$ section of the SPL with added return arcs.

Throughout the thesis, SMD was used for bunch tracking simulations. In addition, it is possible to use the code for particle tracking without taking into account space charge effects. This would enable studies into the behaviour of beam halo under the influence of HOMs or RF errors. Especially the behaviour of non-uniform RF errors on the beam can then be studied in detail since the phase and amplitude error can be applied individually to each cavity.

The thesis answered a number of very important questions regarding HOM-caused beam instabilities. All important parameters are identified in order to define the damping requirements now as a function of the machine operation parameters. In the future, to reduce the uncertainties in the simulations further a detailed model of the dynamic behaviour of HOMs during the beam pulse in terms of frequency, $(R/Q)(\beta)$, and coupling is needed, which takes also into account the active tuning. For such a model, high precision measurement of the HOMs with beam are required in dedicated R&D facilities.

Bibliography

[1] **L. Evans**: *The Large Hadron Collider: a marvel of technology*, Fundamental Sciences (EPFL Press, Lausanne, 2009).
http://cdsweb.cern.ch/record/1193034

[2] Large Hadron Collider (LHC), Homepage (2011.01.17).
http://cern.ch/lhc

[3] **European Organization for Nuclear Research**: About CERN's Name, Homepage (2010.12.22).
http://user.web.cern.ch/user/CERNName/CERNName.html

[4] European Organization for Nuclear Research (CERN), Homepage (2010.12.22).
www.cern.ch

[5] **K. Wille**: *The Physics of Particle Acceerators an introduction* (Oxford, 2000)

[6] **S. Turner**: *CAS - CERN Accelerator School: 5th General Accelerator Physics Course* (CERN, Geneva, 1994).
http://cdsweb.cern.ch/record/254747

[7] **H. F. Schopper and R.-D. Heuer**: *LEP: The lord of the collider rings at CERN 1980-2000. The making, operation and legacy of the world's largest scientific instrument* (Springer, Berlin, 2009)

[8] International Linar Colider (ILC), Homepage (2010.09.17).
http://www.linearcollider.org/

[9] **R. Brinkmann, et al.**: Conceptual Design Report of a 500 GeV e+e- Linear Collider with Integrated X-ray Laser Facility, *Tech. Rep.*, DESY (1997).
http://flash.desy.de/tesla/tesla_documentation/

[10] **K. Yokoya**: Status of the International Linear Collider, *Proceedings of the IPAC'10*, WEYMH01 (2010).
http://accelconf.web.cern.ch/AccelConf/IPAC10/papers/weymh01.pdf

[11] **H.-H. Braun**: Overview of Proposals for Major FEL Facilities, *Proceedings of the LINAC'10, Tsukuba, Japan*, TU102 (2010).
http://silver.j-parc.jp/linac10/TU102.PDF

[12] **H. Weise**: Status of the European XFEL Project, *Proceedings of the LINAC'10, Tsukuba, Japan* (2010).
http://silver.j-parc.jp/linac10/MO102.PDF

[13] **D. H. Bilderback, et al.**: Energy recovery linac (ERL) coherent hard x-ray sources, *New J. Phys.* 12(3):035011 (2010).
http://dx.doi.org/10.1088/1367-2630/12/3/035011

[14] **G. R. Neil**: Worldwide ERL R&D Overview Including JLAMP, BNL, and Cornell ERLs, *Proceedings of the LINAC'10, Tsukuba, Japan*, TU103 (2010).
http://silver.j-parc.jp/linac10/TU103.PDF

[15] Spallation Neutron Source (SNS), Homepage (2010.09.17).
http://neutrons.ornl.gov/

[16] **F. Mezei**: New perspectives from new generations of neutron sources, *C. R. Phys.* 8(7-8):909 (2007).
http://dx.doi.org/10.1016/j.crhy.2007.10.003

[17] European Spallation Source (ESS), Homepage (2010.07.16).
http://ess-scandinavia.eu/

[18] **J.-L. Biarrotte, et al.**: A reference accelerator scheme for ADS applications, *Nucl. Instrum. Methods Phys. Res., Sect. A* 562(2):656 (2006).
http://dx.doi.org/10.1016/j.nima.2006.02.127

[19] **The European Technical Working Group on ADS**: A European Roadmap for Developing Acelerator Driven Systems (ADS) for Nuclear Wast Incineration, *Tech. Rep.*, ENEA (2001).
http://inrwww.fzk.de/ads-roadmap.pdf

[20] **R. Sheffield and E. Pitcher**: The Role of Accelerators in the Energy Problem, *Proceedings of IPAC'10, Kyoto, Japan*, TUZRA01 (2010).
http://accelconf.web.cern.ch/AccelConf/IPAC10/papers/tuzra01.pdf

[21] **H. Abderrahim, et al.**: MYRRHA: A multipurpose accelerator driven system for research & development, *Nucl. Instrum. Methods Phys. Res., Sect. A* 463(3):487 (2001).
http://dx.doi.org/10.1016/S0168-9002(01)00164-4

[22] MYRRHA: Multi-purpose hybrid research reactor for high-tech applications, Homepage (2010.09.17).
http://myrrha.sckcen.be/

[23] **J. Biarrotte, et al.**: Accelerator reference design for the MYRRHA European ADS demonstrator, *Proceedings of the LINAC'10, Tsukuba, Japan*, TUP020 (2010).
http://silver.j-parc.jp/linac10/TUP020.PDF

[24] European Isotope Separation On-Line Radioactive Ion Beam Facility (EU-RISOL), Homepage (2008.09.11).
http://www.eurisol.org

[25] **P. Zucchelli**: A novel concept for a neutrino factory: the beta-beam, *Phys. Lett. B* 532(3-4):166 (2002).
http://www.sciencedirect.com/science/article/B6TVN-45G0203-6/
2/51460e05937f23c7e0ad0ea09656931b

[26] **P. Gruber, et al.**: The Study of a European Neutrino Factory Complex, *Tech. Rep. CERN-PS-2002-080-PP*, CERN, Geneva (2002).
http://cdsweb.cern.ch/record/610249

[27] **S. D. Holmes**: Project X: A Multi-MW Proton Source at Fermilab, *Proceedings of IPAC10, Kyoto, Japan*, TUYRA01 (2010).
http://accelconf.web.cern.ch/AccelConf/IPAC10/papers/tuyra01.
pdf

[28] **F. Gerigk, et al.**: *Conceptual design of the SPL II: A high-power superconducting H^- linac at CERN*, no. CERN-2006-006 in Yellow Reports (CERN, Geneva, 2006).
http://cdsweb.cern.ch/record/975366

[29] **O. Brunner, et al.**: Assessment of the basic parameters of the CERN Superconducting Proton Linac, *Phys. Rev. ST AB* 12(7):070402 (2009).
http://link.aps.org/doi/10.1103/PhysRevSTAB.12.070402

[30] **R. Garoby**: SPL at CERN, *Proceedings of SRF2009, Berlin, Germany*, FROBAU04 (2009).

```
http://accelconf.web.cern.ch/AccelConf/SRF2009/papers/
frobau04.pdf
```

[31] **F. Gerigk, et al.**: Layout and Machine Optimisation for the SPL at CERN, *Proceedings of the LINAC'10, Tsukuba, Japan*, THP004 (2010).
```
http://cdsweb.cern.ch/record/1302738
```

[32] **F. Gerigk**: 5th SPL Collaboration Meeting Minutes, 25-26 November 2010, EDMS.
```
https://edms.cern.ch/document/1111627/1
```

[33] **F. Gerigk**: private communication

[34] **F. Gerigk, et al.**: Linac4 Technical Design Report, *Technical Design Report CERN-AB-2006-084*, CERN, Geneva (2006).
```
http://cdsweb.cern.ch/record/1004186
```

[35] **M. Vretenar**: Status of Linac4 Construction at CERN, *Proceedings of the LINAC'10, Tsukuba, Japan*, WE103 (2010).
```
http://cdsweb.cern.ch/record/1303332
```

[36] **T. Kroyer, F. Caspers, and E. Mahner**: The CERN SPL Chopper Structure, *Tech. Rep. CERN-AB-2007-004*, CERN, Geneva (2007).
```
http://cdsweb.cern.ch/record/1015712
```

[37] 5th SPL collaboration meeting, WEB (2010).
```
http://indico.cern.ch/event/109664
```

[38] SPL R&D Project, Homepage (2011.01.13).
```
http://cern.ch/project-spl
```

[39] Workshop on cryogenic and vacuum sectorisations of the SPL, WEB (2009).
```
http://indico.cern.ch/event/68499
```

[40] **M. Eshraqi**: Highly segmented SPL as a mixture of Doublet and FODO focusing, 5th SPL collaboration meeting (2010).
```
http://indico.cern.ch/event/109664
```

[41] Online Oxford Dicitonaries, Homepage (2010.09.23).
```
http://oxforddictionaries.com/
```

[42] **M. Vretenar**: Low-Beta Cavities, *CAS - RF for Accelerators* (2010).
```
http://cas.web.cern.ch/cas/Denmark-2010/Lectures/
ebeltoft-lectures.html
```

[43] **F. Gerigk**: Cavity types, *CAS - RF for accelerators* (2010).
http://cas.web.cern.ch/cas/Denmark-2010/Lectures/
ebeltoft-lectures.html

[44] **T. P. Wangler**: *Principles of RF Linear Acceerators* (Wiley-VCH, 2008),
2nd edn.

[45] **P. M. Lapostolle and M. Weiss**: Formulae and procedures useful for
the design of linear accelerators, *Formula summary CERN-PS-2000-001-DR*,
CERN, CERN (2000).
http://cdsweb.cern.ch/record/428133

[46] **H. Padamsee, J. Knobloch, and T. Hays**: *RF Superconductivity for
Accelerators* (WILEY-VCH, 2008), second edn.

[47] **J. Sekutowicz**: SC Cavities, *CAS - RF for Accelerators* (2010).
http://cas.web.cern.ch/cas/Denmark-2010/Lectures/
ebeltoft-lectures.html

[48] **R. Wanzenberg**: Monopole, Dipole and Quadrupole Passbands of the
TESLA 9-cell Cavity, *Tech. Rep.*, DESY (2001).
http://cdsweb.cern.ch/record/533324

[49] **A. Wolski**: Theory of Electromagnetic Fields, *CAS Special Topic "RF for
accelerators"* (2010).
http://cas.web.cern.ch/cas/Denmark-2010/Lectures/
ebeltoft-lectures.html

[50] **J. C. Maxwell**: A Dynamical Theory of the Electromagnetic Field, *Phil.
Trans. R. Soc. Lond.* 155:459 (1865).
http://dx.doi.org/10.1098/rstl.1865.0008

[51] **I. N. Bronstein, et al.**: *Taschenbuch der Mathematik* (Harri Deutsch,
2005)

[52] **H. Padamsee**: *RF Superconductivity* (Wiley-VCH, 2009)

[53] **N. R. A. Valles and M. U. Liepe**: Temperature dependence of the
superheating field in niobium, arXiv:1002.3182v1 (2010).
http://arxiv.org/abs/1002.3182v1

[54] **T. Junginger, W. Weingarten, and C. Welsch**: Intrinsic Limitations
of Niobium under RF, The fourth international workshop on thin films and
new ideas to push the limits of RF superconductivity (2010).
http://surfacetreatments.it/thinfilms

[55] **T. Junginger**: privat communication

[56] **B. Aune, et al.**: Superconducting TESLA cavities, *Phys. Rev. ST AB* 3(9):092001 (2000).
`http://link.aps.org/doi/10.1103/PhysRevSTAB.3.092001`

[57] 1th Baseline Assessment Workshop (2010).
`http://ilcagenda.linearcollider.org/event/4593`

[58] **R. Calaga**: Some Aspects of 704 MHz Superconducting RF Cavities, *Proceedings SRF2009, Berlin, Germany*, THPPO003 (2009).
`http://accelconf.web.cern.ch/AccelConf/srf2009/papers/`
`thppo003.pdf`

[59] **C. Pagani, et al.**: Design Criteria for Elliptical Cavities, *The 10th Workshop on RF Superconductivity, 2001, Tsukuba, Japan*, FA003 (2001).
`http://accelconf.web.cern.ch/AccelConf/srf01/papers/fa003.pdf`

[60] **F. Gerigk**: The Effect of Phase Slippage in Multicell Cavities on Longitudinal Beam Dynamics, *Tech. Rep. CERN-PS-RF-NOTE-2001-009*, CERN, Geneva (2001).
`http://cdsweb.cern.ch/record/505918`

[61] **M. Grecki, et al.**: Compensation of Lorentz Force Detuning for SC Linacs (with Piezo Tuners), *Proceedings of EPAC08, Genoa, Italy*, MOPP129 (2008).
`http://accelconf.web.cern.ch/accelconf/e08/papers/mopp129.pdf`

[62] **W. K. H. Panofsky and W. A. Wenzel**: Some Considerations Concerning the Transverse Deflection of Charged Particles in Radio Frequency Fields, *Rev. Sci. Instrum.* Nov.:967 (1956).
`http://link.aip.org/link/doi/10.1063/1.1715427`

[63] **J. Tückmantel**: Cavity-Beam-Transmitter Interaction Formula Collection with Derivation, *Tech. Rep. CERN-ATS-Note-2011-002*, CERN (2011).
`http://cdsweb.cern.ch/record/1323893`

[64] **P. Bernard, et al.**: Operation of the CERN 5-cell superconducting acceleration cavity in PETRA, 12th *International Conference on High-energy Accelerators, Batavia, IL, USA*, CERN-EF-83-12, p. 5 p (1983).
`http://cdsweb.cern.ch/record/150351`

[65] International Workshop on Higher-Order-Mode Damping Superconducting RF Cavities, WEB (2010).
`http://www.lns.cornell.edu/Events/HOM10/`

[66] **H. Hahn, et al.**: HOM Absorbers for ERL Cryomodules at BNL, *Proceedings of the SRF2009, Berlin, Germany*, THPPO031 (2009).
http://accelconf.web.cern.ch/AccelConf/srf2009/papers/
thppo031.pdf

[67] **D. Boussard, et al.**: The LHC superconducting cavities, *18th Biennial Particle Accelerator Conference, New York, NY, USA*, MOP120, p. 4 p (1999).
http://cdsweb.cern.ch/record/386691

[68] **J. Tückmantel**: private communication

[69] **S.-H. Kim, et al.**: Study on Fault Scenarios of Coaxial Type HOM Couplers in SRF Cavities, *Proceedings of LINAC 2006, Knoxville, Tennessee USA*, THP081 (2006).
http://accelconf.web.cern.ch/AccelConf/l06/PAPERS/THP081.PDF

[70] **H.-W. Glock, et al.**: HOM Spectrum and Q-factor Estimations of the High-Beta CERN-SPL-Cavities, *Proceedings of the IPAC'10, Kyoto, Japan*, WEPEC008 (2010).
http://accelconf.web.cern.ch/AccelConf/IPAC10/papers/wepec008.
pdf

[71] **H.-W. Glock**: HOM coupler modelling for SPL, WEB (2010).
http://indico.cern.ch/event/109664

[72] **S. Molloy, et al.**: High precision superconducting cavity diagnostics with higher order mode measurements, *Phys. Rev. ST AB* 9(11):112802 (2006).
http://link.aps.org/doi/10.1103/PhysRevSTAB.9.112802

[73] **H.-W. Glock**: private communication

[74] **F. Marhauser, et al.**: Search for Trapped Modes in TESLA Cavities, *Proceedings of the PAC'97, Vancouver, B.C., Canada*, 3W004 (1997).
http://accelconf.web.cern.ch/AccelConf/pac97/papers/pdf/3W004.
PDF

[75] **J. Peiró and S. Sherwin**: *Handbook of Materials Modeling. Volume I: Methods and Models, Chaper8.2* (Springer, 2005)

[76] **E. Jensen**: Computational Tools for RF Structure Design, *Joint USPAS-CAS-Japan-Russia Accelerator School on Physics and Technology of Linear Accelerator Systems, Long Beach, CA, USA, 6 - 14 Nov 2002*, CERN-AB-2003-091-RF, p. 25 p (2003).
http://cdsweb.cern.ch/record/677287

[77] **R. L. Courant, K. Friedrichs, and H. Lewy**: Über die partiellen Differenzengleichungen der Mathematischen Physik, *Math. Ann.* 100:32 (1928).
http://dx.doi.org/10.1007/BF01448839

[78] **V. Thomée**: From finite differences to finite elements: A short history of numerical analysis of partial differential equations, *J. Compt. Appl. Math.* 128(1-2):1 (2001).
http://dx.doi.org/10.1016/S0377-0427(00)00507-0

[79] **R. L. Courant**: Variational Methods for the Solution of Problems of Equilibrium and Vibration, *Bull. AMS* 49:1 (1943).
http://dx.doi.org/10.1090/S0002-9904-1943-07818-4

[80] **G. Pelosi**: The Finite-Element Method, Part 1: R. L. Courant [Historical Corner], *IEEE Antennas. Propag.* 49(2):180 (2007).
http://dx.doi.org/10.1109/MAP.2007.376627

[81] **T. Weiland**: A discretization method for the solution of Maxwell's equations for six-component Fields, *AEU-INT J ELECTRON C* 31(3):116 (1977)

[82] **M. Clemens and T. Weiland**: Discrete Electromagnetism with the Finite Integration Technique, *PIER* 32:65 (2001).
http://dx.doi.org/10.2528/PIER00080103

[83] **C. Liu**: Various approaches to electromagnetic field simulations for RF cavities, 5th SPL Collaboration Meeting (2010).
http://indico.cern.ch/event/109664

[84] **K. Halbach and R. F. Holsinger**: SUPERFISH - A Computer Program for Evaluation of RF Cavities with Cylindrical Symmetry, *Part. Accel.* 7(LBL-5040):213 (1976).
http://cdsweb.cern.ch/record/700607

[85] Los Alamos Accelerator Code Group, Homepage (2010.10.14).
http://laacg1.lanl.gov/

[86] **P. Pierini, et al.**: Cavity Design Tools And Applications To The Trasco Project, 9th *Workshop on RF Superconductivity, Santa Fe*, WEP004 (1999).
http://accelconf.web.cern.ch/AccelConf/SRF99/papers/wep004.pdf

[87] Computer Simulation Technology (CST), Homepage (2010.10.06).
www.cst.com

[88] **B. Krietenstein, et al.**: The Perfect Boundary Approximation Technique Facing the Big Challenge of High Precision Field Computation, *Proceedings of the Linac'98, Chicago, IL, USA* (1998).
http://accelconf.web.cern.ch/AccelConf/l98/PAPERS/TH4041.PDF

[89] **R. Rannacher**: Numerik 0, Lecture script (2006)

[90] **Ansoft Inc.**: HFSS, Homepage (2010.03.07).
www.hfss.com

[91] **R.-H. Zeng, et al.**: HOM study and parameter calculation of the TESLA cavity model, *Chinese Phys. C* 34:99 (2010).
http://dx.doi.org/10.1088/1674-1137/34/1/018

[92] **F. Bouly and D. Longuevergne**: RF design of the $\beta = 0.65$ 5-cells superconducting cavity for the SPL Program, SPL Cavity WG meeting (2011).
http://indico.cern.ch/event/80053

[93] **J. Pouin**: SPL cavity design by CEA-Saclay, 3rd SPL Collaboration Meeting (2009).
http://indico.cern.ch/event/63935

[94] **G. Olry**: SPL activities at CNRS-IPN-Orsay, 5th SPL collaboration meeting (2010).
http://indico.cern.ch/event/109664

[95] **M. Schuh, et al.**: Higher Order Mode Analysis of the SPL Cavities, *Proceedings of IPAC'10, Kyoto, Japan*, THPE082 (2010).
http://accelconf.web.cern.ch/AccelConf/IPAC10/papers/thpe082.pdf

[96] **S. Molloy**: Simulations and calculations of HOMs in strings of cavities, 5th SPL collaboration meeting (2010).
http://indico.cern.ch/event/109664

[97] **H.-W. Glock**: privat communication

[98] **I. M. Kapchinskiy**: *Theory of Resonance Linear Accelerators* (Harwood academic publishers, 1985)

[99] **J. B. Rosenzweig**: *Fundamentals of beam physics* (Oxford University Press, 2003)

[100] **H. Wiedemann**: *Particle Acceleror Physics*, Advanced Texts in Physics (Springer, 2007), 3 edn.

[101] **J. Tückmantel**: Beam simulations with initial bunch noise in superconducting rf proton linacs, *Phys. Rev. ST AB* 13(1):011001 (2010).
`http://link.aps.org/doi/10.1103/PhysRevSTAB.13.011001`

[102] **S.-H. Kim, et al.**: Higher-order-mode (HOM) power in elliptical superconducting cavities for intense pulsed proton accelerators, *Nucl. Instrum. Methods Phys. Res., Sect. A* 492:10 (2002).
`http://dx.doi.org/10.1016/S0168-9002(02)01286-X`

[103] **P. Wilson**: High energy electron linacs, applications to storage ring RF systems and linear colliders, 1981 summer school on high energy accelerators, *AIP Conference Proceedings*, vol. 87 (American Institute of Physics, 1981).
`http://slac.stanford.edu/pubs/slacpubs/2750/slac-pub-2884.pdf`

[104] Simulate higher order Mode Dynamics (SMD) code repository.
`https://svnweb.cern.ch/trac/splhombbu`

[105] **M. Matsumoto and T. Nishimura**: Mersenne twister: a 623-dimensionally equidistributed uniform pseudo-random number generator, *TOMACS* 8:3 (1998).
`http://doi.acm.org/10.1145/272991.272995`

[106] **R. Brun and F. Rademakers**: ROOT - An Object Oriented Data Analysis Framework, *Proceedings AIHENP'96 Workshop, Lausanne, Sep. 1996*, vol. 389, pp. 81–86 (Nucl. Inst. & Meth. in Phys. Res. A, 1997).
`http://root.cern.ch/`

[107] MAD-X, Homepage (2010.09.15).
`http://mad.web.cern.ch/mad/`

[108] GenLinWin, Homepage (2010.09.15).
`http://irfu.cea.fr/Sacm/logiciels/`

[109] TraceWin, Homepage (2010.11.04).
`http://irfu.cea.fr/Sacm/logiciels/index3.php`

[110] **D. Jeon, et al.**: Cumulative beam break-up study of the spallation neutron source superconducting linac, *Nucl. Instrum. Methods Phys. Res., Sect. A* 495(2):85 (2002).
`http://dx.doi.org/10.1016/S0168-9002(02)01576-0`

[111] **M. Schuh, et al.**: Code Benchmarking of Higher Order Modes Simulation Codes, *Tech. Rep. sLHC-Project-Note-0010*, CERN, Geneva (2010).
`http://cdsweb.cern.ch/record/1235793`

[112] **A. Lombardi, S.-H. Kim, and W. Weingarten**: Summary of the workshop on HOM in SPL, *Tech. Rep. sLHC-Project-Note-0003*, CERN, Geneva (2009).
http://cdsweb.cern.ch/record/1189889

[113] **J. Sekutowicz**: private communication

[114] **F. Marhauser**: private communication

[115] **S. Molloy and R. Calaga**: Simulations of Proposed Accelerating Cavities for the CERN SPL, *Proceedings of IPACâĂŹ10, Kyoto, Japan*, WEPEC055 (2010).
http://accelconf.web.cern.ch/AccelConf/IPAC10/papers/wepec055.
pdf

[116] **M. Liepe, G. Stedman, and N. Valles**: Robustness of the Superconducting Multicell Cavity Design for the Cornell Energy Recovery Linac, *Proceedings of PAC09, Vancouver, BC, Canada*, TU5PFP048 (2009).
http://accelconf.web.cern.ch/AccelConf/PAC2009/papers/
tu5pfp048.pdf

[117] **G. Bellodi, et al.**: End to End Beam Dynamics and RF Error Studies for Linac4, *Proceedings of LINAC08, Victoria, BC, Canada*, MOP086 (2008).
http://accelconf.web.cern.ch/AccelConf/LINAC08/papers/mop086.
pdf

[118] **D. A. Bartkoski, et al.**: High-Dynamic-Range Current Measurements in The Medium-energy Beta Transport Line at the Spallation Neutron Source, *Proceedings of LINAC06, Knoxville, Tennessee USA*, TUP002 (2006).
http://accelconf.web.cern.ch/AccelConf/l06/PAPERS/TUP002.PDF

[119] **M. Eshraqi**: private communication

[120] **S.-H. Kim, M. Doleans, and R. Sundelin**: HOM findings and HOM induced power in the superconducting linac of the intense pulsed proton accelerator, *Technical note 10*, Oak Ridge National Laboratory (2001).
http://neutrons.ornl.gov/APGroup/Papers/TechNotes/2001/HOM.pdf

[121] **C. L. Bohn and J. R. Delayen**: Cumulative beam breakup in linear accelerators with periodic beam current, *Phys. Rev. A* 45(8):5964 (1992).
http://link.aps.org/doi/10.1103/PhysRevA.45.5964

[122] **J. R. Delayen**: Cumulative beam breakup in linear accelerators with random displacement of cavities and focusing elements, *Phys. Rev. ST AB*

7(7):074402 (2004).
http://link.aps.org/doi/10.1103/PhysRevSTAB.7.07440

[123] **J. R. Delayen**: Cumulative beam breakup in linear accelerators with arbitrary beam current profile, *Phys. Rev. ST AB* 6(8):084402 (2003).
http://link.aps.org/doi/10.1103/PhysRevSTAB.6.084402

[124] **N. Solyak, et al.**: Longitudinal and Transverse Effects of HOMs in the Project X Linac, *Proceedings of IPAC'10, Kyoto, Japan*, TUPEA020 (2010).
http://accelconf.web.cern.ch/AccelConf/IPAC10/papers/tupea020.pdf

[125] **J.-L. Biarrotte**: A Statistical Analysis of the Danger Induced by HOM Excitation in a Superconducting Linacs, *Proceedings of the 2001 Particle Accelerator Conference, Chicago*, MPPH137 (2001).
http://accelconf.web.cern.ch/AccelConf/p01/PAPERS/MPPH137.PDF

[126] **M. Lindroos, C. Oyon, and S. Peggs**: The ESS Superconducting Linear Accelerator, *Proceedings of SRF2009, Berlin, Germany*, FROBAU02 (2009).
http://accelconf.web.cern.ch/AccelConf/SRF2009/papers/frobau02.pdf

[127] **M. Eshraqi, et al.**: Conceptual Design of the ESS LINAC, *Proceedings of IPAC'10, Kyoto, Japan*, MOPD053 (2010).
http://accelconf.web.cern.ch/AccelConf/IPAC10/papers/mopd053.pdf

[128] **R. Calaga**: HOMs in elliptical cavities at 704 MHZ and 1.3 GHz, ESS Frequency Advisory Board Meeting (2010).
http://indico.hep.lu.se//conferenceDisplay.py?confId=1011

[129] **Y. Zhang, I. Campisi, and S. Henderson**: The commissioning of the SNS superconducting linac, *Nucl. Instrum. Methods Phys. Res., Sect. B* 261(1-2):1036 (2007).
http://dx.doi.org/10.1016/j.nimb.2007.04.170

[130] **S.-H. Kim**: SNS Superconducting Linac Operational Experience and Upgrade Path, *Proceedings of LINAC'08, Victoria, BC, Canada*, MO103 (2008).
http://accelconf.web.cern.ch/AccelConf/LINAC08/papers/mo103.pdf

[131] **S.-H. Kim**: Status of the SNS Superconducting Linac and Future Plan, *JKPS* 52(93):714 (2008).
http://dx.doi.org/10.3938/jkps.52.714

[132] **Y. Zhang**: Experience and Lessons with the SNS Superconducting Linac, *Proceedings of IPAC10, Kyoto, Japan*, MOZMH01 (2010).
http://accelconf.web.cern.ch/AccelConf/IPAC10/papers/mozmh01.
pdf

[133] **S.-H. Kim**: HOM Experiences at the SNS SCL, *SPL HOM workshop* (2009).
http://indico.cern.ch/event/57247

[134] **S. Henderson**: SNS Operation at 1 MW and Beyond, *Proceedings of the LINAC'10, Tsukuba, Japan*, MO103 (2010).
http://silver.j-parc.jp/linac10/MO103.PDF

[135] SNS Parameters List, WEB (2005).
http://neutrons.ornl.gov/media/pubs/pdf/sns_parameters_list_
june05.pdf

[136] **J. Galambos**: Cold Linac Commissioning Results, ASAC Review (2005)

[137] **W. J. Schneider, et al.**: Design of the SNS Cryomodules, *Proceedings of the 19th IEEE Particle Accelerator Conference, Chicago, IL, USA*, MPPH162 (2001).
http://accelconf.web.cern.ch/AccelConf/p01/PAPERS/MPPH162.PDF

[138] **S.-H. Kim**: private communication

[139] **G. Ciovati, et al.**: Superconducting Prototype Cavities for the Spallation Neutron Source (SNS) Project, *The 10th Workshop on RF Superconductivity, 2001, Tsukuba, Japan*, PT016 (2001).
http://accelconf.web.cern.ch/AccelConf/srf01/papers/pt016.pdf

[140] LHeC, Homepage (2010.04.14).
http://www.cern.ch/lhec

[141] **F. Willeke, et al.**: A Storage Ring Based Option for the LHeC, *Proceedings of the EPAC08, Genoa, Italy*, WEPP052 (2008).
http://accelconf.web.cern.ch/AccelConf/e08/papers/wepp052.pdf

[142] **M. Fitterer**: privat communication

[143] **F. Stephan, et al.**: Detailed characterization of electron sources yielding first demonstration of European X-ray Free-Electron Laser beam quality, *Phys. Rev. ST AB* 13(2):020704 (2010).
http://link.aps.org/doi/10.1103/PhysRevSTAB.13.020704

[144] **J.-L. Biarrotte**: *Etude de cavités supraconductrices pour les accélérateurs de protons de forte puissance*, Ph.D. thesis, l'université Paris XI Orsay, Université de Paris-Sud U.F.R. Scientifique d'Orsay (2000)

[145] **G. Devanz**: private communication

[146] **E. M. McMillan**: The Relation between Phase Stability and First-Order Focusing in Linear Accelerators, *Phys. Rev.* 80(3):493 (1950).
http://dx.doi.org/10.1103/PhysRev.80.493

[147] **P. Lapostolle, et al.**: A New Dynamics Code DYNAC for Electrons, Protons and Heavy Ions in Linacs with Long Accelerating Elements, *Proceedings of the LINAC'90 Albuquerque, NM, USA*, CERN-PS-90-070-DI (1990).
http://cdsweb.cern.ch/record/211868

Appendix A

Bessel Functions

The Bessel functions named after Friedrich Bessel, who was a mathematician and astronomer in the 19th century, are canonical solutions $y(x)$ of the Bessel's differential equation [51]

$$x^2 \frac{d^2y}{dx^2} + x\frac{dy}{dx} + (x^2 - n^2)y = 0 \tag{A.1}$$

for an real or complex number n, which is the order of the Bessel function. Bessel's function are the solution polynomial for the radial part of the Laplace and Helmholtz equation in cylindrical and spherical coordinates and therefore essential for wave propagation and static potential problems.

As 2nd order equation (A.1) has two independent solutions called Bessel function of first and second kind, conventionally written as J_n and Y_n. Since Y_n diverges at $r = 0$ this partial solution cannot be component of a solution in an accelerating cavity with field at $r = 0$ and J_n remains the only radial solution. According to [51] J_n with integer order can be written as power series

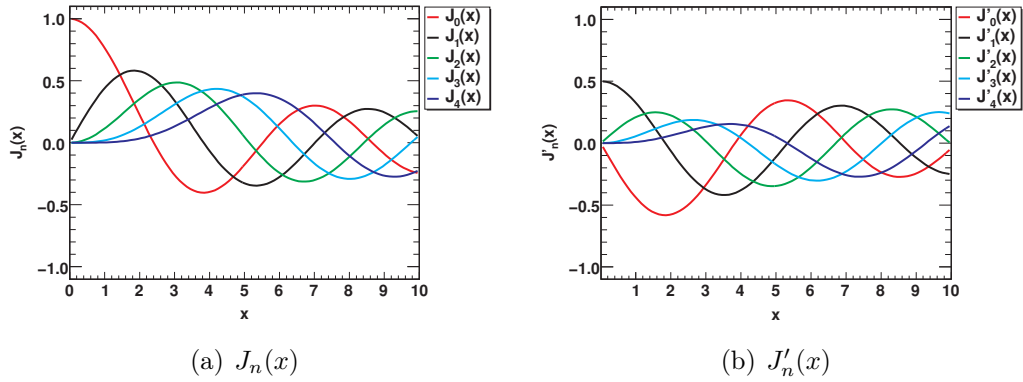$$J_n(x) = \sum_{k=0}^{\infty} \frac{(-1)^k \left(\frac{x}{2}\right)^{n+2k}}{k!\Gamma(n+k+1)} \tag{A.2}$$

where Γ is the Gamma function:

$$\Gamma(x) = \int_0^{\infty} e^{-t^2} t^{x-1} dt \quad (x > 0) \tag{A.3}$$

The first derivative of the J_n can be expressed as

$$\frac{dJ_n(x)}{dx} = -\frac{n}{x}J_n(x) + J_{n-1}(x) \tag{A.4}$$

In Figure A.1 the Bessel function and its derivative are shown up to the 4th order.

(a) $J_n(x)$ (b) $J'_n(x)$

Figure A.1: Plot of the Bessel function first kind and its derivative.

The first roots of the Bessel function and its derivative are listed in Table A.1.

Table A.1: First roots in J_m and J'_m.

| J_m				J'_m			
m	j_{m1}	j_{m2}	j_{m3}	m	j'_{m1}	j'_{m2}	j'_{m3}
0	2.405	5.52	8.654	0	3.832	7.016	10.174
1	3.832	7.016	10.173	1	1.841	5.331	8.536
2	5.136	8.417	11.62	2	3.054	6.706	9.97

Appendix B

Preliminary Symmetric SPL Cavity Design Used in the Beam Dynamics Study

The medium beta cavity is based on [144] and the high beta cavity is a rescaled TESLA cavity [48, 56, 145]. The exact geometries are listed in Table B.1. A HOM analysis was done with HFSS™v11 [90], using post processing scripts [91].

The TM monopole modes, beside the fundamental passband modes and dipole modes with the highest (R/Q) values, found for both cavity families in the considered velocity range, are listed in Table B.2 and B.3. The dipole modes classified as TE modes do also have TM components since pure TE modes do not exist in elliptical cavities due to the openings. This longitudinal E-field component is essential to excite modes. All listed monopole modes are also analysed at β_g using SUPERFISH [84] for comparison. The change of (R/Q) as function of the beam velocity is shown in Fig. B.1. Especially in the medium beta cavity, no mode with a constantly high (R/Q) value can be observed.

197
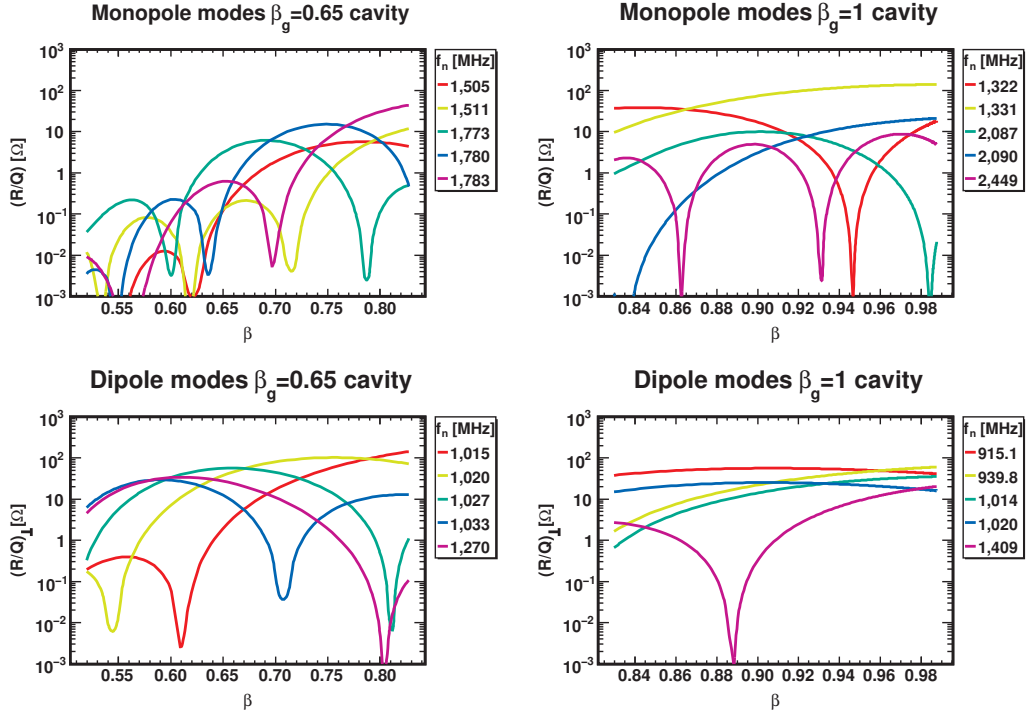
Figure B.1: $(R/Q)(\beta)$ maps of the monopoles and dipoles with high (R/Q) values in the analysed symmetric SPL cavities.
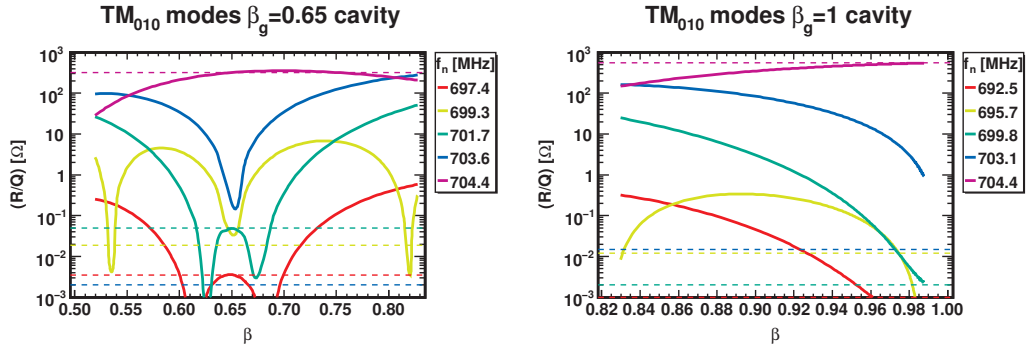
Figure B.2: $(R/Q)(\beta)$ map of the TM_{010} modes in the studied cavity. The dashed line is the (R/Q) value of the mode at the geometrical beta, which can differ several orders of magnitude from the maximum (R/Q) in the covered velocity range.

Table B.1: Shape parameters of the medium and high beta cavities. Both are symmetric 5 cell elliptical SC cavities. All values are given in mm.

Cavity Cell	$\beta_\mathrm{g} = 0.658$ mid	$\beta_\mathrm{g} = 0.658$ end	$\beta_\mathrm{g} = 1$ mid	$\beta_\mathrm{g} = 1$ end
R_arc	186.4	186.4	190.8	190.8
R_iris	45.0	45.0	64.6	70.0
l_cell	70.0	70.0	106.5	103.0
A	45.1	45.1	77.5	76.9
B	45.1	49.6	77.5	74.5
a	12.1	12.1	22.1	18.5
b	15.8	15.7	35.1	24.9

Table B.2: Monopole modes with the highest $(R/Q)(\beta)$ values found in the symmetric SPL cavity shapes. The TM_{010} modes are listed in Table B.4.

Mode	$\beta_\mathrm{g} = 0.65$ f [MHz]	$(R/Q)^\dagger_\mathrm{max}$ $[\Omega]^\ddagger$	Mode	$\beta_\mathrm{g} = 1.0$ f [MHz]	$(R/Q)_\mathrm{max}{}^\dagger$ $[\Omega]^\ddagger$
$TM_{020}, 1/5\pi$	1,505	6	$TM_{011}, 4/5\pi$	1,322	39
$TM_{020}, 2/5\pi$	1,511	12	TM_{011}, π	1,331	140
$TM_{011}, 3/5\pi$	1,773	6	TM_{021}	2,087	10
$TM_{011}, 4/5\pi$	1,780	15	TM_{021}	2,090	21
TM_{011}, π	1,783	44	TM_{022}, π	2,449	9
TM_{01} cutoff	2,550		TM_{01} cutoff	1,639	

† maximum value in covered velocity range; ‡ linac definition

Table B.3: Dipole modes with the highest $(R/Q)_\perp(\beta)$ values found in the symmetric SPL cavity shapes.

Mode	$\beta_\mathrm{g} = 0.65$		Mode	$\beta_\mathrm{g} = 1.0$	
	f [MHz]	$(R/Q)^\dagger_{\perp,\mathrm{max}}$ $[\Omega]^\ddagger$		f [MHz]	$(R/Q)^\dagger_{\perp,\mathrm{max}}$ $[\Omega]^\ddagger$
$\mathrm{TM}_{110}, 1/5\pi$	1,015	143	$\mathrm{TE}_{111}, 3/5\pi$	915	57
$\mathrm{TM}_{110}, 2/5\pi$	1,020	107	$\mathrm{TE}_{111}, 4/5\pi$	940	60
$\mathrm{TM}_{111}, 3/5\pi$	1,027	57	TM_{110}	1,014	36
$\mathrm{TM}_{110}, 4/5\pi$	1,033	30	TM_{110}	1,020	25
$\mathrm{TE}_{111}, 1/5\pi$	1,270	34	Hybrid	1,409	20
TE_{11} cutoff	1,952		TE_{11} cutoff	1255	

† maximum value in covered velocity range; ‡ linac definition

Table B.4: TM_{010} passband modes - SUPERFISH results.

Cavity	$\beta_\mathrm{g} = 0.65$		$\beta_\mathrm{g} = 1.0$	
Mode	f_n [MHz]	$(R/Q)(\beta_\mathrm{g})$ $[\Omega]^\dagger$	f_n [MHz]	$(R/Q)(\beta_\mathrm{g})$ $[\Omega]^\dagger$
$TM_{010}, 0$	697.4	0.003	692.6	0.001
$TM_{010}, 2/5\pi$	699.3	0.019	695.7	0.012
$TM_{010}, 3/5\pi$	701.7	0.049	699.8	0.002
$TM_{010}, 4/5\pi$	703.7	0.002	703.1	0.015
TM_{010}, π	704.4	318.773	704.4	561.928

† linac definition

Appendix C

General Beam Dynamics in an Ion Linear Accelerator

The beam can be represented in six-dimensional phase space by two sets of 3-dimensional coordinates p and q. These coordinates are conjugated, if they satisfy the conditions for each component i

$$\frac{\partial q_i}{\partial t} = \frac{\partial H}{\partial p_i} \quad \text{and} \quad \frac{\partial p_i}{\partial t} = -\frac{\partial H}{\partial q_i} \quad i \in 0, 1, 2 \tag{C.1}$$

where $H = H(p, q, t)$ is a function called *Hamiltonian*. p is the momentum of a particle and q its position.

The conjugate coordinates of the beam particles occupy a volume in phase space which is constant under conservative forces according to *Liouville's theorem*. The 6-D space can be analysed through its two-dimensional phase plane projections. Each projection contains one p component and the corresponding q component. They can be represented by ellipses, assuming linear equations of motions with a constant surface in case there is no coupling between the individual planes. This area is called *normalised emittance*. The position x and the divergence x' are not conjugated and nor is the corresponding emittance. By multiplying with $\beta\gamma$ these variables can be normalised. In beam dynamics, one usually establishes equations of motion in the longitudinal and transverse phase planes [45].

The general beam dynamics in an ion linear accelerator, separated into longitudinal and transverse motion is discussed here. Most of the expressions are taken from [44, 45]. A more general introduction into the beam dynamics in accelerators can be found in various textbooks such as for example [5, 6, 98–100].

C.1   Longitudinal Beam Dynamics

Longitudinal and transverse particle motion can be treated independently to first order. There is a major difference in the longitudinal beam dynamics between electron and ion linacs due the to mass difference of the particles, which leads to a different velocity evolution in the linac. Electrons can be treated as ultra relativistic ($\beta = 1$) already at moderate energy ($W = 10\,\mathrm{MeV} \hat{=} \beta = 0.99$). This has to be taken into account in the beam dynamics.

First, a *synchronous particle* is defined, which travels in perfect synchronism with the RF system through the accelerating structure. It is referred to as the design particle ina linear accelerator. All other particles are defined relative to the synchronous one. For a high current beam the trajectories around the synchronous particle must be stable and a longitudinal focusing is required, which is realized by choosing the synchronous phase as shown in Fig.C.1.
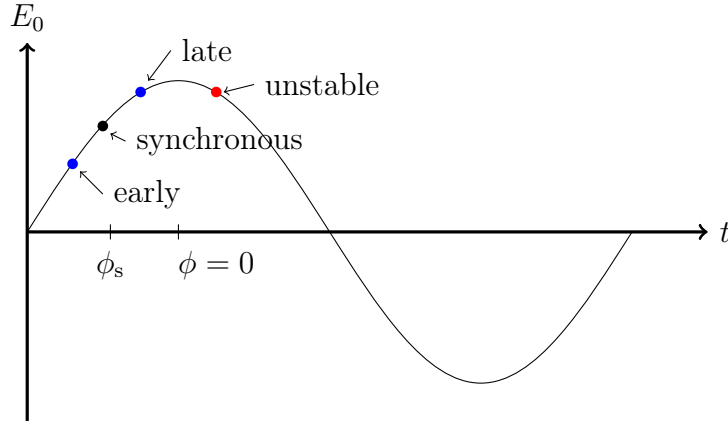
Figure C.1: Field evolution. Stable synchronous phase ϕ_s marked is marked.

Particles arriving later than the synchronous particle in an accelerating element are accelerated more due to the smaller $|\phi|$ and the high resulting field. Particles arriving earlier than the synchronous particle are accelerated less. This lead to a longitudinal focusing. The acceleration is maximum at $\phi = 0°$ and zero at $\phi = -90°$.

An $e^\pm$ linac operates on crest ($\phi = 0$), because an energy deviation does not lead to a time of flight variation as it is the case for ions hence less longitudinal focusing is needed. In an ion linac with operates with $-90° < \phi_\mathrm{s} < 0°$. In circular machines, in contrast to linacs the origin of the phase is normally set to the zero crossing of the field and not the crest.

The general relation between an arbitrary particle and the synchronous one

are discussed in the next subsection and analytic boundary conditions for stable operations are derived.

C.1.1   Synchrotron Equations in an Ion Linac

For simplification the formulae are derived for an arbitrary particle with mass m and charge q.

An arbitrary particle receives a different energy gain travelling through an accelerating gap with length l and a different phase ϕ than the synchronous particle (ϕ_s). This can be expressed by

$$\Delta W = qE_0 T(\beta) l (\cos(\phi) - \cos(\phi_s)), \tag{C.2}$$

where $E_0 T(\beta)$ the effective energy gain taking into account the transit time factor of the particle with a velocity of βc.

More interesting than the energy difference after one gap is the energy difference after the complete linac to determine the energy spread of the particles afterwards. Therefore a continuous acceleration is assumed and the variation of ΔW along the axis s is then

$$\frac{d}{ds} \Delta W = qE_0 T (\cos(\phi_s + \Delta\phi) - \cos(\phi_s)), \tag{C.3}$$

where $\Delta\phi = \phi - \phi_s$ is the difference in phase between the test particle and the synchronous one. The effect of transit time factor changes due to velocity changes of the arbitrary particle that lead to a different energy gain, is not considered here. The variation of $\Delta\phi$ with s is

$$\frac{d}{ds} \Delta\phi = \omega \left(\frac{dt}{ds} - \frac{dt_s}{ds} \right) = \frac{\omega}{c} \left(\frac{1}{\beta} - \frac{1}{\beta_s} \right) \cong -\frac{\omega}{\beta_s c} \frac{\Delta\beta}{\beta_s} = -\frac{\omega}{mc^3 \beta_s^3 \gamma_s^3} \Delta W. \tag{C.4}$$

Equation (C.3) and (C.4) are coupled differential equations and are called *synchrotron equations*. For a constant frequency ω, ΔW, and $\Delta\phi$ are *canonically conjugate variables*. Linearising (C.3) using $\cos(\phi_s + \Delta\phi) - \cos(\phi_s) \approx -\Delta\phi \sin(\phi_s)$, which is valid for $\Delta\phi << 1$, leads to

$$\frac{d}{ds} \Delta W = b^2(s) \cdot \Delta\phi, \quad \frac{d}{ds} \Delta\phi = -a^2(s) \cdot \Delta W, \tag{C.5}$$

where $a(s)$ and $b(s)$ are defined by the linearised equations (C.3) and (C.4). Because of the slow variation of $a(s)$ and $b(s)$ with s, ds can be eliminated and one gets the equation of an ellipse

$$\frac{(\Delta\phi)^2}{a^2} + \frac{(\Delta W)^2}{b^2} = \text{const}, \tag{C.6}$$

which represents the phase space plane of ΔW and $\Delta \phi$ for small $\Delta \phi$. It is referred to as *longitudinal emittance* $\epsilon_l(\Delta W, \Delta \phi)$ and is normalised. The axis ratio of this ellipse is

$$\frac{\Delta \hat{W}}{\Delta \hat{\phi}} = \frac{b}{a} = \sqrt{\frac{-mc^3 \beta_s^3 \gamma_s^3 q E_0 T \sin(\phi_s)}{\omega}} \propto (\beta \gamma)^{\frac{3}{2}} \qquad (C.7)$$

From (C.5) a second order differential equation of the type

$$\frac{d^2}{du^2} \Delta \phi + K(u) \Delta \phi = 0 \qquad (C.8)$$

can be obtained, where $K(u)$ varies very slowly with u. This second order differential equation can be solved analytically and the solution is

$$\Delta \phi(s) = C \cdot \Delta \hat{\phi}(s) \cdot \sin \left(\int_0^s k_s(s') ds' + \phi_0 \right), \qquad (C.9)$$

where C and ϕ_0 are integration constants and k_s the phase advance per unit length. If the phase oscillations are small, k_s is

$$k_s(s) = \frac{2\pi}{\Lambda_s(s)} = \left[\frac{-\omega q E_0 T \sin(\phi_s)}{mc^3 \beta_s^3 \gamma_s^3} \right]^{\frac{1}{2}} \propto (\beta_s \gamma_s)^{-\frac{3}{2}} \qquad (C.10)$$

where $\Lambda_s(s)$ is the *synchrotron wavelength*. The amplitude of the small phase oscillation is then

$$\Delta \hat{\phi}(s) \propto \left[\frac{-mc^3}{\omega q E_0 T \sin(\phi_s) \beta_s^3 \gamma_s^3} \right]^{\frac{1}{4}} \propto (\beta_s \gamma_s)^{-\frac{3}{4}}. \qquad (C.11)$$

The phase excursion of $\Delta \hat{\phi}(s)$ decreases during acceleration which is called *adiabatic phase damping*. The synchronous phase advance k_s decreases also while the energy spread increases with $\Delta W \propto (\beta_s \gamma_s)^{\frac{3}{4}}$.

Using (C.3) and (C.4) without linearisation, but assuming β_s , $\gamma_s \hat{=}$ constant the following second order differential equation is obtained

$$\frac{d^2}{ds^2} \Delta \phi + \frac{-\omega q E_0 T}{mc^3 \beta_s^3 \gamma_s^3} \left[\cos(\phi_s + \Delta \phi) - \cos(\phi_s) \right] = 0 \qquad (C.12)$$

which can be transformed to

$$\frac{d}{ds} \left[\frac{1}{2} \left(\frac{d\Delta \phi}{ds} \right)^2 + U(\Delta \phi) \right] = 0 \qquad (C.13)$$

where the expression in the brackets is constant and is called the *total energy of oscillation H* and is a Hamiltonian. Having a closer look on the potential $U(\Delta \phi)$,

which has got a potential well for $-\pi < \phi_{\mathrm{s}} < 0$ and two fixed points (extrema: $\frac{dU(\Delta\phi)}{d\Delta\phi} = 0$); one stable at $\Delta\phi = 0$ (minimum) and one unstable at $\Delta\phi = -2\phi_{\mathrm{s}}$ (maximum).

The total energy H can be written as

$$\frac{\omega}{mc^3\beta_{\mathrm{s}}^3\gamma_{\mathrm{s}}^3}\left\{\frac{\omega}{2mc^3\beta_{\mathrm{s}}^3\gamma_{\mathrm{s}}^3}(\Delta W)^2 + qE_0T\left[\sin(\phi_{\mathrm{s}} + \Delta\phi) - \Delta\phi\cos(\phi_{\mathrm{s}}) - \sin(\phi_{\mathrm{s}})\right]\right\} = H \tag{C.14}$$

by using (C.4) and requiring $U(0) = 0$. There is a trajectory for each H in the ($\Delta\phi$, ΔW) phase plane. The trajectory for $H = H_{max} = U(-2\phi_{\mathrm{s}})$ is called *separatrix*

$$\frac{\omega}{2mc^3\beta_{\mathrm{s}}^3\gamma_{\mathrm{s}}^3}(\Delta W)^2 + qE_0T\left[\sin(\phi_{\mathrm{s}} + \Delta\phi) + \sin(\phi_{\mathrm{s}}) - (2\phi_{\mathrm{s}} + \Delta\phi)\cos(\phi_{\mathrm{s}})\right] = 0. \tag{C.15}$$

The area inside the separatrix is called *bucket* and extends from $\Delta\phi \cong -2|\phi_{\mathrm{s}}|$ to $\Delta\phi_{\mathrm{s}} = +|\phi_{\mathrm{s}}|$, hence over $3|\phi_{\mathrm{s}}|$. Particles inside the bucket stay there and is the phase space area which is used for stable acceleration. Particles outside the buckets cannot be stable accelerated and are lost.

The separatrix, the corresponding potential and accelerating field are illustrated in Figure C.2.

In case of $\phi_{\mathrm{s}} = -90°$ the phase acceptance is maximum, extending over the full $360°$ as shown in Figure C.3, but there is no acceleration. The other extrema is $\phi_{\mathrm{s}} = 0°$, where the phase acceptance vanishes and acceleration is maximised.

For $\Delta\phi = 0$ the maximum allowed ΔW on the separatrix is:

$$\Delta\hat{W}_{max} = \pm 2\left[\frac{mc^3qE_0T(\phi_{\mathrm{s}}\cos(\phi_{\mathrm{s}}) - \sin(\phi_{\mathrm{s}}))\beta_{\mathrm{s}}^3\gamma_{\mathrm{s}}^3}{\omega}\right]^{\frac{1}{2}} \tag{C.16}$$

The separatrix is derived under the assumption that β_{s}, $\gamma_{\mathrm{s}} \hat{=}$ constant. In this case a *stationary bucket* is obtained. Taking into account energy variation along the linac the bucket shape transforms to a golf club shape as illustrated in Figure C.4

C.1.2   Adiabatic Phase Damping

Assuming a small acceleration rate, the parameters of the phase space ellipses for small oscillations vary slowly. As described previously the phase space ellipse area is an adiabatic invariant during the acceleration process and the area can be expressed as

$$\text{Area} = \pi\Delta W\Delta\phi = \Delta\phi^2\sqrt{qE_0Tmc^3\beta_{\mathrm{s}}^3\gamma_{\mathrm{s}}^3\sin(-\phi_{\mathrm{s}})/\omega} \tag{C.17}$$
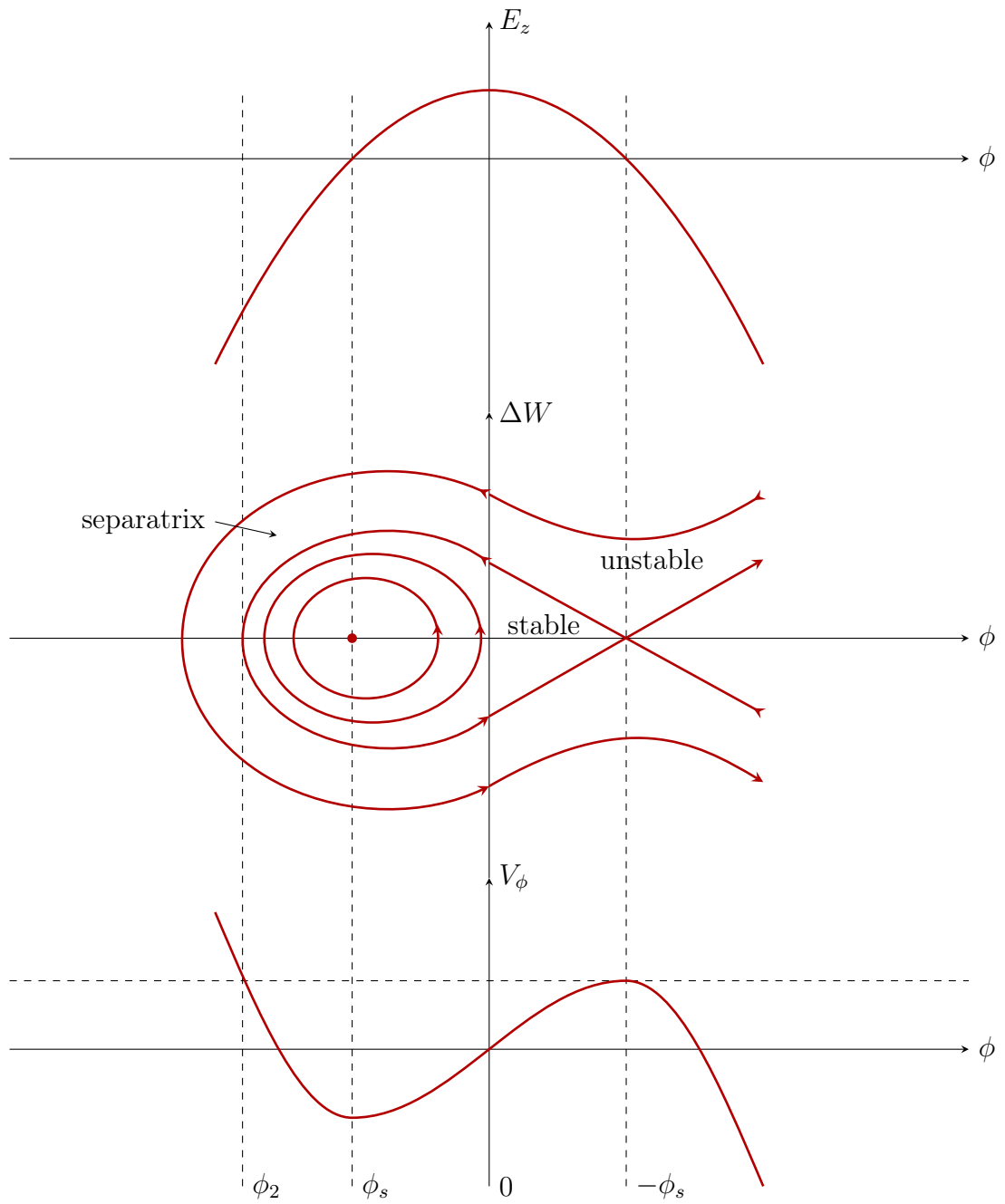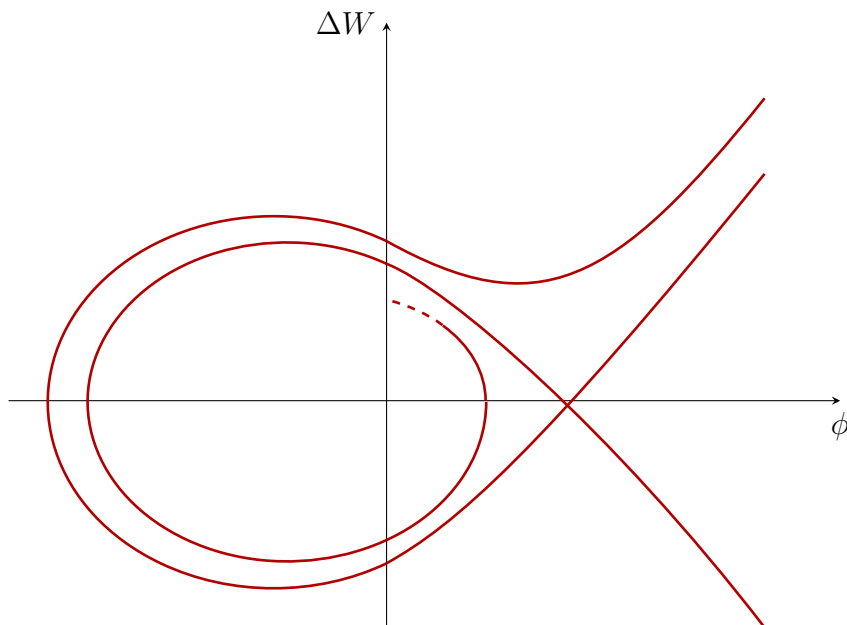
Figure C.2: Stationary separatrix. Accelerating field, corresponding separatrix, and potential well of the synchrotron oscillation.
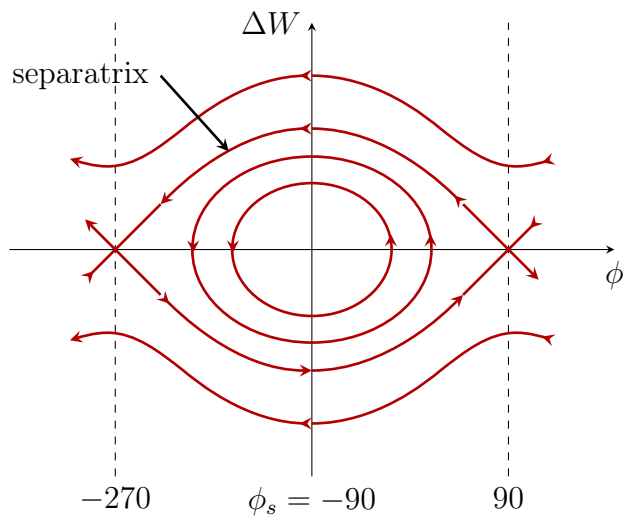
Figure C.3: Separatrix with $\phi_\mathrm{s} = 90°$, where phase acceptance is at is maximum and no acceleration takes place.

Figure C.4: Dynamic separatrix. It has the shape of a golf club when acceleration is taken into account.

or

$$\Delta\phi = \text{const} \cdot \left[qE_0 Tmc^3 \beta_s^3 \gamma_s^3 \sin(-\phi_s)/\omega \right]^{-1/4} \tag{C.18}$$
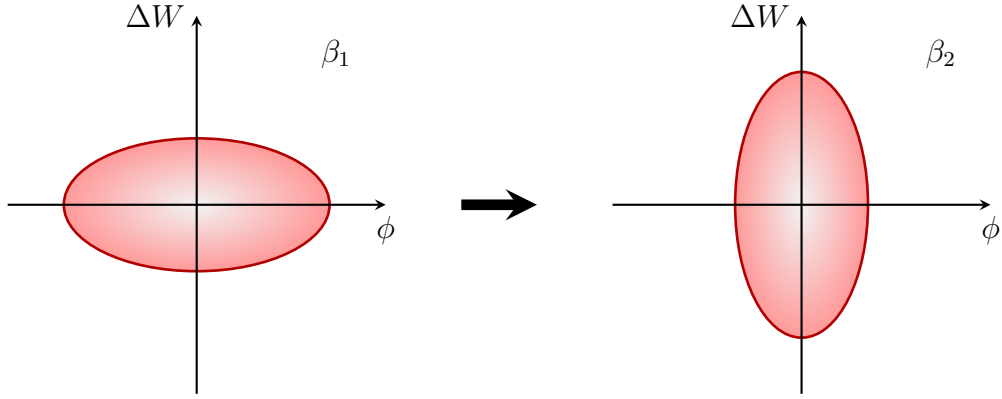
If accelerating field and synchronous phase are fixed one gets

$$\Delta\phi = \frac{\text{const}}{\left(\beta_s\gamma_s\right)^{3/4}} \tag{C.19}$$

and accordingly

$$\Delta W = \text{const} \cdot \left(\beta_s\gamma_s\right)^{3/4} . \tag{C.20}$$

These results describe a decrease of the phase amplitude and an increase of the energy amplitude of the phase oscillations during acceleration in a linac. This process is illustrated in Figure C.5.

Figure C.5: Adiabatic phase damping. Phase damping of the longitudinal beam ellipse by acceleration. The phase width decreases while the energy width increases. The area of the ellipse stays constant.

C.1.3 Zero Current Longitudinal Phase Advance

The RF system provides a longitudinal focusing force on the beam as shown in subsection C.1.1. A measure of the focusing strength is the longitudinal phase advance (C.10).

A linac consist of periodic structures (periods), e.g. a doublet of magnets and several cavities hosted in one or several cyro-modules. Particles passing a focusing period of the linac are moving a certain angle in phase space. For beam stability reasons, this angle should not succeed 90°, otherwise a coupling to the other planes

occurs which can drive instabilities. The angle can be directly calculated from (C.10), assuming that space charge effects are neglected

$$\sigma_{\mathrm{l}} = k_{l0} l_{Period} = \sqrt{\frac{\omega q E_0 T \sin(-\phi_{\mathrm{s}})}{mc^3 \beta_{\mathrm{s}}^3 \gamma_{\mathrm{s}}^3}} l_{\mathrm{Period}}. \tag{C.21}$$

This angle strongly depends on the particle's kinetic energy and shrinks with increasing energy. Hence, it has got its maximum at the entrance of each linac section. In order to decrease the phase advance in the beginning of a section, the accelerating gradient $E_0 T$ of the cavities has to be reduced.

Space charge effects are not included here, which is commonly indicated by the term "zero current". Introducing space charge, the rotation velocity in phase space is reduced and is not discussed here. Further information on this topic can be found in [98, chap. 3].

C.2 Transverse Beam Dynamics

Special measures must be taken to confine the particles close to the beam axis either by additional focusing with for example static electromagnetic fields or special shaped RF structures, which simultaneously accelerate and focus the particles.

There are three main sources that give rise to transverse beam defocusing in a linear accelerator according to [44, 98].

1. Transverse thermal motion of the particles.

2. Defocusing action of the RF field inside the cavities.

3. Electric repulsion of particles of the same charge, so called space charge effects.

The last source is considered to be a second order effect and is not covered in this thesis. The second source can be split into two effects, the defocusing forces introduced by the accelerating mode, which is discussed in the next subsection and deflecting higher order modes such as dipole modes which are one major subject in this thesis and is discussed in chapter 6.

After discussing the transverse effects of the RF structures and electromagnetic lenses, the transfer function formalism is introduced. This describes all focusing and defocusing elements in a systematic way.

All formulae introduced in this section assume perfect magnets without fringe fields and that the magnets are perfectly aligned. The effects introduced by magnet errors and their analytical or numerical description as well as their compensation is covered in textbooks [44, 100]. Here, only the linear beam dynamics is discussed.

C.2.1   Transverse RF Focusing and Defocusing

The electric field lines of the accelerating mode inside an accelerating cell are not perfectly parallel to the beam axis as illustrated in Figure C.6. The net transverse effect is non zero for particles travelling with a speed less than the speed of light and is the result of three possible mechanisms:

1. Field variations as function of the time while the particle crosses the cell.

2. Field depends on the radial displacement of the particle, which is not necessarily constant.

3. Particle velocity increases, that leads to a different time of flight in the first and second half of the cell
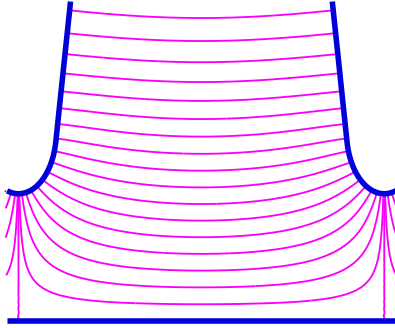
(a) Equipotential lines of the electric field
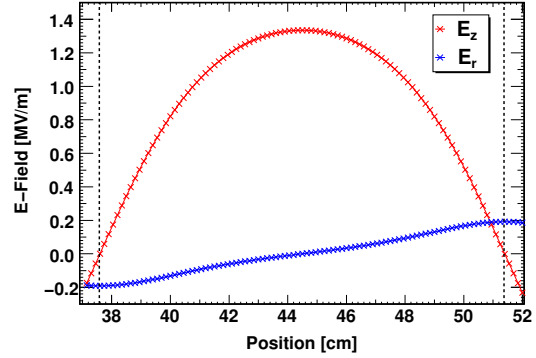
(b) Off-axis field components

Figure C.6: Electric field inside an accelerating cell. The field (a) and the field components on an off axis path at distance 1 cm (b). The data is taken from a SUPERFISH simulation of the accelerating mode in the mid cell of a five cell $\beta_\mathrm{g} = 0.65$ SRF elliptical cavity. The field lines bend towards the cell iris and introduce a radial field component off axis.

In ion linacs the first item is the dominant mechanism since ϕ_s must be negative for stable operation in the longitudinal plane. This leads to a rising field, while the particle is passing the accelerating cell and is known as *RF defocusing force*. In [146] it is shown that longitudinal focusing which requires a rising RF field with time, is incompatible with radial focusing at the same time. This becomes also clear by looking at the Laplace's equations in the rest frame of the particle, where only electrostatic forces are present

$$\frac{\partial^2 V}{\partial x^2} + \frac{\partial^2 V}{\partial y^2} + \frac{\partial^2 V}{\partial z^2} = 0. \tag{C.22}$$

If the longitudinal force provides a focusing at a given point the two transverse components cannot both provide also a focusing force at the same point in order to fulfil (C.22).

In a travelling wave structure the radial Lorentz force component is

$$\frac{dp_r}{dt} = q(E_r - \beta c B_\theta) \tag{C.23}$$

Using a smooth focusing approach in which the transverse impulse is replaced by an average effective force that acts continuously on the beam, one can develop a smoothed differential equation of motion with $\beta \approx \beta_\mathrm{s}$

$$\frac{1}{\gamma_\mathrm{s}\beta_\mathrm{s}}\frac{d}{ds}\gamma_\mathrm{s}\beta_\mathrm{s}r' - \frac{k_{l0}^2}{2}r = 0, \tag{C.24}$$

where

$$k_{l0}^2 = \frac{2\pi q E_0 T \sin(-\phi)}{mc^2\lambda(\gamma\beta)^3} \tag{C.25}$$

is the longitudinal wave number.

There are several other approaches to describe this effect in more detail. These are discussed in [44]. A very compact and elegant method to describe the transverse motion in an accelerating structure close to the beam axis is introduced by Lapostolle [45, 147], using a reduced radius $R = r\sqrt{\beta\gamma}$

$$\frac{\mathrm{d}^2 R}{\mathrm{d}z^2} = \left[\frac{q}{2m_0c^2(\beta\gamma)^3}\frac{\partial E_\mathrm{z}}{\partial t} - \frac{(\gamma+2)}{(\beta\gamma)^4}\left(\frac{q}{2m_0c^2}\right)^2 E_\mathrm{z}^2\right] R. \tag{C.26}$$

The first term on the right hand side is the RF defocusing term and the second term is the electrostatic term. Dependent on the particle mass and kinetic energy either the electrostatic term or the RF defocusing term is dominant.

C.2.2 Focusing with Quadrupole Fields

Electromagnetic lenses are used to compensate transverse RF defocusing effects as well as dipole kicks and keep the beam focused in the transverse plane. At very low energy, electric fields are more effective than magnetic fields, which can be shown by looking at the Lorentz force. At higher energy magnets are used for the focusing. The field pattern inside a quadrupole magnet and a electrostatic quadrupole are shown in figure C.7

In an ideal quadrupole the transverse field gradient is constant

$$G = \frac{\partial B_x}{\partial y} = \frac{\partial B_y}{\partial x} \tag{C.27}$$

(a) Magnetic quadrupole   (b) Electric quadrupole
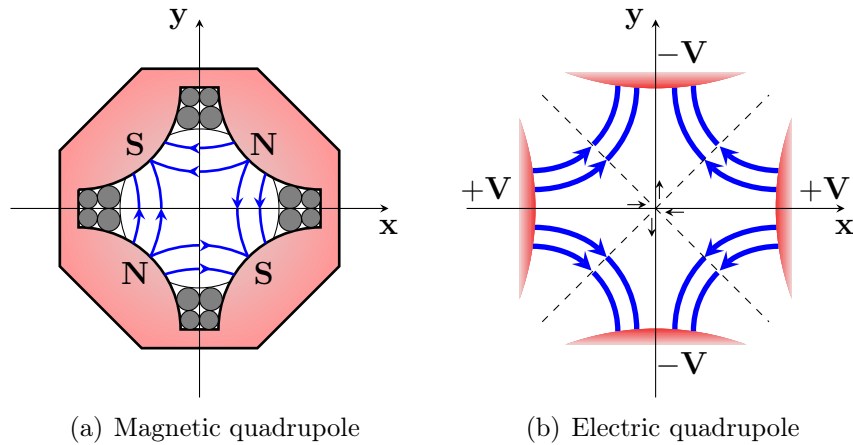
Figure C.7: Field distribution in a magnetic and electric quadrupole.

The Lorentz force components are then given by

$$F_x = -qvGx \quad F_y = qvGy \tag{C.28}$$

for particles moving along the z-axis with velocity v and at a transverse position (x, y). The particles get focused in one plane and defocused in the other. To reach an overall focusing in both transverse planes at least two quadruples with different polarity have to be used. The trajectory through a pair of quadrupole magnets is illustrated in Figure C.8.

(a) Focusing-Defocusing   (b) Defocusing-Focusing
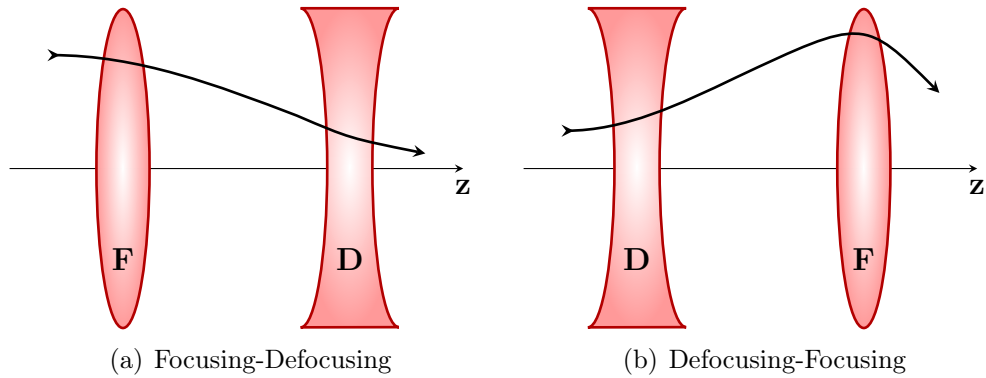
Figure C.8: Quadrupole focusing. Trajectories along the main axis through a pair of quadrupole magnets with opposite polarities. In (a) the particle is first bend towards the axis and then away from the axis, vice versa in (b).

The equations of motion of a particle at an axial position s, at (x,y) with

velocity $v = \beta c$ through a perfect quadrupole are then

$$\frac{d^2x}{ds^2} + \kappa^2(s)x = 0, \quad \text{and} \quad \frac{d^2y}{ds^2} - \kappa(s)y = 0, \tag{C.29}$$

where

$$\kappa^2(s) = \frac{qG(s)}{mc\gamma\beta}. \tag{C.30}$$

Including the quadrupole term of the RF defocusing in (C.29), using (C.24) and (C.25), this leads to

$$\frac{d^2x}{ds^2} + \kappa^2(s)x - \frac{k_{l0}^2}{2}x = 0, \quad \text{and} \quad \frac{d^2y}{ds^2} - \kappa(s)y - \frac{k_{l0}^2}{2}y = 0 \tag{C.31}$$

Typically, the quadrupole magnets are arranged in a regular lattice. Therefore different configurations exist such as for example FODO, FOFODODO or FDO (*doublet*). F stands for focusing, D for defocusing and O for the drift space in between, where for example the accelerating cavities are located. Such structure is referred to as *lattice*.

Equation (C.31) is an example of *Hill's equation* and has the general form

$$x'' + K(s)x = 0 \tag{C.32}$$

It is based on a restoring force that is a linear function of the displacement from the equilibrium orbit. In a linac with an ideal focusing lattice it can be normalised to

$$\frac{d^2x}{d\tau^2} + \left(\theta_0^2 F(\tau) + \Delta\right)x = 0 \tag{C.33}$$

where $\theta_0^2 = q\beta G\lambda^2/\gamma mc$ is a dimensionless measure of the quadrupole focusing strength, $\Delta = \pi q E_0 T\lambda\sin(-\phi)/\gamma^3 mc^2\beta$ is a dimensionless measure of the RF defocusing force, $\tau = s/\beta\lambda$ is the normalised axis variable and $F(\tau) = -1, 0, 1$ the periodic function. To get the equation for y, $F(\tau)$ has to be replaced by $-F(\tau)$.

C.2.3   Transfer Matrix Method

The particle motion in the transverse plane with a periodic focusing structure can be described by the Hill's equation (C.32). A possible way to display the solution of this linear second order differential equation is a 2×2 matrix representation, the so-called *transfer matrix*, which describes the change in position and momentum of a particle passing through an accelerator element such as for example a drift space or a magnet. It can be shown that the determinate of the transfer matrix

M is unity and the criteria for stability is $|\text{Tr}M| < 2$, where $\text{Tr}M$ is the trace of the transfer matrix.

$$\begin{pmatrix} x \\ x' \end{pmatrix} = \begin{pmatrix} a & b \\ c & d \end{pmatrix} \begin{pmatrix} x_0 \\ x_0' \end{pmatrix} \tag{C.34}$$

A list of some elements and their transfer matrix is given in [44].

- Drift space:

$$M = \begin{pmatrix} 1 & l \\ 0 & 1 \end{pmatrix} \tag{C.35}$$

- Focusing Quadrupole: $K = \frac{qG_q}{mc\beta\gamma} > 0$

$$M = \begin{pmatrix} \cos\left(\sqrt{K}l\right) & \frac{1}{\sqrt{K}}\sin\left(\sqrt{K}l\right) \\ -\sqrt{K}\sin\left(\sqrt{K}l\right) & \cos\left(\sqrt{K}l\right) \end{pmatrix} \tag{C.36}$$

where l is the length of the element and G_q the quadrupole field gradient.

- Defocusing Quadrupole: $K = \frac{qG_q}{mc\beta\gamma} < 0$

$$M = \begin{pmatrix} \cosh\left(\sqrt{|K|}l\right) & \frac{1}{\sqrt{|K|}}\sinh\left(\sqrt{|K|}l\right) \\ \sqrt{|K|}\sinh\left(\sqrt{|K|}l\right) & \cosh\left(\sqrt{|K|}l\right) \end{pmatrix} \tag{C.37}$$

- Thin lens approximation of a quadrupole:

$$M = \begin{pmatrix} 1 & 0 \\ \pm\frac{1}{f} & 1 \end{pmatrix} \tag{C.38}$$

where f is the focal length and is defined as $\frac{1}{f} = |K|l = \frac{|qG_q|l}{mc\beta\gamma}$. The positive sign corresponds to defocusing and the negative sign to focusing. The thin-lens approximation is valid, if $\sqrt{|K|}l \to 0$ while $|K|l$ stays finite.

The transfer matrix of several elements can be obtained by multiplying the matrices of the single elements $M = M_n...M_3M_2M_1$, when the beam passes through these elements in the order $1, 2, 3, ..., n$. The order is important since the matrices of single elements are not commutative ($M_1M_2 \neq M_2M_1$).

C.2.4 Twiss Parameters

Is case $K(s)$ is a periodic function, Hill's equation has a solution similar to that of a harmonic oscillator and its general solution is called *phase-amplitude from*

$$x(s) = \sqrt{\epsilon_1 \tilde{\beta}(s)} \cos(\phi(s) + \phi_1), \tag{C.39}$$

where $\tilde{\beta}(s)$ and $\phi(s)$ are called *amplitude* and *phase* function, and ϵ_1 and ϕ_1 are constants determined by the initial conditions. The relation between $\tilde{\beta}(s)$ and $\phi(s)$ is

$$\phi(s) = \int \frac{ds}{\tilde{\beta}(s)}. \tag{C.40}$$

It is useful to introduce two additional functions

$$\tilde{\alpha}(s) = \frac{1}{2} \frac{d\tilde{\beta}(s)}{ds} \tag{C.41}$$

$$\tilde{\gamma}(s) = \frac{1 + \tilde{\alpha}(s)}{\tilde{\beta}(s)}. \tag{C.42}$$

The set of functions $\tilde{\alpha}(s)$, $\tilde{\beta}(s)$, and $\tilde{\gamma}(s)$ are called *Twiss* or *Courant-Snyder parameters* and are periodic functions with the same period length as $K(s)$. $\tilde{\beta}(s)$ and $\tilde{\gamma}(s)$ are always positive and the coordinates x and x' fulfil the the ellipse equation

$$\tilde{\gamma}(s)x^2 + 2\tilde{\alpha}(s)xx\prime + \tilde{\beta}(s)x'^2 = \epsilon_1 \tag{C.43}$$

with an invariant area $A = \pi\epsilon_1$ with respect to s.

The transfer matrix P through one focusing period is then

$$P \equiv M(s \to sP) = \begin{pmatrix} \cos\sigma + \tilde{\alpha}\sin\sigma & \tilde{\beta}\sin\sigma \\ -\tilde{\gamma}\sin\sigma & \cos\sigma - \tilde{\alpha}\sin\sigma \end{pmatrix} \tag{C.44}$$

where $\sigma = \Delta\phi$ is the phase advance per period. To satisfy the stability requirements and not to focus too weak or too strong, the phase advance per period must be $0 < \sigma < \pi$. The phase advance per period length L depends on the $\tilde{\beta}$ function as

$$\sigma = \int^L \frac{ds}{\tilde{\beta}(s)} \tag{C.45}$$

and the average $\tilde{\beta}$ value over the period L is $< \tilde{\beta} >= L/\sigma$.

From (C.44) the Twiss parameters and the phase advance per period can be calculated by transporting two orthogonal trajectories over a full period using transfer matrices, starting at any location s, and comparing the matrix elements.

C.2.5   Smooth Focusing Approximation

A smooth focusing approximation can be introduced to simplify the description of the periodic transverse focusing. There, the rapid flutter, introduced by the individual lenses, is averaged over a full focusing period. The effective focusing over a period can be obtained by calculating the transfer matrix of a complete period, including all focusing elements and RF defocusing using thin lens approximation. The focal length of a quadrupole is given according to [44] by

$$\frac{1}{f_Q} = \frac{\Delta x'}{x} = \pm \frac{qGl}{mc\gamma\lambda} \tag{C.46}$$

and the focal length of an RF cell is given by

$$\frac{1}{f_g} = \frac{\Delta x'}{x} = \frac{\pi q E_0 T \sin(-\phi) L}{mc^2 \lambda (\gamma\beta)^3}, \tag{C.47}$$

where L is the length over which the RF pulse is integrated.

In case of a FODO lattice with length L between the lenses and a period length of $2L$, the phase advance per period is then

$$\sigma_0^2 \cong \left[\frac{qGlL}{mc\gamma\lambda} \right]^2 - \frac{\pi q E_0 T \sin(-\phi)(2L)^2}{mc^2 \lambda (\gamma\beta)^3} \tag{C.48}$$

and the smoothed wave number

$$k_0^2 = \left(\frac{\sigma_0}{2L}\right)^2 \cong \left[\frac{qGl}{2mc\gamma\lambda} \right]^2 - \frac{\pi q E_0 T \sin(-\phi)}{mc^2 \lambda (\gamma\beta)^3} \tag{C.49}$$

which is independent of L in this lowest order approximation. The same can be done for other lattices. Linac design tools such as for example *GenLinWin* in combination with *TraceWin* [108] can be used to built up the lattice and derive the phase advance per period, which can then be used for general beam dynamics simulations.

With this approach a drift kick model of a linac can be build up, where the beam-HOM interaction takes place at the cavity mid-plane and particles are transported from cavity n to the cavity $n+1$ with the following transfer matrix

$$M_n = \begin{pmatrix} \cos(l_n k_0) & \sin(l_n k_0)/k_0 \\ -k_0 \sin(l_n k_0) & \cos(l_n k_0) \end{pmatrix} \tag{C.50}$$

where l_n is the distance between the cavities.